Universität Bremen

Response of Southwest Pacific storminess to changing climate

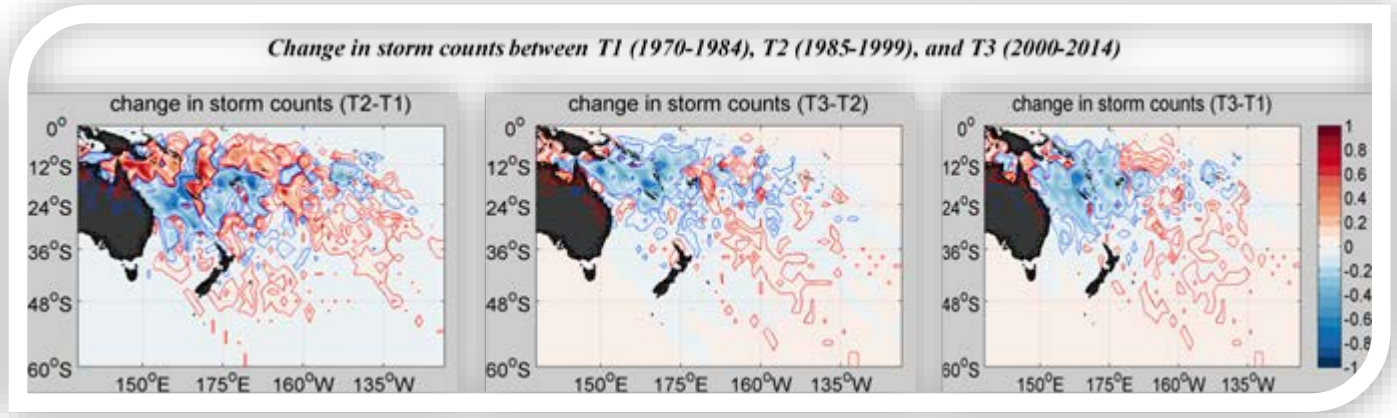

January 14, 2019

Nilima Aditya Natoo
Universität Bremen

marum
Zentrum für Marine Umweltwissenschaften

INTERCOAST

This page has been intentionally left blank

Response of Southwest Pacific storminess to changing climate

Dissertation

zur Erlangung des Doktorgrades der Naturwissenschaften
submitted in partial fulfilment of the requirements for the doctoral degree in natural sciences

Dr. rer. nat.

im Fachbereich 5 (Geowissenschaften) der Universität Bremen
in the Faculty of Geosciences of the University of Bremen

vorgelegt von
by
Nilima Aditya Natoo
14th January 2019

Tag des kolloquiums
Date of colloquium
5th July 2019

Gutachter
Reviewers
Prof. Dr. Michael Schulz (University of Bremen, Germany)
Prof. Dr. Christian Winter (University of Kiel, Germany)

Supervisors
Dr. André Paul (University of Bremen, Germany)
Dr. Mark Hadfield (National Institute of Water and Atmospheric Research, New Zealand)

Prüfungsausschusses
Defence Examining Committee
Prof. Michael Schulz, Prof. Dr. Christian Winter, Prof. Dr. Katrin Huhn-Frehers,
Prof. Dr. Dierk Hebbeln, Prof. Dr. Heiko Pälike, Dr. Ute Merkel, Dr. Heather Johnstone,
Ms. Charlotte Decker, Ms. Sophie Möllenbeck

This page has been intentionally left blank

Versicherung an Eides Statt / *Affirmation in lieu of an oath*

gem. § 5 Abs. 5 der Promotionsordnung vom 18.06.2018 /
according to § 5 (5) of the Doctoral Degree Rules and Regulations of 18 June, 2018

Ich / I, Nilima Aditya Natoo, Bremen, 2458809
(Vorname / First *Name*, Name / *Name*, Anschrift / *Address*, ggf. Matr.-Nr. / *student ID no., if applicable)*

versichere an Eides Statt durch meine Unterschrift, dass ich die vorliegende Dissertation selbständig und ohne fremde Hilfe angefertigt und alle Stellen, die ich wörtlich dem Sinne nach aus Veröffentlichungen entnommen habe, als solche kenntlich gemacht habe, mich auch keiner anderen als der angegebenen Literatur oder sonstiger Hilfsmittel bedient habe und die zu Prüfungszwecken beigelegte elektronische Version (PDF) der Dissertation mit der abgegebenen gedruckten Version identisch ist. / *With my signature I affirm in lieu of an oath that I prepared the submitted dissertation independently and without illicit assistance from third parties, that I appropriately referenced any text or content from other sources, that I used only literature and resources listed in the dissertation, and that the electronic (PDF) and printed versions of the dissertation are identical.*

Ich versichere an Eides Statt, dass ich die vorgenannten Angaben nach bestem Wissen und Gewissen gemacht habe und dass die Angaben der Wahrheit entsprechen und ich nichts verschwiegen habe. */ I affirm in lieu of an oath that the information provided herein to the best of my knowledge is true and complete.*

Die Strafbarkeit einer falschen eidesstattlichen Versicherung ist mir bekannt, namentlich die Strafandrohung gemäß § 156 StGB bis zu drei Jahren Freiheitsstrafe oder Geldstrafe bei vorsätzlicher Begehung der Tat bzw. gemäß § 161 Abs. 1 StGB bis zu einem Jahr Freiheitsstrafe oder Geldstrafe bei fahrlässiger Begehung. / *I am aware that a false affidavit is a criminal offence which is punishable by law in accordance with § 156 of the German Criminal Code (StGB) with up to three years imprisonment or a fine in case of intention, or in accordance with § 161 (1) of the German Criminal Code with up to one year imprisonment or a fine in case of negligence.*

Bremen, 14.01.2019

Ort / *Place*, Datum / *Date*

Unterschrift / *Signature*

This page has been intentionally left blank

Gutachter

Prof. Dr. Michael Schulz

Prof. Dr. Christian Winter

This page has been intentionally left blank

Abstract

The midlatitude countries of Southwest Pacific (SWP) region, like New Zealand (NZ), receive at least one-third of the total tropical storms that develop during summer and autumn (Sinclair 2002), apart from the winter midlatitude storms – this rare combination makes it a unique as well as an interesting area of study. These weather disturbances bring along substantial damages to the lives and properties and therefore are an important subject of study. The process of formation of tropical and midlatitude winter storms; as well as extratropical transitioning storms are examples of tightly coupled air-sea interaction. In this study, *storminess or storm activity of an area* is defined based on the observational records of total storm counts and its intensity. Similarly, change in storminess is simply defined by the changes in these storm indices. Therefore, to study the future change in storminess, a tool that allows frequent interaction between atmosphere and ocean models is a prerequisite to resolve various oceanic and atmospheric processes.

As of now, resolving them using a high resolution global model is computationally expensive. Further, the presence of complex chain of islands, reefs and ridges in the Southwest Pacific (SWP) region modulate the path of South Pacific subtropical gyre. This requires finer resolution ocean model to accurately simulate the turbulent eddies and currents of the study domain. Therefore, in addition to these global models, a regional climate model may be adopted to downscale and simulate additional circulation features at finer scale. In the absence of such a tool for the middle latitudes of the SWP region, a coupled atmosphere-ocean model (hereafter referred as SWP14 model) is developed and evaluated. The atmospheric and oceanic components are represented by WRF and ROMS, respectively. Both the ocean and atmosphere models uses exactly the same grid structure (mean horizontal resolution of 0.25°x0.25°) to avoid complications while exchanging information between the two. The model is integrated over five years period each for historical (1960-64) and RCP8.5 scenario (2095-99) using sequential multiple restart method. Its open boundaries are enforced by CMIP5 IPSL-CM5A-LR global model output. The SWP14 model is evaluated based on two criteria: first of all, model validation is performed by comparing the model output to climatology/reanalysis data; secondly, model performance is tested by comparing the model output to its own forcing data. It is observed that the regional scale circulation features, like, the eastward travelling Tasman Front whose path is modulated by the complicated bathymetry of that region seems to be very well resolved by the SWP14 ocean model and is distinctly visible. Although, the resulting regional circulation pattern is well resolved at chosen scale, however, smaller eddies including few quasi-permanent eddies usually present across the northwest to southeast of the North Island are missing and perhaps demand finer grid resolution. The modelled wind gives best match with that of its forcing IPSL global model, with slight overestimation. At higher latitudes, however, the wind data are incorrectly modelled by the IPSL model and hence carried over to the SWP14 model. Overall, the model performance is good in terms of the input forcing data, however, discrepancies are noted for some sampling stations while validating with the respective regional climatology. This implies that this coupled SWP14 model projection can further be improved by applying a better quality forcing data.

The current study is limited to austral summer-autumn storm season. The second research objective is to elucidate and communicate recent changes in storminess in the study area keeping in mind the ongoing global change in climate. The analysis shows that in spite of an overall reduction in the storminess over the past four decades, the number of extreme storms (category 3 and above), corresponding to the mean maximum sustained storm wind speed, has increased. At the same time, a slight reduction in the corresponding mean minimum central pressure is observed. The transition time from category 1 (weakest) to 3 has reduced substantially (by 12 hours). This indicates possibility of higher availability of favourable conditions supporting quick intensification of storms. Apart from this, in recent decades, perhaps under the

influence of changing climate, such storms over SWP region are observed to travel longer distances towards pole. The meridional variation of depiction of changing storm counts across past four decades demonstrate clearly the presence of increasing number of tropical storms, 1990s onward, which continues even in the current decade of 2010s.

The third and fourth objectives illustrate the importance and role of various large scale environmental (LSE) variables in influencing change in storminess. In the absence of storm observational records, the storm activity as well as its changes are estimated based on the changes in various large scale environmental conditions. Multiple linear regression analysis is used to establish relationship between recent change in storminess and respective change in large scale climate indices, which further is used to construct scenario of likely change in future storminess using simulated (RCP8.5 minus historical) differences. *The analysis asserts that the latent heat flux and specific humidity are found to be the most crucial environmental indices influencing the Southwest Pacific change in storminess.* They are followed by air-sea temperature difference, air and sea surface temperature, gradient SST, PBLH, local wind and precipitation rate. *Any change in the gradient SST has a greater role compared to the change in SST in storm activity. Yet, the role of change in SST in catalysing the background conditions aiding in evolution of un/favourable conditions for storm formation and intensification cannot be ignored. To conclude, SST acts as a 'causal agent' that aids in developing favourable conditions for storm formation and intensification over the SWP midlatitudes in combination with other indices forming regression equations.* On a different note, it cannot be overruled that some of these indices like wind speed and rate of precipitation could be the result of changing storminess in the area, and may not be the cause or source of change in storminess. Based on the change in SST observed for area of EAC split, it is likely that the location where EAC usually bifurcates (at about 31°S) may move polewards by ~2°.

An effort is made to estimate and map the response of change in extratropical transitioning process that influences mid and higher midlatitudes of SWP. Since these extratropical transitioning storms develop/intensify over three known areas storm genesis and/or intensification, these areas are primarily focussed for any future changes. The areas along EAC, northwest to north to northeast of North Island (NI) including the Bay of Plenty, areas far northeast of NI is likely to see an increase in its storminess. During summer (DJF), NI and its surroundings until ~39°S (i.e. until north of Taranaki and northern Hawke Bay) are likely to observe major reduction in storm counts, whereas south of ~39°S a minor rise is expected only over the land area of NI and medium to major rise in counts is expected over the ocean area, south of 45°S. Entire NI and its surroundings until Cook Strait are likely to experience medium to major rise in storm intensity. Further south of Wellington, only minor to medium rise in intensity is likely. *This implies that even if the northern to central parts of North Island are likely to host reduced number of storms, they will be more intense.* Particularly in summer (i) a minor rise in counts with medium rise in intensity implies a slightly greater number of stronger storms that are likely to reach until ~41-44°S. (ii) Although, a greater number of storms are likely to reach higher midlatitudes (~44-55°S or further south), yet stronger ones are likely to influence until ~49.5°S. Further south of Taranaki until Cook Strait a minor rise in number of storms with medium rise in intensity is likely. On the contrary, over ocean a major rise in counts along with minor rise in intensity is likely. *This implies that the southern part of North Island is likely to receive slightly higher number of storms with medium rise in intensity. It can be concluded that greater number of intense storms will be driven to reach higher midlatitudes until ~49.5°S, beyond which the increased storms are no longer severe.*

Moving from summer to autumn season, a slight change in storm intensity is mainly observed. As seen for summer storm, the counts are likely to reduce, however for autumn they are likely to occur with increased intensity - from minor to medium over NI and its surroundings until ~39°S (Taranaki and Hawke Bay) and from medium to major over south of ~39°S. *This implies that particularly from south of central North Island i.e. south of ~39°S (including New Plymouth, Hawke Bay, Napier, Wanganui, Hastings, Palmerstone*

North, Wellington, and Cook Strait) over land and until ~44°S over ocean are expected to receive medium to major rise in intense storminess, which further continues over ocean until ~49°S to host minor to medium rise in intensity. The medium to extreme rise in storminess around NI is in contrary to South Island (SI), which is likely to experience reduced number of storms that too with weaker intensity for entire summer-autumn season. Over ocean, similar changes are noted for autumn as in summer. More intense storms are likely to intrude south of North Island at least until ~49°S. Further south of ~49°S, density of only weaker storms are expected to rise considerably.

Finally, distinct changes in extreme storm activity is also concluded from the analysis: (i) in the southwest Tasman Sea area, which is comparatively a much colder region, an unusually significant warming is likely at (~40°S, 150°E), which is also known as Tasman Sea hotspot. This hotspot and its surroundings particularly in autumn are likely to see a distinct increase in extreme storm activity; (ii) for subtropical areas, north of EAC split location during summer-autumn season; and (iii) over Tasman Sea and its north, for entire North Island, its surrounding islands, for coastal waters including Bay of Plenty, Cook Strait, and Hawke Bay, particularly during summer season. These changes are likely to further cover larger ocean lying east and southeast of South Island particularly during autumn season. In addition to the above, the southern parts of Tasman Sea, especially west of New Zealand will receive lesser and weaker storms.

Based on above analysis following major conclusions are drawn:

- In the light of historical storm validation, it is confirmed that the predicted future change in storm counts and intensity for EAC pathway is accurately mapped, with minute deviations in intensity. For Tasman Flow area, it confirms that over ~25-30°S latitudinal extent, an increased intense storm activity is possible, which further indicates that the storms in this band are likely to undergo rapid extratropical transitioning process.
- A new area of storm genesis or intensification has been detected, known as *Tasman Sea hotspot* (~38-41°S, ~150°E). As the extratropical transitioning process over Tasman Sea area is expected to become more vigorous over ~26-40°S, the North Island is going to receive an increased number of intense Tasman Sea storms from its west. As we move eastward, lesser number of storms are likely to form or traverse through, however, once formed, they are likely to grow into extremely intense system. Further, these systems are expected to transit more vigorously, invading greater distances into the higher latitudes.
- Though austral autumn storms are known to be more strong and devastating than the summer storms however, in our estimation in future the austral summer storms are likely to undergo greater transformations compared to the estimated autumn storms, such that the former storms might achieve the intensity/strength of the latter types.
- This premature attainment of intense storminess particularly in summer indicates towards a greater possibility that extratropical transitioning is expected to go through more vigorous process.
- The summer storms are likely to make an impact mainly over the northern part of NI, whereas the autumn storms will influence/cover almost entire NI. The extreme future storminess is likely to occur both during summer and autumn seasons.

Kurzfassung

Auf die in den mittleren Breitengraden gelegenen Länder der Region Südwestpazifik (SWP), wie Neuseeland, treffen außer den winterlichen Stürme der mittleren Breitengrade auch mindestens ein Drittel aller tropischen Stürme, die sich im Sommer und Herbst entwickeln (Sinclair 2002). Diese seltene Kombination macht sie zu einem einzigartigen und interessanten Forschungsgebiet. Diese Wetterstörungen bringen erhebliche Schäden an Leben und Eigentum mit sich und sind daher ein wichtiges Untersuchungsfeld. Der Prozess der Bildung von Winterstürmen der Tropen und der mittleren Breitengrade, sowie außertropische Übergangsstürme sind Beispiele für eine eng gekoppelte Wechselwirkung zwischen Luft und Meer. In dieser Studie wird die Sturmaktivität eines Gebietes basierend auf den Beobachtungsdaten der Gesamtzahl der Stürme und ihrer Intensität definiert. Ebenso wird die Veränderung der *Sturmaktivität* durch die Veränderungen dieser Sturmindizes definiert. Für die Untersuchung künftiger Veränderungen in der Sturmaktivität ist daher ist ein Softwaretool notwendig, das eine häufige Interaktion zwischen atmosphärischen und Ozeanmodellen ermöglicht, um verschiedene ozeanische und atmosphärische Prozesse zu lösen,

Derzeit ist die Lösung mit einem hochauflösenden globalen Modell rechenintensiv. Darüber hinaus moduliert das Vorhandensein einer komplexen Kette von Inseln, Riffen und Graten in der Region des Südwestpazifiks (SWP) den Weg subtropischer Kreisel im Südpazifik. Dies erfordert ein Ozeanmodell mit feinerer Auflösung, um die turbulenten Wirbel und Ströme der Untersuchungsdomäne genau zu simulieren. Daher kann zusätzlich zu diesen globalen Modellen ein regionales Klimamodell verwendet werden, um zusätzliche Zirkulationsmerkmale in kleinerem Maßstab zu skalieren und zu simulieren. In Ermangelung eines solchen Werkzeugs für die mittleren Breitengrade der SWP-Region wird ein gekoppeltes Atmosphären-Ozean-Modell (im Folgenden SWP14-Modell genannt) entwickelt und bewertet. Die atmosphärischen und ozeanischen Komponenten werden durch WRF bzw. ROMS dargestellt. Sowohl das Ozean- als auch das Atmosphärenmodell verwenden exakt die gleiche Gitterstruktur (mittlere horizontale Auflösung von 0,25°x0,25°), um Komplikationen beim Informationsaustausch zwischen beiden zu vermeiden. Das Modell wird über einen Zeitraum von jeweils fünf Jahren für das historische (1960-64) und das RCP8.5-Szenario (2095-99) mittels sequentieller Mehrfach-Neustart-Methode integriert. Seine offenen Grenzen werden durch die globale Modellausgabe CMIP5 IPSL-CM5A-LR eingeschränkt. Das SWP14-Modell wird anhand von zwei Kriterien bewertet: Erstens wird die Modellvalidierung durch den Vergleich der Modellausgabe mit Klimatologie-/Reanalysedaten durchgeführt; zweitens wird die Modellleistung durch den Vergleich der Modellausgabe mit seinen eigenen Antriebsdaten getestet. Es wird beobachtet, dass die regionale Skala der Zirkulation Merkmale aufweist, wie z.B. die nach Osten verlaufende Tasman-Front, deren Pfad durch die komplizierte Bathymetrie dieser Region moduliert wird, die durch das SWP14-Ozeanmodell sehr gut aufgelöst zu sein scheint und deutlich sichtbar ist. Obwohl das resultierende regionale Zirkulationsmuster auf der gewählten Skala gut aufgelöst ist, fehlen jedoch kleinere Wirbel, einschließlich einiger quasi-permanenter Wirbel, die normalerweise im Nordwesten bis Südosten der Nordinsel vorhanden sind, und möglicherweise eine feinere Gitterauflösung erfordern. Der modellierte Wind ergibt die beste Übereinstimmung mit dem seines globalen IPSL-Antriebsmodells, mit einer leichten Überbewertung. In höheren Breitengraden werden die Winddaten jedoch durch das IPSL-Modell falsch modelliert und in das SWP14-Modell übertragen. Insgesamt ist die Modellleistung in Bezug auf die eingegebenen Antriebsdaten gut, jedoch werden für einige Probenahmestationen Diskrepanzen festgestellt, während sie mit der jeweiligen regionalen Klimatologie validiert werden. Dies bedeutet, dass diese gekoppelte SWP14-Modellprojektion durch die Anwendung einer besseren Qualität der Antriebsdaten weiter verbessert werden kann.

Die aktuelle Studie ist auf die Sommer-Herbst-Sturmsaison der südlichen Hemisphäre beschränkt. Das zweite Forschungsziel besteht darin, die jüngsten Veränderungen der Sturmaktivität im Untersuchungsgebiet unter Berücksichtigung des anhaltenden globalen Klimawandels zu erhellen und

darzustellen. Die Analyse zeigt, dass trotz einer allgemeinen Verringerung der Sturmaktivität in den letzten vier Jahrzehnten die Anzahl der extremen Stürme (Kategorie 3 und höher), die der mittleren maximalen anhaltenden Sturmgeschwindigkeit entspricht, zugenommen hat. Gleichzeitig wird eine leichte Abnahme des entsprechenden mittleren minimalen zentralen Drucks beobachtet. Die Übergangszeit von der (schwächsten) Kategorie 1 zur Kategorie 3 hat sich erheblich verkürzt (um 12 Stunden). Dies deutet auf das Vorhandensein günstigerer Bedingungen für eine schnelle Intensivierung von Stürmen hin. Abgesehen davon werden in den letzten Jahrzehnten, vielleicht unter dem Einfluss des Klimawandels, Stürme über der SWP-Region beobachtet, die größere Entfernungen zum Pol zurückzulegen. Die meridionale Variation der Darstellung wechselnder Sturmwerte in den letzten vier Jahrzehnten zeigt eine deutlich zunehmende Anzahl tropischer Stürme seit den 1990er Jahren, die sich auch im aktuellen Jahrzehnt der 2010er Jahre fortsetzt.

Das dritte und das vierte Forschungsziel veranschaulichen die Bedeutung und Rolle diverser großskaliger Umweltvariablen (LSE), die die Veränderung der Sturmaktivität beeinflussen. In Ermangelung von Sturmbeobachtungsaufzeichnungen werden die Sturmaktivität sowie deren Veränderungen basierend auf den Veränderungen verschiedener großräumiger Umweltbedingungen geschätzt. Die multiple lineare Regressionsanalyse wird verwendet, um den Zusammenhang zwischen den jüngsten Sturmveränderungen und dem jeweiligen Wandel in großskaligen Klimaindizes herzustellen, die ferner dazu verwendet wird, ein Szenario für eine wahrscheinliche Veränderung der zukünftigen Sturmaktivität unter Verwendung simulierter (RCP8,5 minus historischer) Unterschiede zu erstellen. *Die Analyse stellt fest, dass der latente Wärmestrom und die spezifische Luftfeuchtigkeit die wichtigsten Umweltindizes sind, die die Veränderung der Sturmaktivität im Südwestpazifik beeinflussen.* Es folgen Luft-See-Temperaturdifferenz, Luft- und Meeresoberflächentemperatur, der Gradient SST, PBLH, lokaler Wind und Niederschlag. *Die Veränderung des Gradienten SST spielt im Vergleich zur Änderung des SST bei Sturmaktivität eine größere Rolle. Dennoch kann die Rolle der Veränderung von SST für die Entstehung der Hintergrundbedingungen, die letztlich die Entwicklung ungünstiger Bedingungen für die Sturmbildung und -intensivierung begünstigen, nicht ignoriert werden. Zusammenfassend lässt sich sagen, dass SST als "Kausalfaktor" fungiert, der dazu beiträgt, günstige Bedingungen für die Sturmbildung und -intensivierung über die mittleren Breitengrade des SWP in Kombination mit anderen Indizes, die Regressionsgleichungen bilden, zu entwickel*n. Auf der anderen Seite ist anzuerkennen, dass einige dieser Indizes wie Windgeschwindigkeit und Niederschlagsrate möglicherweise das Ergebnis einer sich ändernden Sturmaktivität in dem Gebiet sein könnten, und nicht deren Ursache oder Auslöser. Basierend auf der für die Fläche des EAC-Splits beobachteten Änderung der SST ist es wahrscheinlich, dass sich der Ort, an dem sich das EAC normalerweise gabelt (bei etwa 31°S), um ~2° Richtung Pol bewegen kann.

Es wird versucht, die Reaktion auf Veränderungen im extratropischen Übergangsprozess, die die mittleren und höheren Mittelbreiten des SWP beeinflussen, zu schätzen und abzubilden. Da diese außertropischen Übergangsstürme über drei bekannte Bereiche der Sturmgenese und/oder -intensivierung hinweg entstehen/sich intensivieren, sind diese Bereiche in erster Linie auf zukünftige Veränderungen ausgerichtet. Die Gebiete entlang des EAC, nordwestlich bis nordöstlich der neuseeländischen Nordinsel (NI) einschließlich der Bay of Plenty, und Gebiete, die weit im Nordosten der NI liegen, dürften eine Zunahme ihrer Sturmaktivität verzeichnen. Während des Sommers (DJF) wird die NI und ihre Umgebung bis ~39°S (d.h. bis nördlich von Taranaki und der nördlichen Hawke Bay) wahrscheinlich eine starke Abnahme in der Anzahl der Stürme erleben, während südlich von ~39°S ein leichter Anstieg nur über der Landfläche der NI und ein mittlerer bis starker Anstieg des Auftretens von Stürmen über dem Meeresgebiet südlich von 45°S erwartet wird. Die gesamte NI und ihre Umgebung bis zur Cook Strait werden wahrscheinlich einen mittleren bis starken Anstieg der Sturmintensität erfahren. Weiter südlich von Wellington ist nur ein leichter bis mittlerer Anstieg der Intensität wahrscheinlich. *Dies bedeutet, dass selbst wenn die nördlichen bis zentralen Teile der Nordinsel wahrscheinlich eine geringere Anzahl von Stürmen aufweisen, diese jedoch intensiver sein werden*. Insbesondere im Sommer (i) impliziert ein leichter Anstieg der Anzahl von Stürmen mit mittlerem Intensitätsanstieg eine etwas größere Anzahl stärkerer Stürme, die voraussichtlich bis ~41-44°S reichen werden. (ii) Obwohl eine größere Anzahl von Stürmen wahrscheinlich höhere mittlere Breiten erreichen wird (~44-55°S oder weiter südlich), werden stärkere Stürme wahrscheinlich bis ~49,5°S

Einfluss nehmen. Weiter südlich von Taranaki bis zur Cook Strait ist ein leichter Anstieg der Anzahl der Stürme mit mittlerem Anstieg der Intensität wahrscheinlich. Im Gegensatz dazu ist über dem Ozean ein starker Anstieg der Anzahl bei gleichzeitig geringer Zunahme der Intensität der Stürme wahrscheinlich. *Dies bedeutet, dass der südliche Teil der Nordinsel wahrscheinlich etwas mehr Stürme mit mittlerer Intensität erleben wird. Es kann darauf geschlossen werden, dass sich eine größere Anzahl von intensiven Stürmen in die höheren mittleren Breiten bis ~49,5°S ausdehnen wird, über die hinaus die intensivierter Stürme nicht länger als stark einzustufen sind.*

Von der Sommer- zur Herbstsaison ist vor allem eine leichte Veränderung der Sturmintensität zu beobachten. Wie auch bei den Sommerstürmen zu sehen, dürften die Zahlen ingesamt abnehmen, Herbststürme jedoch mit erhöhter Intensität auftreten – von leicht bis mittel über der NI und ihre Umgebung bis zu ~39°S (Taranaki und Hawke Bay) und von mittel bis stark südlich von ~39°S. *Dies bedeutet, dass insbesondere vom Süden der zentralen Nordinsel, d.h. südlich von ~39°S (einschließlich New Plymouth, Hawke Bay, Napier, Wanganui, Hastings, Palmerstone North, Wellington und Cook Strait) über Land und bis ~44°S über dem Meer ein mittlerer bis starker Anstieg der intensiven Stürme erwartet wird, der sich über dem Ozean bis ~49°S mit geringer bis mittlerer Zunahme der Intensität fortsetzt.* Der mittlere bis extreme Anstieg der Stürme um die NI herum steht im Gegensatz zur Südinsel (SI), die für die gesamte Sommer-Herbst-Saison eine geringere Anzahl von Stürmen erleben dürfte, die ebenfalls mit schwächerer Intensität auftreten. Auf See sind im Herbst ähnliche Veränderungen zu beobachten wie im Sommer. Stärkere Stürme dürften südlich der Nordinsel zumindest bis ~49°S eindringen. Weiter südlich von ~49°S wird erwartet, dass lediglich die Häufigkeit der schwächeren Stürme deutlich ansteigen wird.

Schließlich wird aus der Analyse auf deutliche Veränderungen der extremen Sturmaktivität geschlossen: i) im südwestlichen Teil der Tasmanischen See, der vergleichsweise eine viel kältere Region ist, ist eine ungewöhnlich starke Erwärmung wahrscheinlich (~40°S, 150°E), die auch als Tasmanischer Hotspot bekannt ist. Dieser Hotspot und seine Umgebung werden insbesondere im Herbst wahrscheinlich einen deutlichen Anstieg der extremen Sturmaktivität verzeichnen; (ii) für subtropische Gebiete nördlich der EAC-Splitposition während der Sommer-Herbst-Saison; und (iii) für die Tasmanische See und ihren Norden, für die gesamte Nordinsel, ihre umliegenden Inseln, für die Küstengewässer einschließlich der Bay of Plenty, Cook Strait und Hawke Bay, insbesondere während der Sommersaison. Diese Veränderungen dürften vor allem in der Herbstsaison größere Teile des Ozeans östlich und südöstlich der Südinsel erfassen. Darüber hinaus wird es in den südlichen Teilen der Tasmanischen See, insbesondere westlich von Neuseeland, weniger und schwächer stürmen.

Basierend auf der oben genannten Analyse werden die folgenden wesentlichen Schlussfolgerungen gezogen:

- Im Lichte der historischen Sturmvalidierung wird bestätigt, dass die vorhergesagte zukünftige Veränderung der Sturmanzahl und -intensität für den EAC-Pfad genauestens abgebildet wird, mit geringen Intensitätsabweichungen. Für das Tasmanische Durchflussgebiet wird bestätigt, dass über die Breitengrade von ~25-30°S eine erhöhte intensive Sturmaktivität möglich ist, was weiter darauf hindeutet, dass die Stürme in diesem Band wahrscheinlich einen schnellen extratropischen Übergangsprozess durchlaufen werden.

- Ein neues Gebiet der Sturmgenese oder -intensivierung wurde entdeckt, bekannt als *Tasman Sea Hotspot* (~38-41°S, ~150°E). Da erwartet wird, dass der außertropische Übergangsprozess im Tasmanischen Meeresgebiet über ~26-40°S kräftiger wird, wird die Nordinsel Neuseelands eine zunehmende Anzahl von intensiven Stürmen aus der Tasmanischen See von Westen her erleben. Während wir uns nach Osten bewegen, ist es wahrscheinlich, dass sich weniger Stürme bilden oder durchziehen, aber sobald sich Stürme gebildet haben, werden sie wahrscheinlich zu einem extrem intensiven System heranwachsen. Darüber hinaus wird erwartet, dass diese Systeme kräftiger durchziehen und in größeren Entfernungen in die höheren Breiten eindringen.

- Obwohl südliche Herbststürme bekanntlich stärker und verheerender sind als die Sommerstürme, dürften die südlichen Sommerstürme nach unserer Einschätzung in Zukunft größere Veränderungen erfahren als die erwarteten Herbststürme, so dass die ersteren die Intensität/Stärke der letzteren erreichen könnten.
- Dieses vorzeitige Erreichen einer intensiven Sturmaktivität insbesondere im Sommer deutet auf eine größere Wahrscheinlichkeit hin, dass der außertropische Übergang einen stärkeren Transformationsprozess durchlaufen wird. Die Sommerstürme dürften sich vor allem auf den nördlichen Teil von NI auswirken, während die Herbststürme fast die gesamte NI beeinflussen/bedecken werden. Die extreme zukünftige Sturmaktivität dürfte sowohl in der Sommer- als auch in der Herbstsaison auftreten.

Table of Contents

Abstract ... 9
Kurzfassung ... 12
Table of Contents ... 16
List of Figures ... 20
List of Tables ... 22
List of Appendices ... 22
List of Abbreviations ... 23
Acknowledgements ... 25
A prayer ... 26

CHAPTER 1 ... 27
Introduction ... 27
1.1 Southwest Pacific region ... 28
1.1.1 Southwest Pacific circulation ... 28
1.1.2 Large scale environmental changes as indicators ... 28
1.1.3 South Pacific storm climatology ... 29
1.1.4 Changing storminess ... 32
1.1.5 Existing South Pacific climate models ... 33
1.2 Overview on Research needs, strategy and scope ... 36
1.2.2 Need for development of regional coupled model ... 36
1.2.3 Modelling strategy and scope ... 37
1.2.4 Recently changing storminess and large scale environmental variability ... 41
1.2.5 Large scale environmental variability and scenarios of future storminess ... 44
1.2.6 Research strategy and scope ... 45
1.3 Overview on research objectives and outline of respective chapters ... 46

CHAPTER 2 ... 48
Model description and experimental design ... 48
2.1 Common terminologies ... 49
2.2 Data and methods ... 50
2.2.1 Data ... 50
2.2.2 Introduction to COAWST modelling system ... 50
2.2.3 Southwest Pacific atmosphere model set-up ... 51

2.2.4 Southwest Pacific Ocean model set-up ... 58
2.2.5 Southwest Pacific atmosphere-ocean coupled model set-up ... 64
2.3 Summary: SWP14 modelling strategies ... 69

CHAPTER 3 ... 72
Model validation ... 72
3.1 Data and methods ... 72
3.1.1 Data ... 72
3.1.2 Model evaluation strategy ... 72
3.2 Comparison of large-scale environmental variables ... 75
3.2.1 Sea surface temperature (SST) ... 75
3.2.2 Sea surface salinity (SSS) ... 77
3.2.3 Temperature at 2 m (T2m) ... 80
3.2.4 Wind speed ... 84
3.2.5 U-wind component ... 87
3.2.6 V-wind component ... 90
3.3 Summary: SWP14 model performance ... 94

CHAPTER 4 ... 96
Recent changes in storminess of Southwest Pacific region (1970-2014) ... 96
4.1 Data and Methods ... 96
4.2 Results and Discussion ... 98
4.2.1 Change in recent past storminess ... 98
4.2.2 Change in 15 year mean environmental conditions ... 107
4.3 Summary ... 112

CHAPTER 5 ... 118
Regionalization of large-scale Southwest Pacific circulation by the end of 21st century ... 118
5.1 Evaluation methods ... 118
5.2 Results ... 119
5.2.1 Surface Pressure ... 119
5.2.2 Wind velocity at 10 m ... 121
5.2.3 Temperature of air at 2 m altitude ... 122
5.2.4 Water vapour mixing ratio at 2 m altitude ... 124
5.2.5 TOA outgoing longwave radiation ... 125
5.2.6 Planetary boundary layer (PBL) height ... 125
5.2.7 Latent heat ... 127

5.2.8 Upward heat and moisture flux at the surface ... 127
5.2.9 Sea surface temperature ... 127
5.3 Summary: changes in simulated large scale climate indices ... 133
5.3.1 Austral summer/autumn storm season ... 133
5.3.2 Austral winter/spring storm season ... 136

CHAPTER 6 ... 140
Mapping of response of Southwest Pacific storminess to changing climate ... 140
6.1 Data and Methods ... 140
6.2 Results ... 144
6.2.1 Overview on changes in large-scale climate indices ... 144
A. Zone I (EAC pathway) ... 144
B. Zone II (Tasman Sea) ... 149
C. Zone III (East of NZ) ... 152
6.2.2 Relationship between change in observed storminess and large-scale climate variables 155
D. Zone I (EAC pathway) ... 155
E. Zone II (Tasman Sea) ... 161
F. Zone III (East of NZ) ... 166
6.2.3 Application of regression model equations to predict future change in storminess ... 172
A. Zone I (EAC pathway) ... 172
B. Zone II (Tasman Sea) ... 175
C. Zone III (East of NZ) ... 177
6.3 Validation of historical storm indices ... 179
A. Zone I (EAC Pathway) ... 180
B. Zone II Tasman Sea Pathway ... 184
6.4 Summary ... 189

CHAPTER 7 ... 197
Discussion ... 197
7.1 *Influence of large scale environmental variability on change in storminess* ... 198
7.2 *Scenarios of likely changes in storminess by the end of 21st century* ... 202

CHAPTER 8 ... 210
Summary and Outlook ... 210
8.1 Summary ... 211
8.1.1 SWP14: performance and caveats ... 211
8.1.2 Recent past storminess – an observational study ... 212

8.1.3 Regionalization of large scale circulation 214
8.1.4 Application of SWP14: changing scenarios of future storminess 215
8.2 Outlook 221
8.2.1 Scope for estimation of change in winter storminess 221
8.2.2 Scope for improvement to resolve local scale eddies 222
8.2.3 Scope for improvement of SWP14 settings 223
8.3 Conclusion 223

References 225

Appendices 231

List of Figures

Figure 1 *Bathymetry of the study domain with details of major features of the region portrayed (2-dimensional top view). The shades of white to orange (near coasts, rises, ridges and chain of islands) highlight shallower areas, whereas light blue (cyan) to dark blue highlight deeper water of the region. Refer next figure for a closer 3-dimensional view of these features.*
Figure 2 *Bathymetry (m) for the study domain in 3-dimensional perspective. Several mid-ocean topographic features like trenches, ridges, island chains, seamounts can be clearly seen and has a dominant role in regional circulation.*
Figure 3 *Actual storm distribution observed for every five years span starting from 1970-2013 portraying their respective tracks (source: SPEArTC-GoogleEarth dataset, Diamond et al., 2012)*
Figure 4 *A histogram showing latitudinal variation (@ 5° latitude band) of South Pacific storm counts and its changing pattern for past few decades shows an overall decrease in counts whereas converse for higher midlatitudes. SPEArTC observation data are used for analysis.*
Figure 5 *Overview of experimental set-up*
Figure 6 *Components of WPS, WRF for real data case, source: modified WPS components (WRF_User's_Guide 2012)*
Figure 7 *Trial-1 SP12 (0.5° horizontal grid resolution) model domain covering a much larger area is now reduced to smaller portion to limit computational cost and increase grid resolution to 0.25°, called as SP14*
Figure 8 *Vertical grid structure using terrain following sigma-coordinates shown using transects at 154°E, 165°E and 179°E*
Figure 9 *Schematic diagrams of (a) forcing data, exchange of coupling fields between atmosphere and ocean models within SWP14 model; (b) respective model time-step and coupling interval are illustrated for simplicity*
Figure 10 *Model domain displaying selected 16 sampling stations (or boxes) each of size 2.5° square*
Figure 11 *Comparison of 5-year seasonal mean SST (°C) between (a) HadISST1 (b) IPSL global input (c) SWP14 output*
Figure 12 *Comparison of 5-year seasonal mean SSS (PSU) between (a) CARS (b) IPSL global input (c) SWP14 output*
Figure 13 *Comparison of monthly mean sea surface salinity for 16 sample boxes*
Figure 14 *Comparison of 5 year seasonal mean air temperature at 2 m (°C) between (a) ERA40 (b) IPSL global input (c) SWP14 output*
Figure 15 *Comparison of monthly mean air temperature at 2 m for 16 sample boxes*
Figure 16 *Comparison of 5 year seasonal mean 10 m wind speed (ms^{-1}) between (a) ERA40 (b) IPSL global input (c) SWP14 output*
Figure 17 *Comparison of monthly mean 10 m wind speed plotted for 16 sample boxes*
Figure 18 *Comparison of 5-year seasonal mean u-wind component (ms^{-1}) between (a) ERA40 (b) IPSL global input (c) SWP14 output*
Figure 19 *Comparison of monthly mean u-component of 10 m wind for 16 sample boxes*
Figure 20 *Comparison of 5-year seasonal mean v-wind component (ms^{-1}) between (a) ERA40 (b) IPSL global input (c) SWP14 output*
Figure 21 *Comparison of monthly mean 10 m v-component of wind for 16 sample boxes*
Figure 22 *Change in trends in total annual storm counts (black), annual maximum sustained storm wind speed (red), annual minimum storm central pressure (yellow) for named storms from 1970-2014 in Southwest Pacific basin; also refer* ***Table 15*** *(data source: SPEArTC, Diamond et al., 2012)*
Figure 23 *Normalized 15 years total storm counts climatology (Row-I): (a) T1 (1970-1984), (b) T2 (1985-1999), (c) T3 (2000-2014) and their differences (Row-II): (d) T2 minus T1, (e) T3 minus T2 based on SPEArTC dataset (Diamond et al., 2012), where storms are searched at every 2° square grid. The difference maps clearly denote the locations that received surplus (blue) or deficit (red) number of storms*
Figure 24 *Change in 15 year mean large scale environment variables during summer-autumn storm season (1985-1999 minus 1970-1984)*

Figure 25 *Change in 15 year mean large scale environment variables during summer-autumn storm season (2000-2014 minus 1985-1999)*
Figure 26 *Change in 15 year mean large scale environment variables during winter-spring storm season (1985-1999 minus 1970-1984)*
Figure 27 *Change in 15 year mean large scale environment variables during winter-spring storm season (2000-2014 minus 1985-1999)*
Figure 28 *Five year mean of simulated surface pressure (mb) for different seasons*
Figure 29 *Five year mean of simulated 10 m wind velocity (ms^{-1}) for different seasons*
Figure 30 *Five year mean of simulated 2 m air temperature (°C) for different seasons*
Figure 31 *Five year mean of simulated 2 m water vapour mixing ratio ($kg\ kg^{-1}$) for different seasons*
Figure 32 *Five year mean of simulated outgoing longwave radiation (Wm^{-2}) for different seasons*
Figure 33 *Five year mean of simulated Planetary Boundary Level Height (m) for different seasons*
Figure 34 *Five year mean of simulated latent heat flux ($W\ m^{-2}$) for different seasons*
Figure 35 *Five year mean of simulated upward heat flux at the sea surface ($Q\ m^{-2}$) for different seasons*
Figure 36 *Five year mean of simulated upward moisture flux at sea surface ($kg\ m^{-2}s^{-2}$) for different seasons*
Figure 37 *Five year mean of simulated sea surface temperature (°C) for different seasons*
Figure 38 *Comparison of five year mean of simulated differences in different variables (summer,* ***DJF)***
Figure 39 *Comparison of five year mean of simulated differences in different variables (autumn,* ***MAM)***
Figure 40 *Comparison of five year mean of simulated differences in different variables (winter,* ***JJA)***
Figure 41 *Comparison of five year mean of simulated differences in different variables (spring,* ***SON)***
Figure 42 *Schematic of three different zones used for analysing change in storminess, where major change in bathymetry details are kept as background theme*
Figure 43 *Comparison of change in mean zonal storminess (or storm indices) in the recent past for cases (a) T2 (1985-99)-T1 (1970-84), T3 (2014-2000)-T1 for three different zones: Zone-I (147-157°E), Zone-II (163-173°E), and Zone-III (173-183 ° E). [Columns → zones, Rows → storm indices]*
Figure 44 *Zone-I Comparison of recent and future change in large-scale climate indices: (a) gradient SST (b) SST (c) SAT (d) SST-SAT (e) Specific humidity (f) Latent heat flux (g) Precipitation rate (h) PBLH (i) Wind speed. Recent change: black dashed line, Red dotted and blue lines denote future (simulated) change in DJF and MAM, respectively.*
Figure 45 *Zone-II Comparison of recent and future change in large-scale climate indices: (a) gradient SST (b) SST (c) SAT (d) SST-SAT (e) Specific humidity (f) Latent heat flux (g) Precipitation rate (h) PBLH (i) Wind speed. Recent change: black dashed line, Red dotted and blue lines denote future (simulated) change in DJF and MAM, respectively.*
Figure 46 *Zone-III Comparison of recent and future change in large-scale climate indices: (a) gradient SST (b) SST (c) SAT (d) SST-SAT (e) Specific humidity (f) Latent heat flux (g) Precipitation rate (h) PBLH (i) Wind speed. Recent change: black dashed line, Red dotted and blue lines denote future (simulated) change in DJF and MAM, respectively.*
Figure 47 *Large scale climate variability and changing storm counts (recent past) for Zone-I*
Figure 48 *Large scale climate variability and changing storm intensity (recent past) for Zone-I*
Figure 49 *Large scale climate variability and changing storm central pressure (recent past) for Zone-I*
Figure 50 *Large scale climate variability and changing storm counts (recent past) for Zone-II*
Figure 51 *Large scale climate variability and changing storm intensity (recent past) for Zone-II*
Figure 52 *Large scale climate variability and changing storm central pressure (recent past) for Zone-II*
Figure 53 *Large scale climate variability and changing storm counts (recent past) for Zone-III*
Figure 54 *Large scale climate variability and changing storm intensity (recent past) for Zone-III*
Figure 55 *Large scale climate variability and changing storm central pressure (recent past) for Zone-III*
Figure 56 *Scenarios of likely change in future storminess for* ***Zone-I*** *(147-157°S)*
Figure 57 *Scenarios of likely change in future storminess for* ***Zone-II*** *(163-173°S)*
Figure 58 *Scenarios of likely change in future storminess for* ***Zone-III*** *(173-183°S)*
Figure 59 Storm Counts *Observation vs. Predicted cases (a) DJF (b) MAM* ***(Zone I)***
Figure 60 Storm Intensity *Observation vs. Predicted cases (a) DJF (b) MAM* ***(Zone I)***
Figure 61 Storm central pressure *Observation vs. Predicted cases (a) DJF (b) MAM* ***(Zone I)***

Figure 62 Storm Counts *Observation vs. Predicted cases (a) DJF (b) MAM* ***(Zone II)***
Figure 63 Storm Intensity *Observation vs. Predicted cases (a) DJF (b) MAM* ***(Zone II)***
Figure 64 Storm central pressure *Observation vs. Predicted cases (a) DJF (b) MAM* ***(Zone II)***
Figure 65 *Composite mapping of seasonal variability of future storm indices for two different scenarios*
Figure 66 *Scenarios of future changes in the occurrence of storminess for SWP region. Rows depicts scenario A and B; and Columns depict austral summer (DJF) and autumn (MAM) seasons.*

List of Tables

Table 1 *CMIP5 model (IPSL_CM5A_LR) variables used to force SP14 WRF model*
Table 2 *Variable Table(s) used by WPS ungrib and metgrid programs*
Table 3 *Different model physics schemes and parameterization used*
Table 4 *WRF physics schemes used (reference: WRF User's Guide, 2011)*
Table 5 *SP14 ocean model configuration*
Table 6 *CMIP5 model (IPSL_CM5A_LR) variables used to force SP14 ROMS model*
Table 7 *Properties and its corresponding parameters being exchanged between atmosphere and ocean; and atmosphere and land surface*
Table 8 *Changes in CPP options for uncoupled and coupled ROMS*
Table 9 *Statistical indices computed for 5-year annual mean sea surface salinity*
Table 10 *Statistical indices computed for 5-year annual mean temperature at 2 m*
Table 11 *Statistical indices computed for 5-year annual mean wind speed*
Table 12 *Statistical indices computed for 5-year annual mean u-wind component*
Table 13 *Statistical indices computed for 5-year annual mean v-wind component*
Table 14 *Saffir-Simpson Hurricane Wind Scale (SSHWS)*
Table 15 *Summary of observed storm statistics displaying annual values of (i) total storm counts, (ii) maximum sustained storm wind speed, and (iii) minimum storm central pressure, attained for three selected time-scales (T1:1970-1984, T2:1985-1999, T3: 2000-2014)*
Table 16 *Extreme storm statistics illustratiing (i) duration (ii) translation time from category 1 to attain extreme hurricane scales (categories 3, 4 and 5)*
Table 17 *Summary of change in extreme storm events (T2 minus T1 and T3 minus T2) for Southwest Pacific region*
Table 18 *Comparison of extreme storminess to different ENSO phases*
Table 19 *Color coding used to highlight specific range of correlation coefficients*
Table 20 *Summary of meridional changes in large scale environmental conditions for Zone-I*
Table 21 *Summary of meridional changes in large scale environmental conditions for Zone-II*
Table 22 *Summary of meridional changes in large scale environmental conditions for Zone-III*

List of Appendices

Appendix I *WRF Pre-processing System input script (namelist.wps)*
Appendix II *WRF input script (namelist.input)*
Appendix III *ROMS standalone CPP options*
Appendix IV *Correlation and Regression analysis*

List of Abbreviations

3D	Three dimensional
ABL	Atmospheric PBL
AGRIF	Adaptive Grid Refinement in Fortran
ARW	Advanced Research WRF
BoP	Bay of Plenty
BMJ	Betts-Miller-Janjíc
CARS	CSIRO Atlas of Regional Seas
CCAM	Conformal Cubic Atmospheric Model
COAWST	Coupled Ocean-Atmosphere-Wave-Sediment Transport
CORDEX	Coordinated Regional Downscaling Experiment
CMIP3	Coupled Model Intercomparison Project Phase 3
CMIP5	Coupled Model Intercomparison Project Phase 5
CPP	C-preprocessing
CSIRO	Commonwealth Scientific and Industrial Research Organisation
CSTMS	Community Sediment Transport Modeling System
DARLAM	CSIRO Division of Atmospheric Research Limited Area Model
DJF	December-January-February
EAC	East Australian Current
EAUC	East Auckland Current
ENSO	El Niño Southern Oscillation
ERA40	European Centre for Medium-Range Weather Forecasts reanalysis data
Etopo1	1 minute Arc-Minute Global Relief Model of earth's surface (integrates land topography and ocean bathymetry)
GCM	General Circulation Model
GRIB	GRIdded Binary or General Regularly-distributed Information in Binary form
HadAM3P	Hadley Center Atmospheric General Circulation Model 3P
HadRM3P	Regional model based on HadCM3 GCM
HadISST1	Hadley Centre Global Sea Ice and Sea Surface Temperature (HadISST1, 1°x1°)
IPCC	Intergovernmental Panel on Climate Change
IPSL_CM5A_LR	Institut Pierre Simon Laplace contribution towards CMIP5 with lower resolution option
ITCZ	Inter Tropical Convergence Zone
JJA	June-July-August
KPP	K-profile parameterization
LMD	Large, McWilliams and Doney vertical mixing parameterization
MAM	March-April-May
MCT	Model Coupling Toolkit
MIROC	Model for Interdisciplinary Research On Climate
MPICH	Message Passing Interface over Chameleon (for distributed memory applications)
M-SP14	MARUM **C**oupled **A**tmosphere-**O**cean **S**outhwest **P**acific regional model, using ¼° mean grid resolution (or) MARUM-CAOR-SP14
MYJ	Mellor-Yamada-Janjíc
netCDF	Network Common Data Form
NI	North Island
NOAH LSM	NCEP-OSU-AirForce-HydrologyLab Land Surface Model

NZ	New Zealand
OBL	Oceanic PBL
OCCAM	Ocean Circulation and Climate Advanced Modelling
OLR	Outgoing Longwave Radiation
PBL	Planetary boundary layer
PBLH	Planetary boundary layer height
PGF90	Portland Group Fortran 90 compiler
POAMA	Predictive Ocean-Atmosphere Model for Australia
PRECIS	Providing Regional Climates for Impacts Studies
PSU	Practical Salinity Unit
RCP	Representative Concentration Pathways
RegCM3	Abdus Salam International Centre for Theoretical Physics Regional Climate model version 3
ROMS	Regional Ocean Modelling System
RRTMG	Rapid Radiative Transfer Mode applied for Global Circulation models
SAT	Surface Air Temperature
SCRIP	Spherical Coordinate Remapping Interpolation Package
SEC	South Equatorial Current
SH	Southern Hemisphere
SI	South Island
SON	September-October-November
SP12	SWP model domain with ½° horizontal grid resolution
SP14	SWP model domain with ¼° horizontal grid resolution
SPCZ	South Pacific Convergence Zone
SPEArTC	Southwest Pacific Enhanced Archive for Tropical Cyclones
SSHWS	Saffir-Simpson Hurricane Wind Scale
SSI	Storm Severity Index
SSS	Sea Surface Salinity
SST	Sea Surface Temperature
SWAN	Simulating Waves Nearshore
SWP	Southwest Pacific
T2m	Temperature at 2 m altitude
TKE	Turbulent kinetic energy
TOA	Top of the Atmosphere
UTC	Coordinated Universal Time
Uwind	u-component of wind velocity
Vtable	Variable Table
Vwind	v-component of wind velocity
WPS	WRF Pre-processing System
WPSI	WPS intermediate format
WRF	Weather Research and Forecasting Model
WSM6	WRF Single-Moment 6-class moisture microphysics scheme

Acknowledgements

This project is part of the International Research Training Group, INTERCOAST and has been funded by the Deutsche Forschungsgemeinschaft (DFG), to whom I am highly obliged.

Firstly, I would like to thank my Professor-incharge, Michael Schulz for keeping his trust on me and for providing me firm but kind guidance throughout the period. It not only kept me on my toes but helped me learn the art to *focus-resolve-advance* strategically with available resources. At the same time, I would like to thank my supervisor André Paul for consistently encouraging me to learn various Linux based software, open source model codes and for giving me the opportunity to explore various options, from compilers to models to different analysis methods. I wish to extend special thanks to Andreas Manschke for his ever green smile and untiring technical support throughout the work, especially during the period when I was working from my home country. I would like to extend my heartfelt thanks to Katrin Huhn for her trust and unwavering support.

Heartfelt thanks are extended to Waikato University members: Janet Bornman for providing regular guidance to proceed and encourage fruitful collaboration with NIWA; to Willem de Lange and Cheryl Ward for their support with literature collection, to Donald Neal for technical support to access *Symphony* and many others including Wei Ye, for their support during the research stay. I would like to extend my gratitude towards NIWA to allow collaboration with their scientists during the research stay. I would like to express my heartfelt gratitude towards Mark Hadfield and Stefan Jendersie for prolific discussion and support while experimenting on application of ROMS for Southwest Pacific region.

I extend my heartfelt thanks to Ashok K. Singhvi of Physical Research Laboratory (PRL), Ahmedabad, for introducing me to the director of Indian Institute of Technology (IIT) Gandhinagar, for providing me regular motivation, for arranging access to PRL and for his tenacious support that helped continue the work without pause from home country. Many thanks to Sudhir K. Jain (Director), Pratyush Dayal, T.S. Kumbar, and all supporting members of IIT Gandhinagar for warmly and affectionately allowing me to utilize the institute's high speed internet and library facilities.

I would like to thank several researchers from various internet forums related to ROMS, WRF, COAWST models and CMIP5 data, who lent their support while setting-up different experiments. Special thanks are due to John C Warner for his support with COAWST model setup, especially in testing different compilers. I am thankful to Howard Diamond towards his support in accessing the SPEArTC dataset and in clarifying couple of doubts related to it. Thanks are extended to Stefan Kern for his help in accessing the HadISST dataset for the study domain. I am also thankful to Ute Merkel, Cindy Bruyére, Brett Mullan, Andres Sepulveda, R. Krishnan, B. N. Goswami and K. Hayhoe for brief yet useful discussions. I am thankful to all my friends including INTERCOAST colleagues (to name a few, Belén, Takasumi, Rima, Heather, Frieda, Bryna, Vignesh, Amanda, Sarah, Nicoll, Leslie, Carmen, and many others) for providing learning opportunities and support. It is highly possible that I may have missed some names here, nevertheless, I thank and acknowledge their invaluable contribution and support towards this work.

Finally, I thank the Almighty for giving me all the patience and strength I never imagined I could sustain and to keep my calm even in adverse situations. I am thankful to my parents, Dipali and Narayan C Ghosh; my brother, Dipankar for their love and care. Special thanks are due to my hubby, Aditya, who enacted different roles, while working away from Bremen: as an in-house system administrator and logistics manager. I thank my family members for acting as a mini funding agency at the time of need. I am thankful to two more souls, my dogs, Daisy and Cyrus, who supported me in their own ways.

I take this opportunity to dedicate this work to my parents and to all my teachers.

A prayer

Where the mind is without fear and the head is held high;

Where knowledge is free;

Where the world has not been broken up into fragments by narrow domestic walls;

Where words come out from the depth of truth;

Where tireless striving stretches its arms towards perfection;

Where the clear stream of reason has not lost its way into the dreary desert sand of dead habit;

Where the mind is led forward by thee into ever-widening thought and action;

Into that heaven of freedom, my Father, let my country awake

- *by Gurudev Rabindranath Tagore*
(Nobel Laureate)

CHAPTER 1

Introduction

About 70% of the earth's surface is covered by water including sea-ice at higher latitudes. It makes ocean a primary supplier of water vapour, which is the most abundant and naturally available greenhouse gas responsible in making the earth habitable. Thus, the importance of simple yet dynamic hydrological cycle of the earth increases manifolds while learning about the changing climate. The earth's curvature, rotation on its own axis, together with unequal heating of its surface, gives rise to a unique pattern of general circulation of its atmosphere. The general circulation of earth's atmosphere further drives the general circulation of earth's ocean. To be more precise, general circulation of ocean is driven by the atmosphere-ocean fluxes: transfer of momentum in the form of action of winds and associated stress (mechanical energy); redistribution of heat (thermal energy) due to differential heating around the globe and freshwater balance maintained (available potential energy) mainly by precipitation and evaporation, on ocean surface (Stocker 2013). Both atmosphere and ocean together play a key role in transporting excess heat polewards in order to maintain earth's climate, which directly influences the survival of living beings.

The contribution of ocean circulation in redistributing heat from tropics is manifested by the presence of wind-driven, dynamic subtropical gyral system, which is anticlockwise for the Southern hemisphere. The Southern Pacific Ocean is dominated by vast body of water and the nominal presence of landmass results in relatively lesser land-sea thermal contrast, and helps formation of well-built subtropical highs and clearer circulation patterns. In the present study, we will concentrate on the Southwest Pacific (SWP) region that is governed by the eastward flowing western limb of South Pacific (SP) subtropical gyral system.

In the following sections, we will go through previous research work focusing on the SWP circulation, the SP storm climatology, the changing pattern of storminess in general and specifically for SWP region, and the existing climate models for the region. In addition to them, we will also cover two topics on: role of

greenhouse effect on changing climate and large scale environmental changes as indicators to set the stage for present research topic.

1.1 Southwest Pacific region

1.1.1 Southwest Pacific circulation

The Southwest Pacific region is home to number of island nations including North Island (NI) and South Island (SI) of New Zealand (NZ) and since they are surrounded by vast ocean, they are predominantly influenced by the South Pacific general circulation pattern. The wind-driven westward flowing warm South Equatorial Current (SEC) forms the major part of the subtropical gyre. After reaching Australian coast at about 18°S, it splits into two branches, opposite to each other, one equatorward, as North Queensland Current, and the other poleward, as the East Australian Current (Ridgway & Dunn 2003). Along the eastern coastline of Australia, the East Australian Current (EAC) brings down with it tropical warm water, which due to Coriolis force converges itself into a narrow, fast moving boundary stream of warm current compared to neighbourhood (See Ganachaud et al. 2014 for more details on distinct water masses identified). The EAC splits into streams of ocean currents, approximately at ~30-34°S (Imawaki et al. 2013) into: the northeast-ward flowing South Pacific subtropical counter current; the main core advecting eastwards to North Island along Tasman Sea (called as Tasman Front); and its remainder continuing to flow southward along Australian coast towards Tasmania before advecting westward connecting to southern Indian Ocean as Tasman Outflow (Tilburg et al. 2001). The eastward traveling Tasman Front is greatly modulated by the presence of meridionally aligned Lord Howe Rise and Norfolk Ridge (Imawaki et al. 2013). A part of this Tasman Front following the northeast coastline of North Island travels southeast and called as East Auckland Current (EAUC). A series of eddies that are permanent are also visible along the pathway of EAUC (Ridgway & Dunn 2003). After reaching the easternmost tip of North Island, the East Cape, this EAUC is known as East Cape Current and continues flowing far south (~43°S) before turning eastward to join the Southland Current, where this combined flow is called as the South Pacific Current (Imawaki et al. 2013). This completes a brief description of South Pacific subtropical gyral system. The EAC flows approximately between ~18°S and 35°S (Ganachaud et al. 2007) and plays a major role of transporter of tropical warm water mass down south, keeping New Zealand and Tasmania relatively warmer than they would otherwise have been at such latitudes. For more detailed description on the Pacific Ocean circulation and western boundary current, please see these articles and corresponding illustrations: Hu et al. (2015) and its Figure 1; Figure 2 in Ganachaud et al. (2014); Figure 13.12 in Imawaki et al. 2013; Figure 4 in Petchey et al. (2010).

1.1.2 Large scale environmental changes as indicators

The sea surface temperature (SST) and surface air temperature (SAT) are key indicators of upper ocean and lower atmosphere conditions. The temperature difference between the two (SST minus SAT) serves as a primary source of information on vertical stability in the near-surface region (Cayan, 1980). The study

further highlights that the overall pattern of this index is found positive over larger ocean, which implies sensible heat transport from ocean to atmosphere. Among other parameters, this index are important in driving atmospheric instability, cloud formation, and precipitation pattern, especially along the coastal areas (Nouri et al. 2013). Therefore, this index may be used to analyze the change in strength of coupling between air and sea.

The processes that control the planetary boundary layer (PBL) depth are important to further understand the processes related to various fields of weather, climate, and air pollution (Mcgrath-Spangler & Denning 2013). This turbulent wind layer is the lowest layer of troposphere, lying closer to the earth's surface and responds to the surface frictional disturbances (from surface vegetation or topography) within an hour or less (Wisse & Arellano 2004). This layer actively participate in the exchange of energy, moisture, momentum, carbon and pollutants between surface and atmosphere. The PBL shows greater variability in both gaining (via shortwave radiation) and loosing (via longwave radiation) energy compared to surrounding atmosphere. As both wind speed and volume of air are function of temperature, the PBL depth tends to be enhanced during warmer seasons and daytime allowing greater convective mixing. Similarly, it contracts during cool seasons and night time, identical to compact and denser layer of cold air mass. An increasing amount of moisture and heat within the PBL may drive it to instability. Consequently, the intensity of any convectively driven system, (like thunderstorm or tropical storm) is deeply related to the source of heat and moisture available at its base/surface and is defined by the physical characteristics of PBL, which supports in driving and even sustaining such systems via vertical transport of energy and moisture (Wisse & Arellano 2004). An increased PBL height encourages increased vertical mixing, increased surface temperature and reduced relative humidity (Zhang et al. 2011). As the PBL height controls both radial and vertical distribution of momentum and enthalpy, it plays an important role in transporting energy and hence has a major impact on storm formation and intensification (Mcgrath-Spangler & Denning 2013).

A number of studies emphasize on the role of warmer sea surface and its response on storms in a region. In case of summer/autumn storm formation, one of many necessary conditions that decide the tropical storm formation is the minimum SST of 27-28 °C. In similar context, importance of the role of SST in hurricane-ocean energy exchange and as a source to boost the static energy of PBL in attaining as well as maintaining a specific level of hurricane category is discussed by Ooyama (1969).

1.1.3 South Pacific storm climatology

Depending upon the source of energy, storms can be broadly classified into tropical and extratropical types. However, when favourable conditions occur, sometimes a waning tropical storm may transit into extratropics to eventually re-intensify. These third type are special and infrequent and are commonly called as post-tropical, or more technically as extratropical transitioning storms. The tropical cyclones form over the warm moist ocean near the equator and are driven by the latent energy released while formation of

cloud or rain. An extratropical storm system mainly derives its energy from the horizontal temperature gradient present in the atmosphere. These low pressure systems are associated to cold fronts, warm fronts, and occluded fronts. Since our study area receives both the extratropical and extratropical transitioning storms, therefore we will not restrict our discussion to storms that originate only at extratropics, but to all those types that it receives. The term used for extratropical storm is identical to both midlatitude and baroclinic storm. The following paragraphs provide an overview on storm climatology of the southern hemisphere based on previous works of Taljaard (1967), and Sinclair (1994, 1995, 2002, 2004):

(a) Extratropical storms

While reviewing the southern hemisphere (SH) storm climatology, the genesis region invariably lies between 50° and 65°S throughout the year. So, maximum storms are found close to 55°S latitude. In addition to that, a second maxima in storm activity can be seen in winter along 40°S latitude, which covers almost entire South Pacific Ocean (Sinclair 1994) and is associated with the subtropical jet stream (Sinclair 1994). He further explained that the extratropical regions of the globe, approximately between 30° and 60° latitudes can be characterized as continually moving caravans of migratory synoptic features that include anticyclones, lows and associated fronts. The storms that form in these regions mainly originate from the anticyclones or subtropical ridge or high pressure areas, also historically known as horse latitudes (~ 30° latitude). Once formed they tend to move poleward, however, get steered eastward by the prevailing westerlies. These synoptic features bring substantial change to the local atmospheric conditions or weather. As opposed to the Northern Hemisphere, which has greater land mass and hence larger land-sea thermal contrast, SH storms show lesser regionality. In middle latitudes, during winter, storm genesis locations mainly occur between 35°-55°S, then they migrate eastward or poleward, and finally decay overwhelmingly south of 60°S, which is also known as the graveyard of storms (Taljaard 1967). Nevertheless, some eastward migrating midlatitude storms that originate closer to the east Australian coast, get intensified in the mid-Tasman Sea and continue further east till they reach the western part of the New Zealand to decay. Such storms are commonly known as *Tasman Sea storms*. Due to enhanced heat and moisture fluxes from the relatively warmer East Australian Current (EAC), Tasman Sea storm formation favourably takes place between 35°S and 40°S along the eastern coast of Australia. There are other regions that too show storm genesis during the winter season: area south-east of North Island and north-east of South Island of New Zealand; area at about 30°S, 150°W; areas at 150°E and at the dateline, both south of 60°S latitude.

Although the current study does not aim to cover the influence of change in Southern Oscillation Index on storm activity, it is interesting to learn from Sinclair (1995) that an increase (decrease) in storm activity north of 40°S in the eastern Pacific is connected to the negative (positive) Southern Oscillation Index phase. During La Niña (El Niño) years an increase (relatively decrease) in the storm activity is noteworthy towards north of New Zealand (over Australia). The explosive cyclogenesis location were defined to be most

frequently along a band lying east of Australia and in a zone extending from northeast of New Zealand across Pacific Ocean.

(b) Extratropical transitioning storms

A phenomena, where a poleward moving tropical storm while in middle latitudes slowly losing its tropical characteristic features and eventually acquires midlatitude storm features, is termed as extratropical transition. During this transition, a tropical storm or hurricane starts losing the symmetric cloud cover around its eye that is accompanied by precipitation region and in due course picks up thermal characteristics to sustain in midlatitude zone with more of an asymmetric cloud structure.

Though on rare occasions, at least one out of nine or more tropical cyclones forming every year, are likely to make its way south of 35°S, reaching New Zealand and causing severe damages. According to Sinclair (2002), such devastating events are likely to occur every year between December and April, however, February and especially March are the most notorious months with maximum possibilities of tropical cyclones reaching middle latitudes. It is worth mentioning here that March records the warmest sea surface temperature, which creates favourable and essential condition for tropical storm formation. Looking back into past, few major events can give a glimpse of how important these summer-autumn storms could be for the middle latitude population. One of the most talked about instances is when the tropical cyclone *Gisele* in April 1968 re-intensified while moving over New Zealand. The winds reached up to 75 ms^{-1} in Wellington and 51 lives were lost due to sinking of *Wahine* (an interisland ferry). In another instance in March 1988, when tropical cyclone *Bola* made its way to New Zealand, it produced hurricane-force winds in northern New Zealand pouring heavily more than 900 mm rainfall. Similar consequences were noted when Fergus and Drena hit North Island in December1996.

According to Sinclair (2002), mostly, the mean tropical storm intensity is greatest between 20-25°S and those who travels south towards New Zealand waters, are weaker by then. However, due to thermal (temperature gradient) source of energy it might re-intensify soon. It is astounding that the extratropical transitioning in Southwest Pacific Ocean starts at quite early stage of tropical storm's life, at ~15°S compared to the northern hemisphere. By ~20°S the tropical storms already start to come across baroclinic westerlies that steer them rapidly towards the pole and eastward, so that between 25°-30°S they acquire the extratropical features. He further extended his (Sinclair 2004) study to suggest that the surface storms located between 28°-34°S and those located further south (poleward) gets intensified while they are beneath the equatorial entrance and poleward exit regions of the upper subtropical jet, respectively.

There is a consensus among a large community of tropical storms scientists that the intense tropical storm systems would be increasing in a warming world. The tropical storm that undergoes extratropical transition over Tasman Sea are found to be more vigorous than those east of New Zealand (Sinclair, 2002). Even though rare, but due to the scale of damages they bring into the middle latitude regions, like New Zealand,

there is a need to study the response of extratropical transition with this rise in intense tropical storms in a warming world.

1.1.4 Changing storminess

Several studies (Webster et al. 2005; Klotzbach & Landsea 2015; Hoyos et al. 2006; Bengtsson et al. 2009) indicated that the number of tropical storms or any convectively driven systems would reduce in future scenario. However, once favourable conditions occur, they might grow up into more intense storms causing more destruction. This claim is backed by two simple mechanisms: first, in tropical region, the warmer air parcels can hold higher amount of water vapour and so lesser precipitation. Such a condition has a negative implication on the vertical mass flux of the atmosphere-ocean system (Held & Soden 2006), making less favourable conditions for the onset of the storms. Second, once a storm is formed at the tropics, the relatively warmer atmosphere then supports it to continue to intensify by supplying the additional amount of water vapour it has been holding.

To understand how the extratropical storms might change with warming, at first we have to understand what is baroclinic instability and how does it regulate storm formation in the middle and higher latitudes. The atmosphere continuously work towards maintaining a typical net radiative pattern for any region. Any instability or perturbations therefore immediately draw energy from the mean available potential energy. In tropics, the transport of heat takes place via zonal mean meridional circulations, like Hadley cell. Whereas in middle latitudes, eddies present in the system are responsible for the heat transport. Baroclinic instability is a mechanism by which energy is drawn/tapped from the system/environment where the eddy sits. The mean available potential energy is proportional to the horizontal temperature gradient, which is related to the vertical shear of zonal wind that in turn is proportional to the meridional temperature gradient. It is also known as a type of shear instability (Grotjahn 2002). Extratropical storms get their source of (kinetic) energy required to move, mainly from the conversion of available potential energy and little from the release of latent heat (Bengtsson et al. 2009). Mean available potential energy is proportional to the temperature gradient in the troposphere, which is greatest during winters, in general, hence forming more number of intense storms (Bengtsson et al. 2009; Lim & Simmonds 2009). Therefore, warming up of the poles, especially in winter will reduce the temperature gradient relative to the equator, which will cause weakening of the baroclinicity, resulting into lowering of the extratropical storm activity (Bengtsson et al. 2009).

Whereas, from the model results, it is clear that there are possibilities of differential warming at different layers of the global atmosphere: greater warming in upper-tropospheric layers over tropics, at lower-tropospheric layers over Arctic (Lim & Simmonds 2009), and at mid-tropospheric layers over Antarctic (Lachlan-Cope et al. 2009). Such differential warming at different layers of the global atmosphere, are likely to introduce different consequences: increase (greatly) the baroclinicity at middle (upper) troposphere, and reduce it at near surface, which regulates the formation and intensification of the

extratropical storms. On the same line, Lambert & Fyfe (2006) suggests an overall cooling of the stratosphere and warming over troposphere (greater at poles and continents, during winter). Considering these facts, the winter extratropical storms might reduce. At the same time, in the background there is an acceleration in evaporation process due to warmer surface that is responsible for increase in humidity of the atmosphere (Lambert & Fyfe 2006). This might support an increase in the intensity of the extratropical storm activity. In another set of study (Bengtsson et al. 2009; Inatsu et al. 2003), the authors suggested that the mid and high latitude storm formation and intensification are directly proportional to the change in sea surface temperature gradients rather than the sea surface temperature itself.

A special report (Mullan et al. 2011) on possible scenario of wind and storminess focusing on New Zealand, supports a possible poleward shift in storm tracks (Yin 2005; Bengtsson & Hodges 2006), which is likely to reduce number of extratropical storms passing by the country during winter. Accordingly, they suggested a decrease in rainfall mainly for North Island and east of the New Zealand. During summer, however, they suggested a likely increase in the storm activity over Tasman Sea, and a decrease over south of New Zealand (in agreement with Bengtsson et al. 2009).

Importance of studying any possible changes in storminess in future days due to ongoing rise in warming of the climate is a vast scope of research. Compared to the northern hemisphere, unfortunately, there are limited studies that focus on storms that develop, deepen and influence the middle latitudes of southern hemisphere (Sinclair 1994; Simmonds & Keay 2000; Keable et al. 2002). In addition to that, studies underlining the mechanisms responsible for such changes in the storms many a times do not match with each other and are limited.

1.1.5 Existing South Pacific climate models

While revisiting the existing regional and global circulation models for the study area, a number of models are noted, however, not all could be cited here for the sake of brevity. The first regional climate model, is the CSIRO Division of Atmospheric Research Limited Area Model (DARLAM) by (McGregor et al. 1993) and was improved over the years. It has been extensively used for studying Australasian weather and climate (McGregor et al. 1993; Mcgregor & Walsh 1994; Walsh & Katzfey 2000; Walsh et al. 2004) mostly utilizing the tropical cyclone-like vortices simulated for the study region. The model is said to simulate well the cyclogenesis and related seasonal variability for present climate scenario, with no significant change in genesis region for doubling of CO_2 scenario and little southward shift of vortices genesis (Walsh & Katzfey 2000). The base simulation uses 125 km grid spacing, 9 vertical levels, and lateral boundaries are forced by CSIRO global climate model. They further extended their analysis using a higher resolution (30 km x 18 levels) one-way nested domain over tropical east Australian coast, whose lateral boundaries were forced by the 125 km base model output. The authors found that stronger vortices detected by base simulation are likely to intensify more in finer simulation. However, once formed the storms with warming climate showed a tendency to travel more distance towards pole. They claimed the changed

thermodynamical conditions in enhanced greenhouse scenario along with further southward steering of winds might have contributed towards extension of storm path far south apart from slight southward shift in the vortices formation. (Nguyen & Walsh 2001) uses this base model set-up to study geographical variability in storm formation influenced by the phases of El Niño Southern Oscillation (ENSO). They concluded that under La Niña conditions, the vortices form close to the Australian coast, whereas under El Niño conditions, they form farther east off the Australian coast in line with the observation. Secondly, under enhanced greenhouse scenario, the number of vortices were found to reduce. Another study (Renwick et al. 1999) uses the above mentioned 125 km x 9 levels base model output to force the 50 km grid spacing for NZ region. They found the simulated current-climate surface parameters match well with the observation and highlighted the need for improved details on land surface and clouds, especially over NZ/Tasman Sea area. On future change due to doubling of CO_2 simulation, they concluded a reduction in strength of the westerlies that increases precipitation and low-level cloudiness in eastern NZ along with a reduced diurnal temperature range. The low-level cloudiness and diurnal temperature range are related to the changed modelled circulation. The authors stressed upon the need to use more than one global model output for regional modelling with special emphasis on coupled atmosphere-ocean model for transient simulations to assess response of climate change. Other studies based on DARLAM focusing on NZ precipitation (Katzfey 1995a; Katzfey 1995b), climate of Tasmania (Mcgregor & Walsh 1994), and emission and transport of trace gases in the Australasian atmosphere (Kowalczyk & Mcgregor 2000) are noteworthy.

Another regional atmosphere model is used at very high resolution (8 km) to assess the current climate of two island nations: Fiji and Federated States of Micronesia. The performance of this regional atmosphere model is described by (Chattopadhyay & Katzfey 2015). The dynamical downscaling was carried out in two stages: at first stage, six CMIP3 global coupled model output were downscaled using CSIRO CCAM at 60 km grid resolution and at second stage, three of these 60 km downscaled results were used to force CSIRO CCAM at 8 km grid resolution. The authors described the performance of the downscaled model for each grid scales and concluded that the high resolution simulation improves the representation of current climate. They further concluded that since the orography of a region is capable to influence the wind and precipitation of the region, therefore, selection of higher resolution at 8 km helps simulate the present climate scenario of both the island nations more realistically.

A recent study (Evans et al. 2015) on future change in the strength of South Pacific Convergence Zone (SPCZ) uses two different set of ensemble results. First set of results are produced by four different regional atmosphere models (CCAM, WRF, RegCM3, PRECIS) and second set of results are produced by downscaling six different CMIP3 global model output using same CCAM regional atmosphere model. They concluded no improvement in SPCZ representation by ~50 km grid resolution regional model downscaling when compared to that of 60 km grid resolution global climate models. The authors concluded that large uncertainty on future projection of SPCZ as shown by global climate models remains intact for regional models. They also concluded no change in the strength of SPCZ seen in future during austral

summer time. Chattopadhyay & Katzfey (2015) concluded that in the absence of any topographical features that may influence the rainfall and wind pattern of islands, like in Federated States of Micronesia, use of a finer resolution regional model does not help in increasing the accuracy of results. However, they further added that this is not true for areas (islands), like Fiji, whose wind and rainfall pattern are dominated by topographical features (or orography) where the same regional model simulated realistically the current climate scenario compared to coarser forcing data. Previously, Lal et al. (2008) described similar modelling study using OCCAM at such high resolution and concluded that the regional model output not only captured well the rainfall variability of Fiji but also the effect of ENSO on it. Similar conclusion on rainfall variability as well as the influence of ENSO on rainfall and spatial SPCZ supporting the benefits of adopting finer scale regional model is shown by another study on Fiji. POAMA2 (Cottrill et al. 2013) also boasts to reproduce well the rainfall variability related to ITCZ and SPCZ dynamics. Although, the current study does not focus on SPCZ and its future variability in strength, in a separate note it is to be noted that while working on sensitivity of the model grid resolution, the preliminary results showed that 0.5° horizontal grid resolution underestimated numerous dynamical features of the study domain, possibly due to the complex bottom topography, which were (described in **section 1.2.2** of current article) substantially resolved later by utilizing 0.25° grid.

A recent paper (Black et al. (2016) describes development and evaluation of weather@home Australia-NZ regional climate model. This model is based on offline one-way nesting concept, where daily output of global atmosphere model (HadAM3P, 1.25°x1.875°, 15 minutes time-step) is forced as lateral boundary conditions to the regional atmosphere model (HadRM3P, 0.44°x0.44°, 5 minutes time-step) before proceeding to the next day. The model is said to use improved computation of cloud, convection processes. This is one of those regional model that covers a vast Australasian area simulating regional domain covering both Australia and New Zealand region at comparatively higher resolution (0.44°). The simulated results were said to resolve well various important climatic features of the region including effects of ENSO. To determine the effect of region's topography on splintered zonal jets Couvelard et al. (2008) used a very high resolution (1/12°, 8 km) regional ocean model (ROMS-AGRIF version) over tropical (10-30°S, and 141-191°E) SWP region.

Besides regional climate models, several global ocean general circulation models at nominally high resolution (at 0.25° grid resolution) were previously used by some researchers (Stammer et al. 1996; Webb 2000) to detail out the large scale regional circulation. The latter study described five simulated deep narrow ocean jets formed as a result of splitting up of the SEC. There are similar studies (Semtner & Chervin 1992; Rothstein et al. 1998; Luo et al. 2003; Y. Luo et al. 2005; J. J. Luo et al. 2005 to name a few) that utilize global ocean model focusing on southern Pacific region's ocean circulation, however, are not detailed here. Apart from modelling studies, researchers have also used observational (Morris et al. 1996; Wijffels 2001; Ridgway & Dunn 2007; Kawabe & Fujio 2010) and climatological (Qu & Lindstrom 2002; Ridgway & Dunn 2003) data to describe the structure of the region's general ocean circulation.

There are couple of efforts recognized towards constructing a coupled atmosphere-ocean model for the South Pacific region. As per our knowledge, the very first attempt to use a global coupled atmosphere-ocean model for South Pacific region is described by (Meehl 1989), where he conducted two sets of coupled simulations using same global atmospheric model: first with a simple 50 m thick slab ocean model and second with coarse resolution global ocean model. He studied the tropical ocean-atmosphere coupling process over Indo-Pacific region. He concluded that the inherent shortcomings within coupled ocean component were more likely to introduce errors in a coupled climate simulation, than coupled atmosphere component. In spite of these deficiencies the coupled atmospheric component was able to simulate the low-level winds more realistically in strongly coupled regions like Indo-Pacific tropical regions. Hence, he highlighted the need for improvement of ocean model formulation to improve computation of surface heat fluxes that is input to atmosphere model for overall improvement of coupled simulations. He highlighted the strengths of interactive coupling between atmosphere and ocean components as a research tool in simulating coupling processes better as it also adds to more consistent climate simulations.

Additionally, in recent decades, increasing viability of powerful supercomputers, parallel computation and organized modelling efforts (for example, using results from different versions of CMIP suite of models, CORDEX) made it possible to make use of the coupled general circulation multi-model analysis approach. These coupled general circulation models are increasingly used to resolve each components of the earth system at greater resolution that along with improved versions of sub-grid scale parametrization and allows researchers to predict the region's weather, as well as construct projection of possible climate scenario from past to future time slices using realistic forcing. As per our knowledge, there is only one coupled regional model existing, POAMA (Predictive ocean-atmosphere model for Australia) described by Cottrill et al. (2012, 2013), however, the regional span is limited to tropical South Pacific. This coupled model is a dynamical seasonal forecast system, developed by Australia's Bureau of Meteorology to provide seasonal forecasts for Pacific island nations. The coupled model is concluded to be able to make good prediction on both the ENSO phases about nine months in advance and corresponding spatiotemporal rainfall variability (Cottrill et al. 2012). It consists of Bureau of Meteorology atmosphere model (BAM3.0, 2.5°x2.5°x17 levels) and Australian Community ocean model version 2 (ACOM2, 2° x 0.5° in tropical ocean x 25 levels). The latest version POAMA2 is explained by (Cottrill et al. 2013). As obvious from the objective to help support the Pacific island nations prepare well in advance from extreme events, like, storms, floods, droughts caused due to different phases of ENSO directly, the southernmost limit of the model is 30°S and hence does not cover the middle latitude.

1.2 Overview on Research needs, strategy and scope

1.2.2 Need for development of regional coupled model

As seen in the preceding **sections** (**1.1.5 and 1.1.6**), to understand the behavioural changes of storms in a warming climate, various studies adopted global or regional general circulation models as tools. The middle

latitude region of the SWP hosts both summertime tropical as well as wintertime midlatitude storms. Since the genesis and sustenance of storms are largely dependent upon the processes related to interaction between the atmosphere and upper layers of the ocean, therefore it is a prerequisite to adopt a tool that is capable to allow frequent interaction between the atmosphere model and the ocean model. Although global models are effectively used to understand global changing climate, their usage are many a times is limited by their coarser resolution (order of 100 km horizontal grid or more, (Rummukainen 2010). While studying changing behaviour of storminess in a warming climate, the use of coarser resolution global climate model might fail to represent accurately the resulting change in shift of tracks and its effect (Lambert & Fyfe 2006). The regional models are capable to resolve the local features more accurately than just the signatures of the same features seen in global models. Considering the computational power required for setting up a global coupled model resolving at finer scale, a regional coupled model is preferred for current study to manifest local climate features. This would be an attempt towards resolving complex bathymetry of the SWP Ocean as well as allow real time exchange of variables between the two media, to better resolve the changing storminess. In reality, storm events are examples of tightly coupled atmosphere-ocean processes. Therefore, while modelling the change in storminess, it would be prudent to develop a tool that can adequately resolve the real time air-sea interaction dynamics at planetary boundary layers of air and sea. Both the atmosphere-only and ocean-only models are inadequate in this regard (Aldrian et al. 2005) and justify need for coupled atmosphere-ocean model set-up. In the absence of a regional-scale coupled model for the region, there is a pressing need to develop such a tool. Therefore, this study uses a more realistic approach where large scale coupling between atmosphere and ocean is recreated by application of coupled atmosphere-ocean regional model set-up to downscale global model output on real time slices. In the following section we will discuss more on the strategies to be followed.

1.2.3 Modelling strategy and scope

The western South Pacific is well-known for complex seafloor topography (Black et al. 2016; Webb 2000; Ganachaud et al. 2005; Ganachaud et al. 2014; Couvelard et al. 2008; Ganachaud et al. 2007 and others). For instance, the presence of island ridges and reefs of Coral Sea islands (Fiji, Vanuatu, New Caledonia), along with shallow Queensland Plateau, Lord Howe Rise, Norfolk Ridge, as well as islands of New Zealand, which are mostly meridionally aligned opposite to that of large-scale zonal flow into the region, inevitably splinters the flow (Couvelard et al. 2008; Imawaki et al. 2013) making it more complicated. **Figures 1 and 2** gives a pictorial overview on the extent of the current study domain illustrating the complex sea floor bathymetry and few island nations of the SWP region. A recent article (Mortimer et al. 2017) that claims the existence of eighth geological continent, Zealandia also highlights the presence of elevated bathymetry around NZ, as 94% of the continent is submerged underwater including greater areas of northwest of North Island and including Campbell Plateau and Chatham Rise around South Island (see Mortimer et al. 2017 and Figures 5 and 6). Consequently, the SEC and its southward moving stream, the EAC, is steered through complicated pathways before it completes the gyral system. Several modelling efforts have indicated towards this fact including difficulty in simulating correctly the mean position of the

bifurcation latitude (Ganachaud et al. 2007) implying complication in setting ocean model on regional scale. In present model set-up, **section 2.3.4** explains the same problem while setting up the ocean model, which is solved by smoothening the bathymetry to avoid development of erroneous flow into the region. Despite this complexity, several modelling studies mentioned in previous **section 1.1.6** are dedicated to the region, augmenting knowledge of the region, which is encouraging.

The scope of the current study domain starts from latitudinal extent of ~15°S, hence the tropical SWP is not covered. The current work attempts to contribute towards development of the first regional coupled atmosphere-ocean modelling system for the region, covering sub-tropics to middle latitudes and parts of higher latitudes. The coupled model described in the current study aims at resolving the regional features at 0.25° degree resolution (~25 km) for middle latitudes, especially the coastal area surrounding NZ. At this resolution most of the prominent small scale topographic features are found to be represented correctly and as a result the boundary currents, eddy fields and frontal systems are resolved well (Stammer et al., 1996; Webb, 2000). The experimental set-up is designed keeping in view possible future studies on determining any benefits from coupled model compared to uncoupled model for both the components.

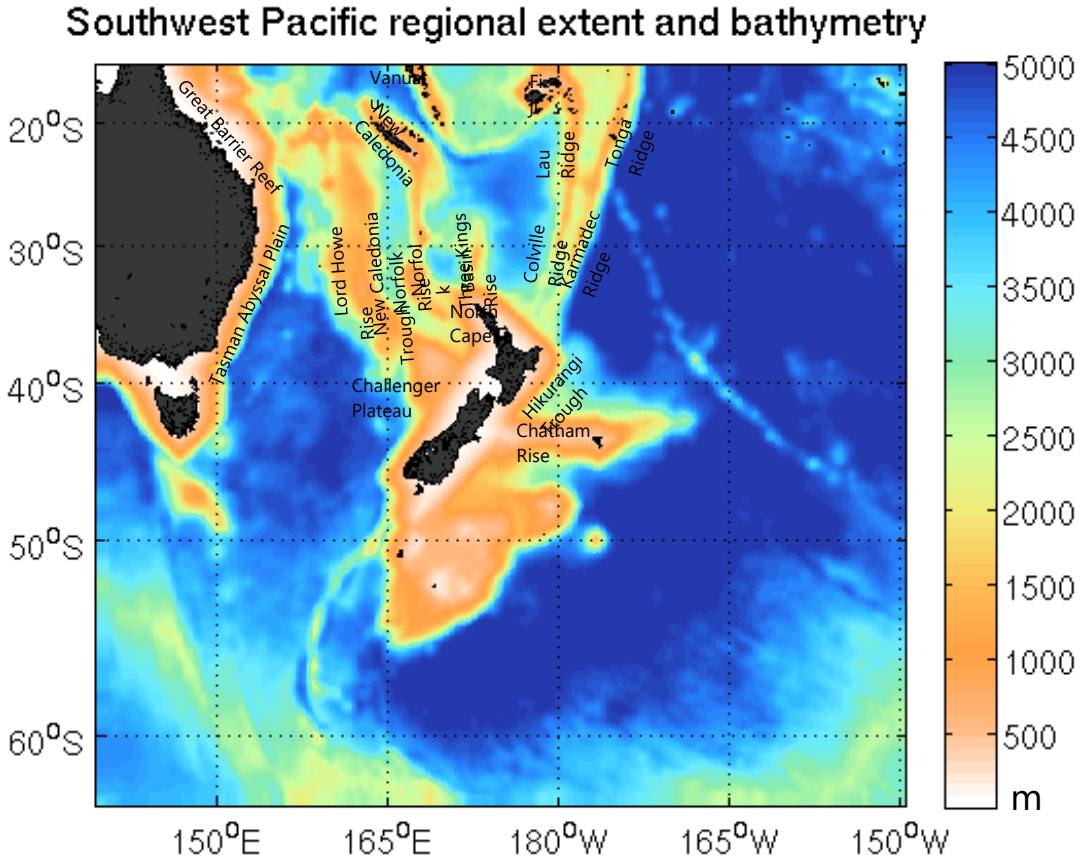

Figure 1 *Bathymetry of the study domain with details of major features of the region portrayed (2-dimensional top view). The shades of white to orange (near coasts, rises, ridges and chain of islands) highlight shallower areas, whereas light blue (cyan) to dark blue highlight deeper water of the region. Refer next figure for a closer 3-dimensional view of these features.*

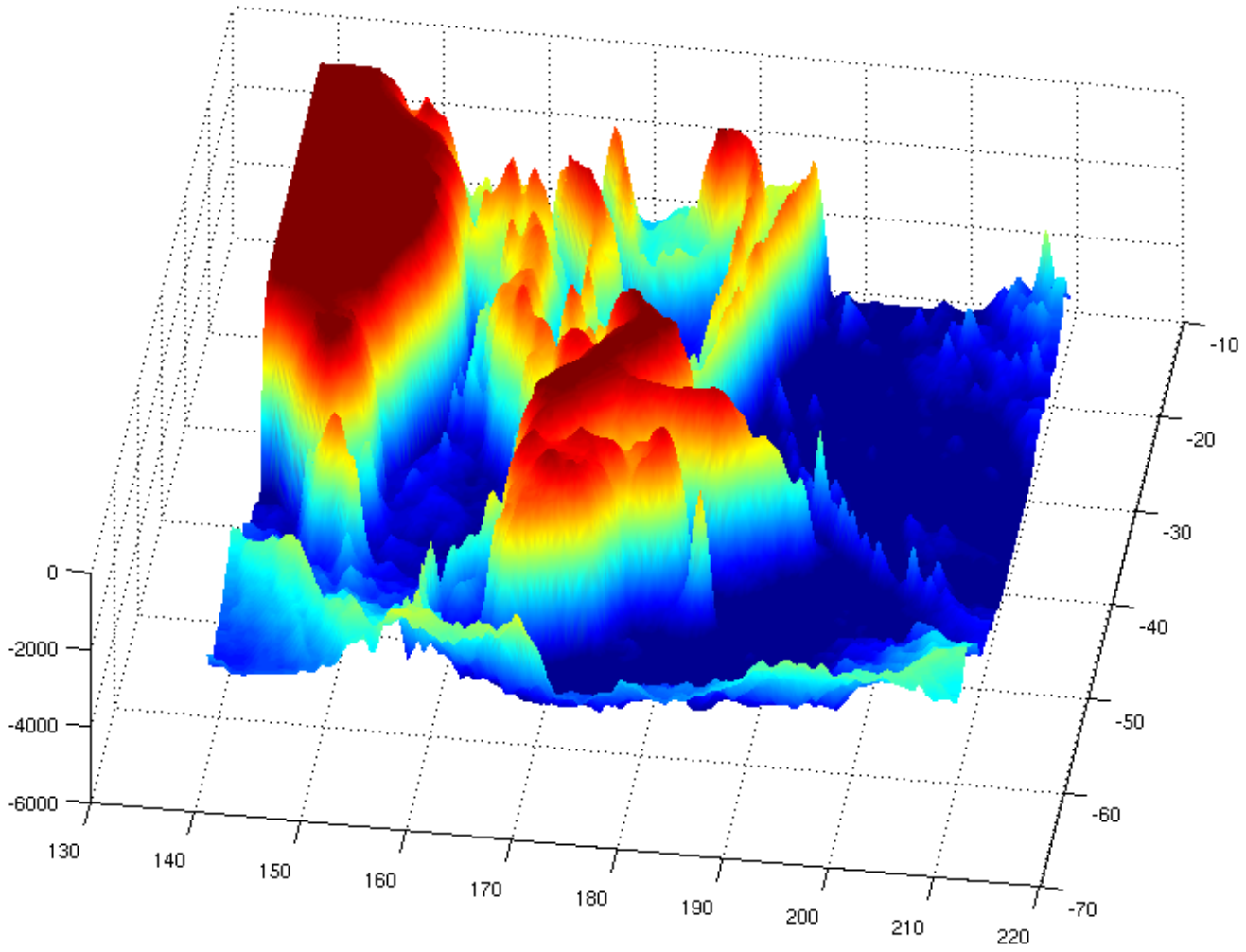

Figure 2 *Bathymetry (m) for the study domain in 3-dimensional perspective. Several mid-ocean topographic features like trenches, ridges, island chains, seamounts can be clearly seen and has a dominant role in regional circulation.*

The regional model coupling demands two models run in parallel as well as exchange information and therefore require huge computation power compared to single regional models or coarser grid coupled models. Aiming at simulating the mean seasonal response in change in storminess of the region, the coupled regional models are planned to be integrated for five years. Such a duration has been previously used by other modelling studies (Döscher et al. 2002; Small et al. 1999).

Based on above mentioned background and strategies, a complete detail on data, methods adopted and model development steps are explained in chapter 2. The validation part is separately explained in chapter 3. A section-wise description of chapters 2 and 3 is outlined under **section 1.3** at the end of this chapter. The next section focuses on the second objective, where trends of storminess are analysed along with the large scale environmental variability for the study domain, to explore potential linkages between the two.

1.2.4 Recently changing storminess and large scale environmental variability

The motivation of this research objective originated from the curiosity to acquire factual information on the real-time recent past storm distribution for the study domain. It will help in establishing and understanding the recent changes in trends of storminess. It uses Southwest Pacific Enhanced Archive for Tropical Cyclones (SPEArTC) dataset (Diamond et al. 2012; Diamond et al. 2013), the most comprehensive and reliable (Magee et al., 2016) observational archive on storms available for the SWP region and long term observational/reanalysis data to understand the changes in recent past storm distribution along with large scale environmental variability.

To start with, let us look into **Figure 3** that gives a pictorial overview on summer-autumn storm tracks for Southwest Pacific region, where each map shows total storms observed for five year time span starting from 1970-1974 to 2010-2013 based on SPEArTC-Google Earth dataset (Diamond et al. 2012). This Figure not only gave an overview on geographical distribution of storm tracks but also outlines the change in its density and path with time. In addition to these five-yearly maps, a histogram showing latitudinal variation at 5° latitude band is derived from the storm dataset, and is depicted by **Figure 4**. In general, the storm counts have reduced during 1970s to 2010s with maximum seen during 1990s. Lowest counts are visible for 2000s compared to other decade.

Over past decades, this figure clearly indicates a gradual reduction in storm counts for lower latitudes and midlatitudes, whereas converse is true for higher midlatitudes. Noteworthy is 1990s, marking as the onset of intrusion of tropical storms to higher midlatitudes, reaching almost about 45° to 50°S and further, hence travelling far distances – which is an unusual feature for the region. In view of that, storm tracks reaching higher midlatitudes are seen maximum for 1990s and lowest for 2000s and noteworthy is their increasing trend in 2010s. The feature of decline in storm density for entire study domain is more evident from 2000-2004 time-slice. Whereas, the second feature of storm tracks gradually reaching greater distances towards pole with the passage of time is slowly making higher/midlatitudes more vulnerable to risks of storms of tropical origin.

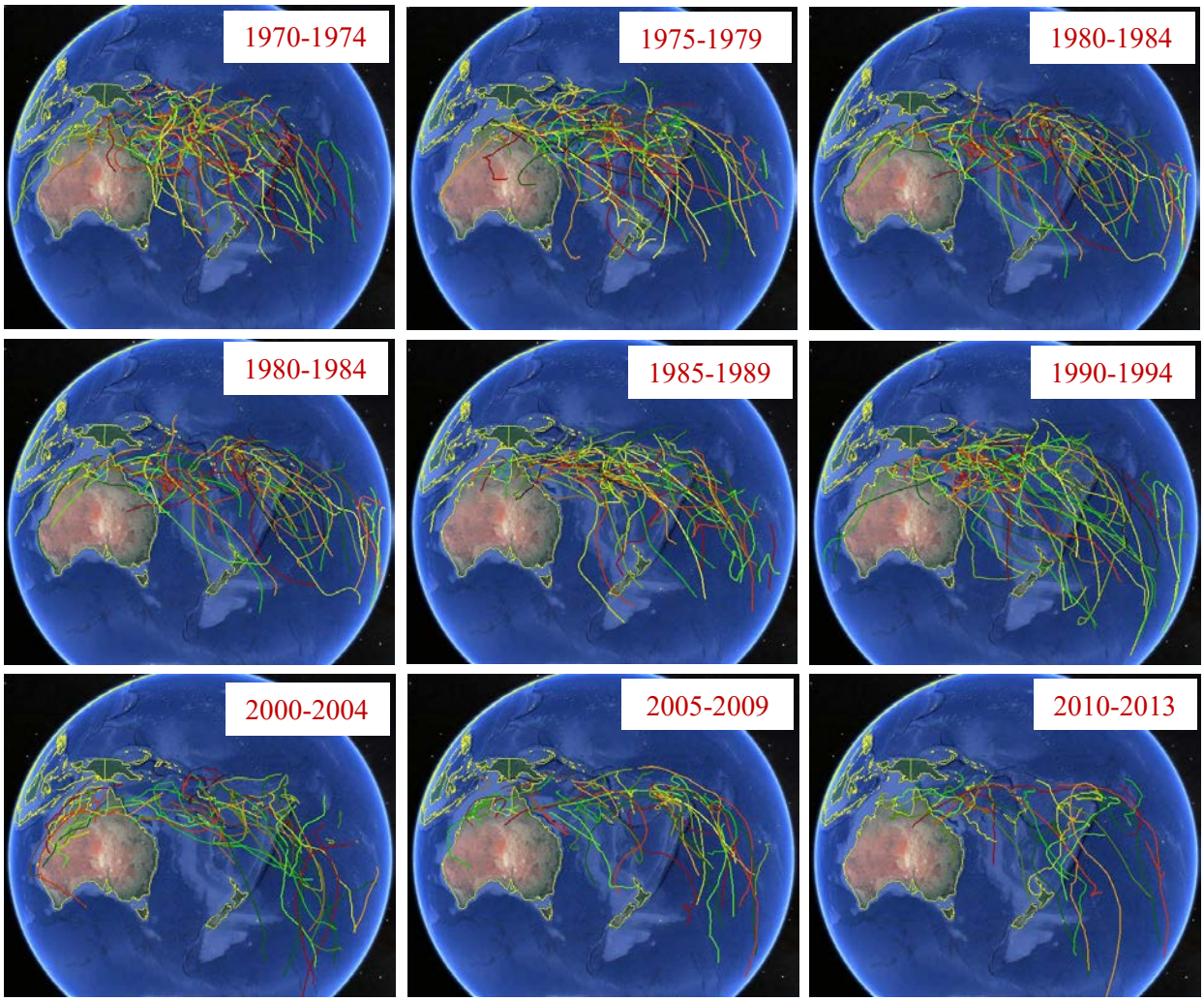

Figure 3 *Actual storm distribution observed for every five years span starting from 1970-2013 portraying their respective tracks (source: SPEArTC-GoogleEarth dataset, Diamond et al., 2012)*

Such changes in storminess of the region is likely shaped by change in large scale environmental conditions. Therefore, it is vital to understand the changes in large scale environmental condition and mechanisms that together are responsible in formulating region's change in storminess. In long term, this knowledge would be helpful in understanding the possible changes in future storminess.

The histogram in **Figure 4** shows reduction in storm counts during 1970s to 2010s with maximum storms noted during 1990s. Lowest counts are visible for 2000s compared to other decades. However, only from 1990s presence of storms is visible around higher midlatitudes (i.e. ~45-50°S). Storm tracks reaching higher midlatitudes are seen maximum for 1990s and lowest for 2000s and showing an increasing trend in 2010s.

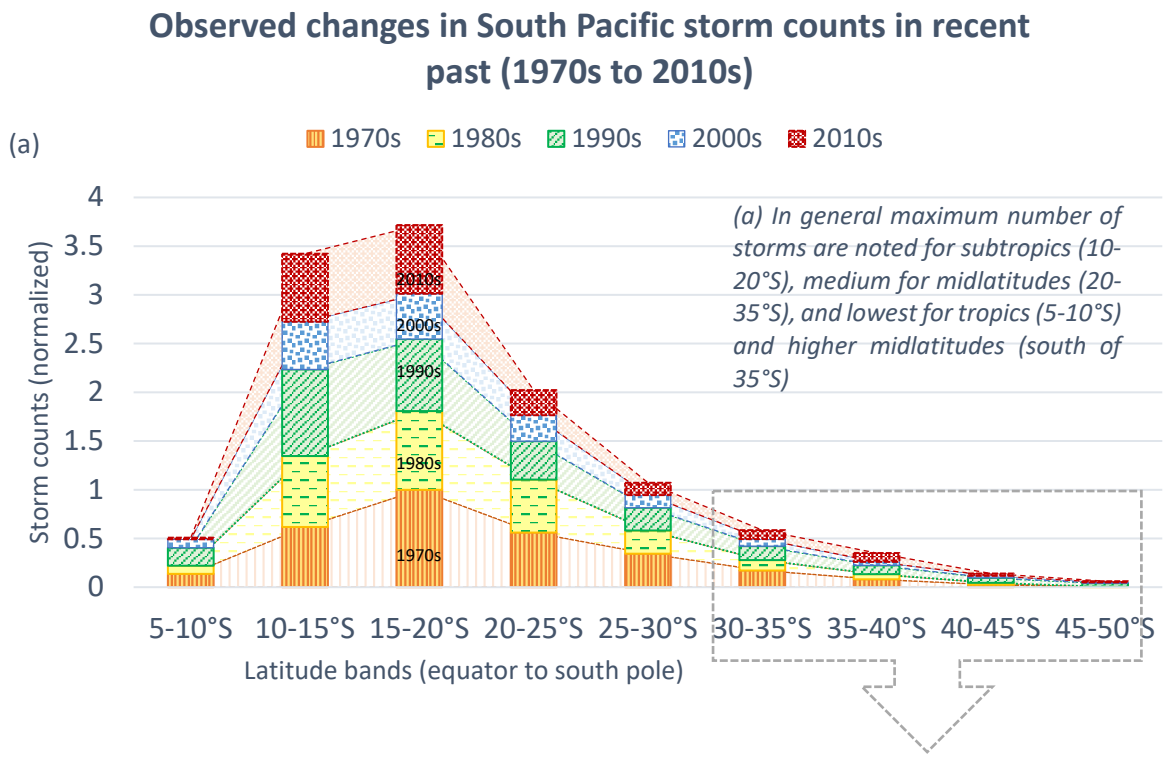

(b) Zoomed into the middle-higher latitudes: as expected, storm counts have reduced for poleward bands, south of 35°S; however, noteworthy here is the increased storm counts at higher latitudes, 45-50°S, where tropical storms commenced only from 1990s, which can also be observed as the maximum storm decade. After a fall in storm counts in 2000s, a rise can be seen in 2010s with higher numbers seen for 30°S, especially critical rise for 35-40°S band. Although counts are reducing towards pole, but an increase in 2010s is evident at 45-50°S, showing more tracks reaching in recent decade.

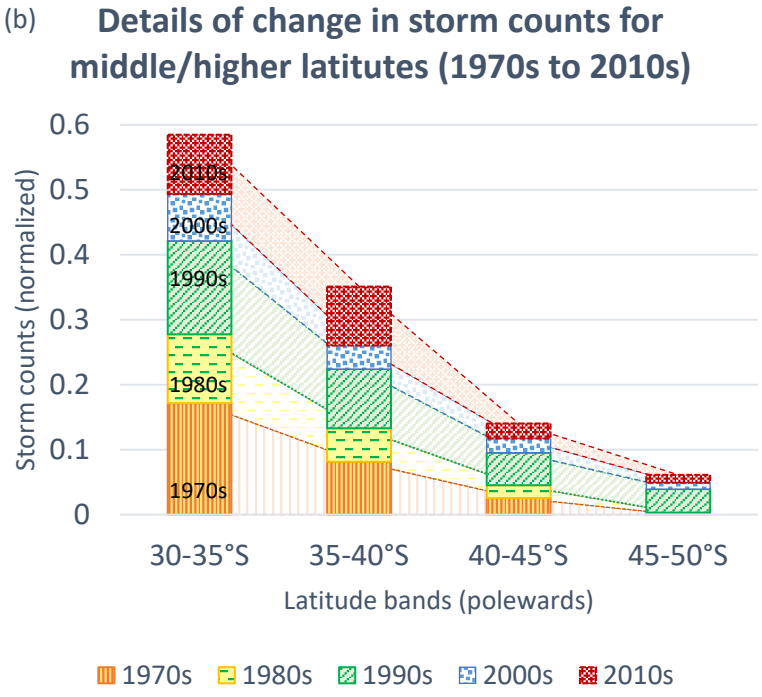

Figure 4 *A histogram showing latitudinal variation (@ 5° latitude band) of South Pacific storm counts and its changing pattern for past few decades shows an overall decrease in counts whereas converse for higher midlatitudes. SPEArTC observation data are used for analysis.*

With this, please refer chapter 4 to learn more on how the storms and corresponding large scale climate variables have changed in the past 45 years. Section-wise description of chapter 4 is detailed in the outline **section 1.3** of current chapter. The aim of this chapter is (i) to develop an understanding on region's storm climate and to determine the changes in storminess in last four decades (1970 to 2014), (ii) to understand the changes in large-scale environmental conditions that might have shaped up the recent change in the frequency and duration of storms. Further to this, note that the South Pacific region also hosts a globally important dynamic feature, commonly known as ENSO that not only has a direct implication on region's weather but also drives the global weather pattern. The present study however, does not aim at studying ENSO, ITCZ, SPCZ phenomena and focuses only on the seasonal response of region's storminess. Diamond et al. (2012) prepared a 41 years (1970-2011) storm climatology of the region (the SPEArTC dataset). The connections of tropical storm climatology to phases of ENSO (Diamond et al. 2013); and to Madden-Julian Oscillation (Diamond & Renwick 2014) are also discussed in detail.

The next section sets stage for third research objective, which is an effort to understand the likely changes in future storminess. It uses the results from newly developed SWP coupled regional model.

1.2.5 Large scale environmental variability and scenarios of future storminess

Although, the regional coupled modelling systems are extremely expensive in terms of computation power and storage space (Rummukainen 2010), its application for coastal regimes and storm forecasts have shown an improvement over shorter time-scales (Edson et al. 2007). The authors further highlight that in coastal regimes, the mesoscale atmospheric circulation, fog formation, coastal upwelling and tidal mixing are mainly driven by the air-land-sea contrasts. The exchange of energy at the air-sea interface attained by a storm from the ocean boundary layer, along with internal dynamics like cloud microphysics, and numerous environmental interactions with large-scale features present in the atmosphere are some of the primary processes that govern any change in the strength and intensity of a storm (Black et al. 2007). The accuracy of storm formation is mainly based on the accuracy in prediction of air-sea exchange of energy over shorter time-scales (Edson et al. 2007). Further, both these drivers, air-land-sea contrasts and air-sea energy exchange are functions of accurate estimates of SST, and is generally missing in observational data needed to initiate a model.

Studies aiming at future projection on storminess require reliable global model results for same time-scales to downscale features at regional scale, numerically or statistically. Accordingly, the regional model boundaries are constrained either using observational/reanalysis or output available from coarser regional or global model. One option would be the usage of computationally less tedious stand-alone atmosphere or ocean model. The objective of present study is to simulate the changing storminess of the study domain. Drawback in using such a stand-alone model, say, atmosphere-only model is that it cannot keep track with the real-time changes in other climate component, (say, ocean), where the ocean representation into the atmosphere model completely relies upon the spatiotemporally prescribed and interpolated SST data, as if the ocean is never influenced by the dynamics of the atmosphere above it. Similarly, an ocean-only model

completely relies on the empirical formulae to compute the surface fluxes within the ocean boundary layer. Both these methods are inadequate as they overlook the interaction dynamics occurring at the planetary boundary layers of air and sea (Aldrian et al. 2005) and hence lack the real-time exchange of variables that may influence the results to a greater extent. Another option is to use a coupled atmosphere-ocean regional model. Application of coupled regional models for studying various coastal processes has recently increased (Renault et al. 2010; Warner et al. 2010; Zou & Zhou 2012; Döscher et al. 2002).

1.2.6 Research strategy and scope

In the light of above facts, along with the dependence of SWP weather on different type of storms throughout the year (summer/autumn convectively driven tropical storms as well as winter storms driven by baroclinic instability in middle latitudes), it is pertinent that in spite of additional computational penalty and complications involved in coupling of air and sea models, studies that aim to simulate changing storminess should opt for techniques that allows frequent interactions and feedbacks between these two large media. To summarize, in this study, we aim to enhance the usefulness of global climate model outcome by utilizing the strengths of regional climate model. Due to confined area of application, the regional models can resolve the local climate features at a much higher detail. This method of complementing the global model outputs is known as dynamical downscaling or limited area modelling (Rummukainen 2010). It helps one realise more accurately and in detail the possible changes that were visible only as signatures in global model outcome. It further allows the regional model to develop its own circulation pattern by including various regional scale features that were either unclear or were completely missing in the global model results.

Further, it must be noted that the present study neither covers the analysis of individual storms, influence of decadal scale phenomena like ENSO, nor attempts to understand the general climate of the study domain, which would require a much longer time scale of about 50 years. Instead we are interested in determining the changes in mean seasonal response using computationally costlier but more comprehensive coupled regional model, whose boundary conditions are forced by global model outputs. Here, the downscaling method chosen uses a numerical coupled regional atmosphere-ocean model whose boundary conditions are continuously forced by IPSL-CM5A-LR global model data, which though uses a coarser resolution but is integrated for longer time-scales to define the long term trend of mean climate of the globe. Despite its computational penalty, a coupled regional model integrated for 5 years would allow determine change in mean seasonal response in storminess of a region. Such, 5 years shorter time-scales were previously used in past studies (for example, Döscher et al. 2002; Small et al. 1999) to understand the mean and interannual variability at regional scale.

In current study, *storminess of an area* is analogous to area's *storm activity*, and is defined by observational records of total storm counts and intensity it hosts. Similarly, *change in storminess* is defined by the changes in storm counts, intensity and central pressure. However, in the absence of storm observational records, the storm activity as well as its changes are estimated based on various large scale environmental conditions.

This concept is in line with the fact that both storm activity and large scale environmental conditions influence each other and can further help understand the underlying physical mechanisms responsible for storm formation, intensification, sustenance and decay. Such mean change in storminess data would be useful for various agencies focusing on: risk management; curbing insurance losses due to extreme events; mapping and adaptation planning of the cities, vulnerable plains, low lying coastal regions and islands.

1.3 Overview on research objectives and outline of respective chapters

---

Research Objective 1: Development and evaluation of coupled atmosphere-ocean Southwest Pacific regional model

(i) setting up of stand-alone SWP regional atmosphere model,
(ii) setting up of stand-alone SWP regional ocean model,
(iii) setting up of coupled atmosphere-ocean SWP regional model
(iv) evaluation of newly set SWP regional model

Chapter 2 explains in detail the model set-up, where at first each stand-alone model is described before explaining about the coupled atmosphere-ocean model set-up. After chapter introduction in **section 2.1**, the following **section 2.2** describes common terminologies repeatedly used in this document, followed by explaining different dataset and methods (**section 2.3**) that are used to set the coupled regional model. A general introduction to COAWST modelling system developed by Warner et al. (2010) is given in **section 2.3.2**. This follows with the description of setting up of stand-alone atmosphere (**section 2.3.3**) and ocean (**section 2.3.4**) models, followed by description of coupled atmosphere-ocean model (**section 2.3.5**), highlighting steps that enable coupling between the two components.

Chapter 3 is dedicated to the evaluation of the set coupled model. It starts with a brief introduction, followed by data and methods (**section 3.2**), and performance evaluation (**section 3.3**) of newly set coupled model with respect to the reanalysis/observation and input forcing data.

In chapter 4, after introduction, **section 4.2** explains in detail different dataset and methods used for analysis. The first part of **section 4.3** gives a detailed picture of change in overall storminess of the region, followed by analysis of extreme storminess. The second part of **section 4.3** talks about the variability of large scale environmental conditions, where an effort is made to determine the mechanisms and variables that play a dominant role in changing the storm climate.

Research objective 2: To draw an overview of geographical distribution of recent (1970-2014) storminess from observational data and to understand large scale environmental conditions and mechanisms supporting changes in storminess

(i) to develop an understanding on region's storm climate and to determine the changes in storminess in last four decades (1970 to 2014),

(ii) to understand the changes in large-scale environmental conditions that might have shaped up the recent change in the frequency and duration of storms

Chapter 5 uses newly set coupled regional model output (as described under chapters 2 and 3) to determine the likely changes in future storminess based on large-scale variability of the region. A seasonal comparison is presented based on the differences between simulated scenario and historical output. It starts with chapter introduction, followed by **section 5.2** that gives a detail on methods used, followed by s**ection 5.3** that presents the results showing the possible changes in climate variables by end of 21st century (years 2095-2099) relative to the control period (years 1960-1965).

Research objective 3: To determine likely changes in the key climatic parameters of SWP region that might follow by end of 21st century compared to recent past

Research objective 4: To eventually construct scenarios of likely changes in the future storminess as a result of the stimulus caused by the changes in large scale climatic conditions

Chapter 6 amalgamates data from chapters 4 and 5 to establish relationship between changing climate variables and storminess for the recent past decades (**section 6.1**), and to apply this relationship to build scenarios of likely change in the future storminess (**section 6.2**). The validation of historical storm indices based on the corresponding storm observational data has been performed (**section 6.3**) and an assessment on how accurately the future changes in storminess have been predicted is concluded (**section 6.4.2**).

Chapter 7 discusses potential linkages between changing large scale environmental conditions and changing storminess (**section 7.1**), and illustrates scenarios of likely changes in the storminess by the end of 21st century (**section 7.2**). Chapter 8 summarizes entire work (**section 8.1**), provides an overview on caveats and gaps of the research work, along with future scope for possible improvement in tools and analysis methods (**section 8.2**), and conclusion of major findings (**section 8.3**).

CHAPTER 2

Model description and experimental design

As per our knowledge on existing models (**section 1.1.6**), none of the regional atmosphere-ocean coupled models cover middle latitudes of the SWP region. A regional scale model that can aid frequent exchange of data between the air and sea is recommended to resolve more accurately the large scale environmental variability that is missing in the IPSL_CM5A_LR (forcing global model) output. This chapter is dedicated to the first research objective (listed in **section 1.3**).

It describes in detail the setting-up of atmosphere and ocean models at regional scale, both in stand-alone and coupled mode. The **co**upled **a**tmosphere-**o**cean **r**egional **S**outhwest **P**acific (**1/4**°) model will be referred to as SWP14 model in this document for brevity. Performance evaluation of SWP14 will be discussed in chapter 3. The model downscales IPSL_CM5A_LR's ocean (2.0° x 2.0° x 31 vertical levels, 0.5° near equator) and atmosphere (1.9° x 3.97° x 39 vertical levels) components into regional scale of 0.25° x 0.25° x 32 vertical levels. Logically, this newly set model, SWP14, can only resolve features limited by its own horizontal resolution. Noteworthy are the specific strategies adopted to simulate the regional climate more closely to the input global forcing, while developing its own regional pattern of circulation. In spite of rich online resources on setting-up each models, it might demand time to get acquainted with specific criteria desirable for a successful simulation This chapter therefore makes an attempt to provide additional information on strategy used with reasoning that can be helpful in setting-up a new application.

2.1 Common terminologies

Several research applications make use of models to predict the future climate scenario and commonly use a terminology, "Representative Concentration Pathway (RCP)". To briefly describe RCP, excerpts from Nazarenko et al. (2011) are noted. The CMIP5 modelling experiments uses 4 set of future scenario simulations in continuation to the historical experiments (1850-2005, starting from 01 January, 2006) to simulate potential impact analysis in response to climate change by the end of 21st century. These four scenarios are predicted based on assumptions of various factors - socio-economic, technical or environmental and range from lowest forcing of 2.6 Wm^{-2} to medium of 4.5 and 6.0 Wm^{-2} to business as usual or highest forcing of 8.5 Wm^{-2}. Further details on RCP8.5 scenario are available in Riahi et al (2011).

Model initialization: A 3-D snapshot taken from either long term mean climatology or output from a global model is normally used to describe the region's initial climatic condition to start a model simulation. To start the model from rest is termed as cold start, whereas when the model is started or continued to run using previous model run output (with a restart file), it is termed as a hot start. For current case, each model set-up (either in standalone or coupled mode) uses a series of initialization files at a specified interval. Hence, both the cold and hot initialization modes are actually used. Such *series of reinitialized runs* or *sequential multiple restart method* are said to better perform than one time initialized long continuous runs (Jimenez et al. 2010). Accordingly, the SWP14 model is initialized from rest as a 'cold start' (at January 01, 1960, 0000 UTC for historical and January 01, 2095, 0000 UTC for scenario experiments) and run for a predefined time period. Once the model is initialized, the next time-period is simulated using the previous restart file as initialization. The restart interval differs for different models in this study and are specified under each set-up in the following sections separately. This method of using restart file as initialization of next model simulation is continued until the end of 5 years simulation (December 1964/2099 for control/scenario runs).

Lateral boundary conditions: Since the regional models are cut out of the globe and left with discontinued outer edges, therefore, they need large scale climate data that can define their open lateral boundaries. These boundary files generally include information on temperature, moisture, winds, SST, sea-ice that periodically feed the regional model as lateral and sea surface boundary conditions (Rummukainen 2010). In the current study, the set of data are taken from IPSL_CM5A_LR global model output for entire simulation period. For further details on how to manage the boundary conditions, kindly refer Rummukainen (2010).

Model Physics/parameterization schemes: It takes care of effects of different unresolved processes of the model domain as well as processes that interact with other components of the climate system other than atmosphere component (ocean, land, cryosphere). In the real atmosphere, each of these parameterization scheme does not act as a separate entity but they closely interact and influence each other through different processes. Within a model this interaction takes place through the model state variables, like temperature, moisture, wind and their tendencies, and via surface fluxes. Noteworthy here is that every physics scheme

present in a model interacts with model's surface physics scheme, which is responsible for updating the land state variables and (anticipated) coupled ocean model set-up). This implies that the numerical models closely try to mimic natural processes that are interdependent. Respective **sections 2.3.3 and 2.3.4** discuss more on different atmospheric and oceanic sub-grid scale processes that are resolved using chosen parameterization schemes.

2.2 Data and methods

2.2.1 Data

The Coupled Model Intercomparison Project Phase 5 (CMIP5, Taylor et al. 2012) suite of model output has been used as forcing data. Based on few criteria like, at least three ensemble members available by August 2012; availability of maximum number of variables required to force both the ROMS and WRF regional models; availability of atmospheric data at higher (~3 hourly) temporal resolution; availability of both historical and worst case emission scenario data, IPSL_CM5A (Institut Pierre Simon Laplace contribution towards CMIP5) model is found to be suitable.

To limit the computational space, *lower resolution* option of IPSL_CM5A model is downloaded from IPCC portal. Any unit discrepancy between the downloaded global model output and that required for two regional model inputs are sorted, for example, temperature (converted from K to °C) and pressure variables (converted from Pa to mbar) for ocean component. The corresponding ROMS and WRF input variables taken from CMIP5 dataset have been tabulated under two different tables: **Tables 1** and **5**, respectively. Some variables are common to both the models. In IPSL model archive 'temperature of soil' up to 3.86 m depth of soil is available, however, the 'water content of soil layer' variable is missing. Since it is required by WRF model, therefore, entire set of soil property are taken from another CMIP5 global model output, MIROC5 (Model for Interdisciplinary Research On Climate). The bottom topography data is extracted from ETOPO1 (1 minute resolution).

2.2.2 Introduction to COAWST modelling system

The **C**oupled **O**cean-**A**tmosphere-**W**ave-**S**ediment **T**ransport (COAWST) Modeling System is used by different research communities for better understanding of the coastal processes at regional scale. The model is described in detail by Warner et al. (2010). This system is an agglomeration of four regional scale models under one umbrella with an aim to approximately represent complete coastal or regional climate system and their relevant processes. Each of these sub-models or components of COAWST are open-source codes: the Regional Ocean Modeling System (ROMS), the Weather Research and Forecasting Model (WRF), the Simulating Waves Nearshore (SWAN) and the Community Sediment Transport Modeling System (CSTMS). These sub-models exchange data fields between them via a coupling interface or coupler, the Model Coupling Toolkit (MCT). Further to handle different grids of the sub-models, interpolation weights are computed by the Spherical Coordinate Remapping Interpolation Package

(SCRIP) that allows the sub-models to exchange data fields. The installation of COAWST modelling package includes installation of a number of supporting software. The Model Coupling Toolkit (MCT) and SCRIP package comes along with the COAWST package. To keep consistency, same compiler (PGF90) is used to simulate all uncoupled and coupled experiments. Other two libraries, the NetCDF library for reading and writing input and output data; and the MPICH2 library to aid parallel computation, are installed before compiling different experimental set-up.

This article focuses on possible changes in extreme storminess, and the storms are mainly driven by ocean surface and overlying atmospheric properties. In other words, we are mainly interested in those processes that defines interaction between atmosphere and ocean through their respective boundary layers. Therefore, for present study objectives, only two of the four sub-models or components of the COAWST Modeling System are chosen: ROMS (Regional Ocean Modeling System) and WRF (Weather Research and Forecasting Modeling System). Each model component is first set and simulated in standalone (uncoupled) mode, and thereafter in coupled mode. An overview of experimental set-up is illustrated by a flowchart in **Figure 5**, which details every stage of model set-up, starting from selection of global model, preparation of input files, selection of time-slices and comparison of results to answer each objectives.

2.2.3 Southwest Pacific atmosphere model set-up

The WRF (http://www.wrf-model.org/index.php) modelling system represents the atmospheric component of COAWST. It is popular among large number of researchers both for ideal and real time weather studies. It is a fully compressible non-hydrostatic model and uses Arakawa-C grid structure. Complete details are available in Skamarock & Klemp (2008). It solves Euler's equations that includes moisture, Coriolis and Curvature terms, mixing terms, and parameterized physics terms. The perturbation form of these equations are given by Skamarock et al. (2008).

Once the WRF software is installed properly, it gives a number of executables that are also symbolically linked to the WRF Pre-processing System (WPS) directory: *geogrid/src/geogrid.exe*, *ungrib/src/ungrib.exe* and *metgrid/src/metgrid.exe* to name the most important binaries. These three binaries are used to collectively prepare input needed by the *real.exe* program that is further needed for real-data simulation. **Figure 6** gives a detailed overview of different components of WPS, their functions, linkages within it and the components of WRF, for real data case.

The external data is pre-processed for static geographical data of 10 minutes (*geog_data_res=10 minutes*) using geogrid program and meteorological data into simple WPS intermediate (WPSI) format using ungrib program with output data interval prescribed at 3 hours (*interval_seconds=10800 s*). This WPSI files are then horizontally interpolated on to the SP14 model grid by *metgrid* program. A *variable table* is required to identify and extract external meteorological dataset (from GRIB1 files) at specific levels, by *ungrib* and *metgrid* programs. A new variable table named as *Vtable.IPSL* prepared for IPSL_CM5A_LR dataset (illustrated by **Table 2**) based on ARW manual. To accomplish all the above, WPS uses an input file,

namelist.wps (**Appendix I**) that requires detail on actual simulation period, geographical extent of study domain, required temporal resolution of WPS output data, anticipated grid resolution, projection type, geographical source data resolution option and path where it is located. **Table 1** gives a detailed overview of the input forcing variables that are required by the WRF SP14 model.

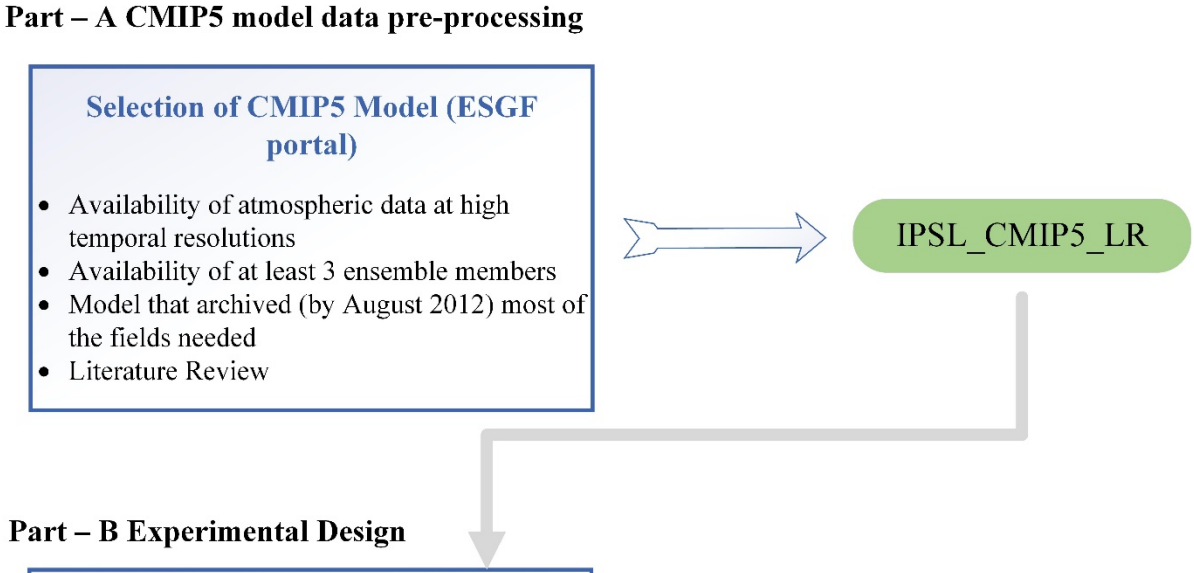

Boundary Conditions	Ensemble members/ realizations	Time slices	ROMS-only simulations
Control Run (Historical)	r1i1p1 r2i1p1 r3i1p1	1960-1964	hisr1 hisr2 hisr3
Scenario Run (RCP8.5)	r1i1p1 r2i1p1 r3i1p1	2095-2099	rcpr1 rcpr2 rcpr3
			hisRavg rcpRavg

Boundary Conditions	Ensemble members/ realizations	Time slices	WRF-only simulation	Coupled WRF-ROMS simulations
Control Run (Historical)	r1i1p1	1960-1964	hisw1	hcr hcw
Scenario Run (RCP8.5)	r1i1p1	2095-2099	rcpw1	rcr rcw
			hisw1 rcpw1	hcw rcw

Figure 5 *Overview of experimental set-up*

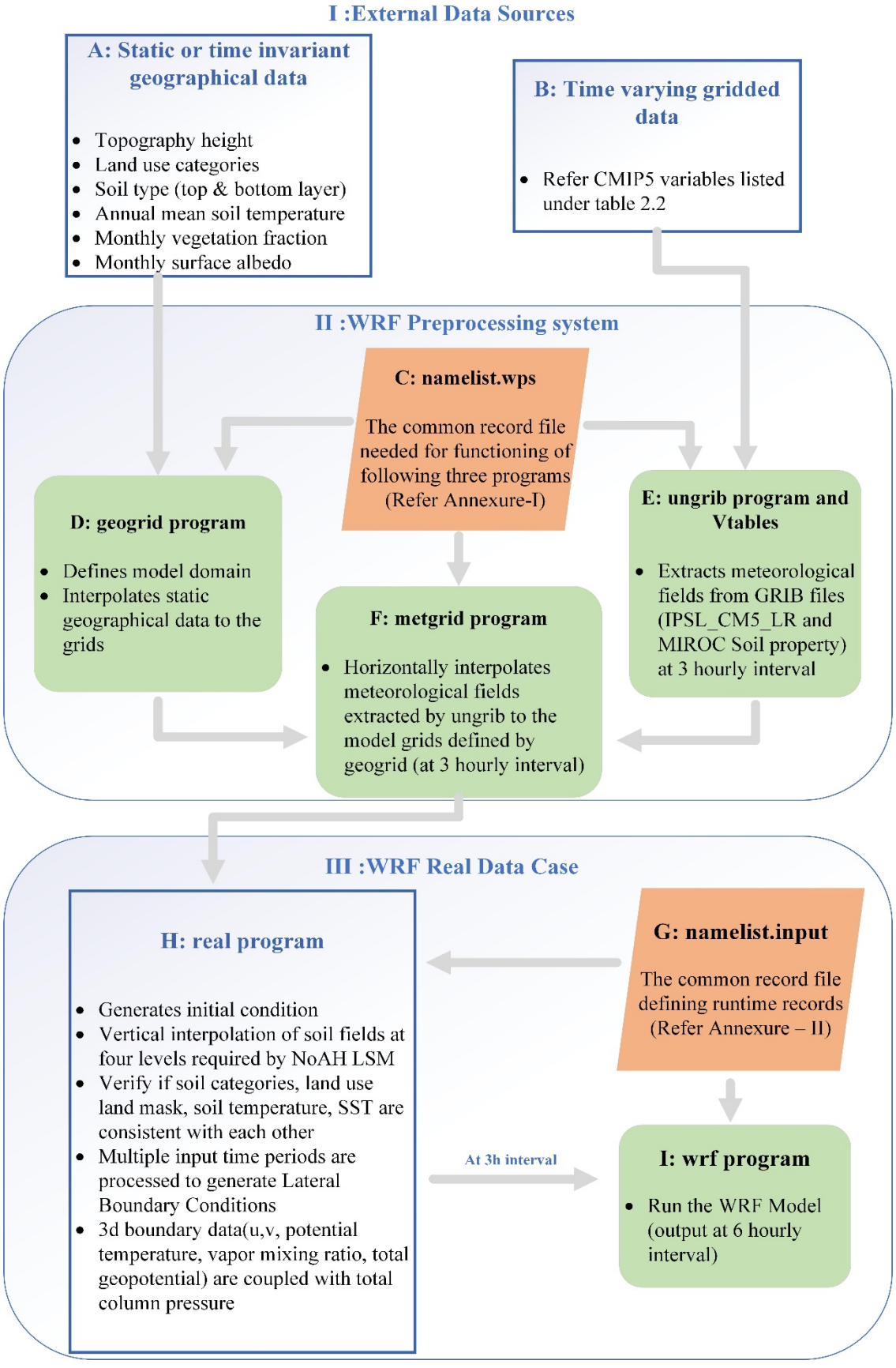

Figure 6 *Components of WPS, WRF for real data case, source: modified WPS components* (WRF_User's_Guide 2012)

Table 1 *CMIP5 model (IPSL_CM5A_LR) variables used to force SP14 WRF model*

CMIP5 variable name	CMIP5 data frequency	CMIP5 units	Description of CMIP5 variable	WRF variable names	WRF units
1. Near-surface atmospheric variables					
tas	3 hourly	K	2 m air temperature	TT	K
uas	3 hourly	m s^{-1}	10 m eastward wind	UU	m s^{-1}
vas	3 hourly	m s^{-1}	10 m northward wind	VV	m s^{-1}
huss	3 hourly	-	2 m specific humidity	SPECHUMD	kg kg^{-1}
2. Surface atmospheric variables					
ps	6 hourly	Pa	Surface air pressure	PSFC	Pa
psl	6 hourly	Pa	Sea level pressure	PMSL	Pa
prsn	3 hourly	kg m^{-2} s^{-1}	Surface snowfall flux	SNOW	kg kg^{-1}
ts	monthly	K	Surface air temperature	TSKIN or SST	K
3. Atmospheric variables at different pressure levels					
ta	6 hourly	K	Air temperature	TT	K
ua	6 hourly	m s^{-1}	Eastward wind	UU	m s^{-1}
va	6 hourly	m s^{-1}	Northward wind	VV	m s^{-1}
hus	6 hourly	-	Specific humidity	SPECHUMD	kg kg^{-1}
4. Soil layers properties (*MIROC5 land-surface model output)					
tsl	monthly	K	Temperature of soil	ST	K
mrlsl	monthly	kg m^{-2}	Water content of soil layer	SM	m^3 m^{-3}

Note: All data listed above are extracted from IPSL_CM5A_LR global model output, except the soil layers properties, which are extracted from MIROC5 global model output

In the second step, another input file, *namelist.input* (**Appendix II**) is prepared, where exact simulation period, physics or parameterization options, restart or cold start, input and output data interval, boundary control, nesting options, other special flags meant for typical cases (e.g. tropical cyclones, long simulation, etc.) are defined. Since the current study is a real data case, *real.exe* program is used to read the static and meteorological input data prepared by WPS *metgrid* program. It vertically interpolates the soil data at four different soil layers (0-5 cm, 5-25 cm, 25-100 cm, 100-200 cm) as required by the NoaH Land Sea Model (LSM) within WRF model in the current set-up. It checks the consistency of various input data with each other before preparing *initial condition, boundary condition and SST update* input files for multiple input time periods, covering entire simulation time period. Once the initial and boundary conditions files are available, the model simulation is initiated and carried out using *wrf.exe* program. Complete flow of working of WPS and WRF is sequentially shown by **Figure 6**. The total number of vertical levels are 34 (eta_levels), densest close to the earth/ocean surface with topmost model pressure level fixed at 50 hPa. The IPSL_CM5A_LR global atmosphere model output (of resolution 1.9° x 3.97° x 39 vertical levels) is

hence interpolated onto the SP14 WRF model grid of 0.25° x 0.25° and 34 vertical levels. The model is cold started, i.e. initiated from rest at 01 January 1960 (2095) for historical (scenario) experiment. The model integration time-step is 90 s (i.e. 1.5 minutes).

Table 2 *Variable Table(s) used by WPS ungrib and metgrid programs*

(a) Vtable.IPSL (for all variables except SST)

GRIB1 Param	*Level Type*	*From Level1*	*To Level2*	*metgrid Name*	*metgrid Units*	*metgrid Description*
11	100	*		TT	K	Temperature
33	100	*		UU	Ms^{-1}	U
34	100	*		VV	Ms^{-1}	V
7	100	*		HGT	M	Height
51	100	*		SPECHUMD	kg kg^{-1}	
	100	*		RH	%	Relative humidity
11	105	2		TT	K	Temperature at 2 m
33	105	10		UU	Ms^{-1}	U at 10 m
34	100	10		VV	Ms^{-1}	V at 10 m
51	105	2		SPECHUMD	kg kg^{-1}	
	105	2		RH	%	Relative humidity
1	1	0		PSFC	Pa	Surface Pressure
2	102	0		PMSL	Pa	Sea-level pressure
81	1	0		LANDSEA		Land/Sea flag
8	1	0		SOILHGT	M	Terrain field of source analysis
11	1	0		SKINTEMP	K	Skin temperature (can use for SST also)
144	112	0	5	SM000005	kgm^{-3}	Soil moist 0-5 cm below grn layer (up)
144	112	5	25	SM005025	kgm^{-3}	Soil moist 5-25 cm below grn layer
144	112	25	100	SM025100	kgm^{-3}	Soil moist 25-100 cm below grn layer
144	112	100	200	SM100200	kgm^{-3}	Soil moist 100-200 cm below grn layer
11	112	0	5	ST000005	kgm^{-3}	Temp 0-5 cm below grn layer (up)
11	112	5	25	ST005025	kgm^{-3}	Temp 5-25 cm below grn layer
11	112	25	100	ST025100	kgm^{-3}	Temp 25-100 cm below grn layer
11	112	100	200	ST100200	kgm^{-3}	Temp 100-200 cm below grn layer
223	1	0	200	CANWAT	kgm^{-2}	Plant canopy surface water
65	1	0		SNOW	kgm^{-2}	Water equiv. of Accum. snow depth
91	1	0		SEAICE	fractional	Fractional Sea Ice

(b) Vtable (SST only)

GRIB1 Code	Level Code	From Level1	To Level2	metgrid Name	metgrid Units	metgrid Description
11	1	0		SST	K	Sea surface temperature

The WRF model provides us with number of sophisticated physics parameterization schemes for treating various important processes, like surface radiation fluxes, boundary layer and precipitation processes. The parameterization schemes that SP14 WRF model uses are discussed here. In this study both longwave and shortwave radiation physics are computed using Rapid Radiative Transfer Mode applied for Global Circulation models or RRTMG (ra_lw_physics and ra_sw_physics = 4) scheme. The Monin-Obukhov atmospheric surface layer model and NOAH Land surface scheme are used along with Mellor-Yamada-Janjíc (MYJ) 1.5-order prognostic turbulent kinetic energy (TKE) planetary boundary layer (PBL) scheme. The WRF Single-Moment 6-class moisture microphysics scheme (WSM6) represents grid-scale precipitation processes (vapor, cloud, rain, snow, ice, and graupel). Betts-Miller-Janjíc (BMJ) cumulus scheme represents sub-grid scale convection and cloud detrainment. See **Table 4** where each of these schemes with options used are described in detail. **Table 3** (Column-I) gives an overview of different model physics schemes and parameterization that are utilized to set-up the SP atmosphere model. Further, Column-2 of the table gives a list of all representative variables of the climate system that are involved and are being resolved by different physics schemes.

Table 3 *Different model physics schemes and parameterization used*

Model physics	Variables resolved by WRF SP14 model
WSM6 microphysics	Vapor, rain, snow, cloud ice, cloud water, graupel
BMJ Cumulus parametrization	Effect of sub-grid scale convective or shallow clouds processes
MYJ surface layer	Accounts for exchanges between atmosphere and corresponding surface type: (i) land (friction velocities, exchange coefficients) or (ii) water (surface fluxes and diagnostic fields)
NoaH land surface model (4-layered)	Soil properties (temperature and moisture) that depends up on vegetation category, monthly vegetation fraction, soil texture
MYJ planetary boundary layer	Parameterizes turbulence or vertical diffusion within the PBL and free atmosphere above it
Atmospheric radiation	Shortwave (vis+u/w) and longwave (TIR or IR absorbed/emitted by gases/surfaces) and upward longwave radiation fluxes

The ARW manual helps understand the interaction between model physics parameterization through the model state variables (Table-8.6, Skamarock et al. 2008). In WRF model, for example: (a) land surface scheme needs radiation fluxes and rainfall fluxes as input, hence radiation scheme, microphysics and cumulus would be among the first processes to be computed after model initialization. The **Table 3** gives a list of variables related to different schemes used by the model. In COAWST configuration, compilation for WRF standalone model needed only one c-preprocessing options (CPP) activated (i.e. #define WRF_MODEL). Refer WRF real data case explained in **Part III** of **Figure 6** for an overall idea.

Table 4 *WRF physics schemes used (reference: WRF User's Guide, 2011)*

Physics options	Dynamics options	Remarks/description
Microphysics (mp_physics)	WRF Single-Moment 6-class (6)	Includes ice, snow, graupel processes suitable for high resolution simulations
Longwave radiation (ra_lw_physics)	RRTMG (4)	Rapid Radiative Transfer Model that is said to be an accurate scheme and uses lookup tables for efficiency. It accounts for multiple bands, trace gases, microphysics species and newly added with MCICA method of random cloud overlap
Shortwave Radiation (ra_sw_physics)	RRTMG (4)	Comparatively newer shortwave scheme includes MCICA method of random cloud overlap
Surface layer (sf_sfclay_physics)	Eta similarity (2)	Based on Monin-Obukhov with Zilitinkevich thermal roughness length and standard similarity functions from look-up tables
Land surface (sf_surface_physics)	Noah Land Surface Model	Unified NCEP/NCAR/AFWA scheme with soil temperature and moisture in four layers, fractional snow cover and frozen soil physics. New modifications are added in version 3.1 to better represent processes over ice sheets and snow covered area
Urban surface (sf_urban_physics)	Nil	Nil
Planetary Boundary layer (bl_pbl_physics)	Mellor-Yamada-Janjic scheme (2)	Eta operational scheme. 1-D prognostic turbulent kinetic energy scheme with local vertical mixing
Cumulus parameterization (cu_physics)	Betts-Miller-Janjic scheme (2)	It is an operation eta scheme and it uses column moist adjustment scheme relaxing towards a well-mixed profile
Other physics options		
Omlcall (sf_surface_physics)		Simple ocean model layer model: 1D ocean
Isftcflx		
Other options for long simulations		
tmn_update	1	Update deep soil temperature
sst_skin	1	Calculate skin SST based on (Zeng & Beljaars 2005)
bucket_mm	1	Bucket reset value for water equivalent precipitation accumulations (mm)
usemonalb		
no_mp_heating		
gwd_opt		
Diffusion and Damping options		

The method of initialization is defined in **section 2.2**. Accordingly, the SP14 WRF model set-up is started as a cold start to save the first restart file after 24 hours of simulation. The second initialization now uses this freshly made restart file and run for another day. Likewise, it continues this hot start mode till the end of simulation period. The restart options are mentioned in namelist.input file (see **Appendix II**). The

multiple time-varying gridded input data files, which includes region's static and dynamic information covering entire simulation period, are available to feed the model and its lateral boundaries.

2.2.4 Southwest Pacific Ocean model set-up

The **R**egional **O**cean **M**odelling **S**ystem (ROMS, https://www.myroms.org) has been extensively applied to a diverse range of applications to study a variety of processes from estuarine to coastal to basin scale. It is a hydrostatic, free-surface, terrain-following, open source code, primitive equation ocean model (Song & Haidvogel 1994; Shchepetkin & McWilliams 2005; Haidvogel et al. 2008) with a choice of several mixing schemes. The primitive equations are evaluated using staggered Arakawa C-grid on horizontal and discretised over variable topography using stretched terrain-following coordinates in the vertical. These stretched coordinates in the vertical, permit an enhanced resolution at required depth, like near sea surface or around thermocline or closer to sea bottom depending on application requirement. Since our major interest revolves around assessing the change in storminess, therefore the stretched coordinate parameters (θ_s, θ_b, T_{cline}) are kept such that a comparatively finer resolution of vertical grids may be achieved near the upper ocean (closer to the sea surface and thermocline). The stretched coordinate parameters used for SP14 ocean domain are listed under model configuration **Table 5**. It solves the fundamental Reynolds-averaged Navier-Stokes equation of motions with hydrostatic and Boussinesq assumptions (Hedström 2009).

In order to find an optimal regional extent and horizontal grid resolution such that the major hydrographic features may be resolved keeping in mind the computational requirement for coupled regional atmosphere-ocean model, a number of trials are conducted. The initial trial uses a horizontal grid resolution of 0.5° or ½° with a much larger regional extent that included Australia and Papua New Guinea is chosen and named as SP12 domain. Several sensitivity tests are performed before arriving at a stable model configuration. It is observed that the model is hydrostatically inconsistent due to spurious currents introduced by horizontal pressure gradient errors.

The presence of complex bathymetry makes the study domain difficult to model the ocean component (see **Figures 1, 2 and 8** and a relevant description in **section 1.2.2**). It is recognized that presence of such unreal current into the system aids unreal higher model simulated temperature. To improve upon this *horizontal pressure gradient error*, at first the bathymetry is smoothened such that it does not smooth out all the real features of the region. The sensitivity tests uses two different r-factors [one with mild smoothening (0.2) and second with heavy smoothening (0.1)] and two different pressure gradient schemes (weighted density Jacobian and Standard density Jacobian). The weighted density Jacobian pressure gradient scheme shows stable model simulation even with lower smoothening option. Using these parameters, the model proves to be stable at this resolution and successfully runs even with a time-step of 800 s (13.33 min).

The preliminary analysis of surface currents, wind vectors etc. with this model set-up, unfortunately misses most of the regional hydrographic features except few major oceanic circulation. This required a second

trial, where the regional extent is reduced but the spatial grid resolution is increased from ½° to ¼°. The SWP regional domain using a horizontal grid resolution of ¼°, hereafter will be called as SP14 domain. **Figure 7** shows both the trial domains, SP12 and SP14 for comparison. The ocean model spatial grid structure exactly matches with that of the atmosphere. Keeping same grid structure, helps avoid few extra computations related to grid mismatch (see Yu, 2004 for details).

Table 5 *SP14 ocean model configuration*

Model parameters	***Respective values***
Model grid resolution:	
Horizontal resolution	0.25 m x 0.25 m (@ midst of domain)
Grid dimension	251 *x-grid,* 235 *y-grid*, 32 *z*-levels
Sigma coordinates options:	
θ_s	3
θ_b	0.4
T_{cline}	5.0 m
$V_{stretching}$	4
$V_{transform}$	2
Model run-time options:	
Time-step (DT)	180 s
Number of time-steps for 3D equations	NTIMES = 14600 i.e. monthly
Number of time-steps for 2D equations between each 3D time-step	NDTFAST = 60
Boundary conditions:	Global model IPSL_CM5A_LR output data
Physics schemes:	
Vertical mixing (surface, ocean interior)	LMD non-local vertical mixing
Boundary layer air-sea exchange	COARE bulk formulation

The longitudinal extent of the region extends from ~139.5°E to ~210.5°E and the latitudinal from ~15°S to ~63°S. The mean model horizontal grid resolution is about 0.25° x 0.25° (i.e. 25 km x 25 km). The grid resolution varies from northern boundary (~14 km), to mean resolution at midst (~25 km) to coarser resolution near southern boundary (~30.5 km). The extent of the model domain has been widened sufficiently from New Zealand coastal waters in all the four directions away from steep topographical gradients. It not only minimises the contamination due to Lateral Boundary Conditions errors from all four open boundaries, but also allows covering most of the prominent hydrographic and topographical features that are known to influence the daily weather parameters of New Zealand. **Figure 1** gives a pictorial

overview of extent of the study domain and **Figure 2** gives a detailed illustration of complex but smoothened bottom topography of SP14 domain, which is used in the model set-up.

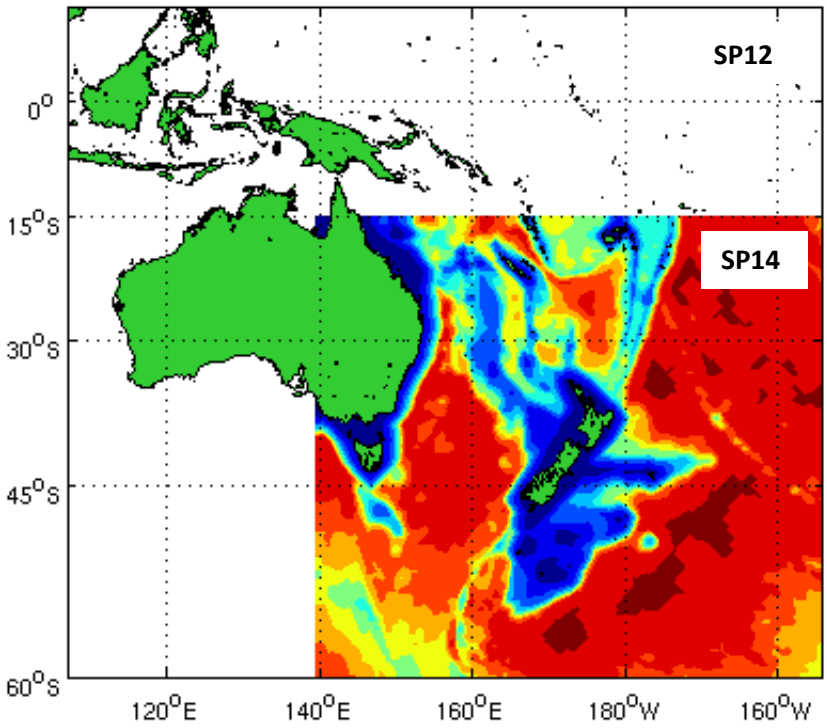

***Figure** 7 Trial-1 SP12 (0.5° horizontal grid resolution) model domain covering a much larger area is now reduced to smaller portion to limit computational cost and increase grid resolution to 0.25°, called as SP14*

To keep the region's complex terrain details near real, the *r-factor* is limited to 0.24, which later demanded a much smaller time-step to keep the model run stable without any intruding pressure gradient errors. As a result, the maximum grid stiffness ratios of *rx0* = 0.12 (Haidvogel & Beckmann 1999) and *rx1* = 3.1 (Haney 1991) are achieved. Sikirić et al. (2009) also highlights the importance of topographic grid stiffness ratio. In simple language, keeping these two *topographic stiffness ratio* within the recommended range helps in limiting the abrupt change in depth between two adjacent or neighbouring wet grid cells. Consequently, it avoids evolution of spurious pressure gradient errors that might introduce unrealistic flows resulting into model instability (Haney 1991). Such conditions may be more prominent near shallower regions, like along coastlines. The minimum or critical depth used is 5.0 m. All the values less than this critical depth are made equal to the minimum value. It is noteworthy that only the wet cells are prescribed depth values, and the land cells are given NaN values on the basis of land-sea mask value already set. As storms are mainly influenced by the ocean surface properties and overlying air, therefore focus is on the planetary boundary interaction of ocean and atmosphere. This is achieved by carefully setting the vertical grid to allow higher resolution (increased number of vertical grid layers) near the ocean surface. In order to better resolve the complex bottom topography and coastline of the region, the model uses the terrain (topography) following vertical grid curvilinear coordinate system. Accordingly, the

stretched coordinate parameters used are: *Vstretching = 4, Vtransform = 2,* $\theta_s = 0.4$, $\theta_b = 3.0$, $T_{cline} = 5.0$ *m* with total 32 vertical layers to define the SP14 ocean model. These layers are shown in **Figure 8**, to get a feel of how these stretched coordinates follow the terrain and help in resolving the ocean vertical resolution. Few selected transects (AA at 154°E, BB at 165°E and CC at 179°E) are plotted on model bathymetry that also illustrate the complex bottom topography present in the study domain, which the ocean model is challenged to resolve. The transect-AA passes through the EAC path; transect-BB through path of Tasman Front; transect-CC passes close to the rugged Karmadec and Tonga ridge line.

Model Forcing data is extracted and interpolated from CMIP5 IPSL_CM5A_LR global model output for selective experiments as per the requirement of the methodology chart (**Figure 5**) for this study. Model is initiated from rest on 1st January 1960 for control (2095 for scenario) using an initialization file that contains data of momentum, water density (T and S), $,u.$ and $,v.$ (derived from u and v) from IPSL_CM5A_LR data. The sequential multiple restart method (see **section 2.2** for definition) is applied with monthly restart interval. Therefore, a series of short one month run results are available for entire five years period with monthly re-initialization or restart results saved along with instantaneous and time-averaged results for the five year simulation period. The output result variables are saved at 6 hourly interval for time-averaged and instantaneous records. The station data are saved at hourly interval. All the restart variables are saved at an interval of 30 days for uncoupled ocean model.

In general, every input data are first extracted from the IPSL_CM5A_LR global (ocean) model result. Later they are interpolated on to the SP14 grid mesh i.e. from coarser grid resolution of 2.0° x 2.0° x 31 vertical levels (with 0.5° near equator) to a finer resolution of 0.25° x 0.25° x 32 vertical levels resolution. To force the regional ocean model, a number of input variables that are needed are listed in **Table 6**. The sub-grid scale processes that needs to be resolved by global or regional ocean model are primarily related to the turbulent mixing and diffusion processes in the water column that ultimately decide water mass properties in it. The parameterization schemes resolves surface fluxes, upper and bottom boundary layers, topographical stress, and vertical mixing within the ocean. Following paragraphs explains the schemes used to parameterize the ocean vertical mixing and boundary layer air-sea exchange.

While discussing on vertical mixing parameterization, Large et al. (1994) mentioned very clearly that a mismatch in the equilibrium surface heat flux between the two interacting or coupled sub-models might lead to climate drift. The sea surface temperature assists in balancing between various oceanic processes, like air-sea energy exchange, oceanic transport and vertical mixing. These exchanges between air and sea takes place at the respective planetary boundary layers (PBL), i.e. the atmospheric PBL (ABL) and the oceanic PBL (OBL). Thus, more accurate modelling of the boundary layer physics at respective PBLs is desirable. For OBL, two different parameterization schemes are necessary to include two fundamentally different types of mixing in the surface and in the ocean interior. The Large, McWilliams and Doney (LMD) vertical mixing parameterization scheme suits well for open ocean applications (Large et al. 1994).

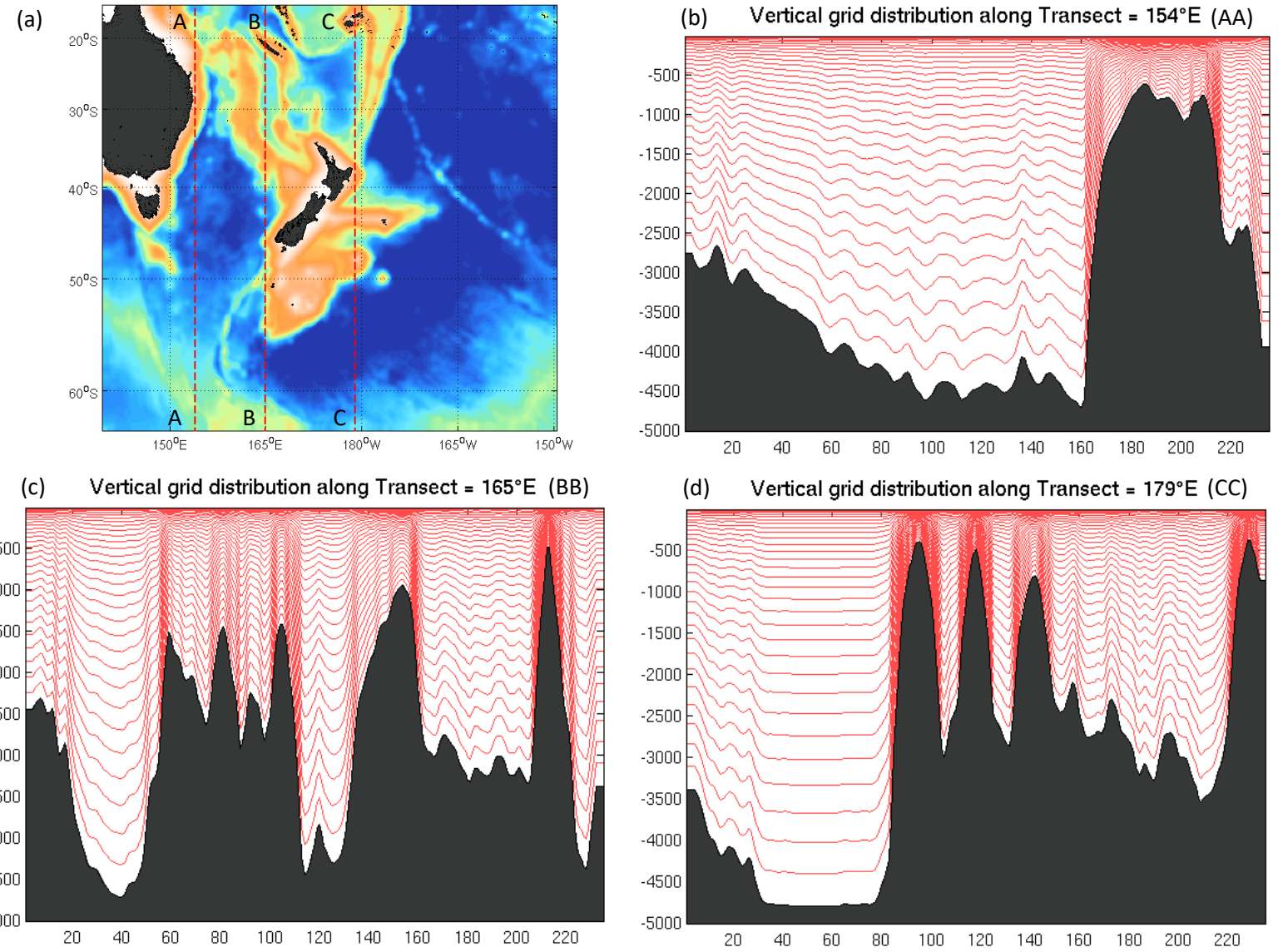

Figure 8 *Vertical grid structure using terrain following sigma-coordinates shown using transects at 154°E, 165°E and 179°E*

Table 6 *CMIP5 model (IPSL_CM5A_LR) variables used to force SP14 ROMS model*

CMIP5 variable name	***CMIP5 data frequency***	***CMIP5 units***	***Description of CMIP5 variable***	***ROMS variable name***	***ROMS units***
1. Near surface atmospheric variables					
tas	3 hourly	K	2 m air temperature	Tair	°C**
uas	3 hourly	ms^{-1}	10 m eastward wind	uwind	ms^{-1}
vas	3 hourly	ms^{-1}	10 m northward wind	vwind	ms^{-1}
huss	3 hourly	-	2 m specific humidity	Qair	$kgkg^{-1}$
ps	3 hourly	Pa	surface air pressure	Pair	mb**
zos	daily	m	sea surface height above geoid	zeta	M
2. Surface atmospheric variables					
pr	3 hourly	$kgm^{-2}s^{-1}$	precipitation flux	rain	$kgm^{-2}s^{-1}$
rlds	3 hourly	Wm^{-2}	surface downwelling longwave radiation flux in air	lrad_down	Wm^{-2}
rlus	3 hourly	Wm^{-2}	surface upwelling longwave radiation flux in air	lrad_down	Wm^{-2}
rsds	3 hourly	Wm^{-2}	surface downwelling shortwave radiation flux in air	sflx	Wm^{-2}
rsus	3 hourly	Wm^{-2}	surface upwelling shortwave radiation flux in air	sflx	Wm^{-2}
3. Oceanic variables at model levels					
thetao	monthly	K	sea water potential temperature	temp	°C**
so	monthly	PSU	sea water salinity	salt	PSU
uo	monthly	ms^{-1}	sea water x-velocity	uvel	ms^{-1}
vo	monthly	ms^{-1}	sea water y-velocity	vvel	ms^{-1}

** *Unit conversion required for these variables*

This scheme is mainly meant for two different regimes: (a) upper ocean or surface boundary layer: this boundary makes an interface between air and the underlying water surface. Most prevalent surface forcing conditions are - stabilizing, destabilizing and wind driven; (b) interior of the ocean is mixed by three processes: internal waves, shear instability and double diffusion. The K-profile parameterization (KPP) scheme is useful for coarser resolution large-scale climate simulation due to its insensitivity towards model vertical resolution (Moum & Smyth 2001). Large et al., (1994) emphasised on the ability of the boundary layer to reach through the stable thermocline for different convective and wind-driven conditions. They concluded that the KPP model works sturdily for a variety of events like: convective boundary layer deepening (LMD_CONVEC), diurnal cycling and storm events.

Although several atmospheric data including wind speed components are available at 3 hourly temporal resolution, however, wind stress data is missing from the selected global model output. Therefore, there is a need to activate the ocean-atmosphere boundary layer to compute the atmospheric fluxes. In ROMS, the

boundary layer is based on the air-sea exchange parameterization designed by Liu et al. (1979). It computes wind stress and net heat flux from available atmospheric input using *bulk_flux.F* routine with #define BULK_FLUXES CPP option activated. This routine is adapted from COARE code explained by (Fairall et al. 1996a; Fairall et al. 1996b). A complete detail on activated ROMS standalone model CPP options are given in **Appendix III**.

2.2.5 Southwest Pacific atmosphere-ocean coupled model set-up

The natural climate system consists of several major components: atmosphere, ocean, land surface, biosphere, and chemistry. Strong interactions between two or more of these components are responsible to bring about different climate phenomena, which might have vital implications on the environment and consequently on the humanity. For example, extreme events like storms, heavy precipitation, El Niño Southern Oscillation are some of the combined effects of ocean and atmosphere forcing. Another example would be deforestation, which is a combined effect of atmospheric processes and human intervention on land surface.

Technically, coupling the two models implies that the models are in interactive mode or in simple language they can communicate with each other via their interfaces. It is very important to understand variables that are exchanged between the sub-models through their interfaces at predefined coupling interval. Before going into the details on model exchange, it would be wise to first understand the physics behind how these two components actually interact in nature. Since this research objective focuses on possible changes in extreme storminess, we are mainly interested in those processes that defines interaction between atmosphere and ocean and how their respective planetary boundary layers aid in this interaction. Further, since storms genesis is influenced either by atmosphere or ocean, therefore we will not dive deep into how the land surface and atmosphere model interact. However, we will try to understand physical basics behind the atmosphere and land surface interaction.

(a) Air and sea interaction: The atmosphere and ocean are two large volume media. On one hand, the atmosphere is surrounding the globe of the earth as a thin outer layer, where gaseous molecules are always in motion. On the other hand, the ocean covers more than 70% of the earth surface and hence has a prominent impact on atmospheric circulation and climate of the globe. The major processes linked to the exchanges between air and sea are well illustrated in Figure 1 of Edson et al. (2007). When the moving atmosphere meets the earth surface (land and ocean), its motion retards in relation to the properties of the underlying earth surface. This boundary layer flow processes and mechanics when accurately parameterized can help more effective simulation of the air-sea interaction. Characteristics of ocean over atmosphere makes ocean a better heat reservoir than land surface. In nature, complex thermodynamic interactions continuously takes place through the air-sea interface (Csanady 2004), which includes: (a) incoming energetic shortwave solar radiation, (b) reflection of large part of received energy, (c) penetration of portion of radiation that aids in warming up the top 10 m or so of oceanic surface layer via molecular

processes of conduction and diffusion, (d) reflection of longwave radiation back to the atmosphere or space. The heat usually transfers from ocean to the atmosphere through two known corridors: (a) Sensible heat transfer that either raises or lowers the temperature of the overlying air; and (b) evaporation (Latent heat transfer) of water that contribute towards the maximum heat transfer from ocean to atmosphere. For coupled model world, the atmospheric model requires sea surface temperature information so that it can determine the strength and distribution of surface heat, momentum and water fluxes, whereas the ocean model component requires surface fluxes as a forcing for the oceanic circulations. The gist of air-sea interaction implies exchanges of heat, momentum and water fluxes through respective interfaces of each model component. For long term climate applications where only upper ocean circulation is being studied, Yu (2004) mentions that the surface water flux may be neglected. They further added that it is an important parameter when climate studies involve deep ocean circulation, like thermohaline circulation. Accordingly, the coupling interface need to handle four different parameters, namely (a) sea surface temperature, (b) surface heat flux, (c) surface wind stress, (d) surface water flux.

(b) Air and land-surface interaction: The atmosphere model component also needs to manage its interaction with the land-surface. Atmosphere interacts in similar way with land surface as it does with ocean in the form of heat, momentum and water fluxes. The land surface unlike ocean has a much lower heat capacity and is more heterogeneous unlike ocean surface (due to different types of vegetation and soil). In terms of thermal capacity or thermodynamics, land surface with low heat capacity thus can respond to any change in the atmospheric forcing much faster than ocean. The different types of vegetation responds (intercept, absorb and scatter) differently to solar insolation and hence with different rates of evaporation, mainly through vegetation (evapotranspiration). **Table 7** provides in detail the list of parameters that are related to atmospheric interaction with ocean (column 2) and land surface (column 3), respectively.

The atmospheric model component thus requires land surface heat capacity and albedo from the land-surface sub-model to compute the surface energy budget. At the same time, it also requires soil moisture and vegetation type from the land-surface sub-model data to compute surface water budget. It further requires downward shortwave flux, longwave flux, precipitation, surface air temperature, surface air humidity, and surface wind data from the atmosphere component model to compute heat, radiation, and moisture properties related to the land surface. Consequently these surface properties help compute the forcing of land surface on atmosphere, from these parameters: surface albedos, upward longwave radiation, sensible and latent heat flux, water vapour flux and surface wind stress (Yu 2004). In this application, the relevant exchange processes between the air and land surface are included through the atmosphere sub-model that includes NOAH 4-layered Land Surface Model. The schematic of variables being exchanged between the components are depicted in **Figure 9**, with MCT as coupling interface or coupler.

Table 7 *Properties and its corresponding parameters being exchanged between atmosphere and ocean; and atmosphere and land surface*

Properties exchanged	***Atmosphere interacting with ocean (parameters involved)***	***Atmosphere interacting with land-surface (parameters involved)***
Heat	Surface heat fluxes o Sensible heat flux o Latent heat flux o Shortwave radiation flux o Longwave radiation flux	Land surface energy budget o Heat capacity o Albedo Downward shortwave radiative flux Longwave radiation fluxes
Momentum	Surface wind stress or surface momentum flux	Land surface properties o surface wind stress o surface air humidity o surface air temperature
Water	Freshwater and salinity budget o Precipitation (from the atmosphere) o Evaporation (from the ocean)	Surface water budget (from land surface) o Soil moisture o Vegetation type Precipitation (from the atmosphere) Evapotranspiration (from the vegetation) and evaporation in general

(c) Coupling of Southwest Pacific atmosphere and ocean models: In nature, the exchange of fluxes is continuous, which would be computationally costlier in the modelling world. In case of coupled models, the coordinated back and forth exchange of simulated state variables between model components or sub-models is termed as interaction, which takes place at a particular frequency and is aided via the coupling interface. Based on the available computational resources and climate problem being addressed, an optimal coupling frequency is chosen. In current study, where ocean and atmosphere models are working at a time-step of 180 s and 90 s, respectively, the optimal coupling frequency used is a reasonably smaller value of (540 s or 9 minutes). Alike uncoupled or standalone model simulation, the coupled model is also integrated for five long years, each for historical and scenario experiments (see **Figure 5**).

Accordingly, under coupled mode, a special flag MCT_LIB is used to allow the two sub-models interact with each other at specific interval. This specific interval is called the coupling interval where both ocean and atmosphere components exchange coupling variables to each other. Note here that WRF-ROMS coupling mainly amends the method of computation of atmospheric fluxes relative to that of uncoupled WRF. Other physics schemes remain exactly the same as for uncoupled ROMS**. Table 8** gives differences in CPP (or c-preprocessing) options showing major changes for uncoupled and coupled ROMS and WRF. Coupling enables coupled WRF to utilize SST computed by concurrently running ROMS model instead of using global model SST and enables coupled ROMS to utilize the atmosphere model computed flux and transfer it to the ocean model at the time of coupling to retain the near real atmosphere ocean tight coupling. As per the coupled code (mct_roms_wrf.F, COAWST), MCT aids exchanging variables between the models: at first WRF model computes atmospheric fluxes, transfers them to ocean and then receives the sea surface potential temperature from ocean.

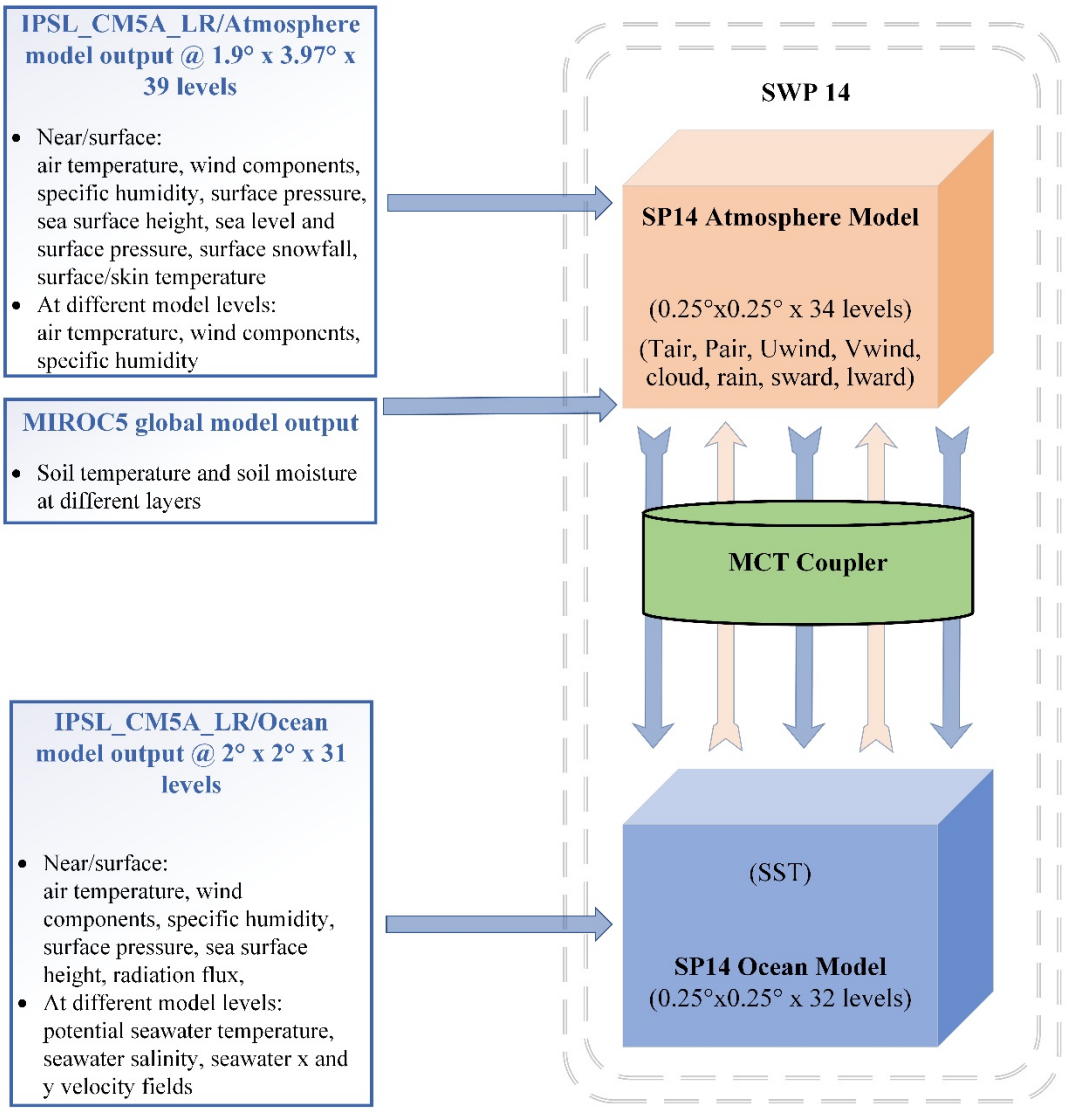

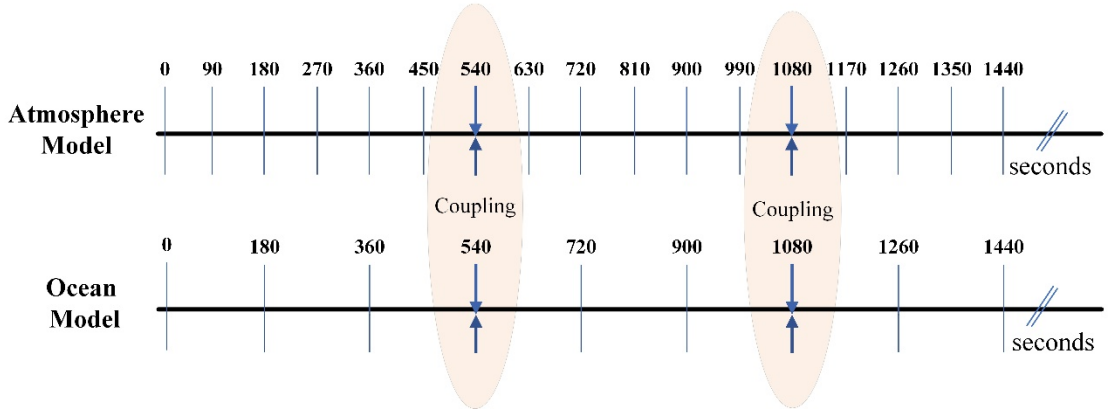

Figure 9 *Schematic diagrams of (a) forcing data, exchange of coupling fields between atmosphere and ocean models within SWP14 model; (b) respective model time-step and coupling interval are illustrated for simplicity*

Note: Exchange of atmospheric fluxes (heat, momentum and freshwater) from atmosphere model (time-step = 90 s) to ocean model (time-step =180 s), and SST from ocean model to atmosphere model at coupling interval of 540 s (or 9 minutes)

Table 8 *Changes in CPP options for uncoupled and coupled ROMS*

Uncoupled ROMS	***Coupled WRF-ROMS***
#define BULK_FLUXES	#define ROMS_MODEL
	#define WRF_MODEL
	#define MCT_LIB
	#define ATM2OCN_FLUXES
	#undef BULK_FLUXES
Uncoupled WRF	
#define WRF_MODEL	

In coupled code, this is aided by a flag *ATM2OCN_FLUXES*, which allows the atmosphere and ocean models to use exactly the same fluxes at their interface. The flag *undef BULK_FLUXES* at the same time confirms that the computation of atmospheric heat and momentum fluxes will not be made by the bulk parameterization formulae. So in coupled model, the presence of above mentioned two CPP options together commands the atmospheric heat/momentum fluxes that is being computed by WRF model to be directly utilized by the ocean model at their interface. The computation of this atmospheric flux is now continuously updated at coupling interval of 540 s based on the surface scheme chosen in the WRF model, the MYJ surface scheme and not on the bulk formulae. An uncoupled ocean computes atmospheric flux depending upon the CPP options chosen for longwave calculation. In present case longwave_down is read from the input file, which is then used by bulk formulation to compute ocean surface stress, and ocean surface heat fluxes. For the coupled mode, bulk formulation is not used, rather the MCT coupler helps exchange variables from both ocean and atmosphere model components of the coupled model system at every 540 s coupling interval. Please refer to **Figure 9** for schematic representation of overall functioning of the SWP14. The first **Figure 9a** illustrates the IPSL global forcing data used to enforce the SWP14 and exchange of coupling fields. While coupling, the atmosphere model serves ocean model with a number of atmospheric fluxes, like wind speed at 10m, air pressure, air temperature at 2 m, relative humidity, cloud, rain, shortwave and net longwave radiation and ocean model serves SST to the atmosphere model. Another simple schematic diagram, **Figure 9b** illustrates the respective time-step for atmosphere model (time-step = 90 s), ocean model (time-step = 180 s) and the coupling interval (540 s) at which they exchange their respective coupling fields.

Model initialization follows the same sequential multiple restart method described in **section 2.2** and same input files to initiate the two sub-models as is used in standalone mode. The differences between coupled ROMS and uncoupled ROMS are noted below: The coupled model set-up considers the leap-year concept and each sub-models saves daily restart records to match each other at the end of one month, so as to start the next month simulation using the recent restart outputs from ROMS and WRF, respectively. The coupled ROMS model now chooses to simply update the restart file's last two records on daily basis

(LcycleRST = T and NRST = 480) until it reaches the end of one month simulation. Other options remains the same, where initializing the next month uses NRREC = -1 to utilize the recent output restart file as initialization. So, with reference to **Table 5**, only two options (LcycleRST = T and NRST = 480) of restart are changed for coupled ROMS. Each sub-model independently writes monthly time-averaged output in netCDF format, saving output at 6-hourly interval. Coupled ROMS also saves instantaneous or history files at 6-hourly interval and station output results at hourly interval.

2.3 Summary: SWP14 modelling strategies

With an aim to understand any change in SWP future storminess, it is prudent to develop a tool that can adequately resolve the real time air-sea interaction dynamics at regional scale. Both the atmosphere-only and ocean-only models are inadequate in this regard (Aldrian et al. 2005) and this justifies the usage of coupled regional atmosphere-ocean model to resolve the dynamics of air and sea at respective planetary boundary layers. In the absence of any such regional-scale coupled model, focusing on the middle latitudes of the SWP, the first objective of this study is defined. The current section discusses the newly developed coupled atmosphere-ocean regional SWP14 model, primarily focusing on the middle latitudes. The SWP14 covers an area from ~139.5 to ~210.5°E, longitudinally and from ~15°S to ~63°S, latitudinally. The mean model horizontal grid resolution is about 0.25° x 0.25° (about 25 km x 25 km) at middle latitudes. It varies from finer resolution at northern boundary (~14 km) to coarser resolution near southern boundary (~30.5 km). Here we summarize the strategies followed while setting up the SWP14, which are different from normally used default settings:

(i) The stand-alone atmosphere, stand-alone ocean and coupled experiments uses congruent grid structure. Keeping exactly same grid structure helps in avoiding few extra computations related to grid mismatch (see Yu, 2004 for details) while exchanging information during coupling of two models.

(ii) Generally, a 3-D snapshot taken from either long term mean climatology or output from a global model is used to describe the region's initial climatic condition to start a model simulation. In current study, however, model initialization follows the sequential multiple restart method. Such *series of reinitialized runs* are said to perform better than one time initialized long continuous runs (Jimenez et al. 2010). Each model set-up uses a series of initialization files saved at a specified (pre-defined) interval (monthly for ocean model and daily for atmosphere model). Once the model is initialized, the next time-period is simulated using the previous restart file as initialization. This method of using restart file as initialization of next model simulation is continued until the end of 5 years simulation. Accordingly, the SWP14 model is initialized from rest as a 'cold start' (at January 01, 1960, 0000 UTC for historical and January 01, 2095, 0000 UTC for scenario experiments). The uncoupled atmosphere model set-up is started as a cold start to save the first restart file after 24 hours of simulation. The second initialization now uses this freshly made restart file and run for another day. Likewise, it continues this hot start mode till the end of simulation period. The uncoupled ocean

model set-up also follows exactly the same concept, except that the restart variables are saved at an interval of 30 days.

(iii) The output of IPSL_CM5A_LR global model (includes atmosphere data at 1.9° x 3.97° x 39 levels and ocean data at 2.0° x 2.0° x 31 levels) are used to drive the SWP14 experiments. It is chosen mainly because its output included atmospheric output at higher temporal resolution and most of the output variables required by the ocean model are available. To limit the consumption of computational space, lower resolution option is downloaded. The multiple time-varying gridded input data files, which includes region's static and dynamic information covering entire simulation period are prepared to feed the model and its lateral boundaries.

(iv) The atmospheric component is based on the Weather Research and Forecasting model. A new variable table named as *Vtable.IPSL* has been prepared based on ARW manual, to identify, extract and interpolate IPSL_CM5A_LR meteorological dataset at specific levels using *ungrib* and *metgrid* programs (illustrated by **Table 2**).

(v) The sub-grid scale parameterization schemes within atmosphere model resolves various processes of surface radiation fluxes, air-sea interaction, air-land surface interaction, planetary boundary layer, convection and cloud. To be more precise: RRTMG for radiation; the Monin-Obukhov atmospheric surface layer model and NOAH Land surface scheme are used along with MYJ 1.5-order prognostic turbulent kinetic energy PBL scheme; the WSM6 microphysics scheme represents grid-scale precipitation processes; BMJ cumulus scheme represents sub-grid scale convection and cloud detrainment schemes are opted.

(vi) The oceanic component is based on the Regional Ocean Modelling System. Since our major interest revolves around assessing the change in storminess, therefore in ocean model, the stretched coordinate parameters (θ_s, θ_b, T_{cline}) are kept such that a comparatively finer resolution of vertical grids may be achieved near the upper ocean (closer to the sea surface and thermocline). The minimum or critical depth used is 5.0 m. All the values less than this critical depth are made equal to the minimum value.

(vii) To improve upon this horizontal pressure gradient error, the bathymetry is smoothened such that it does not smooth out all the real features of the region. Simultaneously, to keep the region's complex terrain details near real, the r-factor is limited to 0.24, which later demanded a much smaller time-step to keep the model run stable without any intruding pressure gradient errors. In simple language, keeping these topographic stiffness ratio within the recommended range helps in limiting the abrupt change in depth between two adjacent or neighbouring wet grid cells. Consequently, it avoids evolution of spurious pressure gradient errors that might introduce unrealistic flows resulting into model instability (Haney 1991). Such conditions may be more prominent near shallower regions, like along coastlines. Any abrupt change in depth near the open boundaries are also considered.

(viii) The parameterization schemes within ocean model resolves surface fluxes, upper and bottom boundary layers, topographical stress, and vertical mixing within the ocean. Precisely: the boundary layer air-sea exchange parameters are resolved by surface bulk parametrization, wind stress and net

heat flux are computed from available atmospheric fields, ocean vertical mixing processes are resolved by LMD vertical mixing parameterization scheme.

(ix) The atmosphere model integration time-step is 90 s, which is half of that used by its ocean counterpart (180 s). Each of the uncoupled and coupled experiments are integrated for five years and their output are saved at every 6 hour interval. To maintain consistency, same compiler, PGF90 is used to compile and simulate all the experiments.

(x) The coupled model set-up considers the leap-year concept and each sub-models saves daily restart records to match each other at the end of one month, so as to start the next month simulation using the recent restart outputs from ROMS and WRF, respectively. The coupled ROMS model now chooses to simply update the restart file's last two records on daily basis (LcycleRST = T and NRST = 480) until it reaches the end of one month simulation. Other options remains the same, where initializing the next month uses NRREC = -1 to utilize the recent output restart file as initialization.

(xi) The coupled model set-up is based on COAWST code and uses MCT coupler to couple the interacting sub-models. WRF-ROMS real-time coupling brings major change in computation of atmospheric fluxes. Coupling enables coupled WRF to utilize SST computed by concurrently running ROMS model (instead of using global model SST) and coupled-ROMS to utilize the atmosphere model computed fluxes (instead of using surface bulk parameterization). To retain the near-real atmosphere-ocean tight coupling, a comparatively frequent coupling interval of 540 s is used. As per the coupled code (mct_roms_wrf.F, COAWST), MCT aids exchanging variables (controlled by ATM2OCN_FLUXES and BULK_FLUXES flags) between the models: at first WRF model computes atmospheric fluxes, transfers them to ocean and then receives the sea surface potential temperature from ocean. Apart from this, all other physics schemes remain exactly same as for uncoupled ROMS.

CHAPTER 3

Model validation

This chapter describes performance of the newly set SWP14 whose set-up has been described in chapter 2. The SWP14 is evaluated based on two criteria: first of all, model validation is performed by comparing the model output to climatology/reanalysis data; secondly, model performance is tested by comparing the model output to its own forcing data.

3.1 Data and methods

3.1.1 Data

The SWP14 model output data that are saved at 6 hourly interval are processed to attain the five year (i) monthly mean, (ii) seasonal mean and (iii) annual mean for different large scale variables. To evaluate the set coupled model, the long term observational or reanalysis (referred as climatology in general) dataset are primarily taken from second generation European Centre for Medium-Range Weather Forecasts reanalysis data (ERA40, T85 resolution). Apart from these data, sea surface temperature data are taken from Hadley Centre Global Sea Ice and Sea Surface Temperature (HadISST1, 1°x1°) and sea surface salinity data from CSIRO Atlas for Regional Seas (CARS, 0.5° grid resolution).

3.1.2 Model evaluation strategy

All the seasons referred to in this article are for the southern hemisphere or austral seasons. For example, winter season refers to the months of June-July-August and summer to December-January-February. The performance analysis is based on two criteria: one relative to the climatology and second relative to the input forcing. Reanalysis dataset mentioned in **section 3.2.1** are used to understand if the regional model

could produce long term standard or known conditions (climatology) of the region. A simultaneous exercise is performed to determine the reliability of the forcing data with respect to the climatology of the region. Hence, validation of the IPSL global model data is also presented besides validation of the SWP14 model data with respect to the regional climatology. However, apart from validating the model output with respect to regional climatology, it is also essential to check how the model performs with respect to the input data forcing. In other words, it would be necessary to determine the actual performance of the SWP14 model irrespective of bias introduced due to global forcing model. This exercise would verify the *actual model performance* relative to input data forcing (IPSL) apart from validating the SP14 results with standard conditions. Further, it would give a direct indication on whether the SP14 (relatively finer grid) outputs are able to evolve and depict the regional scale features that are either unclear or completely missing in the global input data (due to coarser resolution). Multiple variables are chosen to perform a more generic verification on model performance from different perspectives and to avoid any bias that is likely to arise by choosing just one variable. The climate indices that are selected for comparison are: (1) sea surface temperature, (2) sea surface salinity, (3) temperature at 2 m, (4) wind speed at 10 m (5) u-wind component at 10 m, and (6) v-wind component at 10 m.

Step-1 At first step, three different sources of data (i) the climatology/reanalysis data, (ii) the SWP14 output, and (iii) the coarser resolution global input/forcing data, are placed beside each other. A visual comparison is made using the three different data sources and through presentation of separate figures illustrating *five-year mean* of each climate indices (see **Figures 11, 12, 14, 16, 18** and **20**). The first column (climatology) and third column (SWP14 output) are compared to help determine the behavior of the SWP14 output relative to the climatology. The first column and the second column (global input data) help in determining the reliability of the input or forcing data for the region. The comparison of second column and third column helps determine whether the finer grid SWP14 could outperform the coarser global input data (IPSL) and evolve regional scale features that are missing/invisible otherwise. It is noteworthy here that the coarser climatology and global forcing data are first interpolated on to the SP14 grid structure for validation. Each of the rows depict four different seasons, starting from austral winter (DJF), autumn (MAM), summer (JJA) and spring (SON). While presenting each indices, they are illustrated using a specific color axis.

Step-2 In the second step, apart from comparing five-year seasonal mean plots of each variable, it is also be interesting to compare and determine range of changes in five-year monthly mean trend for entire year of the study area. Instead of taking mean of larger region within the study area, a number of sampling stations are selected that can illustrate and represent every station's mean trend and variations. Since the focus is mainly on lower to middle latitude zones, therefore **Figure 10** shows sixteen sampling stations (or sample boxes), each of 2.5° square size, which are picked up systematically to represent the middle latitude of the study domain. It includes the southward flowing EAC and eastward moving Tasman Front, influencing the day-to-day weather conditions of New Zealand and its long term climate. The sample boxes are chosen from 25°S to 42.5°S and 152°E to 182.5°E, at a distance of 2.5° from each other latitudinally

and 7.5° longitudinally (except first two longitudinal bands that are 5.5° apart). When analyzing the performance of regional scale models, the authors believe that this approach of selecting a number of sample boxes will help detect the variation in the dynamics of climate indices that are closely located (~2° to 7° apart) to each other in contrast to a single large sized sample box that often dilutes the typical local behavior and dynamics. See **Figures 13, 15, 17, 19, 21** respectively for sixteen sampling stations depicting five-year mean monthly trend for six different climate indices.

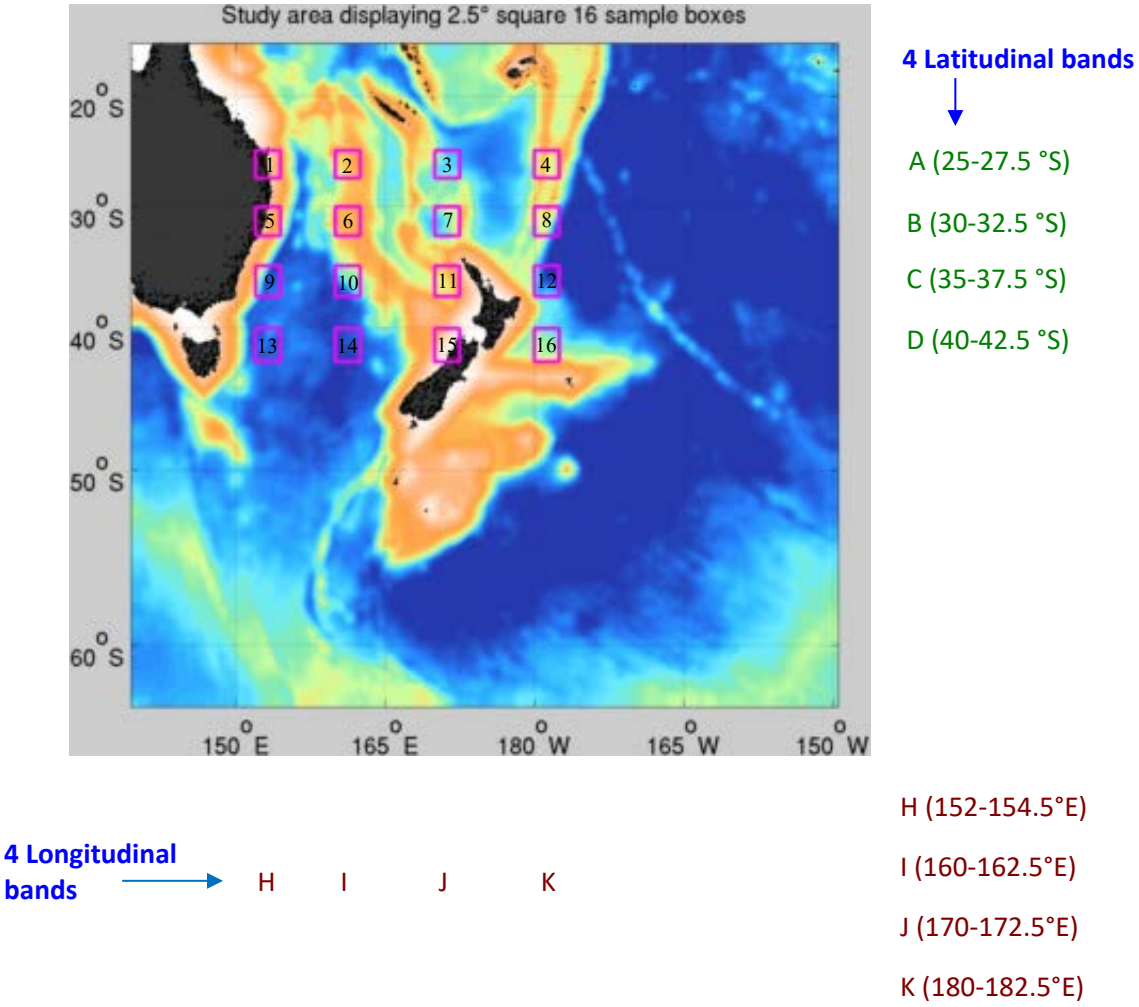

Figure 10 *Model domain displaying selected 16 sampling stations (or boxes) each of size 2.5° square*

Step-3 Finally, the third step is to make statistical analysis to quantify the skills of SWP14 with respect to IPSL and climatology data. Two different statistics are used, namely, correlation coefficient and centered root mean square difference, and are computed for five year annual mean. They are defined by equations 1 and 2, respectively, where, o = observed/true data, p= predicted/modelled data, $\acute{o}$ = observed mean, $\acute{p}$ = predicted or modelled mean, n = number of time-steps.

$$R = \frac{\frac{1}{N}\sum_{n=1}^{N}(p_n-\bar{p})(o_n-\bar{o})}{\sqrt{\frac{1}{N}\sum_{n=1}^{N}(p_n-\bar{p})^2}\sqrt{\frac{1}{N}\sum_{n=1}^{N}(o_n-\bar{o})^2}} \quad (1)$$

$$E'^2 = \frac{1}{N}\sum_{n=1}^{N}[(p_n-\bar{p})-(o_n-\bar{o})]^2 \quad (2)$$

These statistics are used to quantify the model efficacy (in addition to their illustration in above two steps that uses 2-dimensional 5 year seasonal mean and 5 year monthly mean variability plots) over 16 different sample stations distributed over a larger middle latitudes of SWP. Mean of respective latitudinal and longitudinal bands are also given for both the statistical indices.

3.2 Comparison of large-scale environmental variables

Following above mentioned strategy, each of the six climate variables are analyzed and discussed separately in the following sections. Estimation of correlation coefficient and root mean square differences are computed for each sample boxes with respect to the climatology and input IPSL data to provide an additional support for the above analysis and presented in tabular format. **Tables 9, 10, 11, 12,** and **13** depicts the statistical indices for 5 year annual mean of SST, SSS, 2 m air temperature, 10 m wind speed, u-wind component and v-wind component, respectively for each sample boxes.

3.2.1 Sea surface temperature (SST)

SST has a vital role in development of storms especially in tropics. It is also a major indicator of overall sea state and any significant change in its magnitude indicates significant change in the long term climate for the region. **Figure 11** provides a visual illustration of five-year seasonal mean for each of three data sources. At first glance, it clearly depicts that SWP14 modelled SST is underestimated, whereas, the IPSL forcing shows a better match with that of the HadISST1 data. However, both the global input and HadISST1 data fail to show any regional circulation features that are very well resolved by the SWP14 output. For example, the wavy and meandering eastward moving zonal flow across the Tasman Sea (commonly the Tasman Front) is well depicted.

While analyzing the SWP model SST output with SST observational data, it is interesting to note that the SST climatology/observation (CARS and HadISST) for SWP are not very precise and even differ considerably. These findings are also supported by others like Edson et al. (2007), who highlights about the inaccuracy of the observed SST data for the SWP region.

Climatology (HadISST) IPSL forcing SWP14

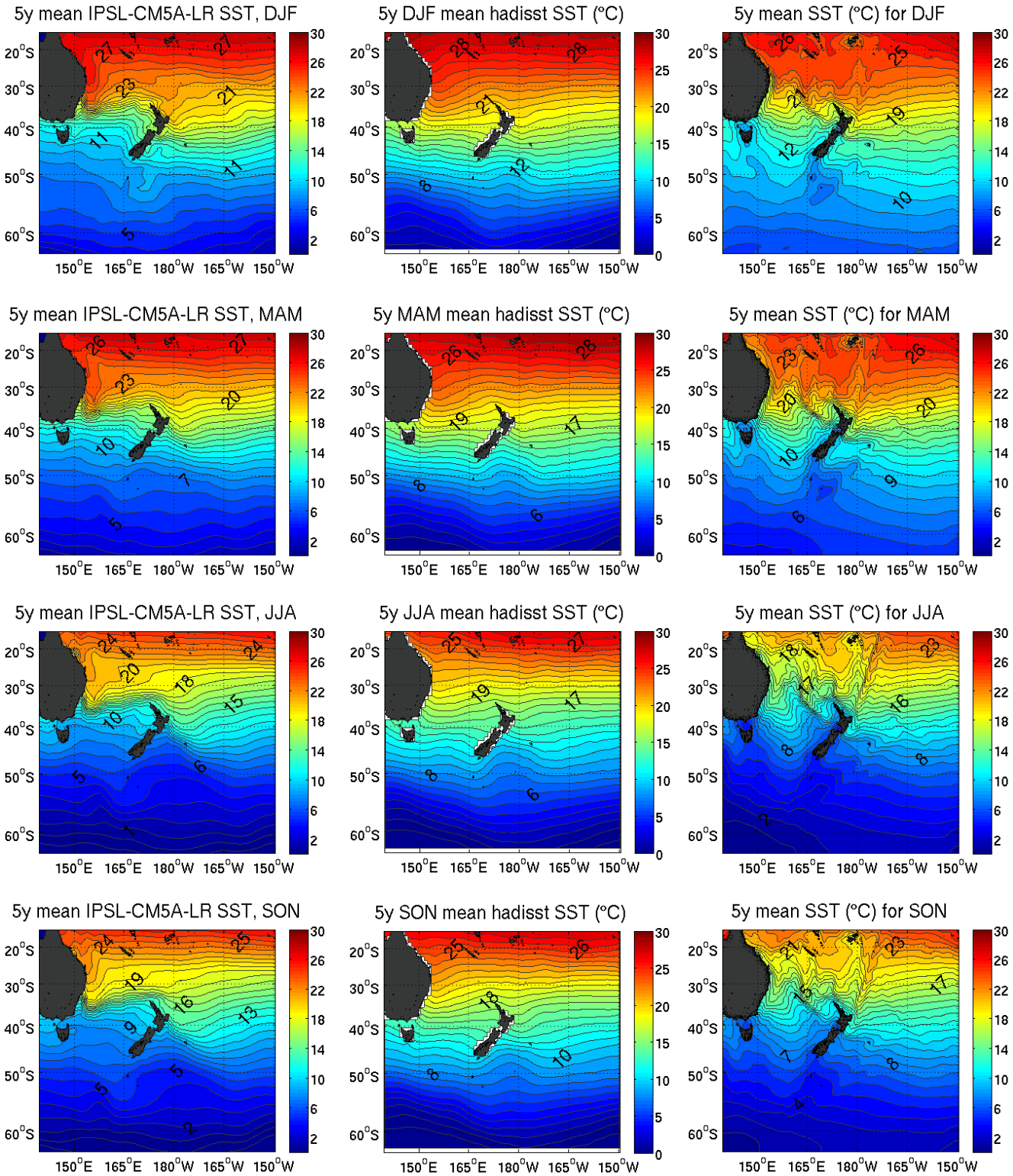

Figure 11 *Comparison of 5-year seasonal mean SST (°C) between (a) HadISST1 (b) IPSL global input (c) SWP14 output*

Unlike these flaws in regional climatology/observational dataset, the SWP model SST output does show more detailed features, especially, across the Tasman Sea, where we can observe the meandering of Tasman Flow moving towards North Island of New Zealand through the region's complex topographic features. *With respect to these flaws related to the regional climatology/observational dataset, it is therefore decided that validation of regional model would not be performed for SST.*

3.2.2 Sea surface salinity (SSS)

It is the representation of amount of dissolved salts in water and varies slightly with season. This index is very important as even a little change in its magnitude may have a dramatic effect on the hydrological cycle and as a result on the ocean circulation. Salinity raising factors (for example, sea-ice formation, evaporation, weathering of rocks) counter-balances its decreasing factors (for example, melting of sea-ice, rainfall, river input, etc.). Higher salinity in tropics may be due to higher amount of evaporation, or due to lack of sources of freshwater, like in the midst of the ocean basins.

At first glance at **Figure 12**, it can be seen that both the IPSL global input (column-II, more than 36 PSU) and as a result the SWP14 (column-III) SSS also shows higher values compared to that of the CARS climatology (column-I, lesser than 35.5 PSU) for ~20-35°S. Further, careful observation shows that the SWP14 mollify the simulated SSS over the region compared to incorrectly higher values of forcing SSS. The meandering of the Tasman Front is clearly visible in SWP14 output (column III) too alike SST, which is missing in both climatology and IPSL forcing. Second observation is the missing freshwater at higher latitudes (south of 50°S) in IPSL and SWP14, which is visible in CARS. SWP14 simulated SSS though gives higher freshwater at higher latitudes than that of IPSL input, especially for summer and autumn seasons. Thirdly, when focused on column II and III, in general, SWP14 SSS follows IPSL input forcing, however, with comparatively lower values of simulated SSS than that of IPSL. It further clearly illustrates the regional features of EAC travelling southward and meandering as Tasman Front that are missing in the IPSL forcing as well as in the climatology. Finally, the IPSL output shows presence of freshwater for all the seasons for entire western coast of New Zealand. Whereas, the SSS simulated by the SWP14 does not follow the IPSL forcing but follows similar pattern of CARS climatology.

In **Figure 13**, the monthly mean trend of SSS for all samples show very little change and in some cases nil or unclear seasonal trend. Closest match of SWP14 SSS with that of climatology can be seen for boxes 2, 5, 7, 9, 12, 16, i.e. for lower latitude including EAC path (5, 9) and Tasman Front (7, 8, 12). The SWP14 output shows overestimated values relative to climatology for boxes 1, 3, 4, 8 i.e. approximately for lower latitude up to 27.5°S and underestimated values for boxes 6, 10 11, 13, 14, 15 i.e. approximately from south of 30°S (band C and D).

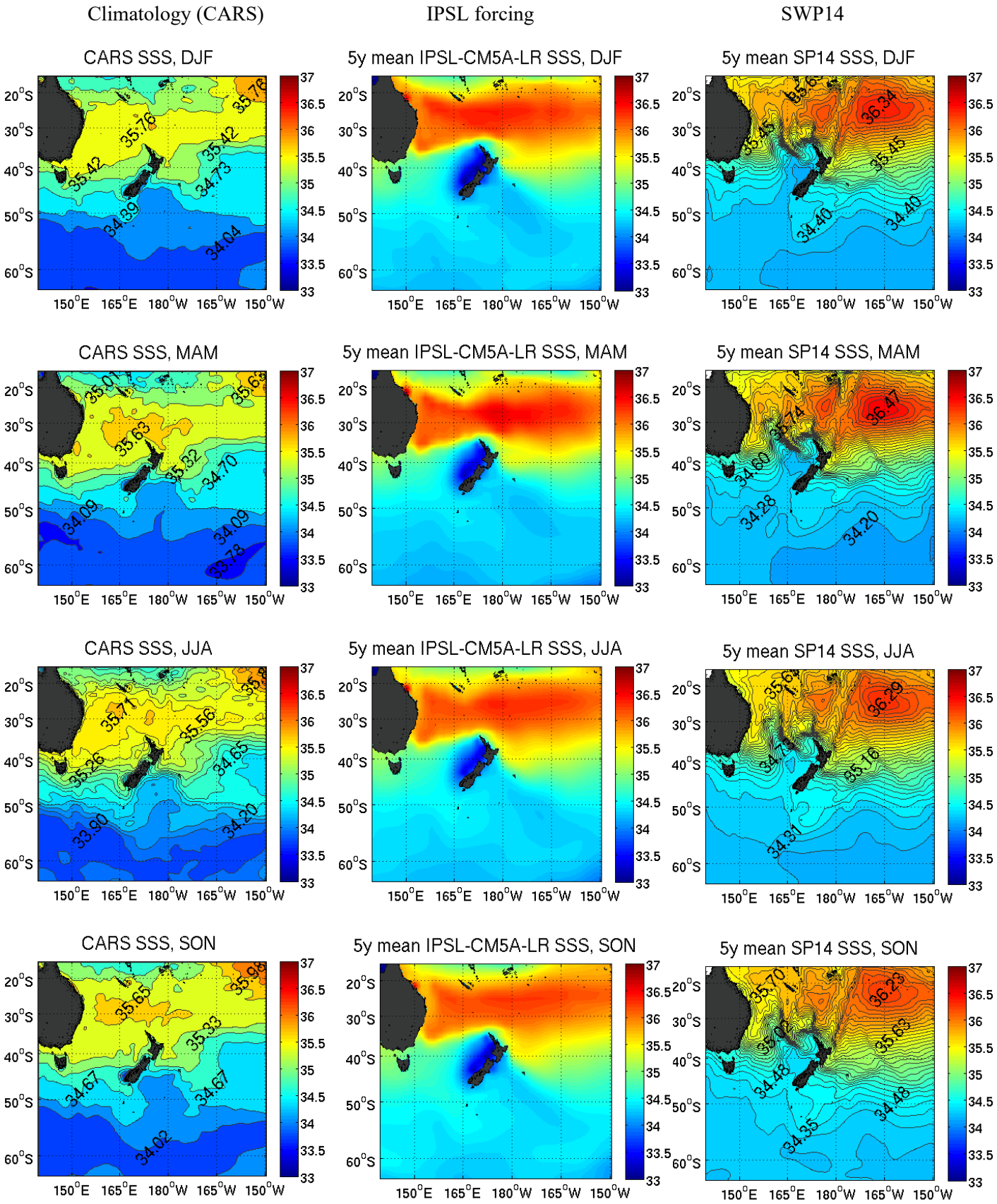

Figure 12 *Comparison of 5-year seasonal mean SSS (PSU) between (a) CARS (b) IPSL global input (c) SWP14 output*

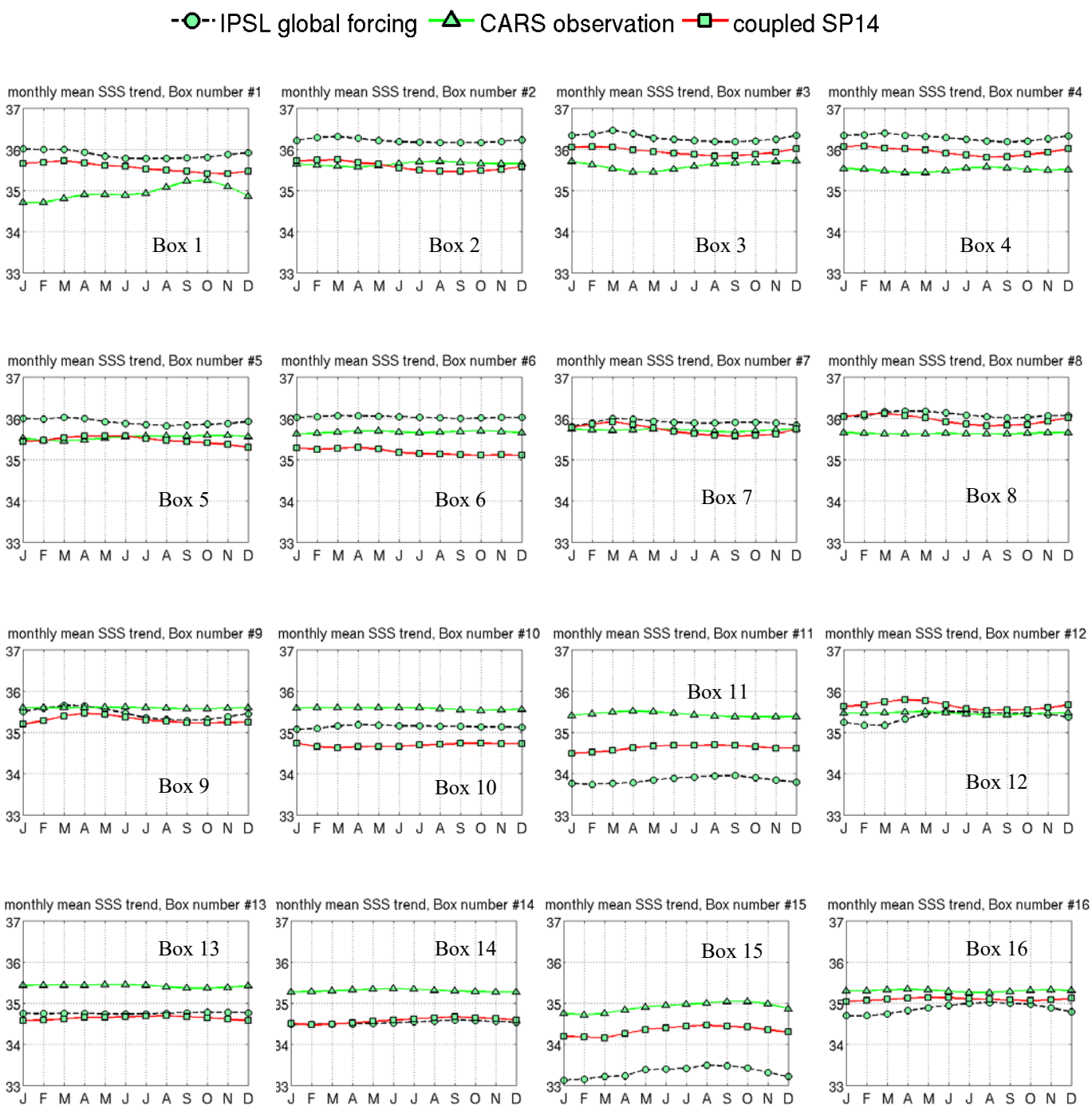

Figure 13 *Comparison of monthly mean sea surface salinity for 16 sample boxes*

Following salient points are concluded:

- IPSL gives overestimated values between ~20-35°S compared to CARS climatology
- IPSL gives fresh water values especially at west of New Zealand, which is incorrect when compared to CARS. Although SWP14 is forced by these higher and incorrect SSS values, the simulated SWP14 SSS shows normal surrounding contextual values around New Zealand

- SWP14 simulates lower values of SSS than IPSL values however they are still higher than CARS climatology
- Unlike CARS and IPSL, SWP14 simulated SSS resolves the pattern of EAC and Tasman Front paths similar to that of SST

Table 9 *Statistical indices computed for 5-year annual mean sea surface salinity*

Sea surface salinity (annual)											
Centered RMS difference							Correlation coefficient				
Band-A	**1**	**2**	**3**	**4**	***Latitudinal mean***		**1**	**2**	**3**	**4**	***Latitudinal mean***
CARS_CROMS	0.31	0.07	0.06	0.13	*0.14*		-0.83	-0.82	-0.07	-0.49	*-0.55*
IPSL_CROMS	0.11	0.12	0.08	0.07	*0.10*		0.67	0.91	0.92	0.93	*0.86*
CARS_IPSL	0.23	0.18	0.09	0.06	*0.14*		-0.72	-0.85	-0.30	-0.59	*-0.62*
Band-B	**5**	**6**	**7**	**8**			**5**	**6**	**7**	**8**	
CARS_CROMS	0.21	0.33	0.26	0.06	*0.22*		-0.48	-0.19	0.55	0.22	*0.02*
IPSL_CROMS	0.11	0.44	0.23	0.13	*0.23*		0.22	0.78	0.36	0.57	*0.48*
CARS_IPSL	0.15	0.13	0.09	0.15	*0.13*		-0.91	0.01	-0.17	-0.27	*-0.34*
Band-C	**9**	**10**	**11**	**12**			**9**	**10**	**11**	**12**	
CARS_CROMS	0.31	0.91	1.05	0.09	*0.59*		0.54	-0.78	-0.13	0.91	*0.13*
IPSL_CROMS	0.28	0.08	1.19	0.69	*0.56*		0.69	-0.49	0.87	-0.48	*0.15*
CARS_IPSL	0.56	0.87	2.22	0.72	*1.09*		0.58	0.16	-0.42	-0.35	*-0.01*
Band-D	**13**	**14**	**15**	**16**			**13**	**14**	**15**	**16**	
CARS_CROMS	1.05	1.09	0.92	0.57	*0.91*		-0.17	0.10	0.95	0.03	*0.23*
IPSL_CROMS	0.29	0.46	1.42	0.64	*0.70*		-0.31	0.97	0.95	0.33	*0.48*
CARS_IPSL	1.33	1.53	2.33	1.20	*1.60*		-0.85	-0.10	0.92	-0.51	*-0.14*
Longitudinal mean	**Band H**	**Band I**	**Band J**	**Band K**			**Band H**	**Band I**	**Band J**	**Band K**	
CARS_CROMS	*0.47*	*0.60*	*0.57*	*0.21*			*-0.23*	*-0.42*	*0.33*	*0.17*	
IPSL_CROMS	*0.20*	*0.28*	*0.73*	*0.38*			*0.32*	*0.54*	*0.78*	*0.34*	
CARS_IPSL	*0.57*	*0.68*	*1.18*	*0.53*			*-0.47*	*-0.20*	*0.01*	*-0.43*	

3.2.3 Temperature at 2 m (T2m)

To measure the temperature of air near the earth surface and not of a surface that is warmed by the Sun, there is a standard practice in meteorology to record temperature at about 2 m above the ground. It gives an overall idea of the air temperature couple of meters away from the sea or land surface. It has a direct influence on SST, wind, local weather, on forecast and so on and is therefore one of the vital indices required by meteorologists and is under regular observation. We will use the term T2m in the following paragraphs.

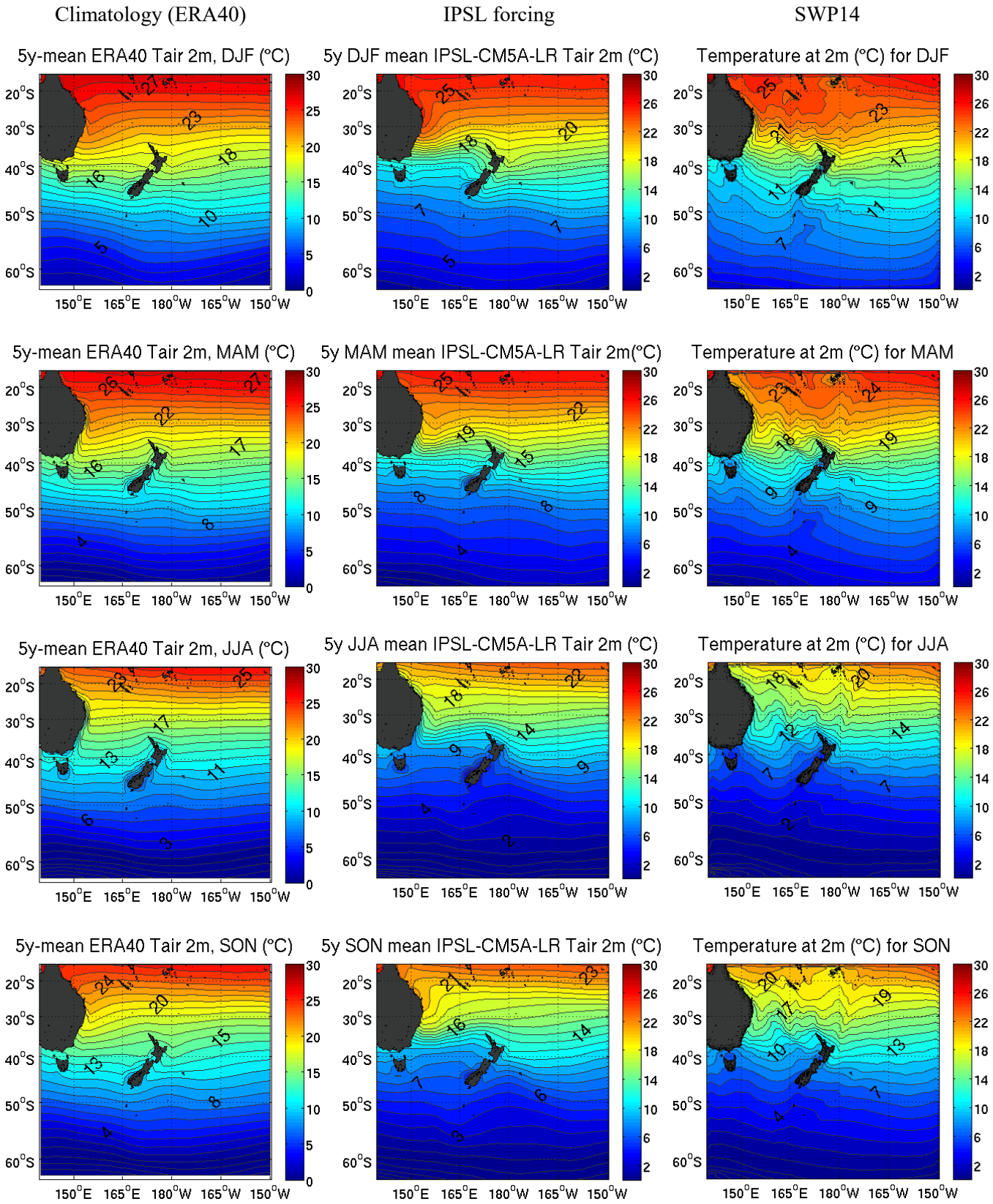

Figure 14 *Comparison of 5 year seasonal mean air temperature at 2 m (°C) between (a) ERA40 (b) IPSL global input (c) SWP14 output*

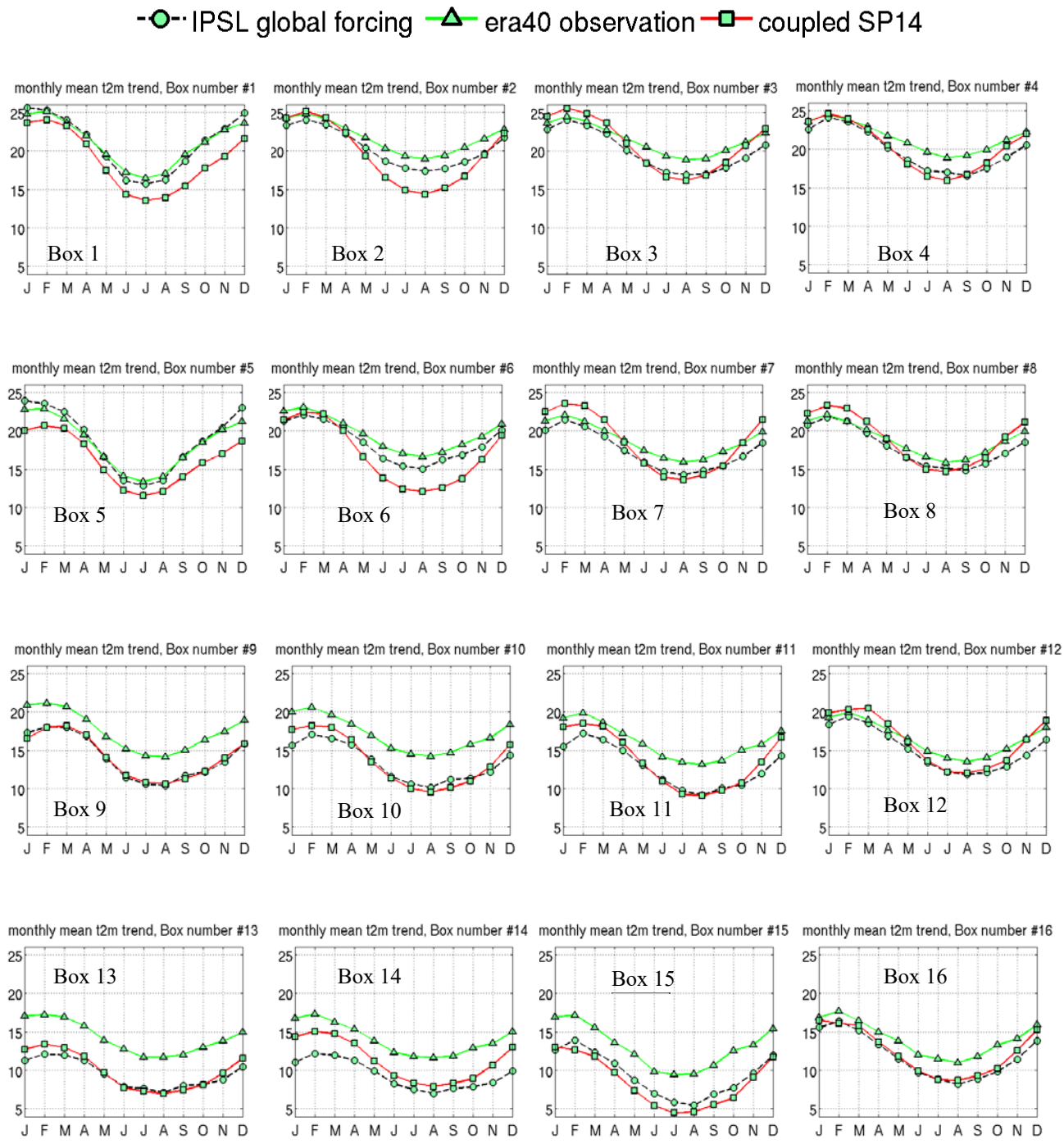

Figure 15 *Comparison of monthly mean air temperature at 2 m for 16 sample boxes*

A number of points are observed from **Figure 14**. Firstly, the IPSL input shows an underestimated T2m values for summer and spring, which when used as a forcing to SWP14 simulates further lower values of T2m. The branching off of a major part of EAC flow eastward (closer to 30-32°S) and its continuation in meanders and eddies forming the Tasman Front is clearly visible for all the seasons. Of course, the temperature of air 2 m above the surface of water that branches off to form part of the Tasman Front varies season to season alike temperature of the sea surface.

The **Figure 15** depicts the monthly mean trend of T2m for all samples and clearly shows that the SWP14 simulated T2m values in general are underestimated. T2m behaves similar to the SWP14 SST and shows significantly lower values for boxes 2 and 6 when compared to the climatology and global input data. Secondly, focusing on column II and III, the SWP14 T2m values best matches with that of IPSL forcing for all the boxes, except for boxes 1, 2 (showing the EAC path) and boxes 5, 6 (showing the Tasman Front), where IPSL forcing matches well with that of the climatology. The third observation is that the SWP14 simulated T2m best matches to both IPSL forcing and climatology for boxes, 3, 4, 7, 8 i.e. for the region up to 35°S at EAC path and both west and east of New Zealand. Finally, for region south of 35°S, the SWP14 T2m values illustrates exact match to that of IPSL forcing, however, both are underestimating to that of climatology. Overall, the T2m values behave similar to that of SST and match the IPSL forcing rather than climatology. The salient concluding points are similar to that of SST.

Table 10 *Statistical indices computed for 5-year annual mean temperature at 2 m*

2 m temperature (annual)											
Centered RMS difference							**Correlation coefficient**				
Band-A	**1**	**2**	**3**	**4**	***Latitudinal mean***		**1**	**2**	**3**	**4**	***Latitudinal mean***
ERA40_CWRF	0.46	0.43	0.65	0.24	*0.44*		0.97	1.00	0.99	0.99	*0.99*
IPSL_CWRF	1.42	0.35	0.80	0.67	*0.81*		0.97	0.99	0.99	0.97	*0.98*
ERA40_IPSL	1.16	0.20	0.41	0.58	*0.59*		0.99	0.99	0.99	0.99	*0.99*
Band-B	**5**	**6**	**7**	**8**			**5**	**6**	**7**	**8**	
ERA40_CWRF	1.50	1.18	1.43	1.74	*1.46*		0.98	0.99	0.99	0.99	*0.99*
IPSL_CWRF	2.15	1.29	1.70	1.56	*1.68*		0.98	0.99	0.99	0.97	*0.98*
ERA40_IPSL	1.24	0.42	0.37	0.42	*0.61*		1.00	0.99	1.00	0.99	*0.99*
Band-C	**9**	**10**	**11**	**12**			**9**	**10**	**11**	**12**	
ERA40_CWRF	2.10	1.84	0.95	1.37	*1.56*		0.97	0.99	0.99	0.99	*0.98*
IPSL_CWRF	1.08	0.92	1.40	1.66	*1.26*		0.99	0.99	0.98	0.98	*0.99*
ERA40_IPSL	2.28	2.68	2.24	0.41	*1.90*		0.98	0.97	0.98	0.99	*0.98*
Band-D	**13**	**14**	**15**	**16**			**13**	**14**	**15**	**16**	
ERA40_CWRF	2.91	1.39	3.09	0.80	*2.05*		0.99	0.99	0.98	0.98	*0.99*
IPSL_CWRF	0.95	2.38	0.84	1.27	*1.36*		0.99	0.98	0.99	0.99	*0.99*
ERA40_IPSL	3.71	3.62	2.56	1.14	*2.76*		0.98	0.96	0.98	0.99	*0.98*
Longitudinal mean	**Band H**	**Band I**	**Band J**	**Band K**			**Band H**	**Band I**	**Band J**	**Band K**	
ERA40_CWRF	*1.74*	*1.21*	*1.53*	*1.04*			*0.98*	*0.99*	*0.99*	*0.99*	
IPSL_CWRF	*1.40*	*1.23*	*1.19*	*1.29*			*0.98*	*0.99*	*0.99*	*0.98*	
ERA40_IPSL	*2.10*	*1.73*	*1.39*	*0.64*			*0.99*	*0.98*	*0.99*	*0.99*	

3.2.4 Wind speed

Wind speed and its direction are vital to determine the real time weather pattern as well as the long term climate of any region. The subtropical gyral systems around all major ocean basins are primarily wind-driven. Winds are capable of influencing the rate of evaporation and mixing of the water at the surface of water. They are further responsible for contributing towards the development of seiches, storm surges and hence are capable of either strengthening or weakening the pressure system of the region.

Figure 16 shows the seasonal comparison of three datasets for wind speed. The first observation is that the simulated SWP14 mean wind speed pattern illustrates exactly similar pattern to that of IPSL forcing, except that the SWP14 overestimates values (or simulates stronger winds compared to the IPSL) for entire study domain. Secondly, the horse latitudes are distinctly visible in IPSL input as well as SWP14 and are lying along ~30-32°S. However, this position does not match with that of the climatology (ERA40) data, except for the winter season. Finally, IPSL shows lowest wind speed at higher latitudes (south of ~50°S) and this behavior is contrary to that of the climatology data. This contrary behavior is also simulated by SWP14.

In **Figure 17**, band A illustrates the best match between climatology, IPSL forcing and SWP14 wind speed. It continues to band B but only for the first half of the year (up to May/July). Second important observation is that the SWP14 winds gives best match for all the sample boxes from 1 to 16. Thirdly, both IPSL and SWP14 overestimates the wind speed values for bands C and D (at and south of 35°S) when compared to the climatology values for all three seasons except austral winter (JJA). Major points are noted below:

- Overall, up to 30-32.5°S the wind speed pattern matches to that of the climatology, however at a higher strength.
- Apart from a slight mismatch in representation of horse latitudes for all seasons, a major flaw is noted for the modeled (IPSL forcing and SWP14) wind speed compared to the climatology data: it is seen that there exists a contradiction in wind speed pattern at higher latitudes, beyond ~50°S.
- The SWP14 performs well in simulating the IPSL forcing and demonstrates the best match. When compared to the climatology data, the SWP14 modelled monthly mean wind speed trend are most reliable at middle latitudes for band A for 25-27.5°S.

Climatology (ERA40) IPSL forcing SWP14

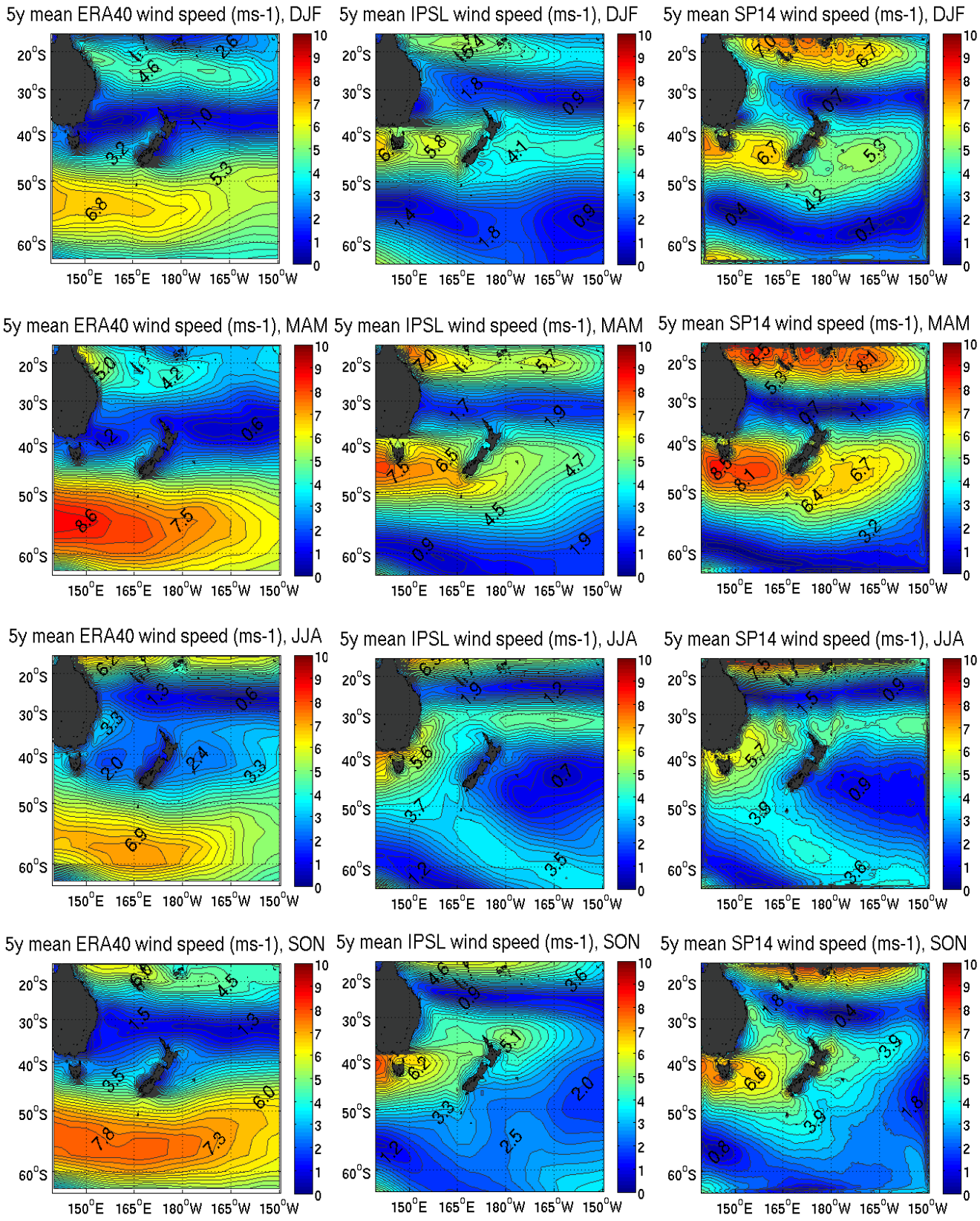

Figure 16 *Comparison of 5 year seasonal mean 10 m wind speed (ms^{-1}) between (a) ERA40 (b) IPSL global input (c) SWP14 output*

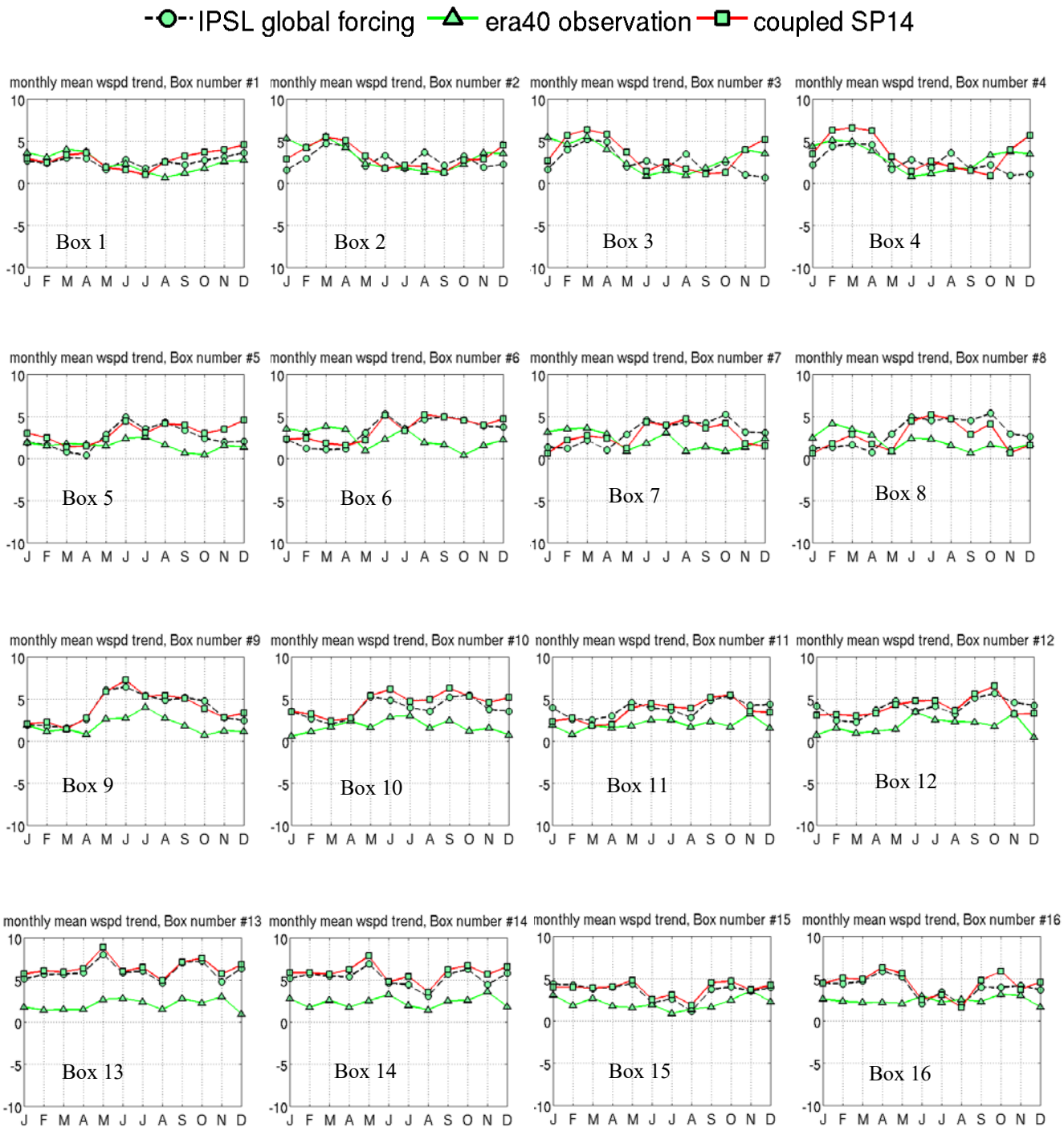

Figure 17 *Comparison of monthly mean 10 m wind speed plotted for 16 sample boxes*

Table 11 *Statistical indices computed for 5-year annual mean wind speed*

Wind speed (annual)											
Centered RMS difference							Correlation coefficient				
Band-A	**1**	**2**	**3**	**4**	***Latitudinal mean***		**1**	**2**	**3**	**4**	***Latitudinal mean***
ERA40_CWRF	0.90	0.36	0.45	0.55	*0.57*		0.37	0.79	0.72	0.75	*0.66*
IPSL_CWRF	0.93	0.27	0.46	0.49	*0.54*		0.78	0.51	0.47	0.47	*0.56*
ERA40_IPSL	0.59	0.20	0.40	0.35	*0.38*		0.48	0.22	0.29	0.36	*0.34*
Band-B	**5**	**6**	**7**	**8**			**5**	**6**	**7**	**8**	
ERA40_CWRF	1.48	1.93	1.58	1.67	*1.66*		-0.05	-0.56	-0.32	0.04	*-0.22*
IPSL_CWRF	0.59	0.98	1.10	1.30	*0.99*		0.74	0.93	0.73	0.74	*0.79*
ERA40_IPSL	1.38	1.48	1.20	1.51	*1.39*		0.19	-0.67	-0.72	-0.55	*-0.44*
Band-C	**9**	**10**	**11**	**12**			**9**	**10**	**11**	**12**	
ERA40_CWRF	1.95	2.25	1.52	2.01	*1.93*		0.68	0.27	0.32	0.37	*0.41*
IPSL_CWRF	1.13	1.38	1.45	1.48	*1.36*		0.96	0.89	0.75	0.68	*0.82*
ERA40_IPSL	1.97	1.62	1.62	1.90	*1.78*		0.64	0.20	0.37	0.14	*0.34*
Band-D	**13**	**14**	**15**	**16**			**13**	**14**	**15**	**16**	
ERA40_CWRF	3.12	2.54	1.30	1.65	*2.15*		0.31	0.14	0.28	-0.23	*0.12*
IPSL_CWRF	1.12	1.04	1.13	1.23	*1.13*		0.97	0.94	0.93	0.88	*0.93*
ERA40_IPSL	2.88	2.33	1.51	1.47	*2.05*		0.28	0.12	0.41	-0.33	*0.12*
Longitudinal mean	**Band H**	**Band I**	**Band J**	**Band K**			**Band H**	**Band I**	**Band J**	**Band K**	
ERA40_CWRF	*1.86*	*1.77*	*1.21*	*1.47*			*0.33*	*0.16*	*0.25*	*0.23*	
IPSL_CWRF	*0.94*	*0.92*	*1.04*	*1.13*			*0.86*	*0.82*	*0.72*	*0.69*	
ERA40_IPSL	*1.70*	*1.41*	*1.18*	*1.31*			*0.39*	*-0.03*	*0.09*	*-0.09*	

3.2.5 U-wind component

The component of wind that is moving in east-west plane (zonal wind velocity) is discussed here using the term u-wind component. The signs that come along the values of the wind are important, where positive sign indicates the eastward moving u-wind vector and the negative sign indicates the westward moving u-wind vector. **Figure 18** clearly shows that there is an overall matching in the pattern of the u-wind vector between the IPSL forcing and simulated SWP14 with slight intensification shown by SWP14 in autumn. Second observation is that at higher latitudes, south of ~ 55°S, both the IPSL and as a result in SWP14 represents easterlies, which is incorrect when seen in the light of climatology of the region, which shows westerlies (or positive u-wind vectors). Additionally, the SWP14 simulated westerlies shows stronger values compared to the IPSL forcing for all seasons. Another observation is for the horse latitude that matches well for all three datasets for winter season (JJA, row-III). However, in other seasons the position of horse latitude shows a northward shift in other two datasets when compared to climatology.

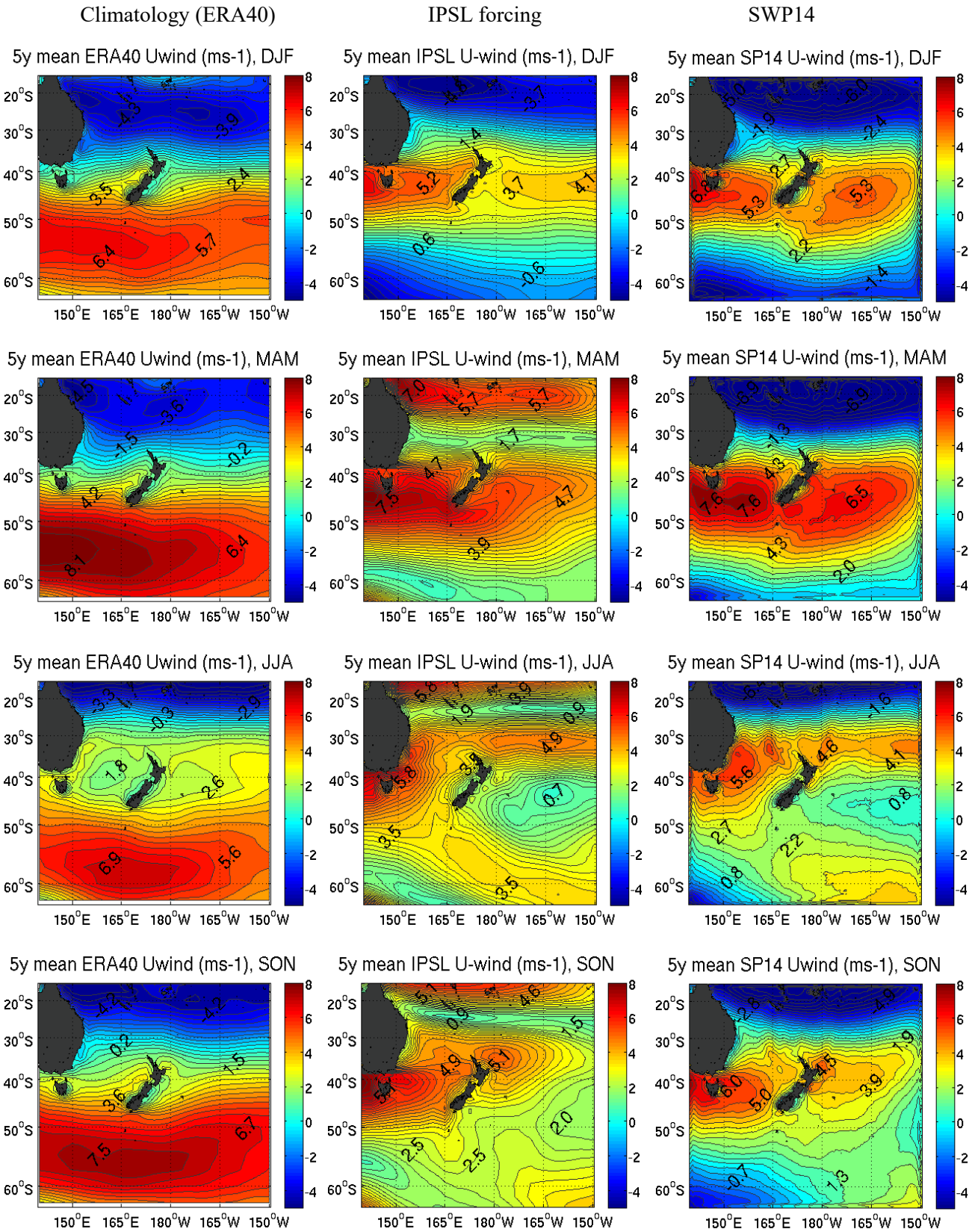

Figure 18 *Comparison of 5-year seasonal mean u-wind component (ms^{-1}) between (a) ERA40 (b) IPSL global input (c) SWP14 output*

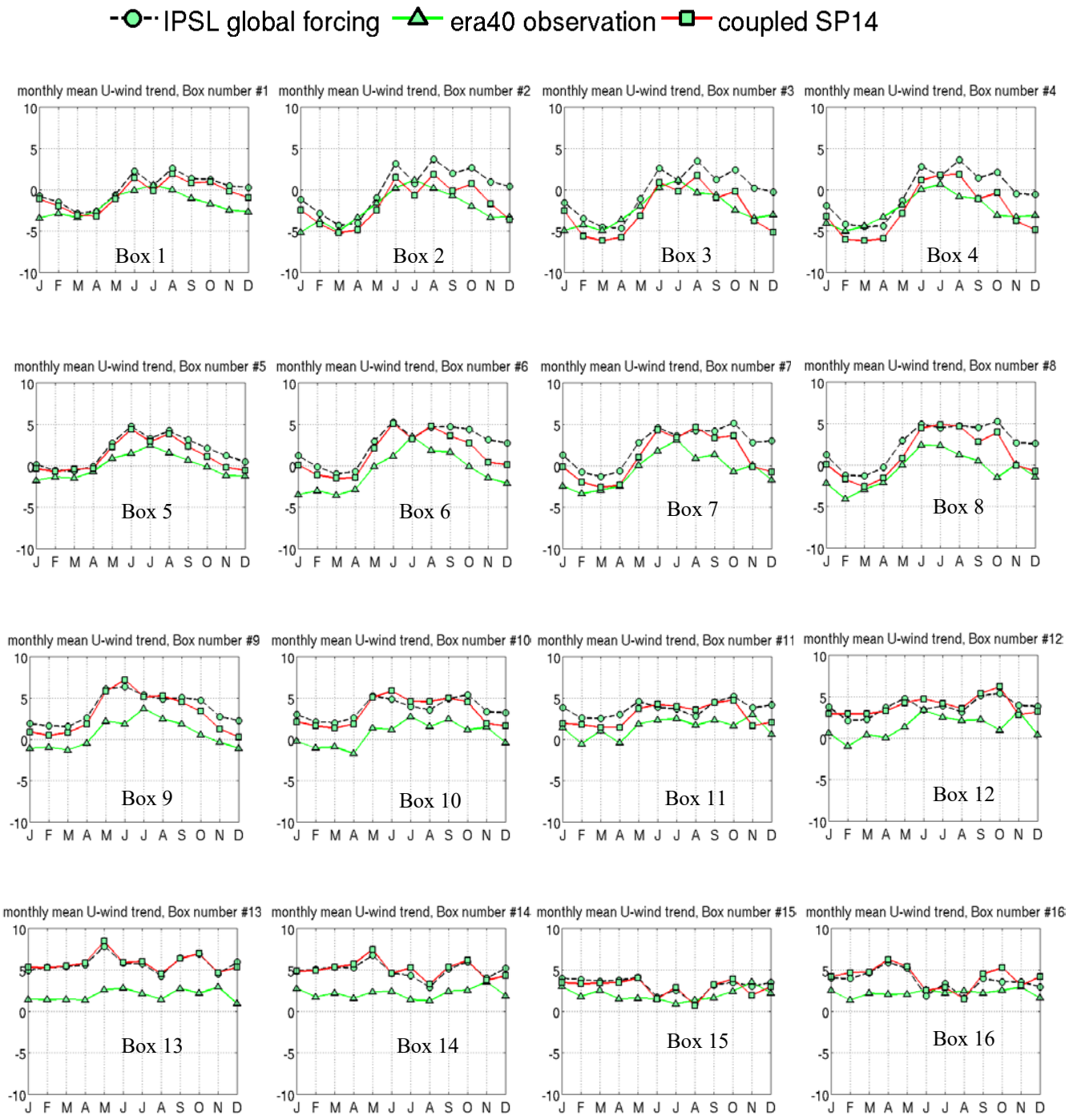

Figure 19 *Comparison of monthly mean u-component of 10 m wind for 16 sample boxes*

Figure 19 illustrates monthly mean trend comparison for all the sample boxes. Phase of SWP14 wind matches exactly to that of IPSL, however for band A the values are closer to that of the climatology. In all other bands B, C, D, the SWP14 wind vectors are slightly higher than the climatology. In addition to the phase, the SWP14 u-wind magnitudes also match to that of the IPSL input. The closest trend of u-wind for all the three data sources are seen for boxes: 2, 3, 15. Moreover, this matching trend continues also for boxes 1, 4, 5, 7, 8 but only for the first half of the year. At middle and higher latitudes, shown by boxes

from 9 to 16, the u-wind vectors simulated are on higher side than the climatology. Overall noteworthy points are:

- The SWP14 simulated u-wind vector illustrates best match with the IPSL forcing with a slight intensification in its magnitude compared to the latter. The easterlies could be seen nearby 60°S in SWP14 simulated u-wind alike IPSL forcing, which are not seen in climatology
- All the zonal wind bands shows slight shift towards northern boundary for IPSL forcing and as a result in simulated SWP14. Similarly, the horse latitude in general shows northward shift in its position too (for both IPSL forcing and SWP14) when compared to the climatology

Table 12 *Statistical indices computed for 5-year annual mean u-wind component*

Uwind (annual)											
Centered RMS difference							**Correlation coefficient**				
Band-A	**1**	**2**	**3**	**4**	***Latitudinal mean***		**1**	**2**	**3**	**4**	***Latitudinal mean***
ERA40_CWRF	1.04	0.35	0.64	0.81	*0.71*		0.70	0.78	0.80	0.87	*0.79*
IPSL_CWRF	1.10	0.28	0.63	0.56	*0.64*		0.99	0.95	0.91	0.93	*0.95*
ERA40_IPSL	0.37	0.28	0.20	0.39	*0.31*		0.71	0.72	0.76	0.79	*0.74*
Band-B	**5**	**6**	**7**	**8**			**5**	**6**	**7**	**8**	
ERA40_CWRF	1.40	2.13	1.46	1.88	*1.72*		0.93	0.90	0.85	0.82	*0.88*
IPSL_CWRF	1.21	0.77	0.79	0.73	*0.88*		0.97	0.93	0.91	0.92	*0.93*
ERA40_IPSL	1.07	1.68	1.34	1.59	*1.42*		0.90	0.81	0.80	0.82	*0.83*
Band-C	**9**	**10**	**11**	**12**			**9**	**10**	**11**	**12**	
ERA40_CWRF	2.57	2.87	2.01	2.89	*2.59*		0.90	0.78	0.56	0.34	*0.65*
IPSL_CWRF	1.19	1.51	1.12	1.90	*1.43*		0.97	0.88	0.63	0.75	*0.81*
ERA40_IPSL	1.87	2.14	1.82	2.12	*1.99*		0.90	0.74	0.50	0.36	*0.62*
Band-D	**13**	**14**	**15**	**16**			**13**	**14**	**15**	**16**	
ERA40_CWRF	4.01	3.36	2.07	2.90	*3.08*		0.40	0.03	0.12	-0.42	*0.03*
IPSL_CWRF	1.84	1.78	1.53	2.25	*1.85*		0.96	0.90	0.92	0.89	*0.92*
ERA40_IPSL	2.73	2.36	2.07	2.30	*2.37*		0.33	0.18	0.38	-0.30	*0.15*
Longitudinal mean	**Band H**	**Band I**	**Band J**	**Band K**			**Band H**	**Band I**	**Band J**	**Band K**	
ERA40_CWRF	*2.25*	*2.18*	*1.55*	*2.12*			*0.73*	*0.62*	*0.58*	*0.40*	
IPSL_CWRF	*1.33*	*1.08*	*1.02*	*1.36*			*0.97*	*0.91*	*0.84*	*0.87*	
ERA40_IPSL	*1.51*	*1.62*	*1.36*	*1.60*			*0.71*	*0.61*	*0.61*	*0.42*	

3.2.6 V-wind component

The component of wind that is moving in north-south plane (meridional wind velocity) is discussed here using the term u-wind component, where positive sign indicates the northward moving v-wind vector and the negative sign indicates the southward moving v-wind vector. **Figure 20** illustrates the vertical wind component in the study domain from three different data sources.

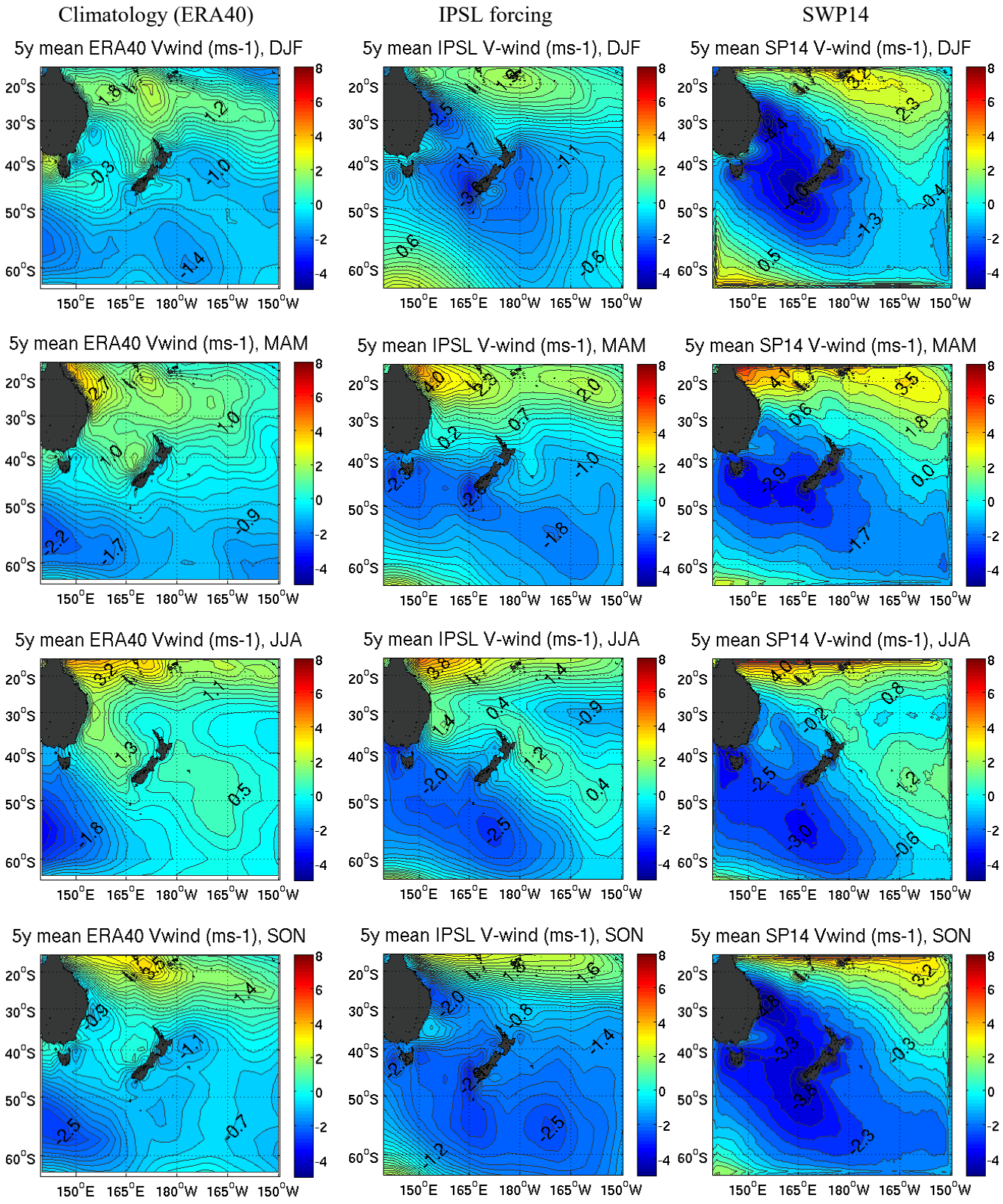

Figure 20 *Comparison of 5-year seasonal mean v-wind component (ms^{-1}) between (a) ERA40 (b) IPSL global input (c) SWP14 output*

The first observation is that the v-wind pattern for SWP14 and IPSL forcing are similar, with an enhancement in magnitude of the simulated SWP14 southward moving winds around middle latitudes,

especially in summer and autumn season compared to the IPSL forcing. Secondly, the climatology, in general is similar to the IPSL forcing except for the area south of 60°S and between 140 and 160°E. Thirdly, both the positive (northward moving) and negative (southward moving) winds are well replicated for each season and can be seen best for the austral winter (JJA) season extending from tropics to higher latitudes.

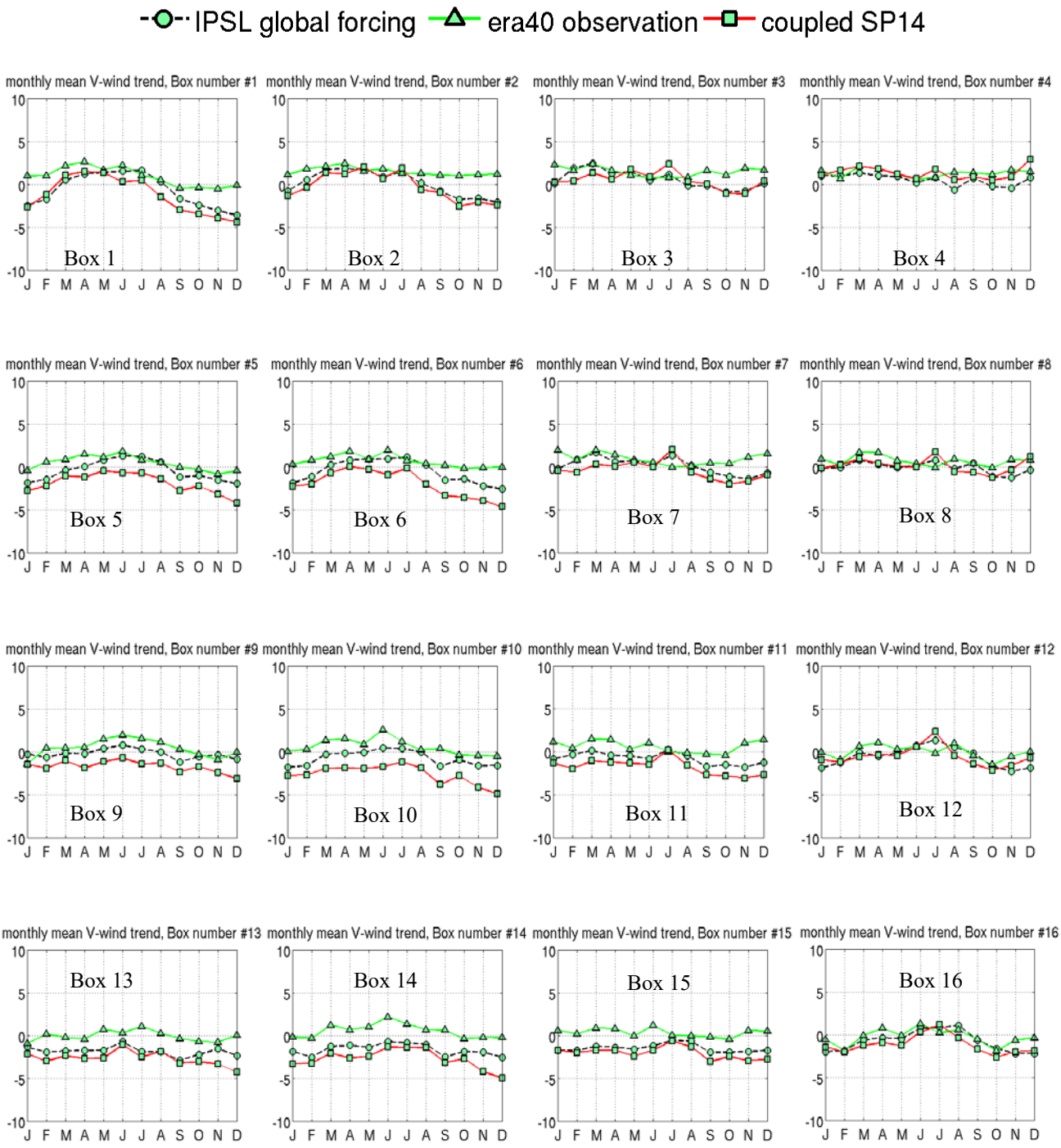

Figure 21 *Comparison of monthly mean 10 m v-component of wind for 16 sample boxes*

At first glance, **Figure 21** illustrates the best match of SWP14 simulated v-wind components seen in boxes: 3, 4, 7, 8, 12, and 16 i.e. all the boxes lying at J and K longitudinal bands. Second observation is more generic and holds true for all the locations, highlighting an important fact that the monthly mean trend of SWP14 simulated v-wind vectors are almost exactly matching that of IPSL forcing except some underestimated values for a couple of months in the latter half of the year. The largest mismatch between IPSL forcing and SWP14 is seen for boxes: 5, 6, 9, 10 throughout the year and for boxes: 1, 2, 7 for part of the year. Third observation shows that the SWP14 simulated v-wind component though follows the IPSL trend, however, the magnitude has slightly enhanced everywhere for southward moving wind (negatively marked in **Figure 20**, column III). The poleward wind vector strengthens the most for EAC to Tasman Front areas (boxes 1, 5, 6, 9, 10, 11) and slightly strengthens for boxes south of 40°S and east of New Zealand (including boxes 7, 11, 13, 14, 15, 16). So, it is concluded that the v-wind vectors pointing towards pole is overestimated at several places. Some of the salient points noteworthy are:

- SWP14 simulated v-wind replicates the trend of that of IPSL with minor change in intensity. This implies the SWP14 simulates well when meridional wind is concerned.
- In addition, SWP14 v-wind also compare well with corresponding regional climatological data, except for higher latitudes (south of 60°S)

Table 13 *Statistical indices computed for 5-year annual mean v-wind component*

Vwind (annual)											
Centered RMS difference							**Correlation coefficient**				
Band-A	**1**	**2**	**3**	**4**	***Latitudinal mean***		**1**	**2**	**3**	**4**	***Latitudinal mean***
ERA40_CWRF	1.03	0.50	0.32	1.39	*0.81*		0.91	0.66	-0.25	0.25	*0.39*
IPSL_CWRF	0.70	0.34	0.55	0.81	*0.60*		0.93	0.97	0.74	0.68	*0.83*
ERA40_IPSL	0.83	0.29	0.48	0.71	*0.58*		0.78	0.78	0.19	0.14	*0.47*
Band-B	**5**	**6**	**7**	**8**			**5**	**6**	**7**	**8**	
ERA40_CWRF	1.33	1.44	0.45	0.82	*1.01*		0.85	0.81	-0.08	0.18	*0.44*
IPSL_CWRF	1.34	1.42	0.42	0.55	*0.93*		0.90	0.93	0.85	0.60	*0.82*
ERA40_IPSL	0.77	0.46	0.35	0.50	*0.52*		0.81	0.78	0.03	0.20	*0.45*
Band-C	**9**	**10**	**11**	**12**			**9**	**10**	**11**	**12**	
ERA40_CWRF	1.52	2.00	1.29	0.96	*1.44*		0.52	0.72	0.08	0.46	*0.44*
IPSL_CWRF	1.27	1.92	1.01	0.52	*1.18*		0.80	0.83	0.90	0.77	*0.82*
ERA40_IPSL	0.90	0.89	0.67	0.83	*0.82*		0.63	0.77	0.16	0.51	*0.51*
Band-D	**13**	**14**	**15**	**16**			**13**	**14**	**15**	**16**	
ERA40_CWRF	1.96	2.10	1.43	0.94	*1.60*		0.22	0.77	0.17	0.77	*0.48*
IPSL_CWRF	1.02	1.29	0.66	0.62	*0.90*		0.71	0.84	0.86	0.85	*0.82*
ERA40_IPSL	1.48	1.29	1.01	0.92	*1.18*		0.07	0.78	0.15	0.74	*0.44*
Longitudinal mean	**Band H**	**Band I**	**Band J**	**Band K**			**Band H**	**Band I**	**Band J**	**Band K**	
ERA40_CWRF	*1.46*	*1.51*	*0.87*	*1.03*			*0.62*	*0.74*	*-0.02*	*0.41*	
IPSL_CWRF	*1.09*	*1.24*	*0.66*	*0.63*			*0.84*	*0.89*	*0.84*	*0.72*	
ERA40_IPSL	*1.00*	*0.73*	*0.63*	*0.74*			*0.57*	*0.77*	*0.13*	*0.40*	

3.3 Summary: SWP14 model performance

Considering the complexity (as seen in **section 1.2.2**) and variability of SWP region, a number of sampling stations (**Figure 10**) are selected to illustrate dynamics of different stations. This approach of selecting a number of sample boxes instead of single large box negates the dilution of local behavior and dynamics and can illustrate them distinctly.

At preliminary stage of model evaluation, the simulated SSTs from coupled ocean and atmosphere components are compared, where ocean SST showed underestimation and larger deviation than atmosphere SST, when compared to the regional climatology. Therefore, coupled atmosphere results are used for model evaluation and to investigate the applicability of SWP14 data in future storminess. The SWP14 is evaluated based on two criteria: first of all, the model validation is performed by comparing the model output to climatology/reanalysis data; secondly, the model performance is tested by comparing the model output to its own forcing data. The IPSL global model wind data (used to force SWP14) when compared to the regional climatology data, shows an overall overestimation of u-wind component and wind speed and slight underestimation of v-wind component. To be more specific, the u-wind component and wind speed shows best fit with regional climatology for lower middle latitudes (25° to 27.5°S) that continues up to 32.5°S, however only for initial months until June. Further south of 35-37.5°S both these variables show stronger or overestimated values. The SWP14 simulation continues to carry forward this bias in IPSL global model data, such that the SWP14 simulated wind components and wind speed closely resembles to that of IPSL forcing data with minor overestimation. At higher latitudes, south of 55°S, IPSL winds are incorrectly represented when compared to the climatology and similar results are reproduced by SWP14. This implies that at higher latitudes, the modelled winds cannot be trusted.

In terms of surface water properties compared to that of regional climatology: The IPSL SSS shows a number of mismatches with respect to the regional climatology. **Figures 12 and 13** illustrate a comparatively higher IPSL SSS values up to middle latitudes and presence of fresher water around entire western coasts of NZ. IPSL SSS also shows presence of higher salinity values at higher latitudes (south of ~50°S), which in other words mean missing fresher water at higher latitudes. Although the SWP14 is forced by higher values of SSS values the SWP14 model results shows commendably lower values which are more close to the regional climatology. This implies, that in spite of incorrect values of IPSL salinity values, the SWP14 simulates closer to regional climatology values. It also does not reproduce the unusually fresher water across the western coast of NZ that is shown by IPSL data. In case of SST, the IPSL forcing SST shows best match when compared to the HadISST1 climatology, especially for middle latitudes starting from 25°S until 32.5°S. Although similar SST values are simulated for 25°-32.5°S latitude by SWP14, except for the EAC and Tasman Front area, giving lower SST values there. At higher middle latitudes south of 35°S, the IPSL SST data shows an underestimated values, and similar values are simulated by the SWP14. A distinct change in the properties of surface temperature and salinity indicates the changed water properties after branching off of the EAC. Here, the regional scale circulation features, like, the eastward

travelling Tasman Front whose path is modulated by the complicated bathymetry of that region seems to be very well resolved by the ocean model, hence, the meandering Tasman Front is also visible.

CHAPTER 4

Recent changes in storminess of Southwest Pacific region (1970-2014)

The motivation of this chapter originated from the curiosity to acquire a background knowledge on the real-time recent past storm distribution for the study domain. It will help in establishing and understanding the recent changes in trends of storminess. It uses SPEArTC storm dataset is the most comprehensive and reliable (Magee et al., 2016) observational archive available for the SWP region and long term observational/reanalysis data to understand the changes in recent past storm distribution along with large scale environmental variability. Any such analysis would also be helpful as a baseline study for investigation of possible future changes.

The analysis in this chapter refers to the research objective 2 discussed in section 1.3 of chapter 1.

4.1 Data and Methods

The first objective of this study focus on recent past change in storminess of the region. The study uses 45 years (1970-2014) Southwest Pacific Enhanced Archive for Tropical Cyclones or SPEArTC dataset (Diamond et al. 2012; Diamond et al. 2013). At present, SPEArTC is the most comprehensive dataset on historical storms, starting from 1840 until present, covering entire Southwest Pacific basin (135°E-120°W, 0°-50°S or further south following any storm's track). The selection of start of analysis period is based on most reliable period of satellite era (Diamond et al. 2012), 1970 onwards. Entire storm data analysis is based on the *named* storms, i.e. storms that were named by the competent authorities are included except otherwise stated. The storm database provides wind data in knots, which are converted to International system units (m/s). Preliminary result shows (a) a decreasing trend in total storm counts, (b) an increasing trend in mean annual storm wind speed, and (c) a decreasing trend in mean annual storm central pressure. Based on this preliminary analysis of mean annual storm wind speed, three major dips, each accompanied by a 5 m/s ascent, are observed [1970 (35 m/s), 1986 (40 m/s), and 2000 (45 m/s)]. Approximately

immediately after those dips (or ascents in wind) a blatant ascent in storm wind trend is witnessed. Therefore, the analysis periods are sub-divided into three time-slices, each of 15 years duration, as follows: 1970-1984 (T1), 1985-1999 (T2) and 2000-2014 (T3) to equally divide the entire length of study. In general, the tropical storms are active during November and April, however, while analyzing the storm dataset, several storms were found during the month of October (thirteen), May (nine), June (four) and July (one). As the storm counts in May and October are sizeable, therefore, in this study, the summer-autumn storm analysis period is taken from October to May. Following this length of storm season, the winter-spring analysis period is also kept of similar length from May to December. To determine any change in storminess in the last four decades, three fifteen years long total (both named and unnamed storms included) storm climatology are compared. Subsequently, the total storm count is based on a search engine that focuses at 2°x2° grid cell at a time and finds the number of storms that passes through it. In other words, the total storm count at a 2° square grid is determined by counting the number of occasions when storm passes through it. These storm counts were normalized before presenting storm counts climatology shown by **Figure 23** for three time-slices and before computing their differences.

Often while discussing about the potential damages or dangers related to an approaching storm, we come across a wind based scale commonly called as Saffir-Simpson Hurricane Wind Scale (SSHWS). This scale was built to communicate the extent of possible potential loss of life and property damage and works as a warning for government and public from any approaching weather disturbance. Originally, this scale was formulated in 1971 based on the wind speed that showed expected damage to structures and further appended by corresponding pressure, and storm-surge ranges. Recently, in 2009, the National Hurricane Center transformed the scale into a pure wind scale and another adjustment related to category 4 wind ranges in 2012 was added. It rates hurricane's sustained wind speed in a 1 to 5 scale (**Table 14**).

Table 14 *Saffir-Simpson Hurricane Wind Scale (SSHWS)*

SSHWS Category	*Maximum sustained wind speed*			*Damage level*
	knot	*mh^{-1}*	*ms^{-1}*	
1	64-82	74-95	33-42.47	minimal
2	83-95	96-110	42.48-49.17	moderate
3	96-112	111-129	49.18-57.67	extensive
4	113-136	130-156	57.68-69.74	extreme
5	≥ 137	≥ 157	≥ 69.75	catastrophic

According to this scale, storms that achieves the wind speed of category 3 (maximum sustained wind speed of more than 49 m/s) or more are considered as major (or extreme) storms and are expected to become potential cause of significant loss of life and property. The threshold used to determine the extreme storms in this study is based on the definition of SSHWS. Different named storms are first categorized/sorted into category 1 to 5 based on the storm wind speed for entire analysis period. It automatically excludes the

weaker than category 1 events. In second step, only those named storms are retained, whose maximum sustained wind speed touched at least category 3. In third step, several short-lived major storms, i.e. those who could not sustain for more than six hours duration are excluded. All storms that reached category 4 and 5 wind speed are included irrespective of their length of sustenance.

One obvious caveat is present in our analysis of extreme storminess: the storm dataset offers corresponding storm wind speed at a temporal resolution of six hours, therefore several storms that did not sustain for more than six hours as a major category are either excluded or are underrated one scale lower to what it might have actually achieved in its life time. This study is strictly based on pure wind scale, and does not consider the minimum surface pressure records in categorization. In a separate analysis, where surface pressure were based to categorize storms, it is seen that many of the major (category 3 or 4) storms listed in this analysis actually made it to the next higher category (category 4 or 5 respectively).

The second objective of this chapter is to determine changes in the large scale environmental conditions and try to link them to change in storm climate. The six hourly SST data is taken from HadISST dataset (Rayner et al. 2003). Similarly, six hourly 20th century reanalysis (http://www.esrl.noaa.gov/psd) surface and near surface atmospheric data are used to depict the large-scale environmental conditions. Each parameters are processed for the study domain for three time-slices and differences between consecutive time-slices are computed and compared with each other.

4.2 Results and Discussion

4.2.1 Change in recent past storminess

The preliminary analysis of storminess looks into three storm parameters on annual basis: minimum storm central pressure, maximum sustained storm wind speed and total number of named storms. **Figure 22** graphically depicts these annual values from 1970 to 2014, where total storm counts and maximum sustained wind speed (m/s) are shown by the left vertical axis, and lowest storm central pressure (mb) is shown by the right vertical axis. The total annual storm count trend shows usual interannual variability between 12 to 17 counts from 1970 to 1987 with just one peak noticed in 1972 (19 storms). The reducing trend in counts curve is first observed for 1988 (8 storms) and this reduction is continued till present, with only two peaks noticed in 1993 (17 storms) and 1998 (24 storms). The second parameter is the annual lowest value of minimum storm central pressure, which shows an overall decline in 1980s compared to 1970s. The third parameter is the maximum sustained storm wind speed that is strongly but negatively correlated to the central pressure trend and shows a rising trend in contrast to other two parameters. Some of the major stormy years as function of windiness are observed for 1972 (17 storms, 940mb, 63m/s), 1984 (13 storms, 920 mb, 57 m/s), 1988 (8 storms, 925 mb, 62 m/s), 1992 (14 storms, 920 mb, 60 m/s), 1998 (24, 900mb, 65 m/s), 2003 (12, 886 mb, 68 m/s), 2006 (8 storms, 898 mb, 70 m/s). Interestingly, after 2006 the declining trend of the annual central pressure now (2010 onwards) shows a slight rise and is coincident with lowering of annual maximum sustained storm wind speed.

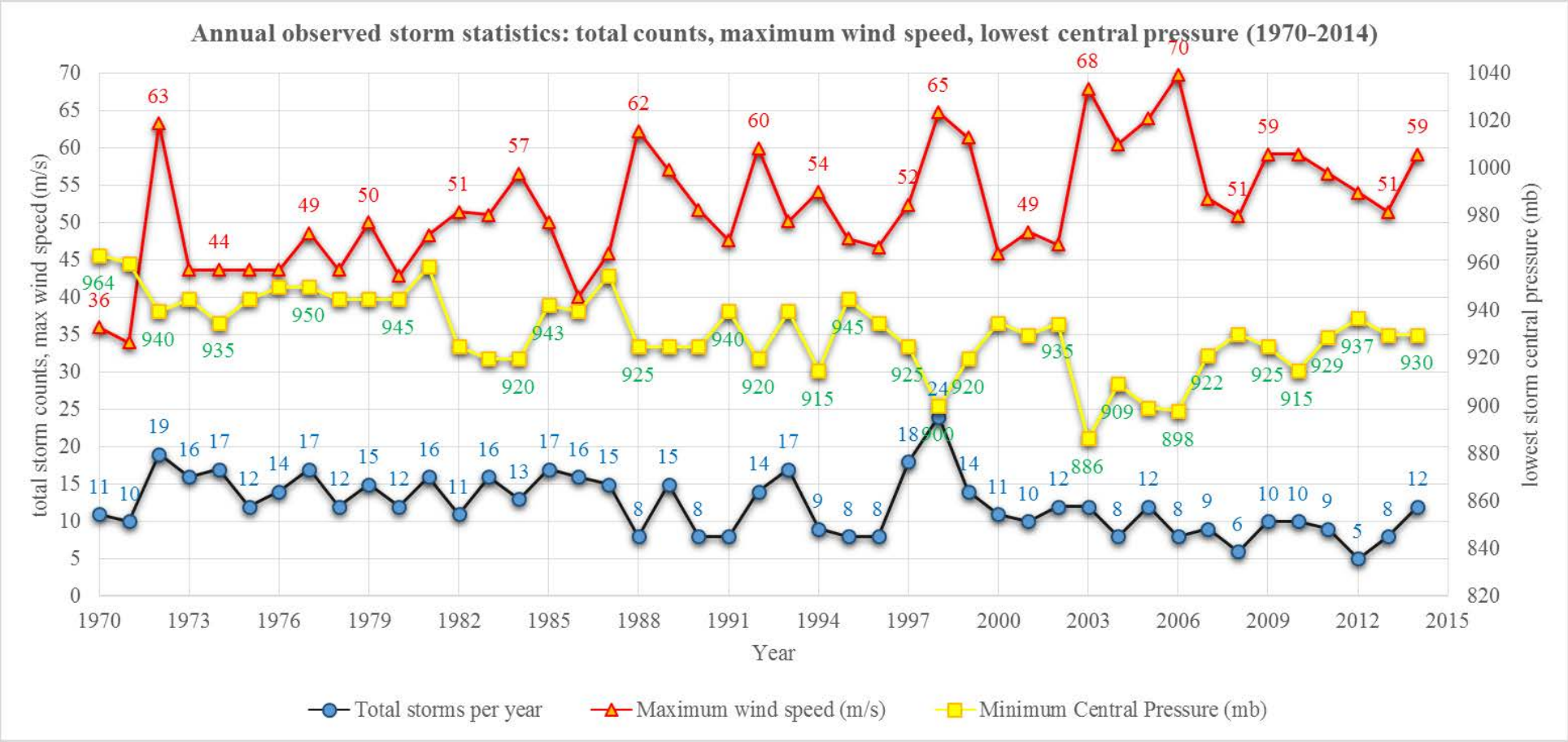

Figure 22 *Change in trends in total annual storm counts (black), annual maximum sustained storm wind speed (red), annual minimum storm central pressure (yellow) for named storms from 1970-2014 in Southwest Pacific basin; also refer* ***Table 15*** *(data source: SPEArTC, Diamond et al., 2012)*

Table 15 *Summary of observed storm statistics displaying annual values of (i) total storm counts, (ii) maximum sustained storm wind speed, and (iii) minimum storm central pressure, attained for three selected time-scales (T1:1970-1984, T2:1985-1999, T3: 2000-2014)*

T1 (1970-84)				***T2 (1985-99)***				***T3 (2000-14)***			
Storm season (Year)	*total storm count*	*maximum wind speed (m/s)*	*minimum central pressure (mb)*	*Storm season (Year)*	*total storm count*	*maximum wind speed (m/s)*	*minimum central pressure (mb)*	*Storm season (Year)*	*total storm count*	*maximum wind speed (m/s)*	*minimum central pressure (mb)*
1970	11	36.01	963.50	1985	17	50.06	942.50	2000	11	45.94	935.00
1971	10	33.95	960.00	1986	16	40.13	940.00	2001	10	48.77	930.00
1972	19	63.28	940.00	1987	15	45.94	955.00	2002	12	47.07	934.70
1973	16	43.73	945.00	1988	8	62.30	925.00	2003	12	67.96	886.30
1974	17	43.73	935.00	1989	15	57.05	925.00	2004	8	60.55	909.30
1975	12	43.73	945.00	1990	8	51.75	925.00	2005	12	64.00	899.30
1976	14	43.73	950.00	1991	8	47.59	940.00	2006	8	69.81	898.00
1977	17	48.61	950.00	1992	14	59.98	920.00	2007	9	53.19	921.50
1978	12	43.73	945.00	1993	17	50.16	940.00	2008	6	50.88	930.30
1979	15	50.06	945.00	1994	9	54.17	915.00	2009	10	59.16	925.00
1980	12	42.85	945.00	1995	8	47.89	945.00	2010	10	59.16	915.00
1981	16	48.36	958.50	1996	8	46.71	935.00	2011	9	56.59	929.00
1982	11	51.44	925.00	1997	18	52.42	925.00	2012	5	54.02	937.00
1983	16	51.08	920.00	1998	24	64.77	900.00	2013	8	51.44	930.00
1984	13	56.59	920.00	1999	14	61.42	920.00	2014	12	59.16	930.00
total storms	*211*				*199*				*142*		
average	*14.07*	*46.73*	*943.13*		*13.27*	*52.82*	*930.17*		*9.47*	*56.51*	*920.69*
% change					***-5.69***	***13.05***	***-1.37***		***-28.64***	***6.99***	***-1.02***

NOTE: (1) The total storm counts have ***reduced by 5.69%*** *for T2 (1985-1999) when compared to T1 (1970-1984) and by* ***28.64%*** *from T3 (2000-2014) to T2. (2) The maximum sustained storm wind speed has* ***increased by 13.05%*** *from T2 to T1, and by* ***6.99%*** *from T3 to T2. (3) The minimum central pressure attained by storms has* ***reduced by 1.37%*** *for T2 wrt T1 and* ***1.02%*** *for T3 wrt T2. See* ***Figures 3 and 4*** *for pictorial representation*

These values are further tabulated in **Table 15** and statistical inferences are drawn to conclude the percentage change in storm parameters. Based on this mean annual storm wind speed trend, three major dips each accompanied by 5 m/s ascent are observed [1970 (36 m/s), 1986 (40 m/s), and 2000 (45 m/s)]. Approximately immediately after those dips (or ascent in wind) a blatant ascent in storm wind trend is witnessed. Therefore, further the analysis period of storms is sub-divided into three time-slices, each of 15 years duration: 1970-1984 (T1), 1985-1999 (T2) and 2000-2014 (T3) to equally divide the entire length of study.

The second stage of analysis focuses on the change in geographical distribution of occurrence of storms in the last four decades. The total number of storms are first searched at every 2° square grid of the study domain to construct the storm counts climatology. Accordingly, the search engine determines if a particular geographical location hosts a storm event for entire analysis period and if so, counts the number of occurrences. This way, the most vulnerable zones within the Southwest Pacific region is counted, normalized and mapped in **Figure 23** (Row I) for three time-slices. Both T1 (**Figure 23a**) and T2 (**Figure 23b**) shows stronger presence of storms, with highest contour values observed for T2 seen predominantly around the latitudinal band of 12°S to 18°S throughout the period of analysis making the island nations most vulnerable. The expanse of storm counts or track density varies from T1 to T3, with maximum expansion seen during T2 (**Figure 23b**) and reduced track density seen for T3 (**Figure 23c**). The contour values between 0.4 and 1.0 representing the maximum storm counts or densest storm tracks are primarily covering the latitudinal extent between ~8°-23°S and longitudinally between ~147°-180°E for T1. In comparison to T1, this densest storm track coverage during T2 has shifted westward ranging between ~142°-175°E and northward ranging between ~8°-18°S. In T3, this densest storm track coverage has further contracted and can be seen only at northern coast of Australia between ~10°-18°S and ~140°-150°E.

The 0.1 contour line for T2 shows an eastward expansion at subtropics (~173°-160°W) and southward expansion towards North Island between ~24°-32°S and 175°E-180°E. It also shows a northward contraction in Tasman Sea and northwest North Island, between 150°-175°E compared to T1. Further to this contraction in T2 compared to T1, a major contraction of 0.1 contour line is seen in T3 period, where it has shifted northwards from ~32°S to ~24°S between ~150°E to 170°W and contracted ~4° westward at east of 160°W at subtropics between ~10°-18°S.

The 0.05 contour line shown by separate green contour for T1, covers northern Tasman Sea up to ~37°S between 150°-175°E, excluding northern North Island and again covering northeast of North Island, where it reaches close to ~40°S approximately at the dateline. In case of T2, the 0.05 contour line shows a flat line at ~32°S between 150°-175°E, with (a) about 13° northward contraction noticed at subtropics (150-154°E) reaching near 24°S; and (b) about 5° southward expansion reaching northwest of South Island. Further to this, the 0.05 contour line in T2 shows a southward expansion towards north of North Island when compared to T1.

I. Storm counts ***(a) T1 (1970-1984*** ***(b) T2 (1985-1999)*** ***(c) T3 (2000-2014)***

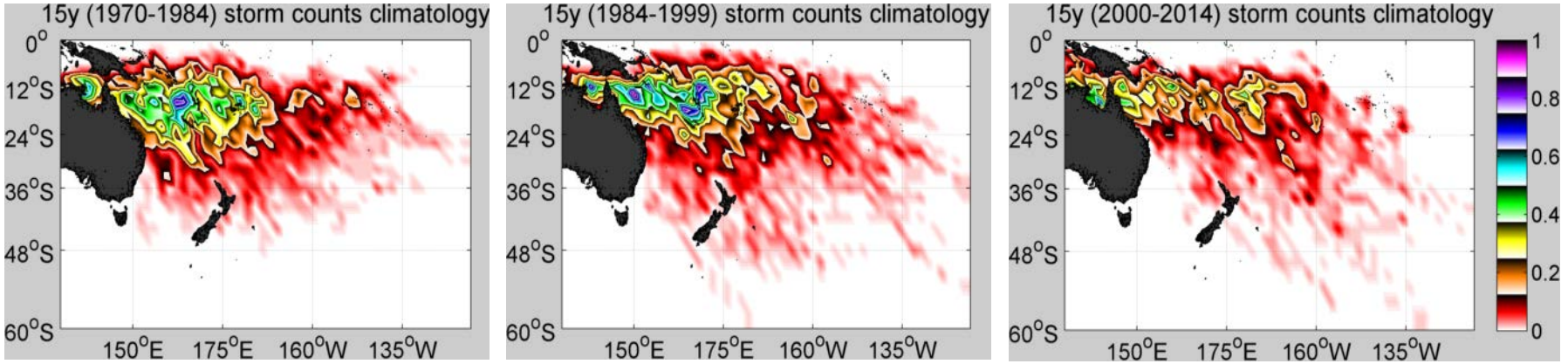

II. Change in storm counts (d) T2 minus T1 ***(e)T3minusT2*** ***(f) T3 minus T1***

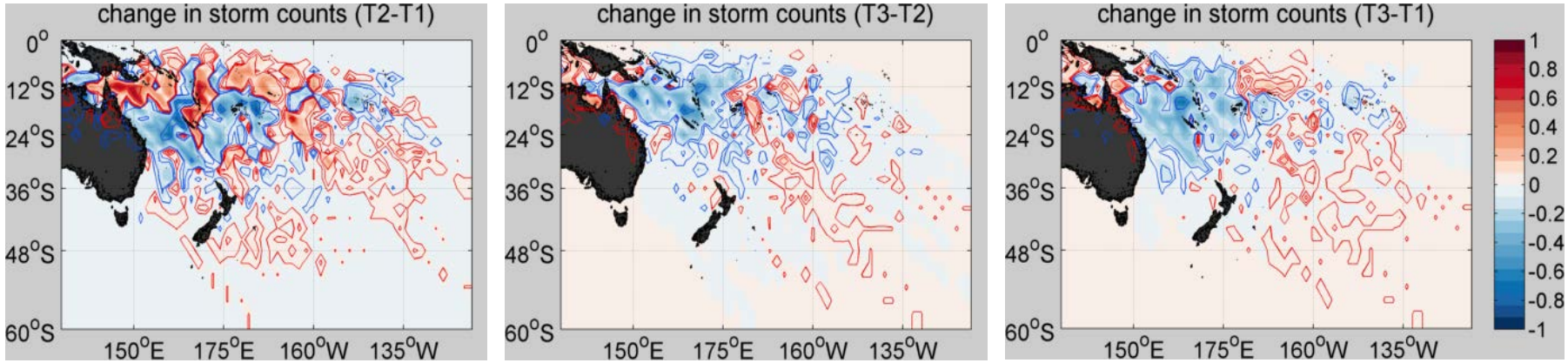

Figure 23 *Normalized 15 years total storm counts climatology (Row-I): (a) T1 (1970-1984), (b) T2 (1985-1999), (c) T3 (2000-2014) and their differences (Row-II): (d) T2 minus T1, (e) T3 minus T2 based on SPEArTC dataset (Diamond et al., 2012), where storms are searched at every 2° square grid. The difference maps clearly denote the locations that received surplus (blue) or deficit (red) number of storms*

In case of T3, the 0.05 contour line shows a marked northward contraction relative to T2 between 150-175°E reaching close to ~26°S leaving only one flank up to 34°S between 170-175°E at northwest of North Island and another closed contour in proximity to west of North Island. However, a major expansion of 0.05 contour line is seen east of dateline reaching down south until 38 °S close to 164-160°W.

The 0.01 contour line shown by a separate red contour in T1, covers almost entire southern Tasman Sea reaching close to 45-46°S on an average throughout 150°E-175°W excluding South Island. In case of T2, it includes northwest to southeast of North Island with a major expansion seen over east of South Island reaching south of 50°S between 175°E-160°W.

Contrarily, in T3 when compared to T1, 0.01 contour line moves northwards reducing its extent over western Tasman Sea from ~45°S to ~30°S. At the same time, 0.01 contour line shows an overall poleward expansion between ~180°E and ~135°W. This indicates that the present storm track density has reduced over western Tasman Sea and increased over east of NZ, indicating a southeastward shift of recent storm tracks. These facts are further confirmed by **Figures 23d and 23e**, illustrating those locations that hosted a surplus (blue) and deficit (red) number of storms for T2 and T3 time period relative to respective reference time T1 and T2. Note that the difference values less than -0.04 are not shown by these difference maps.

To summarize the findings of overall storminess trend of last four decades from above analysis, percentage change in storminess is computed for T2 minus T1 and T3 minus T2 using equation 1. For example, the percentage change in storminess for T2 with respect to T1 as reference is computed as the ratio of their difference (T2 minus T1) to the reference, (T1).

$$\%\ change\ T2\ T1 = \frac{(T_{2,average} - T_{1,average})}{T_{1,average}} * 100 \qquad (1)$$

Accordingly, following observations are drawn: (a) a decreasing trend in total storm counts is observed: the total storm counts have reduced by 5.69% for T2 relative to T1, and 28.64% for T3 relative to T2; (b) a decreasing trend in mean annual storm central pressure is observed: the annual minimum central pressure has reduced by 1.37% for T2 relative to T1, and 1.02% for T3 relative to T2; (c) an increasing trend in mean annual storm wind speed is observed: the maximum sustained storm wind speed has risen by 13.05% from T2 relative to T1, and 6.99% for T3 relative to T2.

Following above findings on overall storm climatology, storms that converts into major or extreme events are studied. The extreme storm analysis included only those storms that crossed category 3 and higher wind speed following categorization mentioned by SSHWS given by **Table 14**. In the present study, any named storm that reaches category 3 wind speed and sustains for more than a day has been included in the analysis. For detail review on the criteria of selection of extreme events kindly refer **section 4.2**. Here we will use major or severe or extreme words interchangeably, all meaning the same. Based upon the criteria discussed,

a number of *major storm events* are identified and tabulated under **Table 16**. The duration and translation time from category 1 to any major category is computed based on six hourly sustained wind speed data. While discussing about severe storms, some events are noteworthy: (i) Carlotta (1972): It sustained as category 3 for more than 162 hours and as category 4 for more than 126 hours, and therefore marked as one of the most severe storms of Southwest Pacific region; (ii) Meli (1979): It intensified twice as category 3 in its lifetime, and took just 24 hours to transform from category 1; (iii) Kathy (1984): It took just 12 hours or so to translate into category 3 from category 1; (iv) Rewa (1994): It intensified to category 3 twice in its lifetime and stayed for more than 12 and 18 hours respectively. Although it took about 60 hours to translate into category 3 in its first stint but was faster (within just 24 hours) in its second stint; (v) Gavin (1997): It shows two category 3 peaks each of more than 18 hours duration and before that it spent as category 2 storm for about 30-36 hours; (vi) Susan (1998): It might have churned its environment as major

Table 16 *Extreme storm statistics illustratiing (i) duration (ii) translation time from category 1 to attain extreme hurricane scales (categories 3, 4 and 5)*

Storm season	*Storm names (1970-2014)*	*maximum sustained wind speed (m/s)*	*minimum storm central pressure (mb)*	*Duration of category 3 (hours)*	*Duration of category 4 (hours)*	*Duration of category 5 (hours)*	*Translation time from category 1 to 3 (hours)*	*Translation time from category 1 to 4 (hours)*
Time-slice I (1970-1984)								
1972	CARLOTTA (NZ)	63.28	940	162	126		96	120
1979	MELI (NZ)	50.06	945	6			24	
				< 6				
1982	GYAN (NZ)	51.44	925	6			36	
1983	OSCAR (NZ)	51.08	920	6			42	
1984	KATHY	56.59	920	24			12	
Time-slice II (1985-1999)								
1988	ANNE (NZ)	62.30	925	36	6		18	30
1989	HARRY (NZ)	57.05	925	36			96	
1989	AIVU (NZ)	52.11	937.5	6			18	
1990	OFA (NZ)	51.75	925	24			54	
1992	VAL (NZ)	51.44	940	24			24	
1992	FRAN (NZ)	59.98	920	36	12		24	36
1992	ESAU (NZ)	53.76	925	24			18	
1994	REWA (NZ)	54.17	925	12			60	
				18			24	
1994	THEODORE (NZ)	53.40	915	36			24	
1997	GAVIN (NZ)	52.42	925	18			18	
				18				
1998	SUSAN (NZ)	64.00	900	78	60		18	24
1998	RON (NZ)	64.77	900	66	48		24	30

Storm season	Storm names (1970-2014)	maximum sustained wind speed (m/s)	minimum storm central pressure (mb)	Duration of category 3 (hours)	Duration of category 4 (hours)	Duration of category 5 (hours)	Translation time from category 1 to 3 (hours)	Translation time from category 1 to 4 (hours)
1999	THELMA	61.42	920	72	36		12	30
1999	DANI (NZ)	50.78	925	6			18	
Time-slice III (2000-2014)								
2003	ZOE (NZ)	67.96	886.3	54	30		18	24
2003	BENI (NZ)	56.59	918.7	18			24	
2003	DOVI (NZ)	57.36	916.7	36			12	
2003	ERICA (NZ)	59.06	913.3	24	6		18	30
2003	ESETA (NZ)	49.39	937.3	12			24	
2004	HETA (NZ)	60.55	909.3	42	24		24	30
2004	FAY	56.18	916	36			66	
				< 6				
2005	MEENA (NZ)	58.29	915.3	24	0		30	42
2005	OLAF (NZ)	63.02	907.3	84	30		12	42
2005	NANCY (NZ)	53.14	930.7	12			12	
2005	PERCY (NZ)	64.00	899.3	12	30		30	96
2005	INGRID (NZ)	62.40	917.7	42	18		18	24
				30	12		6	18
				18			30	
2006	LARRY	51.75	941	6			18	
2006	MONICA	69.81	898	60	42	18	78	90
2009	HAMISH	59.16	925	42	24		36	48
2010	OLI	51.44	925	18			12	
2010	TOMAS	51.44	925	18			24	
2010	ULUI	59.16	915	78	12		12	18
2011	WILMA	51.44	939	6			24	
2011	YASI	56.59	929	30			36	
2012	JASMINE	54.02	937	36			18	
2013	EVAN	51.44	943	24			78	
2013	FREDA	51.44	940	6			24	
2013	SANDRA	51.44	930	12			24	
2014	IAN	56.59	935	36			42	
2014	GILLIAN	56.59	937	36			42	
2014	ITA	59.16	930	126	84		96	120

Note: (i) Severe storm Monica: being the only one that reached category 5 (as per this analysis based on six hourly data), the table do not show the translation time from category 1 to 5, which is 114 hours; (ii) Colour codes:The storms that sustained as category 4 or 5 status for more than a day are shown by orange filled red texts; the minimum translation time of 6 to 12 hours taken by category 1 to become category 3 are shown by yellow filled dark yellow texts, whereas those transformed from category 1 to 4 within 18 to 24 hours are shown by green filled dark green texts.

category 3 for more than 78 hours and took just 24 hours or less to translate itself into category 4 storm, where again it stayed for 60 hours; (vii) Similar pattern of quick translation is shown by Thelma (1999), Zoe (2003) and Dovi (2003), where they took just 12 to 18 hours to translate themselves into category 3 storm from category 1. Further, Zoe took just 24 hours or so to transform itself into category 4 from category 1; (viii) Ingrid (2005): It is the most remarkable storm among others, which peaked as category 3 thrice in its lifetime, and every time starting from category 1. At first instant it remained in category 3 for more than 42 hours and then in next 6 hours it strengthened itself to category 4 storm (i.e. just 24 hours to transform from category 1 to 4), where it remained for more than 18 hours duration and started waning into a weaker storm of category 1. Interestingly, in its second lap, it took just 6 hours to become category 3 from 1 and within next 12 hours to become stronger category 4; (ix) Monica (2006): It is the most catastrophic storm learnt from this analysis because it not only reached category 5 strength but remained there for more than 18 hours duration. Before attaining the severest level, it must have already created havoc or huge damages while it was a category 3 (for more than 60 hours) and category 4 (for more than 42 hours). It took just 114 hours (not shown in **Table 16**) or 4.75 days to intensify as most severe category 5 storm from weaker category 1; (x) Ita (2014): It stayed for longer hours as category 3 (126 hours) and as category 4 (84 hours), similar to Carlotta (1972) [names marked by red text].

Some major storms, such as Thelma (1999), Dovi (2003), Olaf (2005), Nancy (2005), Oli (2010) and Ului (2010) took less than 12 hours to transform from category 1 to category 3. Similarly, those which got transformed from category 1 to 4 within 18 to 24 hours are Susan (1998), Zoe (2003), Ingrid (2005), and Ului (2010). Other worth mentioning major storms are Rewa (1994), Fay (2004) and Ingrid (2005), who managed to sustain themselves as category 4 even while waning away. This feature is missing in all other storms, implying that other storms decayed faster than these ones. The storms that sustained their category 4 or 5 status for more than 24 hours are shown by orange filled red texts. The minimum translation time of 6 to 12 hours taken by category 1 to become category 3 are shown by yellow filled dark yellow texts, whereas those transformed from category 1 to 4 within 18 to 24 hours are shown by green filled dark green texts. Severe storm Monica being the only one that reached category 5 (as per this analysis based on six hourly data), the table does not show the translation time from category 1 to 5, which is 114 hours.

Some important inferences can be drawn for change in extreme storminess (see **Table 17**) that are in contradiction to the overall reduction in the Southwest Pacific summer/autumn storminess for the analysis period. The number of extreme storms (category 3 and above) has increased 2.8 (1.93) times during T2 (T3) to T1 (T2). The corresponding rise in mean maximum sustained storm wind speed is 3.47% (1.12%) with a decrease (slight increase) in corresponding mean minimum central pressure by 0.86% (0.10%). The transition time from category 1 (weakest) to 3 has reduced from an average of 42 hours to 30 hours. Further to this, earlier (during T1 and T2) where just one or two category 1 storms took less than 12 hours to

intensify to category 3, now (during T3) at least six to seven storms take less than 12 hours to intensify to category 3. This indicates towards higher availability of favourable condition supporting quick intensification of storms to become a major storm. Further, it is concluded that the minimum time taken by category 1 to become 3 (4) is found to have reduced over the last four decades to less than 12 (18) hours.

Table 17 *Summary of change in extreme storm events (T2 minus T1 and T3 minus T2) for Southwest Pacific region*

	T1	T2	T3	Change T2T1	Change T3T2
Total storm count	5	14	27	2.80	1.93
Mean maximum sustained wind speed (m/s)	54.49	56.38	57.02	3.47	1.12
Mean maximum sustained wind speed (m/s)	930.00	921.96	922.85	-0.86	0.10

4.2.2 Change in 15 year mean environmental conditions

To determine the changes that took place during past four decades, 15 year mean surface and near-surface data were plotted for the study domain for three different time-slices. In this section, we refer to the differences under two case studies, to discuss what and how they changed over past decades. **Figure 24 to 27** provides a set of illustrations, where mean change in different large-scale environment variables are brought together. The first two combinations are for austral summer-autumn storm seasons, whereas the latter two combinations are for austral winter-spring storm seasons; where each storm seasons are accompanied with two different case studies or time-slices.

(a) Austral summer-autumn storm season:

(i) Case-study I (T2 minus T1)

Referring to **Figure 24** that illustrates a combination of 15 year mean change in various large scale environmental conditions that took place during T2 period compared to T1, for austral summer-autumn season. The first column shows change in mean SST, mean SAT, along with their differences (SST minus SAT). The warming pattern over air and sea surface looks similar at a larger scale. However, while looking closely along the east coast of Australia and New Zealand (NZ), the SST minus SAT map shows a contrast in warming pattern of air and sea, especially along the middle latitudes: (i) positive change i.e. higher SST observed along the East Australian Current (EAC) until south of Tasmania and further south of 48°S at higher latitudes, which indicates usual ocean to atmosphere transfer of sensible heat; (ii) negative change

i.e. higher SAT observed over Tasman Sea, around NZ coastal waters and east of NZ beyond dateline with maximum values seen at south-east of South Island and north of North Island. These areas of higher SAT are also largely coincident with the maps of raised latent heat flux indicating the presence of air retaining high latent heat, increased PBL height, and presence of convective cloud. Further an increased specific humidity at north-east to east of NZ is also witnessed which resembles to the pattern of presence of precipitable water (not shown). Such areas of negative SST minus SAT index are indicators of areas with vigorous atmospheric instability forming clouds and even shape up the region's precipitation. The surplus storm counts climatology (shown by **Figure 23d**, T2 minus T1) do coincide with the increase in latent heat flux, PBL height and specific humidity and wind intensity. The surface pressure has lowered for tropics and subtropics, whereas increased at middle latitudes: over Australia and east of NZ (~40°S, 160°W), with almost no change in pressure around north of NZ. Such surface pressure difference maps are indicative towards likely change in the storm tracks.

(ii) Case-study II (T3 minus T2)

Similarly, for second case study, we refer to **Figure 25** that illustrates changes in various large-scale variables during T3 compared to T2. At first glance, the changes in this case looks completely different than case-1 discussed above. The SST and SAT difference maps show major warming trend along a larger atmosphere-ocean part that is diagonal, showing a southeast-ward warming pattern with maximum values seen along the middle latitudes (north-east of NZ). The specific humidity difference map also follow this southeast-ward increasing pattern closely resembling to that of SAT. For SST minus SAT difference map, there are major pockets showing negative changes along: prominently from south of 36°S around southern Tasman Sea extending down south of Tasmania; between 24°-48°S east of NZ; and along subtropics. In middle latitudes, south of 36°S, the presence of negative SST minus SAT difference pockets also support the presence of rise in latent heat flux, PBL height, with slight rise in specific humidity. In addition to these changes, surface pressure difference maps show two high pressure centers, one over Tasman Sea to south of Tasmania and second over open ocean ~40°S, ~140°W; with reduced pressure values covering areas of tropics to middle latitudes reaching parts of northeast and even east of NZ. Such condition would encourage more storms to reach east of NZ and lesser to reach high pressure centers (example, to Tasman Sea), which corroborates with the shrinking pattern of storm climatology (seen in **Figure 23e**, T3 minus T2). Although the wind difference map shows largely a reduction for east of NZ, it also shows small pockets of increased windiness in the mid ocean northeast of NZ, coinciding with increased atmospheric instability and rise in total storms. The map also shows greater winds between 12 and 36°S along EAC and northern Tasman Sea, which also coincides with the region of air holding higher amount of latent heat to help intensify the storms passing by.

A. Austral summer-autumn storm season: *15 year mean differences* ***(T2** [1985-99] **minus T1** [1970-84])*

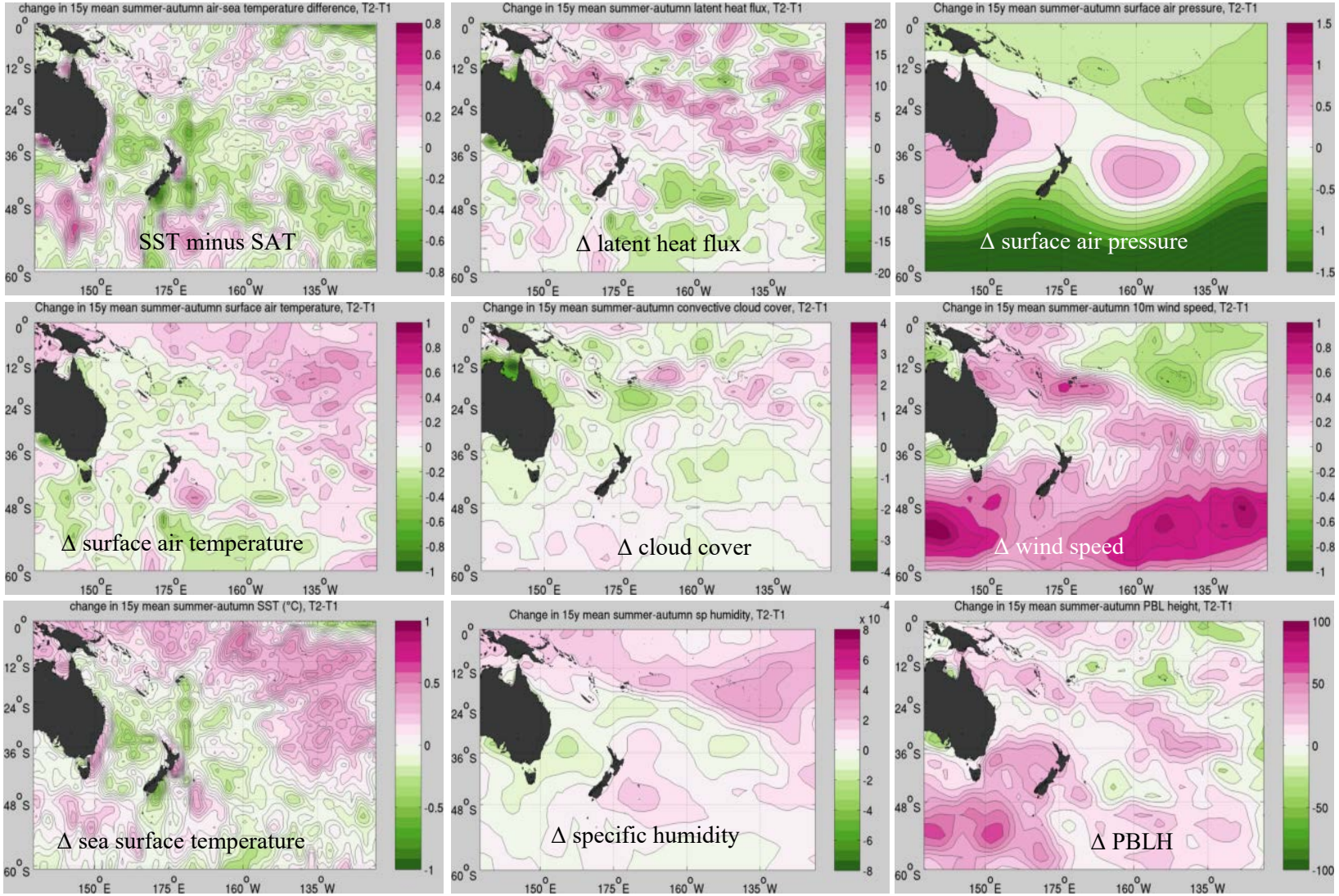

Figure 24 *Change in 15 year mean large scale environment variables during summer-autumn storm season (1985-1999 minus 1970-1984)*

B. Austral summer-autumn storm season: *15 year mean differences* ***(T3** [2000-2014] **minus T2** [1985-1999])*

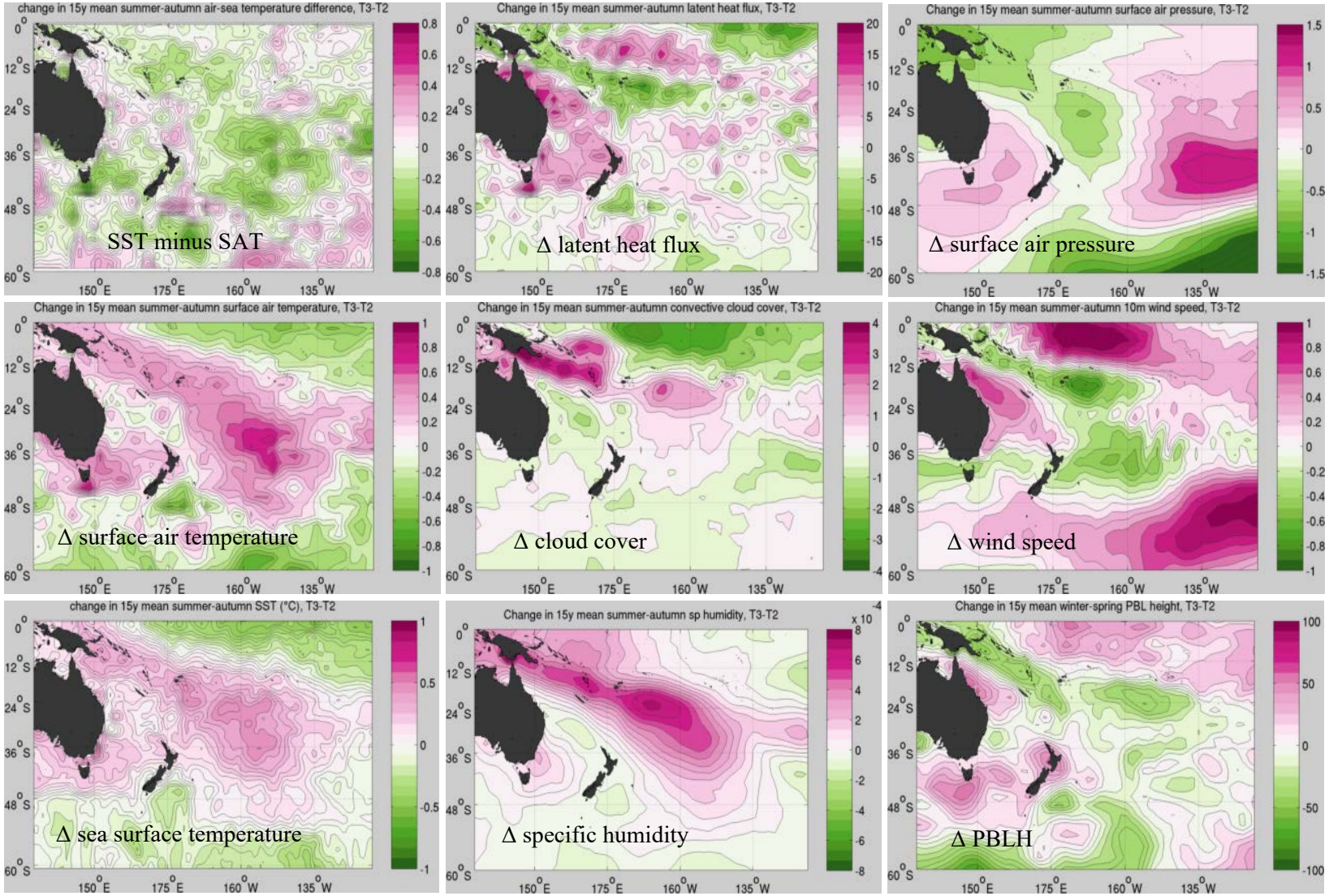

Figure 25 *Change in 15 year mean large scale environment variables during summer-autumn storm season (2000-2014 minus 1985-1999)*

(b) Austral winter-spring storm season:

The midlatitude winter storms are also classified as frontal storms, since their formation is sourced from horizontal temperature gradient due to higher differential heating between equator and midlatitudes during winter. This section of discussion does not have any storm observation or climatology to refer to. Based on the changes in large scale conditions we will try to analyze how the storminess might have changed for austral winter-spring season in recent decades.

(i) Case-study I (T2 minus T1)

The change in large-scale environmental conditions during T2 compared to T1 for austral winter-spring season is presented in **Figure 26**. While looking at the middle latitudes, the SST minus SAT map shows an increase in atmospheric instability over Tasman Sea and around coastal NZ, especially southeast of South Island. This also coincides with rise in specific humidity, latent heat flux, PBL height and wind intensity. Additionally, the cloud coverage shows an overall decline except for areas along EAC that further its branch moving eastward over northern Tasman Sea until northwest of North Island; and over southeast of South Island. Interestingly, the surface pressure map shows rise in pressure over the subtropical and especially over middle latitudes countries, implying a possible decline in total storm counts between about 32°-38°S, 150°E-160°W. However, if in case a storm is formed, it is likely to intensify and sustain longer and produce higher precipitation. Similar phenomena of increased specific humidity, latent heat flux, can be seen for tropical areas which are marked by higher PBL height. Corresponding surface pressure map shows an overall reduction in pressure, implying higher windiness in tropical zone. Finally, at higher latitudes, south of 48°S, the overall cloud coverage has increased along with increase in latent heat flux and pronounced decrease in sea surface pressure. This also coincides with maximum rise in the PBL height and greater windiness when compared to entire study domain. Overall an increase in midlatitude winter-spring storminess is observed south of 36°S with maxima noted south of ~46°S during T2 period compared to T1. It is interesting to note a marked increase in SST at higher latitudes, south of South Island, which indicates warming up of upper layers of ocean.

(ii) Case-study II (T3 minus T2)

This case study is based on change in large-scale environment during T3 period compared to T2 for winter-spring storm season and is illustrated by **Figure 27.** The warming up of air and sea surface is noticed in a diagonal fashion from tropics to east of NZ. A significant increase in latent heat flux is observed mainly over subtropics, along Australian coasts, south of 12°S, which continues until south of Tasmania, around coastal waters of NZ extending widely at east of NZ, with smaller pockets of reduction over Tasman Sea. The surface pressure shows a reduction south of 38°S towards higher latitudes, which is supplemented by the increase in cloudiness, higher PBL height and an increase in windiness. On the contrary, the areas where

surface pressure shows a rise are centered at Tasman Sea, extending north and northeast of NZ beyond the dateline, indicating of reduction in wind speed. Hence, it is concluded that an overall increase in winter-spring storminess is observed over higher middle latitudes between 36°-50°S that is accompanied by an increase in intensity for areas around NZ and its east, at tropics and at subtropics south of 12 -24°S. On the contrary, a reduction in storminess is seen at higher latitudes, south of 53°S.

Another interesting fact worth noting is the increase in SAT at higher latitudes south of South Island, which is inconsistent to the observation made during case-study I (T2 minus T1) for the same season. This implies that in recent years (T3), warming is evident at lower troposphere compared to T2 and T1 that may further lead to atmospheric instability.

4.3 Summary

Since only austral summer-autumn storm season data is used for analysis, we will limit our discussion to the same. The large scale variability that gave rise to the recent changes in storm climatology of SWP region has been analyzed for three time-slices in this chapter and is summarized here. Here we will focus our discussion on areas that show changing pattern of large scale environmental variables coinciding with the changing pattern of storm climatology.

For the first case (T2: 1985-99 minus T1:1970-84), the 15 year mean change shows a contrast in warming pattern of air and sea, specifically along the middle latitudes: mean change in storm climatology for areas covering Tasman Sea, around NZ coastal waters and area between northeast to east of NZ extending beyond dateline at south-east of South Island and north of North Island. The surplus storm counts climatology (shown by **Figure 23d**, T2 minus T1) in these areas also matches with the negative values of SST minus SAT index, which promotes instability in the atmospheric conditions. This atmospheric instability also coincides with an increase in latent heat flux, PBL height, precipitable water, cloud cover and wind intensity. The surface pressure difference maps are indicative towards likely change in the storm tracks. The changes in these difference maps show a drop for tropics and subtropics and a rise for middle latitudes. The drop is accompanied by possibility of surplus in storm counts over the tropics and subtropics. Whereas the rise implies a possibility of deficit of storm counts over the middle latitudes, i.e. over Australia and east of NZ (~40°S, 160°W). Almost no change in storm counts for areas around north of NZ is noted in this period.

Similarly, for the second case (T3: 2000-2014 minus T2:1985-1999), the 15 year mean change also shows a contrast in warming pattern of air and sea. However, the changes are completely different to that observed in case-study I (**Figure 25**), showing southeast-ward or diagonal warming pattern with maximum values along the middle latitudes (north-east of NZ). The SST, SAT difference maps show major warming trend across a larger part of atmosphere-ocean region. The pockets of negative SST minus SAT index is seen along south of 36°S around southern Tasman Sea extending down south of Tasmania, between 24°-48°S

east of NZ. This coincides with the presence of rise in latent heat flux and PBL height. The wind difference map similarly shows greater winds between 12° and 36°S along EAC and northern Tasman Sea.

C. Austral winter-spring storm season: *15 year mean differences* ***(T2** [1985-1999] **minus T1** [1970-1984])*

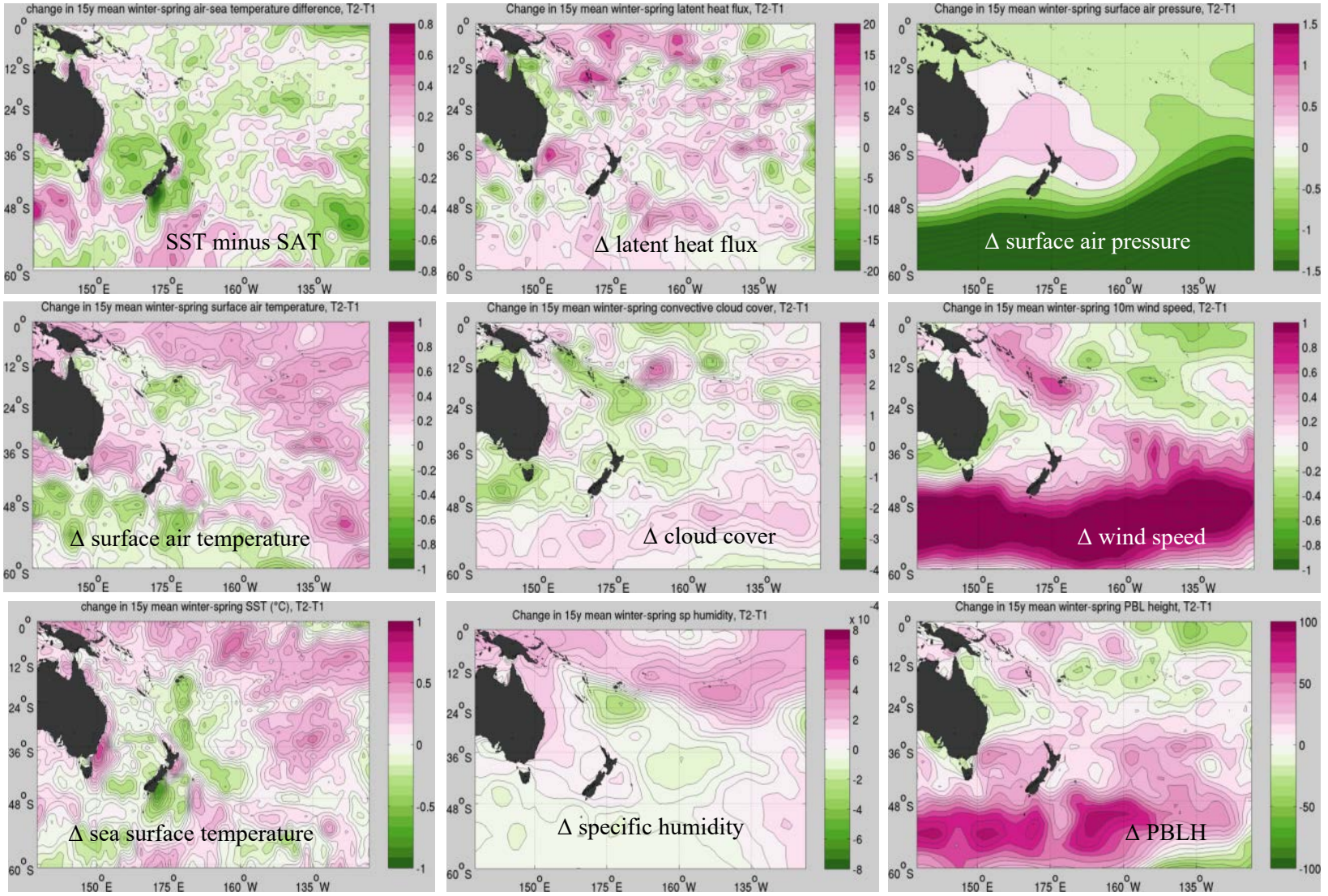

Figure 26 *Change in 15 year mean large scale environment variables during winter-spring storm season (1985-1999 minus 1970-1984)*

D. Austral winter-spring storm season: *15 year mean differences* ***(T3** [2000-2014] **minus T2** [1985-1999])*

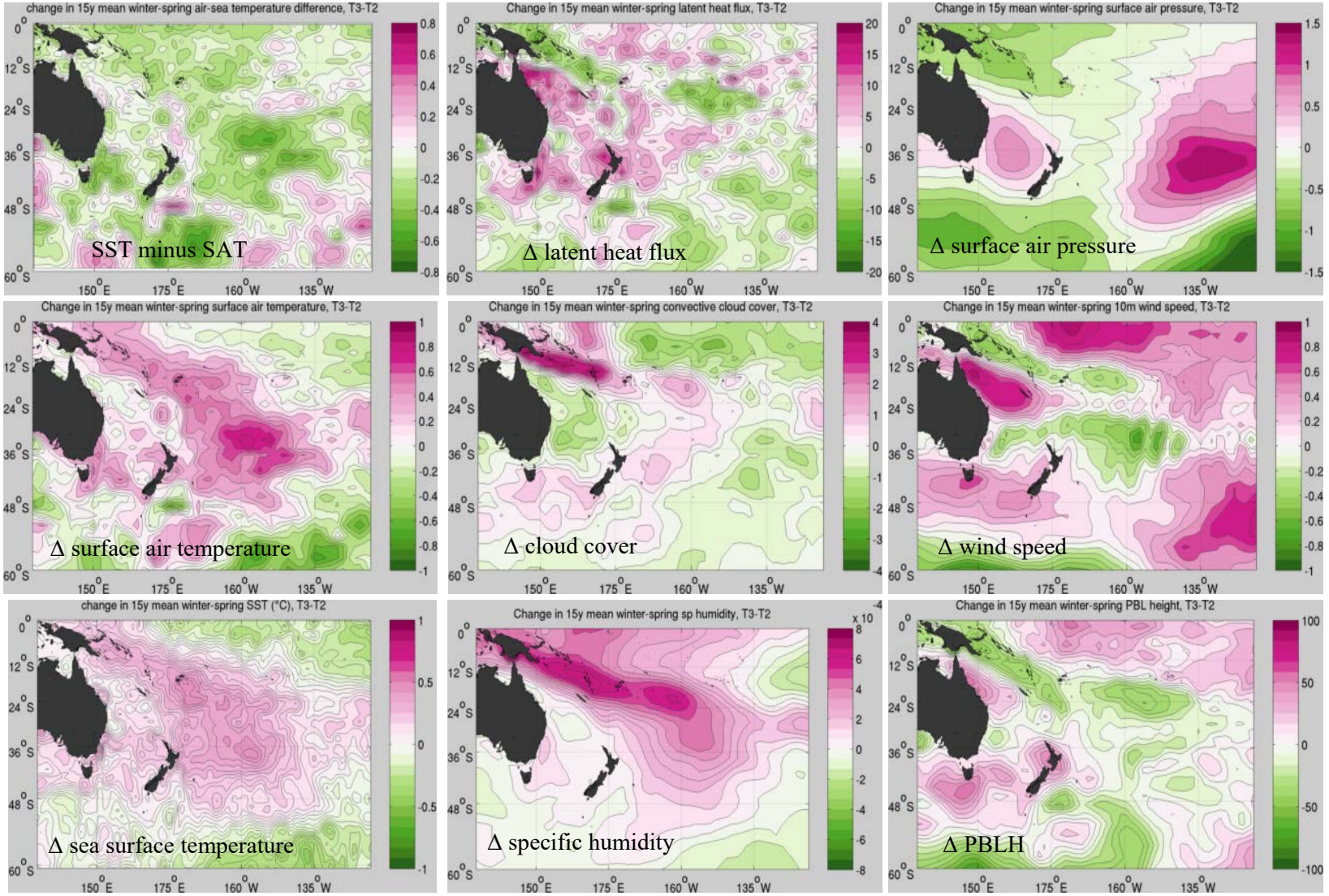

Figure 27 *Change in 15 year mean large scale environment variables during winter-spring storm season (2000-2014 minus 1985-1999)*

east of NZ. This coincides with the presence of rise in latent heat flux and PBL height. The wind difference map similarly shows greater winds between 12° and 36°S along EAC and northern Tasman Sea.

This also coincides with the region of air molecules holding higher amount of latent heat, possibly useful in intensifying the storms passing by. These areas show a possibility of rise in storm counts and also matches with the changing storm climatology maps (**Figure 23e**, T3 minus T2) in this period.

The surface pressure difference maps show two positive pressure centers, one over Tasman Sea to south of Tasmania and second over open ocean ~40°S, ~140°W. However, reduced pressure values covering areas from tropics to middle latitudes reaching parts of northeast until east of NZ: such conditions would encourage more storms to reach east of NZ and lesser to reach high pressure centers (example, to Tasman Sea), which corroborates with the shrinking pattern of storm climatology (seen in **Figure 23e)** in this period. The differences observed for two case studies (T2 minus T1 and T3 minus T2) are found to show an overall warming of the region for both the storm seasons. However, the most striking feature is the fact that both the case-studies show a completely different pattern of warming, hinting towards different mechanisms that may have been instrumental. This has further been discussed in chapter 6.

However, the most striking feature is the fact that both the case-studies show a completely different pattern of warming, hinting towards different mechanisms that may have been instrumental in the background. Here, the influence of different phases of El Niño Southern Oscillation (ENSO) acting in the background cannot be ruled out along with the rise of greenhouse effect. Although, this study does not aim at analysis of ENSO effect on recent changes in storminess, the occurrence of extreme storminess coinciding with the prevalence of negative ENSO phase cannot be ignored and are tabulated for T2 and T3 period (see **Table 18**).

Table 18 *Comparison of extreme storminess to different ENSO phases*

Time-slices	***Positive SO or El Niño***		***Negative SO or La Niña***	
	moderate to strong years	*counts, wind speed (m/s)*	*moderate to strong years*	*Counts, wind speed (m/s)*
T1	1972-73	19, 63	1970-71	11, 36
	1982-83	11, 51	1973-74	16, 44
			1975-76	12, 44
T2	1986-87	16, 40		
	1987-88	15, 46	1988-89	8, 62
	1991-92	8, 48		
	1997-98	18, 42	1998-99	24, 65
T3			1999-00	14, 62
	2002-03	12, 48	2007-08	9, 53
	2009-10	10, 59	2010-11	10, 59

Maximum storminess is noticed during La Niña years for T2 and T3 period, which is found to be in contrary to that in T1. T2 is dominated by moderate to very strong El Niño years, following La Niña years that

correspond to intense storminess. Similarly, the La Niña years during T3 period are also marked by increased storminess but with reduced counts and southeastward shift in storm track density. When seen area wise, the storm track density is found to have increased during T2 for Tasman Sea, north of NZ and eastern Pacific but reduced for northwest of NZ. Whereas, for T3, storm track density shows an increase for northwest and southeast of NZ but reduced over western Tasman Sea. Similar studies showing an increase in storm activity over eastern Pacific and north of NZ during La Niña years are discussed by Sinclair (1995).

CHAPTER 5

Regionalization of large-scale Southwest Pacific circulation by the end of 21st century

As mentioned in chapter 1, numerical models can only resolve those features that are equivalent to their horizontal grid scale, which are usually of the order of about 100 km or so for global models (Rummukainen 2010). Studies aiming at future projection on storminess in regional scale, hence require finer resolution regional models that are capable to resolve the local features more accurately than just the signatures of the same features seen in global models, like IPSL_CM5A_LR. This chapter uses the SWP14 model output to determine the likely changes in future storminess, presenting the third objective of the study.

The analysis in this chapter refers to the research objective 3 mentioned in section 1.3 of chapter 1. A seasonal comparison of various large scale environmental variables for future and historical experiments are presented along with their respective differences to sense the likely change in future. The SWP14 model resolves global model features at about 25 km mean grid scale across the middle latitudes of SWP region. It is noteworthy that in addition to the limitations related to horizontal grid scale, regional scale model projections also depend on the availability of reliable global model forcing.

5.1 Evaluation methods

Different climate variables help describe and understand a region's weather and climate. The results have been subdivided into three main columns depicting five-year mean condition for control, scenario and their differences. Additionally, since we focus on seasonal changes, therefore each variable is accompanied by four rows. This comparative illustration of simulated results will assist describe in detail each of the climate variables to help sense the worst possible scenario that might develop by the end of 21st century, if emissions continue to rise throughout 2100 (RCP8.5).

5.2 Results

In the current study, we have taken the worst possible scenario, in which the greenhouse gas emission and concentration are likely to increase significantly over time due to absence of any specific climate mitigation target, such that the resulting Radiative Forcing is expected to reach up to 8.5 Wm^{-2} (RCP8.5) by the end of 21st century. As a result, the corresponding likely rise in global mean temperature by 2.6 to 4.8°C (mean of 3.7°C) and the projected sea level by 0.45 to 0.82 (mean 0.63 m). In this section, the focus is to highlight all possible changes that might result in future based on the SWP14 output. To start with, we will look at the changes likely to occur for entire study domain with this question:

***Question**: Does the downscaled or regionalized large scale environmental variables could resolve the global signatures into regional features? What changes are likely by the end of this century?*

The question is, if the emission continues to rise throughout the 21st century (RCP8.5) without considering any climate mitigation aids, what would be the likely repercussions or influence on the large scale environment around the region! To answer this, following variables will be discussed in sequence: surface pressure, wind speed, 2 m air temperature, SST, PBLH, water vapour mixing ratio, sensible and latent heat fluxes, upward moisture flux.

5.2.1 Surface Pressure

Refer **Figure 28:** In austral summer (JJA), compared to control simulation, subtropical high pressure belt shows an intensification from 1017 mb (centred at ~32°S) to 1020 mb (centred at ~36°S) by end of 21st century (intensified by 3 mb). This belt has also shifted its mean position poleward by about 4° from its control position. Similarly, the polar low pressure belt has also intensified by about 5 mb from 995 to 990 mb. It has shifted its position poleward from ~ 54°-55°S to ~ 60°-61°S. During austral winter (DJF), the subtropical belt intensifies from 1017 to 1020 mb (i.e. intensified by 3 mb) and the polar low pressure belt intensifies from 991 to 983 mb (i.e. intensified by 6 mb). Hence, it is concluded that both the pressure belts have intensified, expanded their coverage and shifted poleward in each season. The scenario minus control difference map in summer/autumn shows a rise in surface pressure values between 40°-50°S, with dual location of pressure maxima: one at east of New Zealand (7 mb) and the second, at south of Tasmania (6-8 mb). The reduced pressure values for polar belt between 55°-65°S are reduced by 5-9 mb. The difference map in winter, shows a rise in surface pressure values between 30°-40°S by 8 mb at east of North Island of New Zealand. Further, a decrease of 6-10 mb is observed between 50°-65°S. It is noteworthy here that during summer the subtropical high are considered to be stronger contrary to their relationship to the weaker descending branch of the Hadley cell (Li et al. 2012).

historical (hcw) rcp8.5 (rcw) Δ rcw-hcw

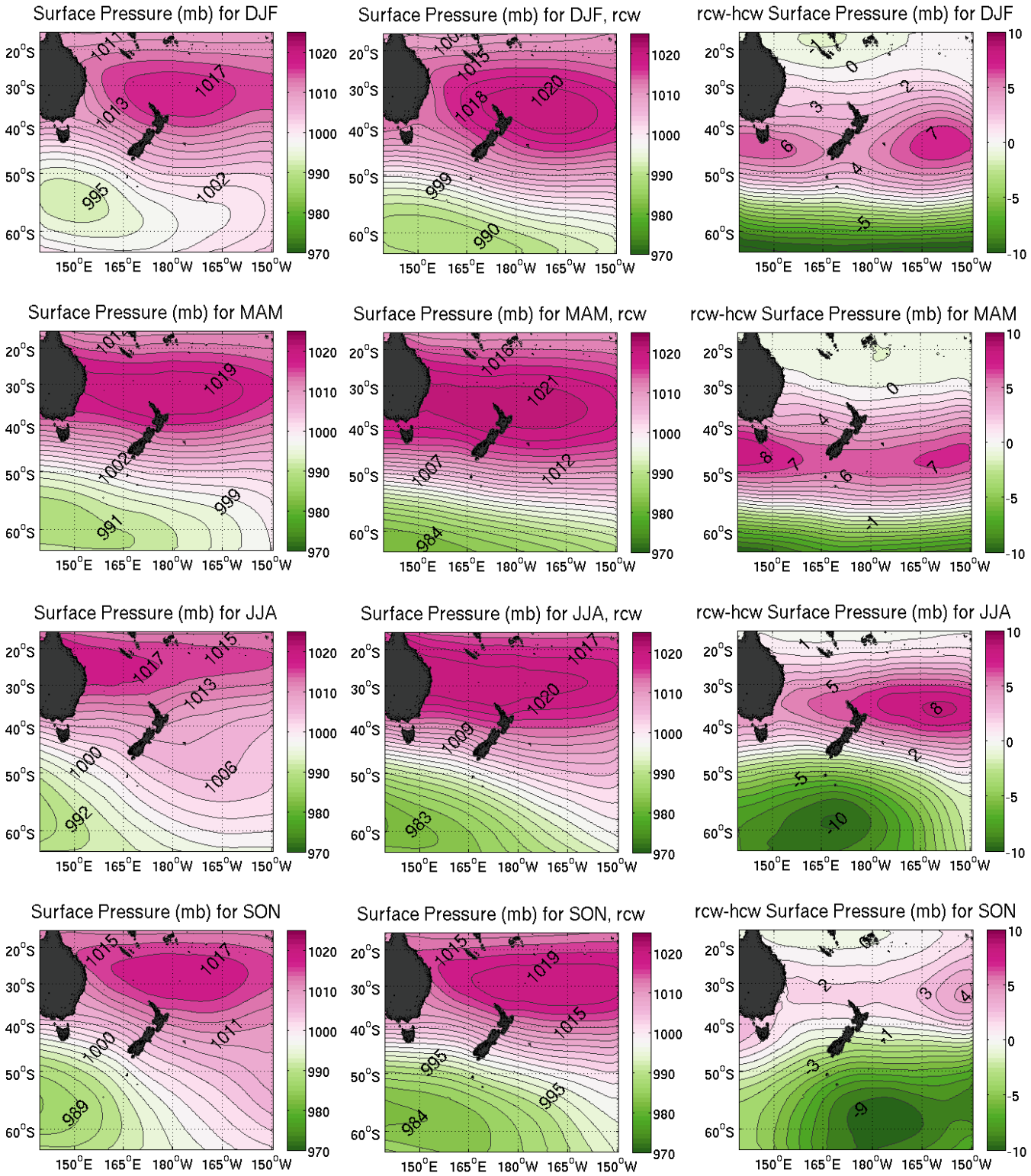

Figure 28 *Five year mean of simulated surface pressure (mb) for different seasons*

(Rows 1-4 implies austral summer (DJF), autumn (MAM), winter (JJA), spring (SON)) for control (Column I), scenario (Column II) and their differences (Column III)

5.2.2 *Wind velocity at 10 m*

historical (hcw) rcp8.5 (rcw) Δ rcw-hcw

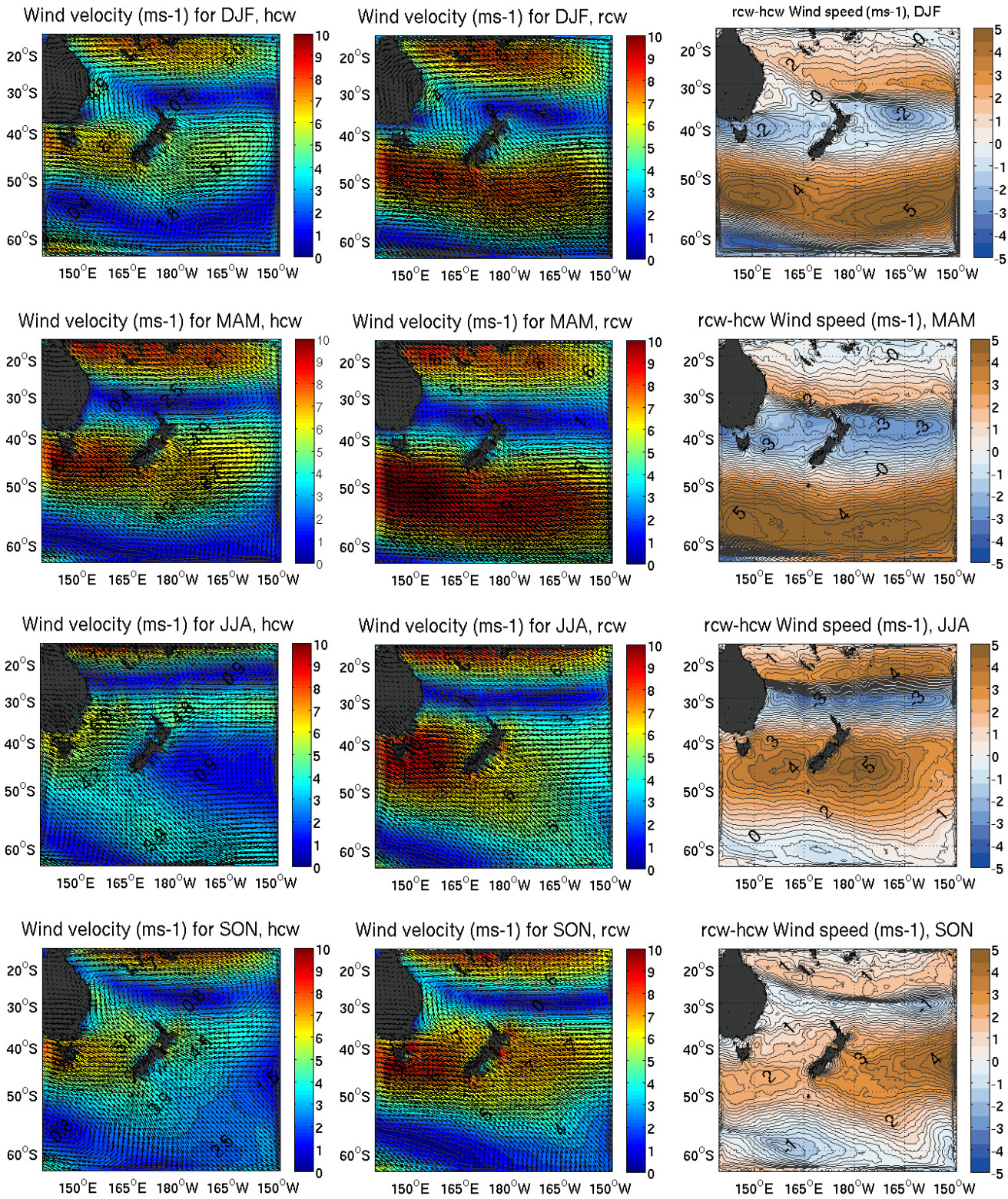

Figure 29 *Five year mean of simulated 10 m wind velocity (ms^{-1}) for different seasons*

(Rows 1-4 implies austral summer (DJF), autumn (MAM), winter (JJA), spring (SON)) for control (Column I), scenario (Column II) and their differences (Column III)

Refer **Figure 29**: In austral summer (DJF), the intensity of trade winds in subtropics (15°-25°S) has intensified by 1-3 ms^{-1}. To closely observe the change in wind, let us divide the study area equally into four quadrants.

At Northeast quadrant where it is ocean, it is noted that the magnitude of trade winds at subtropics has intensified maximum by 1-3 ms^{-1}. It extends between 27°-32°S, 170°-150°W. In contrast to that, a comparatively much little rise in wind is observed at Northwest quadrant of the study area. Coming southward to the middle latitude zone, that is known for presence of calmer winds and if seen precisely is the belt where the winds change their direction. This latitudinal belt is historically known for its calmness (horse latitudes). The difference map (**Figure 29**) shows that by end of 21st century the trade winds have intensified by 1 ms-1 and have extended themselves from 28°S (control) to 32°S. The calm zone which is usually located at ~30°-32°S have also shifted poleward to 34-36°S. In difference map, this shift can be seen as a zone of reduced (by 2 ms^{-1}) winds observed at the lower Northeast quadrant of study area.

At higher latitudes (46°-58°S), a significant rise in wind speed can be seen for reaching up to 5 ms^{-1}. The 5 ms^{-1} (westerly wind) contour shows a poleward shift from 39°S (control) to 42°S (scenario) and extends with relatively higher speed covering higher latitudes up to ~55°-58°S. When compared to control, it can be seen for latitude belts between 40°S and 58°S the calmer winds at higher latitudes are replaced by intense winds. Further poleward calm zone is again seen. Alternatively, this implies that the higher latitude calmer belt has shifted itself towards pole and even has narrowed down by end of 21st century (from 52°-58°S to 58°-60.5°S).

During austral winters, the calm belt of wind has shifted poleward (from 25°-29°S). The difference map shows the shifted location. The wind has intensified in subtropics (15°-25°S) by maximum 3 ms^{-1} (northwest quadrant), 4 ms^{-1} (northeast quadrant); in mid and higher latitudes by 4 to 5 ms^{-1} with higher winds centred along latitudinal belt of 45°-46°S. The intensified and expanded westerlies have replaced the calmer zones west of New Zealand by 3-5 ms^{-1}.

5.2.3 Temperature of air at 2 m altitude

Refer **Figure 30**: In general, summer temperature shows an increase in scenario result compared to control, by 3.5-4.8°C (for subtropics, 15°-25°S), by 4.5-6.8°C (for middle latitudes, 30°-45°S) and by 0.7-2 °C (for higher latitudes or south of 50°S).The maximum warming is visible in middle latitudes especially for latitude band between 28°S to 42°S, with highest rise noted near the south of Tasman Sea (by 6.8°C) and northeast of North Island (by 6°C). It shows that the otherwise much colder region at south of Tasman Sea will acquire a significant warming by 6.8°C by the end of 21st century. Certainly such a rise in air temperature will have serious repercussions on the coastal inhabitants, species that either dwell or feed on coastal ecosystem and many other factors.

historical (hcw) rcp8.5 (rcw) Δ rcw-hcw

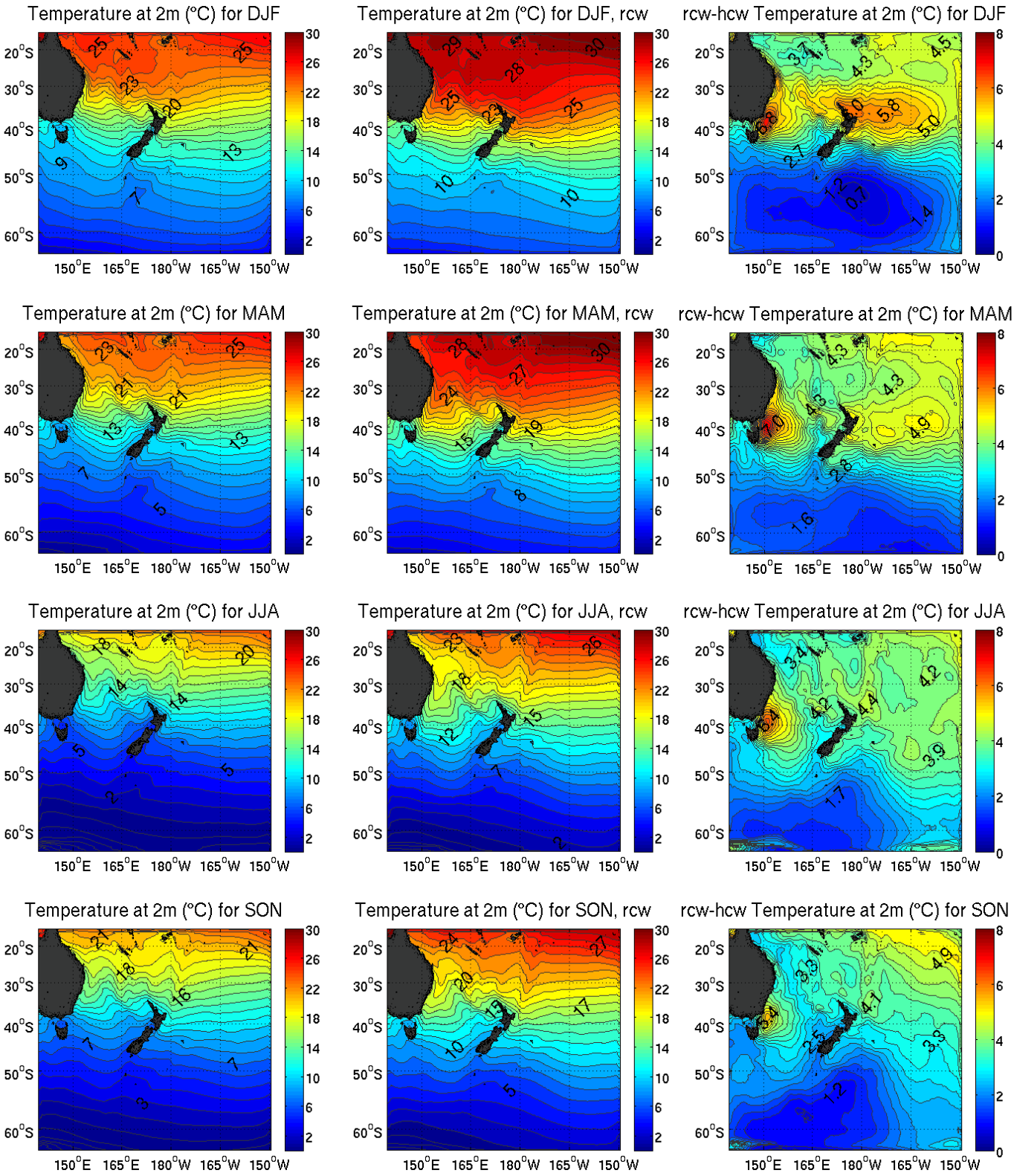

Figure 30 *Five year mean of simulated 2 m air temperature (°C) for different seasons*

(Rows 1-4 implies austral summer (DJF), autumn (MAM), winter (JJA), spring (SON)) for control (Column I), scenario (Column II) and their differences (Column III)

5.2.4 Water vapour mixing ratio at 2 m altitude

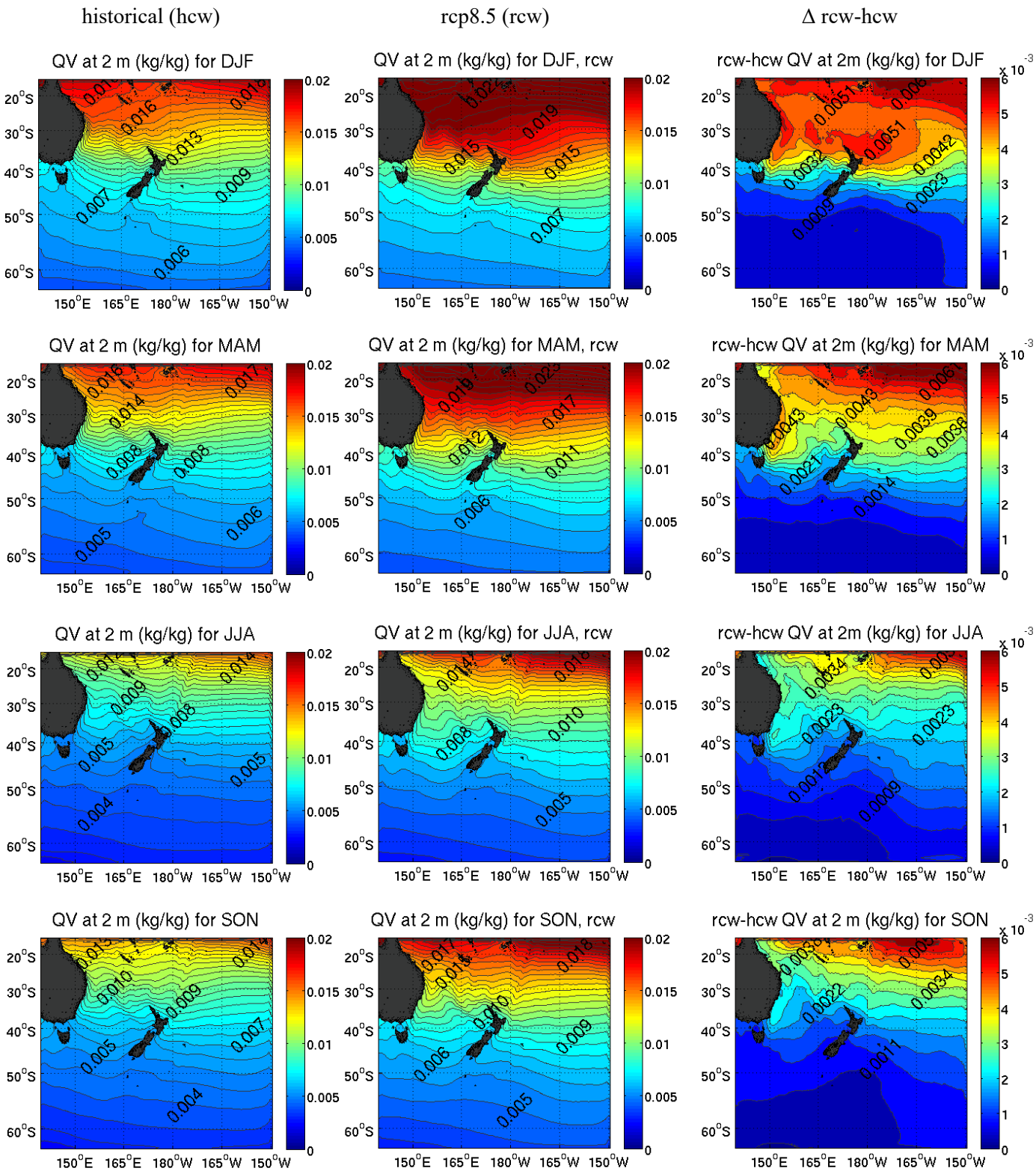

Figure 31 *Five year mean of simulated 2 m water vapour mixing ratio (kg kg^{-1}) for different seasons (Rows 1-4 implies austral summer (DJF), autumn (MAM), winter (JJA), spring (SON)) for control (Column I), scenario (Column II) and their differences (Column III)*

As expected, compared to summer, winter season shows lesser warming up of air at 2 m altitude, nevertheless, winter warming follows similar pattern of that of summer warming: minimum at higher latitudes (1.4-2.4°C); medium at lower latitudes (2.7-4.6°C) and highest at middle latitudes (3.9-6.4°C). The local maxima could also be seen at similar location, that is south of Tasman Sea.

Refer **Figure 31**: In general, this variable has increased for subtropical to midlatitude regions up to 50°S with maximum near subtropics (0.0006 kg kg^{-1}), along EAC, in Tasman Sea along EAC path, and north of North Island extending northeast (0.005 kg kg^{-1}). This increase in mixing ratio matches to that of increase in sea surface temperature pattern for scenario along the EAC. During winter (JJA), there is a general rise similar to summer, but in smaller magnitude and extends to higher latitudes (by 0.001 kg kg-1) with maximum rise at lower latitudes near 15°-20°S by (0.004 kg kg^{-1}). Along EAC, the mixing ratio rises by 0.003 kg kg^{-1}.

5.2.5 TOA outgoing longwave radiation

Refer **Figure 32**: For summer, the magnitude of OLR has increased by at least 2-4 Wm^{-2} in general, except at higher latitudes (beyond 50°S) when compared to control. The maximum increase in OLR could be seen at latitude band between 20°S and 43°S from at least 12 Wm^{-2} to a maximum of 20 Wm^{-2}. A significant value can be noted at south of Tasman Sea (at about 40°S, 150°E). The scenario OLR map clearly depicts not only an increase in the magnitude but also the enhancement of the coverage towards middle latitudes. Further this newer coverage are well depicted by the difference map.

In winter, the OLR shows an increase from 15°S up to 43°S reaching maximum near 35°S, 150°E near south of Tasman Sea (22 Wm^{-2}), along Tasman Sea (~17 Wm^{-2}), north-east of North Island (22 Wm^{-2}). At higher latitudes, the OLR shows a clear decrease by 5 Wm^{-2}.

5.2.6 Planetary boundary layer (PBL) height

Refer **Figure 33**: In summer, it mostly shows a drop in value in entire subtropical and middle latitudes with only smaller pockets of slight rise (such as at north of North Island, east-southeast of North Island, and at subtropical east of Australia). The only location that shows a maximum rise in middle latitude is around south of Tasmania. However, at higher latitudes, the PBL height beyond 50°S to 58°S shows a significant rise. The PBL height changes greatly at higher middle latitudes (beyond ~36°-54°S) in winter compared to summer. During winter, two maxima in height can be seen: one around south of Tasmania at ~37°S and other around southeast of South Island at ~44°S, both spreading out towards pole and east with flow covering larger part of higher middle latitudes. When seen in control map, the maximum height can be seen near EAC path at ~32°S, which has shifted to ~38°S in scenario. However, at higher latitudes, beyond 54°S, the height has again reduced. Apart from this maximum rise in heights, winter season also highlights a maximum drop in height along middle latitudes. The difference map clearly illustrates these depressed values (dark blue colour).

historical (hcw) rcp8.5 (rcw) Δ rcw-hcw

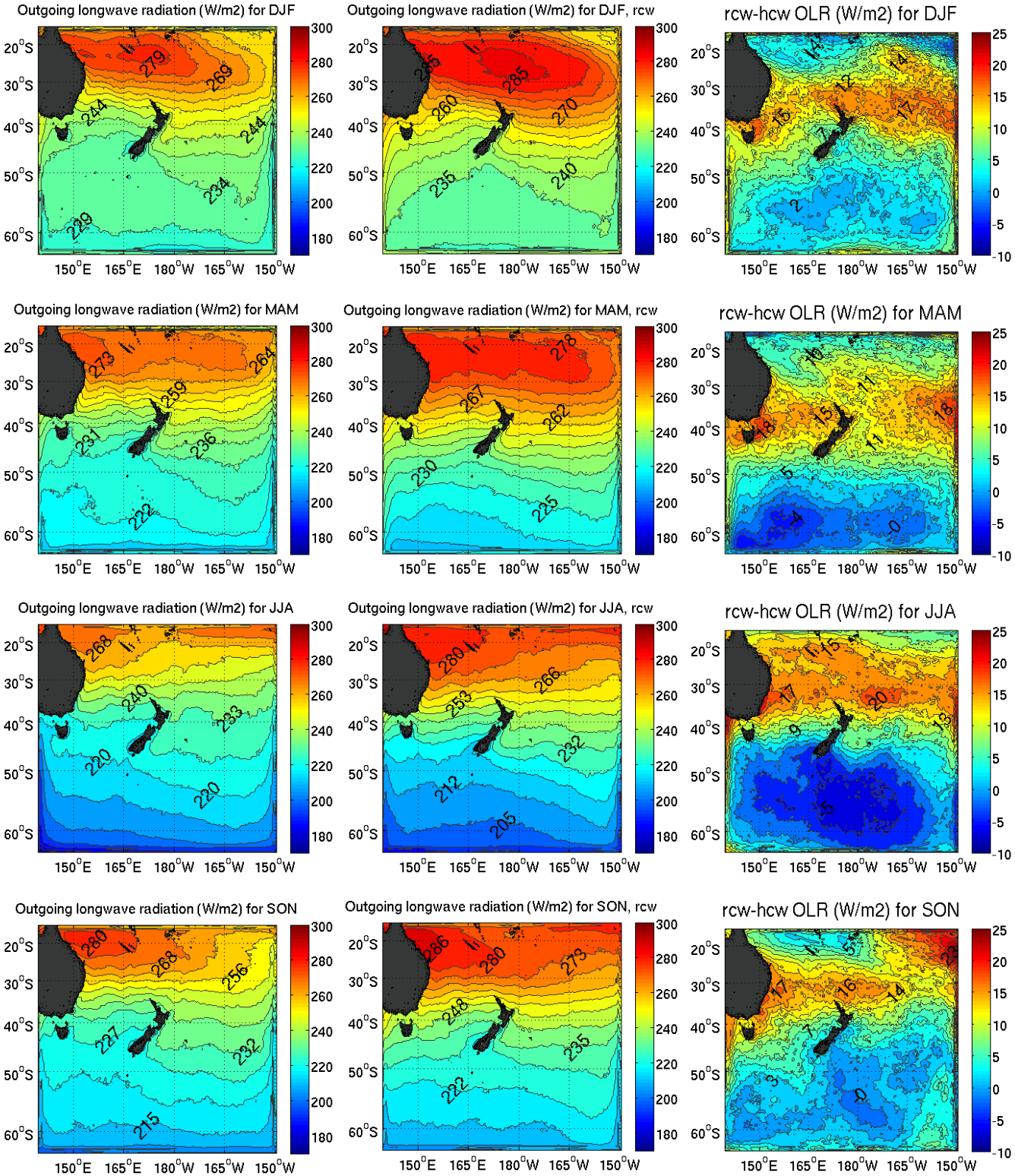

Figure 32 *Five year mean of simulated outgoing longwave radiation (Wm^{-2}) for different seasons (Rows 1-4 implies austral summer (DJF), autumn (MAM), winter (JJA), spring (SON)) for control (Column I), scenario (Column II) and their differences (Column III)*

5.2.7 Latent heat

Refer **Figure 34**: The difference map shows an increase in magnitude for both the seasons. In general, the values have increased for ~20-40°S by at least 20 Wm^{-2} in summer and showing maximum rise of 74 Wm^{-2} close to south of Tasman Sea (~ 40°S, 150°E). However, poleward of 40°S, especially close to the coasts (such as, Tasmania and South Island), the latent heat has reduced by ~12 Wm^{-2}. On open sea, the difference is positive indicating to general rise of latent heat by about 5 Wm^{-2}. Even at coastal areas, nearer to islands close to the northern boundary of the study area, the latent heat shows a reduction of ~12Wm^{-2}. However, a usual increase in 5 Wm^{-2} is normal for over whole of open sea.

In winter, especially for latitude band between 15-33°S (at west of New Zealand and or south of Tasman Sea), the latent heat has reduced. However, when away from coasts/island, the values are positive. Near latitude band ~38-50°S, the latent heat release has reduced by reaching maximum at south of Tasman Sea (by ~130 Wm^{-2}), southeast of South Island (15 Wm^{-2}), east of New Zealand (25 Wm^{-2}). Beyond 50°S (at higher latitudes) the latent heat is reduced. At middle latitudes the latent heat is increased along eastern side of Australia, New Zealand and over open sea. The variability of latent heat changes seems similar to that of PBLH along entire middle latitudes (30-50°S).

5.2.8 Upward heat and moisture flux at the surface

Refer **Figures 35 and 36**: During summer, a local rise in heat flux can be seen at south of Tasman Sea (~ 40°S, 150°E), reaching maximum of 17 Wm^{-2}. Other than that, a reduction in heat flux is visible at south, southeast and east of the South Island of about 7 Wm^{-2}. Looking into the scenario map, compared to control the raised value of 19.2 Wm^{-2} can be seen (~40°S, 150°E).

Similarly, around ~30°S, 150°E, it shows reduced value of 5.4 Wm^{-2}. Relatively higher values of fluxes can be seen for winter compared to summer. The values have rather reduced for middle latitudes in scenario except for south of Tasman Sea, extending southward (38-44°S, 150°E). In general, reduction in magnitude is significant from the difference maps. Similar trend can be seen for upward moisture flux (kgm-2 s-2) at the surface.

5.2.9 Sea surface temperature

Refer **Figure 37**: Alike, air temperature at 2 m, sea surface temperature shows similar rising pattern for the region. Among all the four seasons, summer and autumn sea surface temperature rise is predominant for middle latitudes (between 30-40 °S) zone, with maximum value reaching ~ 8 °C (9 °C) in summer (autumn) near south of Tasman Sea (~40°S, ~150°E), ~ 5 °C along Tasman Front, ~ 6 °C east of North Island. Apart from temperature change, it also illustrates the extension in EAC path before it meanders eastward to Tasman Sea as Tasman Front. In control result, the EAC branched off at ~31°S, whereas in scenario it travelled further south by 2-2.5°S before turning east.

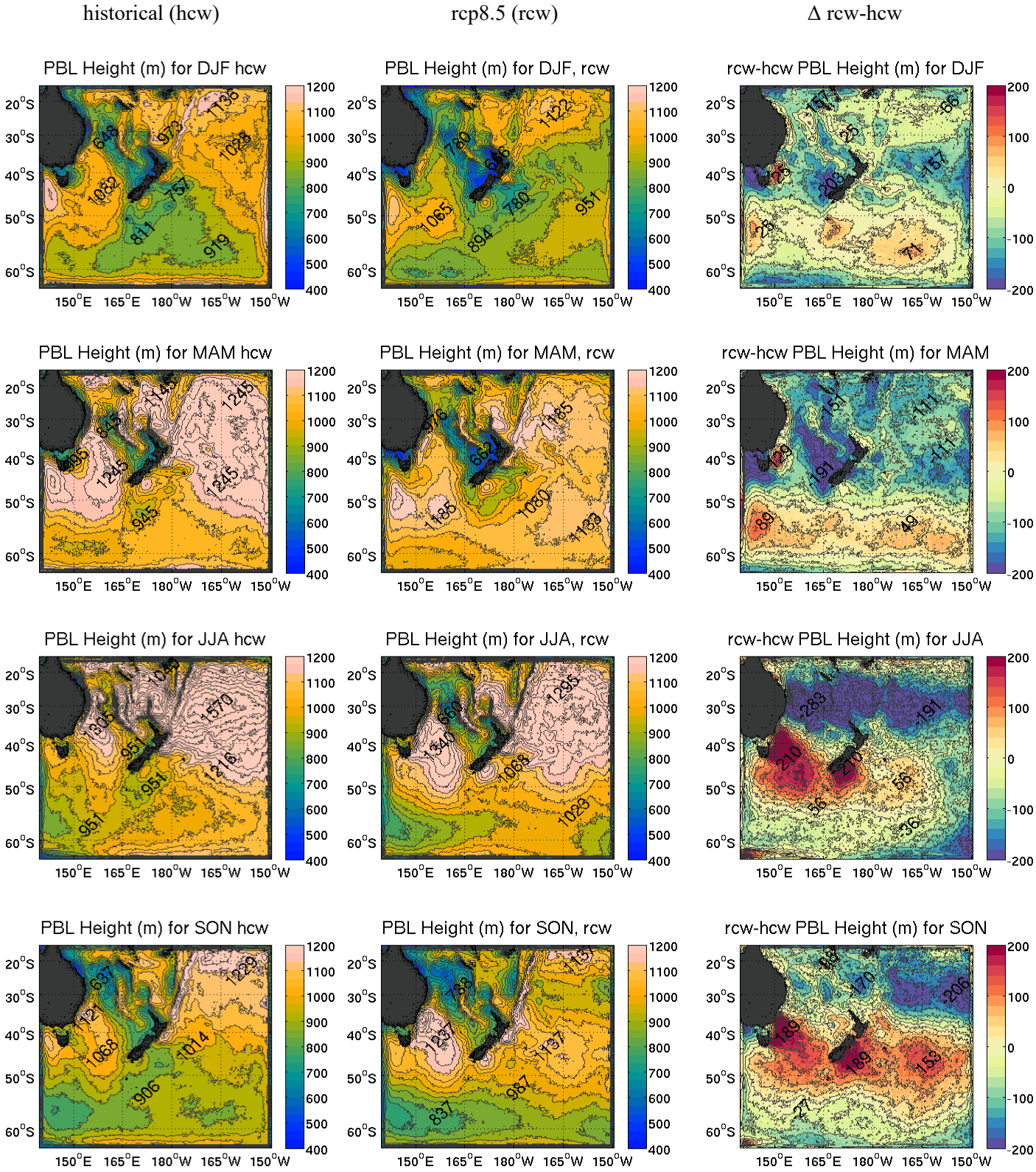

Figure 33 *Five year mean of simulated Planetary Boundary Level Height (m) for different seasons (Rows 1-4 implies austral summer (DJF), autumn (MAM), winter (JJA), spring (SON)) for control (Column I), scenario (Column II) and their differences (Column III)*

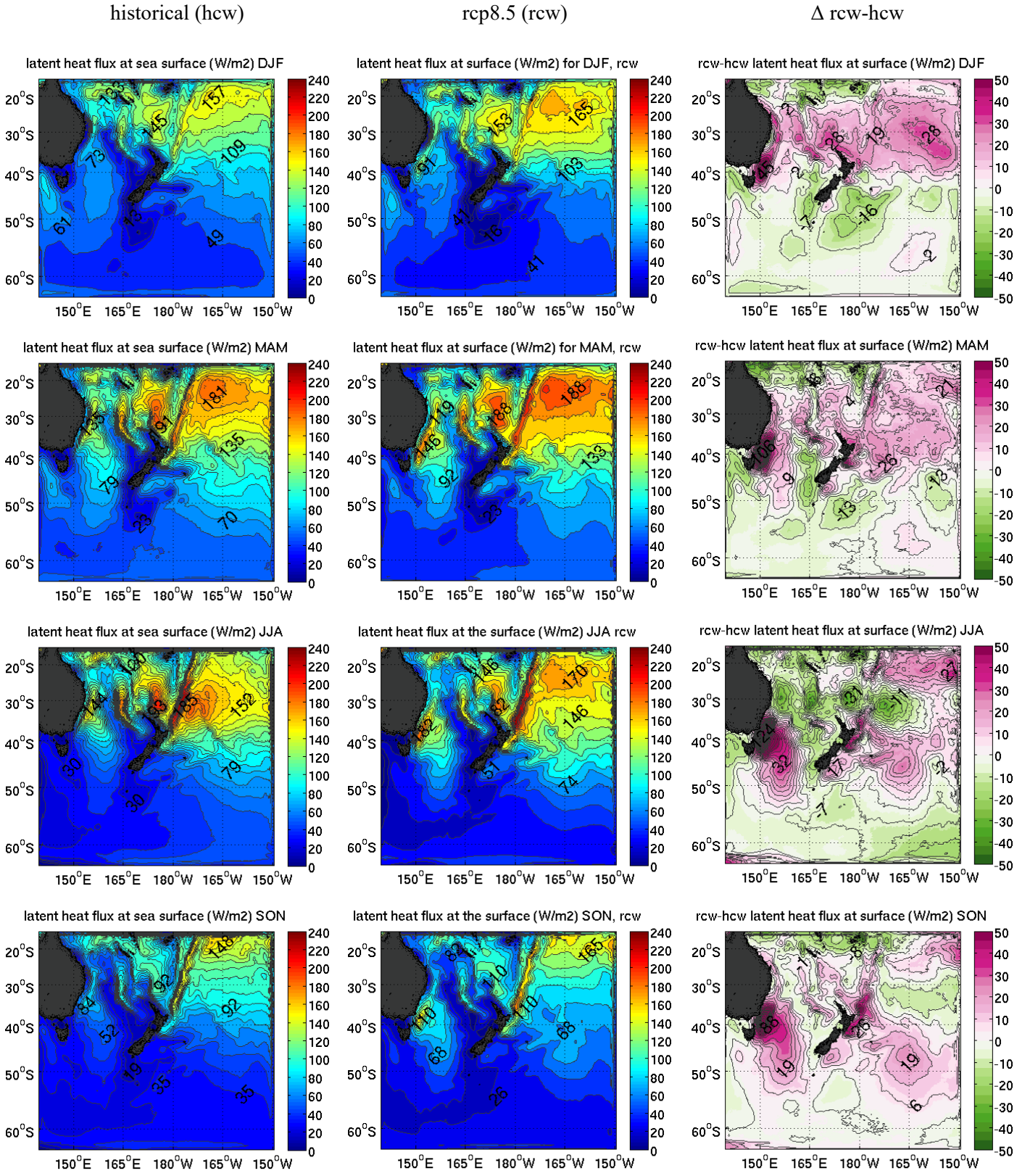

Figure 34 *Five year mean of simulated latent heat flux (W m^{-2}) for different seasons*

(Rows 1-4 implies austral summer (DJF), autumn (MAM), winter (JJA), spring (SON)) for control (Column I), scenario (Column II) and their differences (Column III)

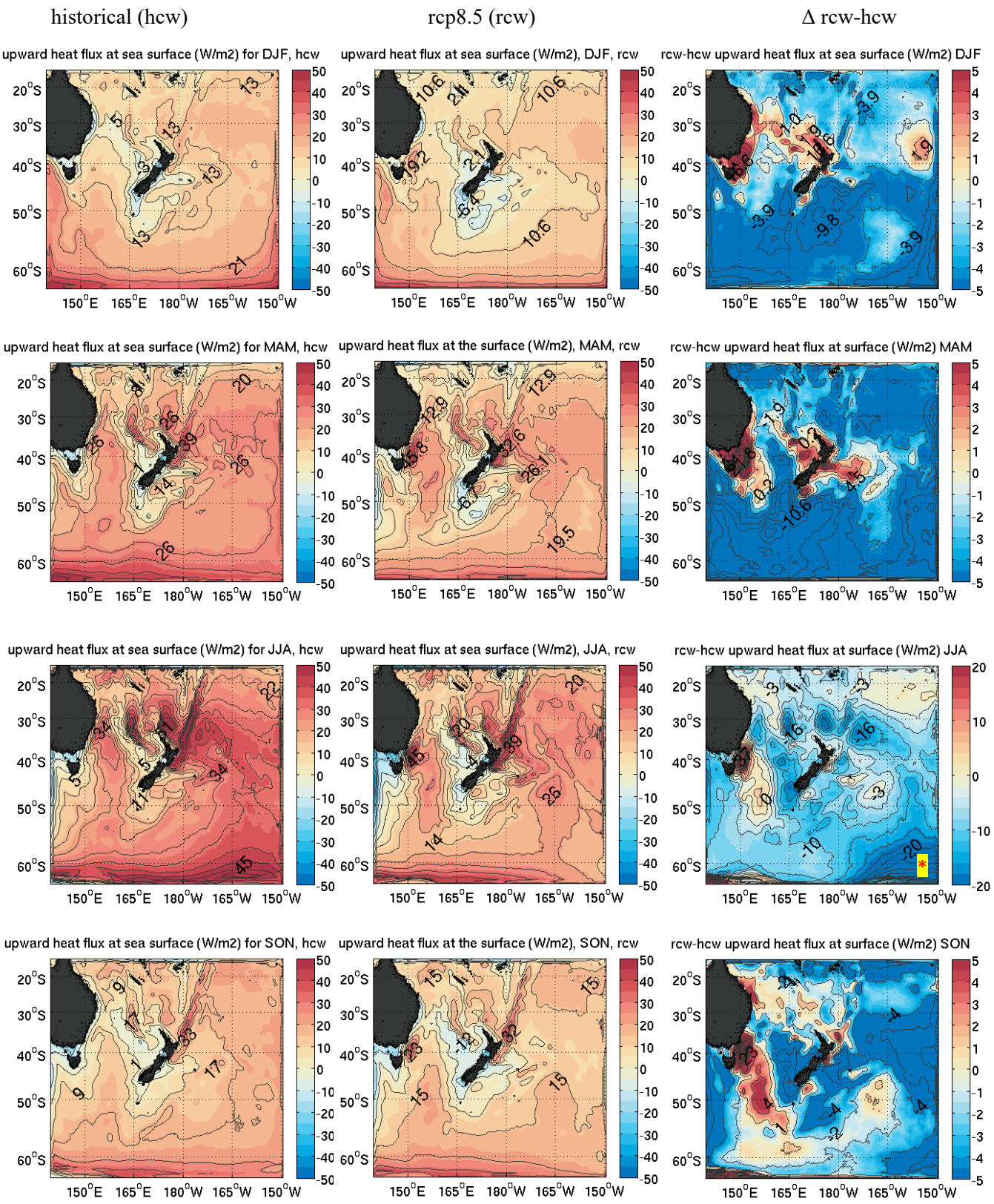

Figure 35 *Five year mean of simulated upward heat flux at the sea surface (Q m^{-2}) for different seasons*

* Note: Unlike other seasons, austral winter season (JJA) shows about four-time higher variation in change of sensible heat flux. Hence, a wider range colour axis (-20 to 20 Wm^{-2} is used instead of -5 to 5 Wm^{-2} used for other seasons) has been used to clearly depict the changing structures in detail.

historical (hcw) rcp8.5 (rcw) Δ rcw-hcw

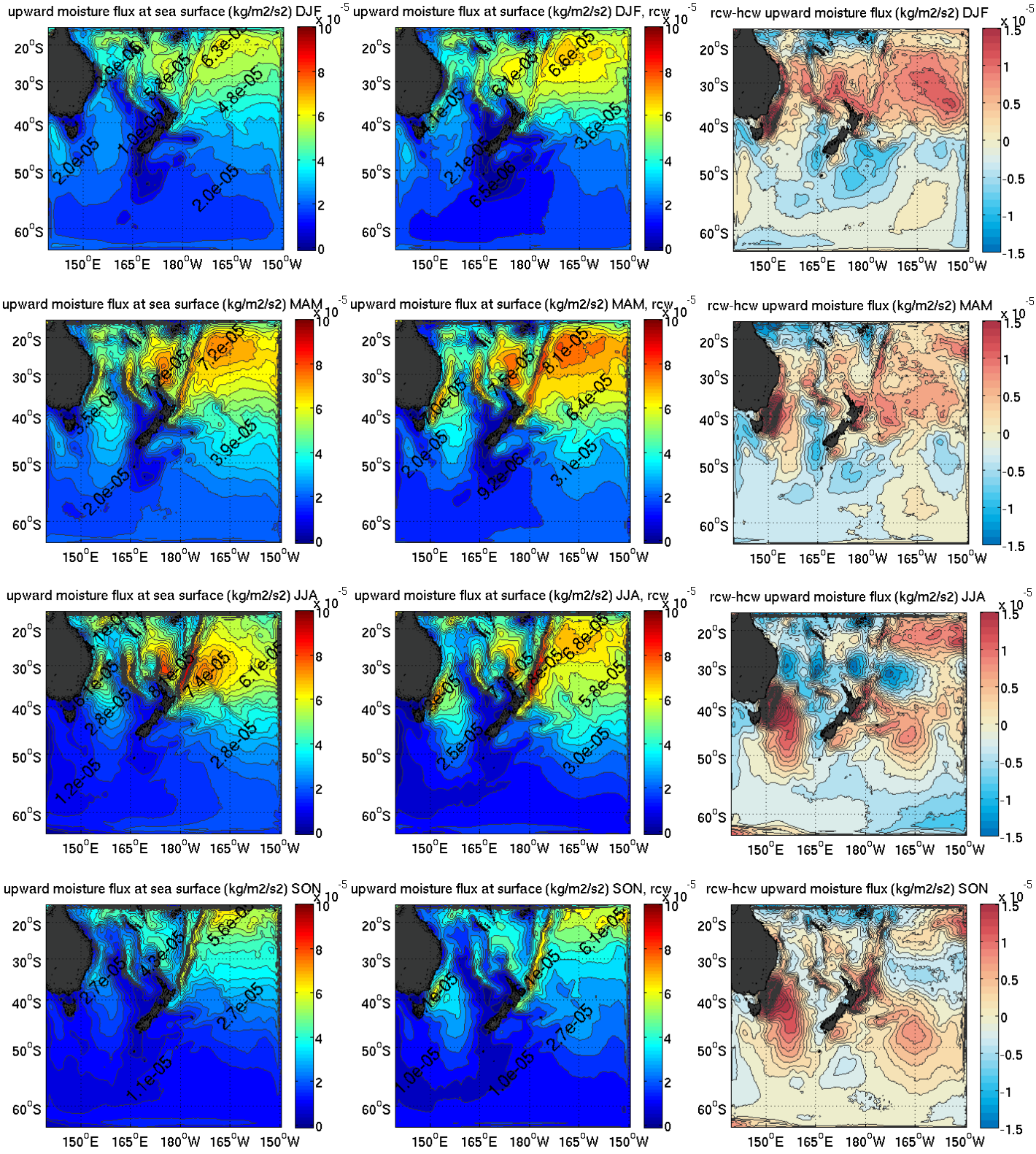

Figure 36 *Five year mean of simulated upward moisture flux at sea surface (kg $m^{-2}s^{-2}$) for different seasons*

(Rows 1-4 implies austral summer (DJF), autumn (MAM), winter (JJA), spring (SON)) for control (Column I), scenario (Column II) and their differences (Column III)

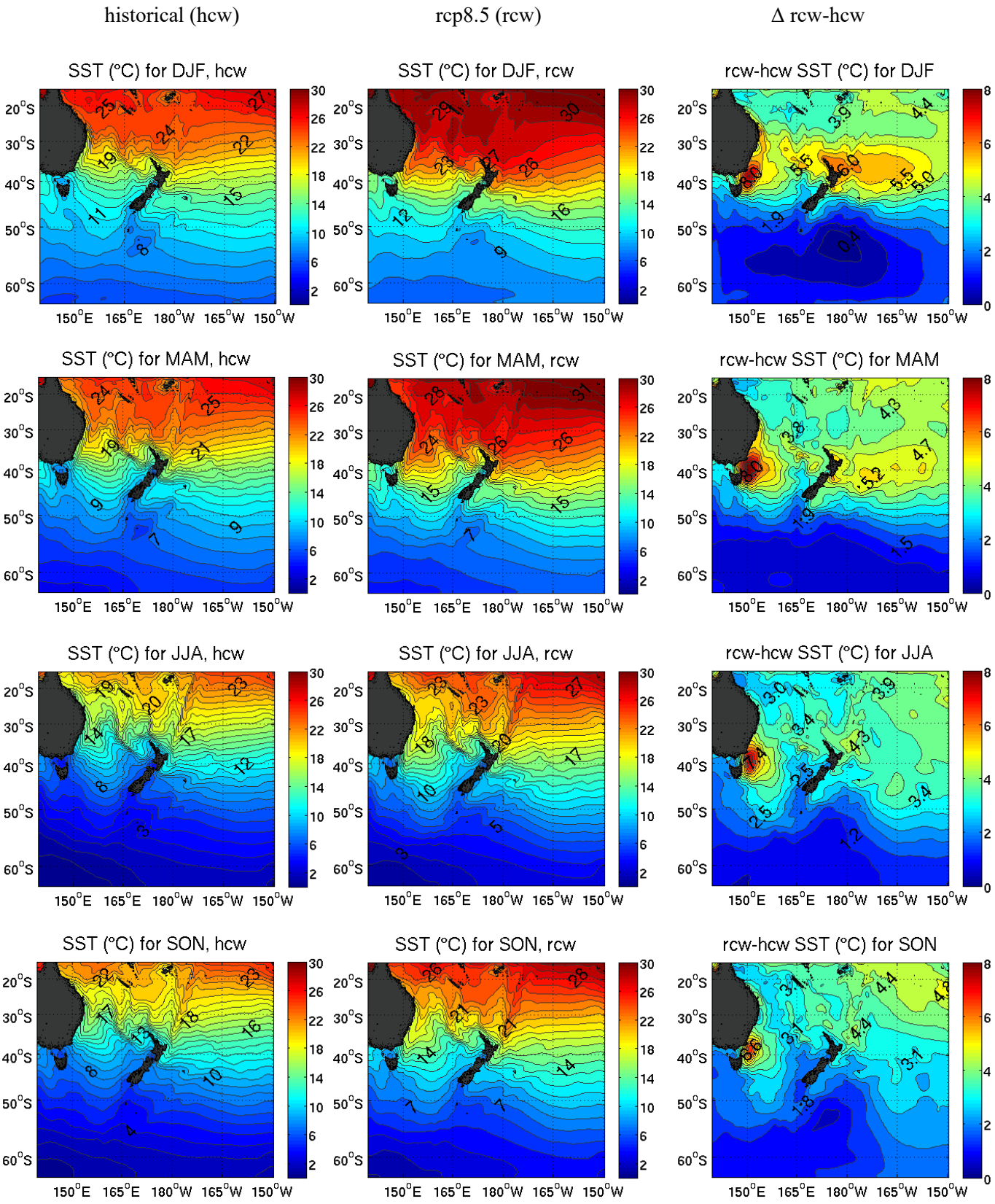

Figure 37 *Five year mean of simulated sea surface temperature (°C) for different seasons*

(Rows 1-4 implies austral summer (DJF), autumn (MAM), winter (JJA), spring (SON)) for control (Column I), scenario (Column II) and their differences (Column III)

5.3 Summary: changes in simulated large scale climate indices

In this section, we have presented the likely changes in selected large scale variables by the end of 21st century with respect to the historical conditions using a regionalization or downscaling tool, SWP14 regional model. These individual changes in environmental variables along with derived climate indices has been summarized for comparison purpose. The derived indices, gradient SST, variance ratio of SST and SAT, and SST minus SAT are computed from the simulated variables to help identify possible changes in regions' storminess.

5.3.1 Austral summer/autumn storm season

Refer **Figures 38 and 39**: First, we will focus on the change in subtropical high and subsequent change in the wind system that prevails. The subtropics show only minor rise in pressure (by 1 mb), whereas, it is the middle latitudes (25-40 °S) that illustrates an intensification (by 2-4 mb) of subtropical high with both poleward (3°) and eastward (5°) expansion of its core. Due to this expansion, the middle latitude zone between 40-50°S are likely to witness about 6-8 mb rise in the pressure around south of Tasman Sea and at open sea east of New Zealand. Coming towards pole, alike middle latitudes, the polar lows of higher latitudes (50-65 °S) are likely to be most affected. Apart from an intensification by 6 mb, they also show an eastward expansion and a poleward shifting of its core by 7-8°.

Looking into the wind velocity, tropical and subtropical (southeast) trade winds show a minor rise of less than 0.5 ms^{-1} for summer, which further weakens by autumn. The horse latitudes, known for their calmness, presently (historical scenario) around 30-32 °S, are expected to shift poleward to 34-36°S and weakened by 1-2 ms^{-1} in summer. During autumn, the winds are likely to further weaken compared to summer by 2-3 ms^{-1}, almost along entire middle latitude between 35-42 °S. This implies that the entire calmer wind belt is likely to shift poleward by 3 to 4°, synchronous to the poleward moving subtropical high. Here, note that when surface pressure is high, the winds are weaker, moving in outward direction of high pressure core i.e. around the subtropical high. This happens more specifically at middle latitudes or in proximity to the horse latitudes.

At higher latitudes, with further reduction in the surface pressure, winds moving inward towards the lowest pressure contour from all direction, shows strengthening in future. In other words, the polar lows are likely to intensify and corresponding winds are likely to strengthen. The climate belts that show a poleward shift in summer, stretch themselves to a maximum southern extent by autumn. The westerlies at ~ 46°-58°S are likely to strengthen, especially beyond 50°S (54°S) in summer (autumn) by ~ 4-5 ms^{-1}. That would result in strengthening of the higher latitude storms that occur all-year-round, or in other words they are likely to get more intense. A rise in maximum PBL height from 70 m (in summer) to 90 m (in autumn) at higher latitudes (between 50±2°S to 58±2°S) denotes a rise in turbulence that may allow higher vertical mixing, hence supports this logic of intensification of storms.

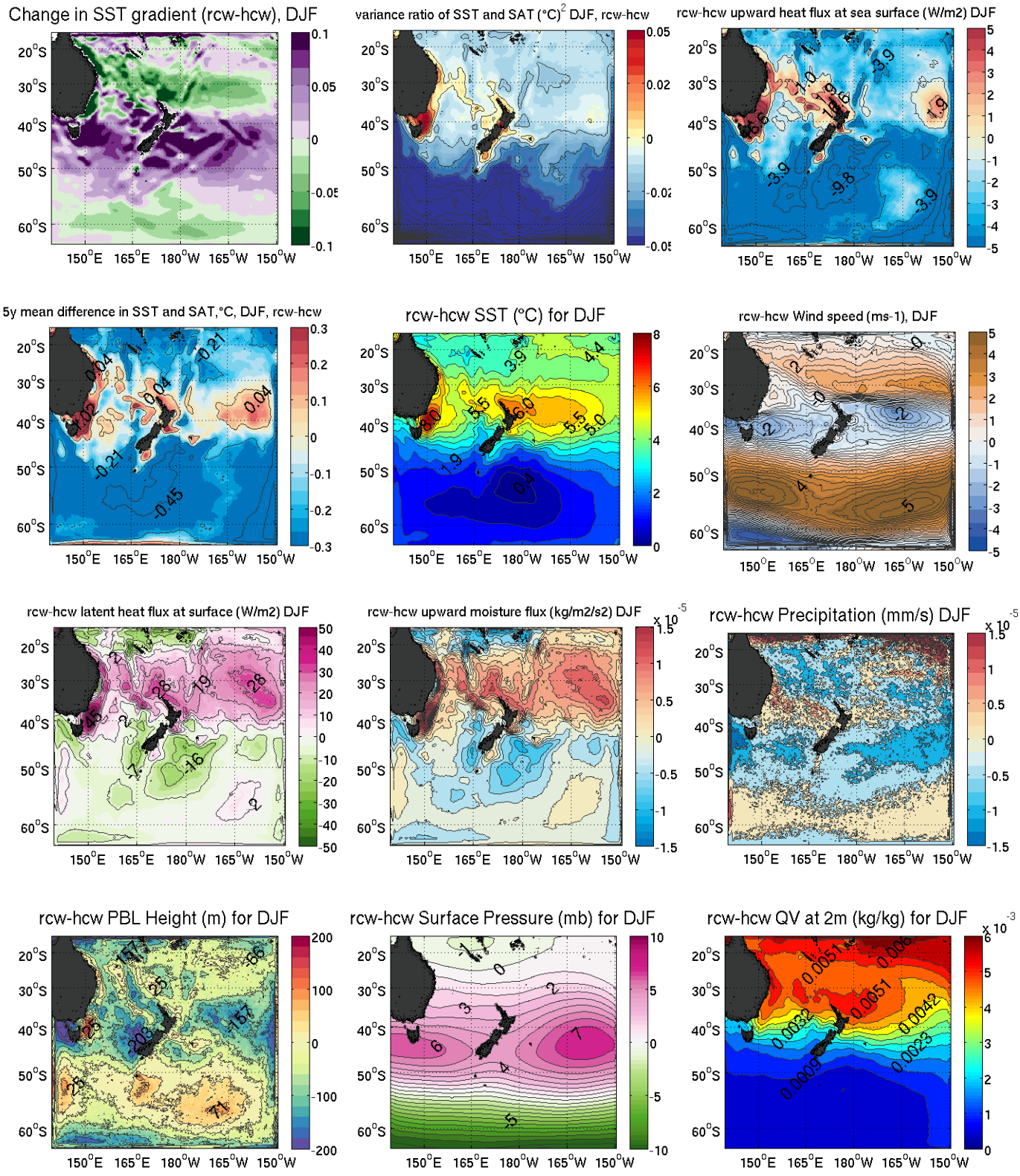

Figure 38 *Comparison of five year mean of simulated differences in different variables (summer,* ***DJF****)*

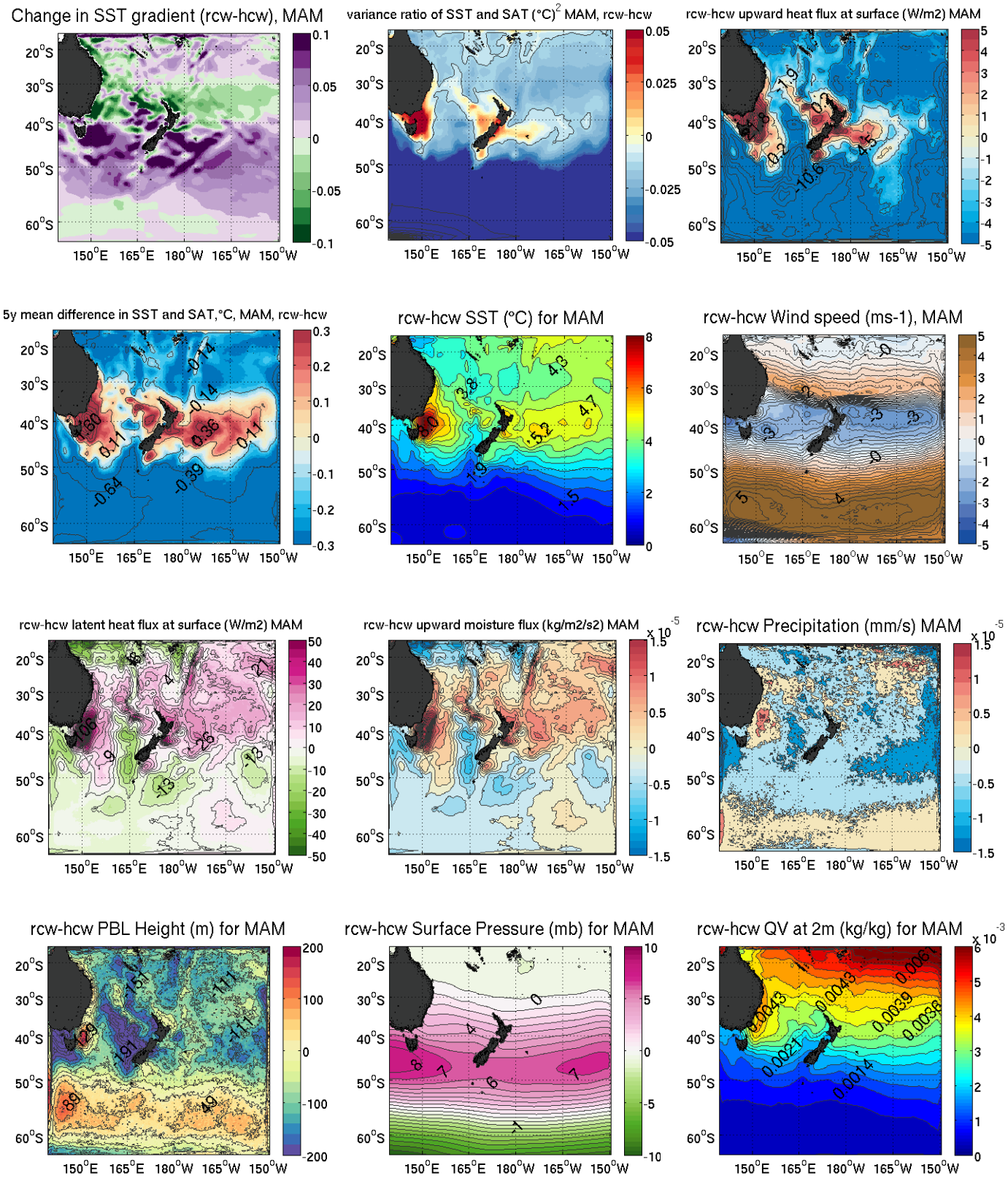

Figure 39 *Comparison of five year mean of simulated differences in different variables (autumn,* ***MAM****)*

Apart from this, an unusually raised value of PBL height that varies from 162 m in summer to 169 m in autumn is noted at south of Tasman Sea (~ 40°S, 150°E), possibly due to considerable rise in surface temperature there.

Second, we will focus on the difference between the simulated scenario and control outgoing longwave radiation (OLR). It clearly shows that there is a likely increase in OLR of about 12 to 20 Wm^{-2} as it varies from season to season. In summer, autumn and spring, this unusual pattern of rise (partially or entirely) in OLR takes place only along middle latitudes, (starting from ~ 24 ± 2°S extending up to ~ 40 ± 2°S). While in winter, it extends from ~ 18°S, covers entire subtropics up to ~ 42°S in middle latitudes. Specifically, talking about summer/autumn, this increased value of escape of radiation (10-20 W m^{-2}) from the earth surface would result into reduction in energy in the middle latitudes. An increase in ocean heat uptake especially in southern ocean is also noted by previous studies (for example, Wu et al. 2010). At the same time, due to escalated hydrological cycle, in tropics and subtropics the opposite (i.e. energy gain) is true (Wu et al. 2010). This increased imbalance observed in future climate hence would require a vigorous mechanism of transport of energy from surplus energy regions (i.e. tropics/subtropics) to deficient energy regions (i.e. the middle latitudes). On the other hand, the simulated differences show a little enhancement in upward moisture fluxes and almost nil heat fluxes in summer and autumn. Storm being one of the major energy transport mechanisms, the change in future scenario of atmospheric circulation largely indicates that it would certainly make the process of transfer more vigorous. In this case, a newly developed tropical storm would carry higher amount of stored energy from the tropics to the middle and high latitudes via intensified storm tracks. A potential exists for development and intensification of storms in future that has more energy to transfer to middle latitudes than it did during control, implying towards a possible rise in counts of intense extratropical transition of tropical storms to intrude into the higher latitudes including increased duration of summer and autumn storms.

5.3.2 Austral winter/spring storm season

Refer **Figures 40 and 41**: As seen from the climatological evidences, the higher latitude storms that form between 50°-55°S are active throughout the year, however the midlatitude storms are active only from June to August, i.e. during austral winter months. Here, we are mainly interested to study the likely changes in the formation and intensification of the wintertime storms that form and live their lives in middle latitudes. Moving from west to east of the study domain, the first set of such storms, are known as Tasman storms. They get their fuel from warmer and moister EAC somewhere over ~35°-40°S and once they move eastward over Tasman Sea they are strengthened and continue to travel eastward till they reach New Zealand. The second set of such storms, form near east-southeast of North Island, at about 30°S, 150°W. These two extratropical winter storm genesis areas and their tracks are likely to be influenced due to changes in the atmospheric circulation. The large scale variables illustrate following changes: intensification of winds by ~4-5 ms-1, along with substantial rise in PBL height by ~60-300 m and accompanied by an increase in latent heat flux by ~6-34 Wm^{-2}, in the middle latitudes between ~37°-53°S.

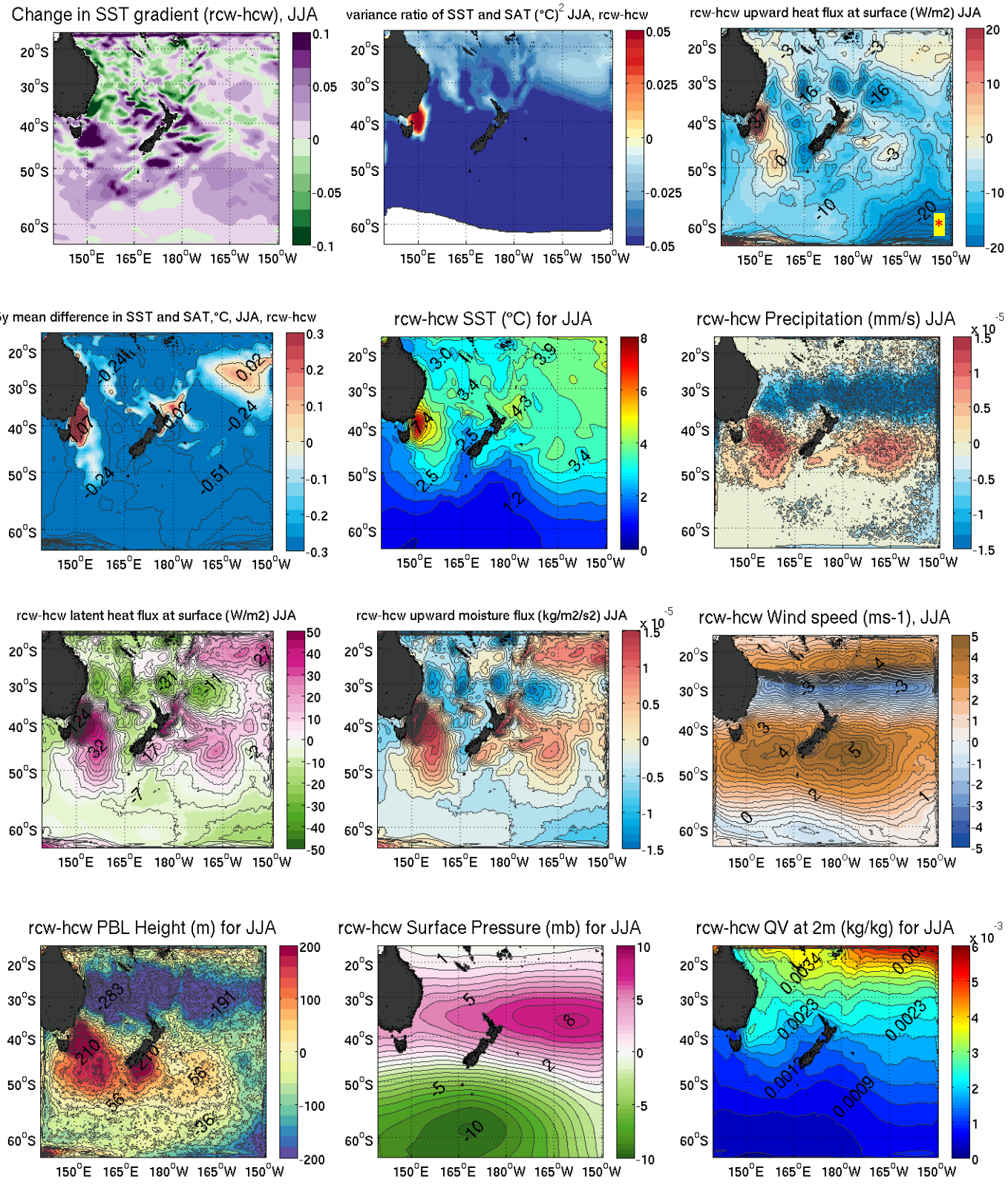

Figure 40 *Comparison of five year mean of simulated differences in different variables (winter,* ***JJA****)*

* *Unlike other seasons, austral winter season shows about four time higher variation in change of sensible heat flux. Hence, a wider range colour axis (-20 to 20 Wm^{-2} is used instead of -5 to 5 Wm^{-2} used for other seasons) has been used to clearly depict the changing structures in detail.*

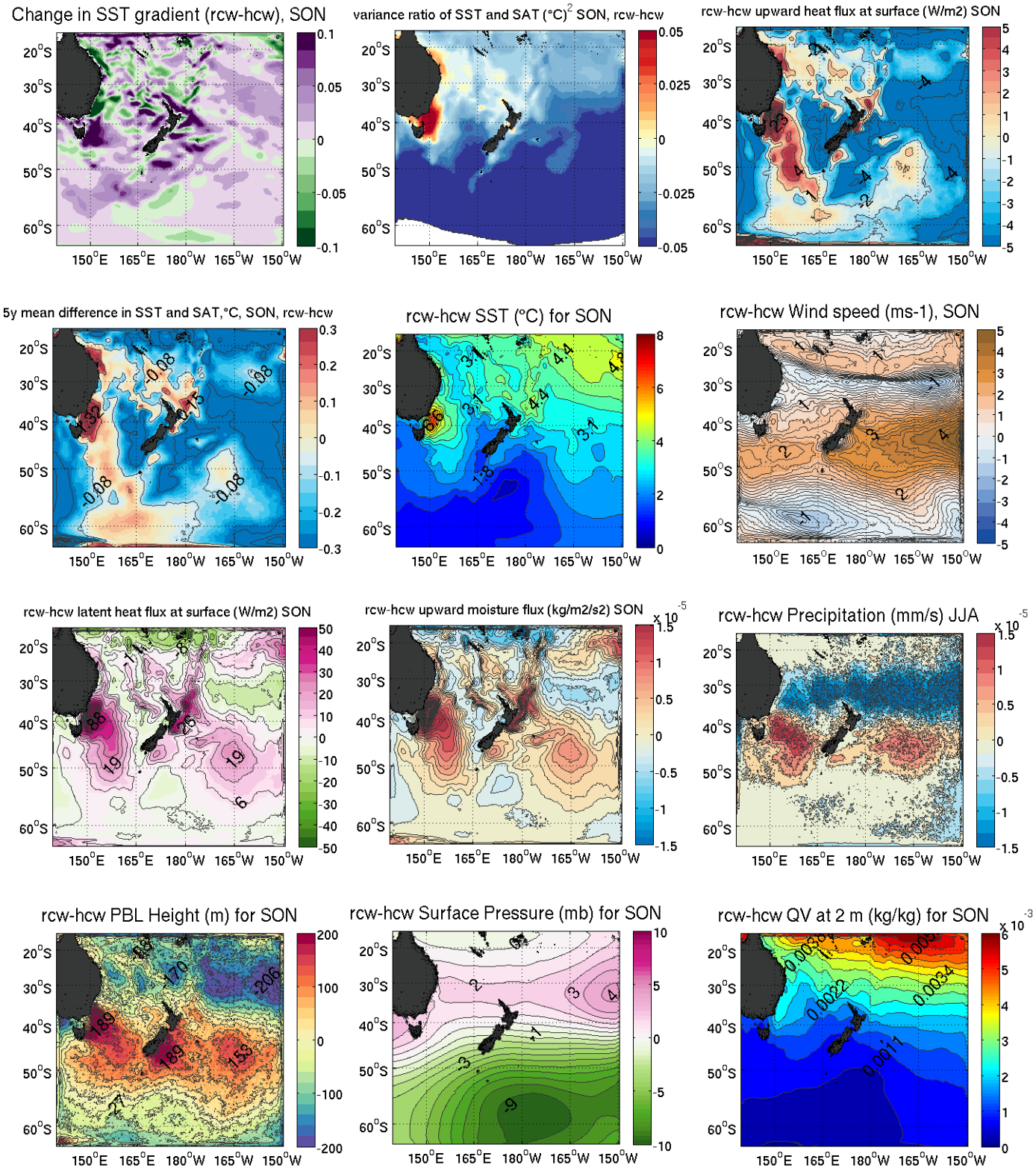

Figure 41 *Comparison of five year mean of simulated differences in different variables (spring,* ***SON****)*

Further, a sharp change in meridional SST gradients especially around the southwest of Tasman Sea hotspot ranging from ~37°-42°S, ~150°-154°E are pronounced that may stimulate more frontal storm formation.

The association and significance of PBL height in studies of climate change is vital. PBL is the bottommost turbulent layer of troposphere, which both influences and is influenced by the earth's surface. It plays a crucial role between surface-atmosphere exchange of heat, moisture, momentum, and chemical constituents like pollutants. However, the processes that control the height/depth of this critical component of climate system are difficult to understand. Mcgrath-spangler & Denning (2013) drew attention to the importance of understanding the processes that influence the height of this critical component of the climate system to understand both the short-term weather changes as well as the long-term climate changes of the region. In relation to storm formation and intensification, PBL height controls both the radial and vertical distribution of momentum and enthalpy, hence it plays a major role in energy transport processes (Zhang et al. 2011). They further highlighted the sensitivity of storm intensity to different PBL schemes used by the same numerical model. The authors related BL height definition with various parameters, like height of maximum total wind speed, inflow layer depth and mixed layer depth, where first two formed the dynamical BL heights and the third alone was referred to as thermodynamical BL height. According to Zhang et al. (2013), with greater PBL height, greater vertical mixing, lower surface pollution concentration, higher surface temperature, and lower relative humidity may be expected. They suggested that higher surface temperature and lower humidity means surface sensible heat fluxes are dominant over latent heat fluxes, tending to increase the buoyancy. Based on that, they suggested that higher surface temperature due to recent climate change may also increase the PBL height.

From the SWP14 simulated results, at middle-higher latitudes, approximately between 37° and 53°S, the maximum simulated differences in PBL height are likely to rise by ~300 m, during winter and spring. As a result, this may act in stimulating the change in behaviour of future midlatitude winter storms.

CHAPTER 6

Mapping of response of Southwest Pacific storminess to changing climate

The objective of current study is to eventually conclude on possible scenarios of likely changes in SWP storminess by the end of 21st century. The variability in large-scale environmental conditions and corresponding change in recent storminess over different period of investigation has been described in chapter 4, where two independent dataset: (a) large scale climate variables, and (b) observed storm data are discussed. These two dataset when seen independently, do not aid in deriving any relationship between a set of variables that is instrumental in the process of change in storm conditions.

In addition to this, CMIP5 GCM results from historical and future RCP8.5 scenario are downscaled to 0.25° resolution spatially and saved every six hours temporally. The five-year mean of climate variables for each scenario and their differences are described earlier in chapter 5. Nonetheless, the simulated future change in large scale climate variables alone cannot indicate any likely change in future storm conditions in the absence of derived relationship as mentioned above.

Therefore, this chapter aims to fill these two gaps of (a) establishing relationship between changing large scale climate variables and changing storminess for selected sampling locations from recent data available, and (b) application of this relationship on simulated (rcp8.5 minus historical) differences, to construct scenario of likely change in future storminess.

6.1 Data and Methods

Throughout this analysis, two different case studies are discussed: T2 minus T1 and T3 minus T1, where T1 implies the 15 years average from 1970 to 1984, T2 from 1985-1999, and T3 from 2000-2014. To

find more about the source of storm data and large scale climate variables included in current analysis, please refer to chapter 4. For the first objective, the link between change in large-scale climatic conditions and change in storminess for recent past cases is established following two different steps: (a) by computing correlation coefficients between observed change in storm data (counts, intensity, central pressure) and change in large scale climate variables, independently for two different cases; and (b) by constructing regression model equation for each of the storm indices, three different zones, and for two case-studies. It is to be noted that (a) the correlated variables did not always helped forming a strong regression model, and that (b) zone-III regression model based on T3-T1 past dataset could not be constructed due to weak correlation between the variables. Hence, in total 15 [{2-cases * 3-storm-indices * 2-zones (I and II) = 12} + {1-case * 3-storm-indices * zone-III = 3) regression model equations are successfully constructed.

The comparative analysis is not done for entire study domain, but is more focused on to the specific areas of known storm genesis or intensification areas. From previous literature (**section 1.1.3**), it is learnt that the most vigorous areas where the storm genesis or intensification generally takes place are (a) closer to the east Australian coast, (b) mid-Tasman Sea, and (c) east of New Zealand. Therefore, these three areas have been considered for analysing the changing storminess for recent past as well as for constructing possible future scenario. See **Figure 42** for pictorial representation of the three zones of analysis. These three sampling boxes are chosen such that each of them are covering three different longitudinal bands: Zone-I (covers 147-157°E), Zone II (163-173°E), Zone III (173-183°E), each covering constant meridional extent between 20 and 55°S.

At first, a search engine is made to find storm indices, namely, storm counts, intensity and central pressure (for data source see section 4.1) within the bounds of zonal extent described above for each of the three time-slices. Similarly, large scale climate variables (extracted from 20CR dataset as explained in section 4.1) differences for three cases are also computed. The list of variables include latent heat flux, specific humidity, SST (extracted from HadISST dataset), SAT, wind, precipitation rate, PBLH, along with two derived variables, namely, SST-SAT, gradient SST. Both the data are extracted for the same season including October to May months. After extracting the target zonal extent, mean over longitude is computed to get the zonal mean over the meridional extent from 20-55°S.

In the second step, the sampled differences are then averaged over longitudinal band to get target zonal mean over meridional extent from 20-55°S. This zonal mean data is normalized [0 1] and difference is computed between three different time-slices (T2 minus T1, T3 minus T2, and T3 minus T1). The differences are further normalized [-1 1] for each indices and presented in **Figure 43,** which illustrates recent change in storminess for each zones for two scenarios (or cases). Similar procedure is followed to extract change in simulated future large scale environmental variables and saved separately. Here also the differences between SWP14 output (RCW1 and HCW1) is computed first, and then normalized

[-1 1]. The meridional variation is presented to illustrate comparison between the two sets of recent (20CR) and future (simulated) large-scale environmental variables for each zones (**Figures 44 to 46**).

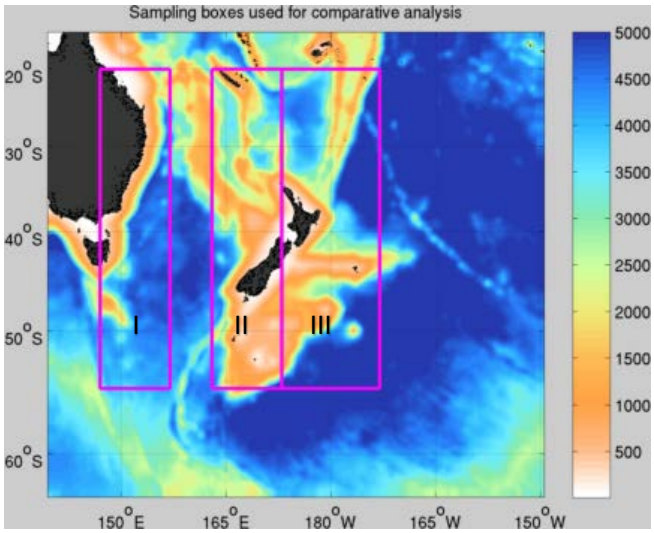

Figure 42 *Schematic of three different zones used for analysing change in storminess, where major change in bathymetry details are kept as background theme*

The third step is to select an appropriate method that can aid establish relationship between recent change in storminess and respective change in large scale climate indices. Statistical methods are considered as boon when used appropriately in transforming a set of raw dataset (either from observation or modelled output) into more eloquent and useful output. The current analysis aims to determine if there exists any statistically significant relationship between the observed change in storm indices *(Y i.e. dependent or response or outcome variable)* and corresponding large scale climate variables *(X_i i.e. independent or predictor or explanatory variables)*. Among several statistical methods of analysis, the most desirable method in establishing any such relationship would be to employ a regression analysis, which is capable to essentially model the relationship, if any. Assuming the dependent variable to be approximately normal and continuous and as there are more than one independent variable, the multiple linear regression model is opted for present analysis. The objective is to assess the influence of multiple large scale climate (or predictor) variables by using a single model that can help predict the outcome *(Y)* based on values of set of predictor variables *(Xi)*.

The multiple regression analysis is explained briefly in this section. For further interesting discussion, please refer papers by Brown (2009); Alexopoulos (2010), Hyötyniemi (2001), and other references cited therein. Brown (2009) defines the regression analysis using simple definitions: “Linear regression is one of the fundamental models in statistics used to determine the relationship between dependent and independent variables. An extension of this model, namely multiple linear regression, is used to

represent the relationship between a dependent variable and several independent variables." A simple mathematical expression of multiple regression model is given by equation (6.1), which includes *k* variables in total.

$$y_i = \beta_0 + \beta_1 x_{i1} + \beta_2 x_{i2} + \cdots + \beta_k x_{ik} + e_i, \quad where\ i = 1,2, \ldots n \qquad (6.1)$$

Note that the method used to estimate the linear regression coefficients is based on the least square criterion, where the best fitting line is achieved by computing a minimum sum of squared residuals (Brown, 2009; Alexopoulos, 2010). Brown explains that these "regression coefficients illustrate the unrelated contribution of each independent variable towards predicting the dependent variable", which is further interpreted by Alexopolous (2010). Brown (2009) further explains that "unlike the simple linear regression, there must be inferences made about the degree of interaction or correlation between each of the independent variables". By computing the *p-values* for a range of possible set of parameter values, which exceeds a specified *alpha level* (typically 0.05) i.e. 95% confidence interval, the unavoidable random errors can be accounted while estimating (Alexopoulos, 2010). While analyzing regression in Data Tool package in Microsoft Excel, note that *collinearity* between two or more independent variables should be avoided to achieve stronger regression relation.

Before applying the regression analysis, the association between each pair of large scale climate variables as well as storm indices are also explored by computing correlation coefficients. This method using Pearson' correlation coefficients *(r)* is computed for each pair of variables (X_i, Y_j), where each correlation coefficient is a measure of linear association between two variables that are normally distributed, without taking other variables in the dataset into account. Pearson's correlation coefficient is computed using Data Tool package in Microsoft Excel.

Accordingly, these normalized dataset are used to compute the coefficients for different zones and tabulated following each graph representing each zone and case study. Correlation coefficients are computed between change in storm data and change in LSEVs for two cases (T2 minus T1 and T3 minus T1). All the correlation tables (listed in **Appendix IV**) follow a particular color coding shown by **Table 19**, opted in sequence to highlight different range of coefficients. Note that the coarser 20CR data are interpolated to match finer storm data and then correlation coefficients are computed. Same interpolated data are used to perform regression analysis.

Table 19 *Color coding used to highlight specific range of correlation coefficients*

Degree of correlation	Correlation values	Colour code used
Low i.e. small correlation	± (0.000 and 0.290)	Grey text
Moderate i.e. medium correlation	± (0.300 and 0.490)	Blue filled (Red text for +ve; Blue text for –ve)
High i.e. strong correlation	± (0.500 and 0.749)	Yellow filled (Red text for +ve; Blue text for –ve)
Very strong correlation	± (0.750 and 0.999)	Pink filled (Red text for +ve; Blue text for –ve)

6.2 Results

Figures 3 and 4 illustrates respectively the geographical as well as meridional distribution of changing storminess for the past four decades. Further to this meridional distribution of past storms, **Figure 43** illustrates future change in each of the three storm indices for two different case studies: T2 minus T1 and T3 minus T1. These case-comparative graphs have been plotted based on normalized data for three samples (or zones) known to be significant areas of austral summer-autumn midlatitude storm genesis and intensification areas. Based on recent (from chapter 4) and simulated future results (chapter 5), this section describes the change in different large scale environmental variables (or climate indices), followed by its relationship with corresponding change in observed storminess.

6.2.1 Overview on changes in large-scale climate indices

A. Zone I (EAC pathway)

Figure 44 shows change in different climate indices for T2T1 and T3T1 cases and are explained below.

Δ SST: For subtropics to lower midlatitudes (~20-35°S) both the future curves (DJF and MAM) indicate towards greater warming. South of 37°S (i.e. over the midlatitudes), these future curves start to behave differently: at first DJF cools down (~37-40°S), and thereafter it shows only a slight warming, whereas MAM continues to warm up until ~47°S. The peak of future autumn curve lies between ~37 and 43°S, which was ~37-39°S for recent curves. *This implies that in future, the midlatitude warming might widen its coverage into the higher midlatitudes, at least until ~45°S, particularly during autumn.*

Δ SAT: In general, the change in future curves of near-surface air temperature follows similar warming pattern of that of sea surface, with some deviations over the subtropics. However, the deviations are worth discussion for middle to higher latitudes: where the future SAT is likely to reduce particularly for DJF and slightly for MAM - which contradicts the possible warming pattern in future SST.

Δ (SST-SAT): The sea-air difference map clearly illustrate how the future atmospheric conditions are likely to develop. During DJF, the subtropics and lower midlatitudes (~24-33°S) are likely to show

sharp rise in magnitude (i.e. positive change), which later (south of ~33.S) is followed by negative changes – this clearly implies possibility of increased vertical instability over the former area, and more stable over the latter. The positive change over subtropics during summer also remains valid for autumn, however, continuing with greater magnitude over ~27-33.5°S. Further during autumn, the index remains positive throughout a large meridional extent (~24-43.5°S). These future curves also show a major hike over the higher midlatitudes (~42-45.5°S for summer and ~39-47°S for autumn) when compared to T2T1 past curve, however, they remain lower than T3T1 curve. *This indicates a possibility of vigorous near-surface atmospheric activity during summer (over subtropics, ~24-33°S and midlatitudes, ~42-45.5°S) and during autumn (from subtropics to midlatitudes, ~24-43.5°S). Hence, a vigorous transfer of heat and moisture is highly possible from subtropics to mid and higher latitudes, perhaps through heightened storm activity.*

Δ gradient SST: The future curves are in phase with T2T1 with milder peaks south of 30°S. Over the subtropics major undulations in future curves is seen over the approximately north of split of EAC (~26.5-28°S), with a considerable hike in magnitude during summer for entire subtropics (20-32°S) and nil change in autumn. Beyond ~35°S, both the recent and future curves follow similar trend, impressive here is the sharpness or rate of the rise or fall of each curve. The autumn curve is sharper for midlatitudes over ~37-43°S, irrespective of the sign. The summer curve over midlatitudes (~38-45°S) matches to that of T2T1 recent changes, however a poleward shift is obvious for MAM for the said area earlier. *As a result, depending upon the sharp variability of these future curves, a major storm activity is likely: (a) over subtropics, north of split of EAC (~26.5-28°S) for both the seasons, with heightened activity possible during summer but unchanged during autumn, (b) over midlatitudes in summer (~38-45°S) and autumn (~37-43°S).*

Δ Specific humidity: A constant and considerable hike in future curves is likely over the subtropics and lower midlatitudes (~20-35°S) during summer-autumn seasons, followed by a gradual fall over middle to higher midlatitudes (~35-50°S) - this fact is contrary to the T2T1 recent change curve; T3T1 does not match T2T1 trend either as it also shows a greater rise from ~26°S onwards until ~45°S. *Since rise in specific humidity over subtropics and lower midlatitudes (~20-35°S) during summer-autumn matches to that of rise in SST - there is a greater possibility that the future atmospheric conditions might develop in such a way that the severe storms are supported in higher numbers. This reasoning is based on the Clausius-Clapeyron relationship, where a warmer surface will result in increased amount of atmospheric humidity that further increases atmosphere's heat trapping capacity.*

Figure 43 *Comparison of change in mean zonal storminess (or storm indices) in the recent past for cases (a) T2 (1985-99)-T1 (1970-84), T3 (2014-2000)-T1 for three different zones: Zone-I (147-157°E), Zone-II (163-173°E), and Zone-III (173-183 ° E).* [Columns → zones, Rows → storm indices]

Δ Latent heat flux: Unlike recent curves, significant changes are observed for the future curves. Over the subtropics and lower midlatitudes comparatively a gradual rise is seen for both future curves until 34°S. Thereafter *the rise steepens and a peak is seen between ~37-42°S. This sharp rise across midlatitudes also show noticeable poleward shift at least by ~5°. This increased amount of heat trapped in the atmosphere of subtropics and particularly midlatitudes (~37-42°S) is crucial, as it has the potential to quickly strengthen storms passing by as well as maintaining their longevity.*

Δ Precipitation rate: The future summer precipitation is likely to increase over the subtropics (~20.5-24°S and ~28-34°S) and over (~20-28°S) in autumn. The autumn precipitation however remains unchanged for almost entire midlatitudes (~30-40°S) although with slight deviations. Further, *polewards of 35°S (40°S), a substantial decrease in summer (autumn) precipitation is likely. This indirectly implies that over subtropics, the number of summer storms are likely to increase for ~20.5-24°S and ~28-34°S, however number of autumn storms are likely to increase over entire subtropics (~20-28°S). Compared to autumn, summer future precipitation is likely to dwindle substantially, particularly over the midlatitudes (~35-45°S). This further implies that a substantial fall in summer storm activity is likely, which is much lower than that of the autumn over the midlatitudes (~35-45°S).*

Δ PBLH: The future curves are closely following the T3T1 recent curve. Over subtropics (~21.5-33°S for summer and ~23-33°S for autumn) both the future curves show a considerable **rise** when compared to the recent changes. The magnitude of summer PBLH rise is prominent as compared to autumn over the said extent of the subtropics. For midlatitudes, along with steep rise in values, a poleward shift (~37.5-44°S) is also likely for both seasons with a higher peak likely during summer. Further to this, the peak is likely to widen its coverage from ~35-40°S to ~37.5-44°S. This implies that subtropical area (~21-33°S) and mid-latitudinal area (37.5-44°S) are likely to observe an enhancement in vertical convective mixing, which in turn plays major role in transporting energy from lower to higher latitudes, in genesis of storms as well as in their intensification. *This infers that the future summer-autumn storms are likely to observe widened meridional extent towards pole by 4° (reaching until ~44°S). As a result, there is a possibility that the storms develop around ~37.5°S (instead of 35°S earlier) and travel 4° further towards the pole until 44°S (instead of 40°S in the past). This is due to development of possible environmental conditions supporting higher storm genesis and intensification over the subtropics (~21.5-33°S) and midlatitudes (~37.5-44°S), particularly during summer.*

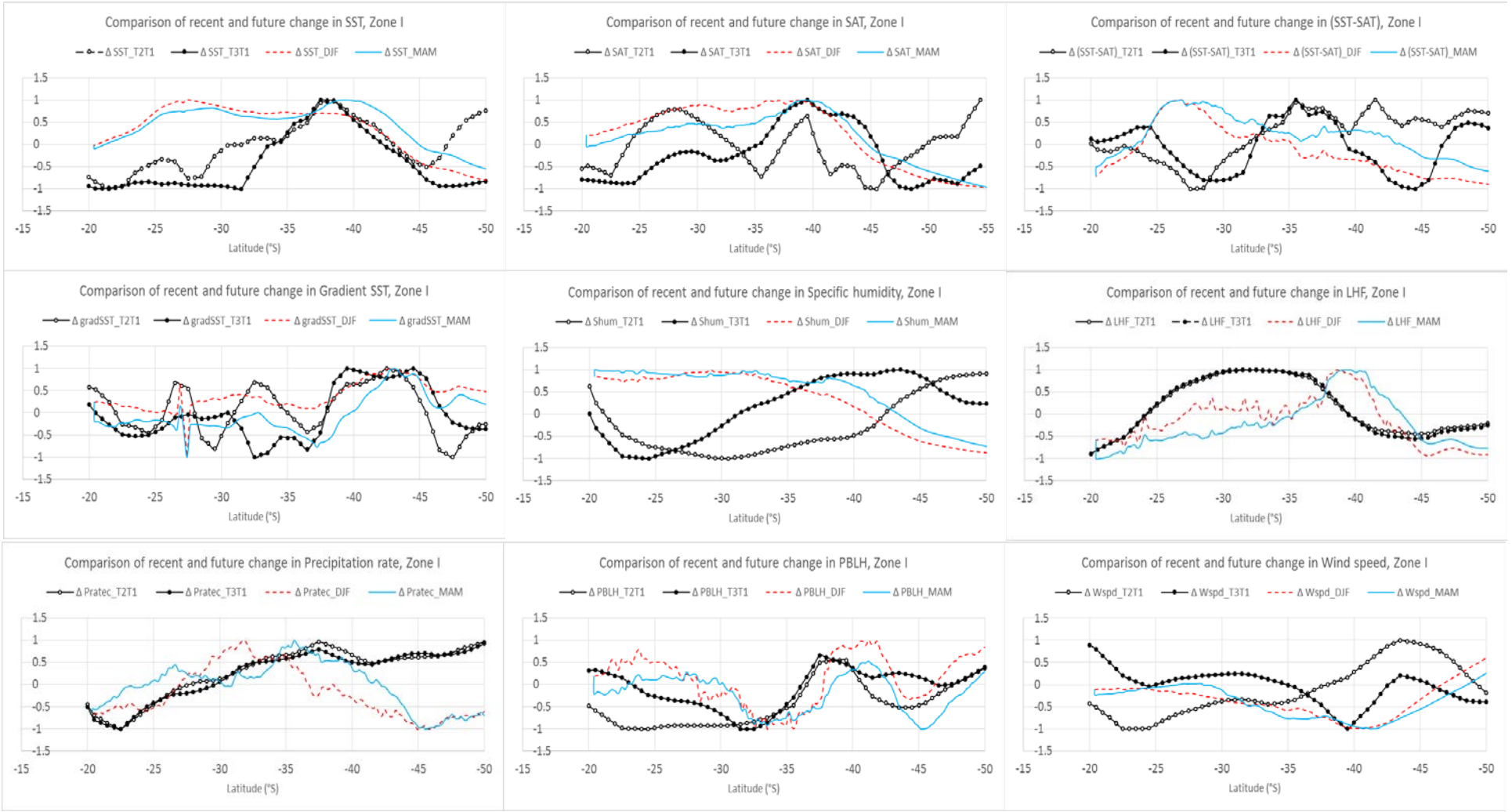

Figure 44 *Zone-I Comparison of recent and future change in large-scale climate indices: (a) gradient SST (b) SST (c) SAT (d) SST-SAT (e) Specific humidity (f) Latent heat flux (g) Precipitation rate (h) PBLH (i) Wind speed. Recent change: black dashed line, Red dotted and blue lines denote future (simulated) change in DJF and MAM, respectively.*

Δ Wind speed: The future wind curves follow similar profile of that of T3T1 recent change curve with further lowered wind values implying possibility of development of weaker wind system. *The weakest winds that was centred at around 38°S earlier (for T3T1) are likely to shift poleward at around 42°S. Further the coverage area of weakened wind is likely to widen from ~38-41°S to ~35-45°S. This implies development of a weakened wind system as well as warmer sea surface particularly around the southwest Tasman Sea hotspot and its surroundings, affecting the southeast coastline of Australia, northeast to east of Tasmania.*

B. Zone II (Tasman Sea)

Referring to **Figure 45**, change in different climate indices for zone-II for T2T1 and T3T1 cases are presented:

Δ SST: The variation in recent change T3T1 curve is more gradual than T2T1. Future curves are in general following T3T1 profile with an overall rise in SST for both the seasons. *An increase in SST is observed over subtropics (~24-40°S) with major rise observed over ~28-36°S during summer and over midlatitude ~36-47°S during autumn. This implies that greatest warming of the sea surface is likely to occur over the subtropics in summer, whereas over midlatitudes in autumn.*

Δ SAT: A considerable **rise** in future curves is observed in general over subtropics (~25-31°S) and in addition over midlatitudes (~32.5-35°S) during summer. This rise over subtropics in particular for autumn is greater than summer particularly over ~20-32°S, which is in contrary to the future SST curves. *In general, both future curves gradually reduce south of ~36°S alike T3T1 recent curve. This major fall is particularly observed during summer. Overall, summer future change remains lower to recent changes over mid and high latitudes.*

Δ (SST-SAT): Both future curves show a positive change over midlatitudes (~33.5-47.5°S) with significant rise observed particularly during autumn. This is likely to lead to enhanced atmospheric instability over midlatitudes ~32.5-47°S in autumn. On contrary, the subtropics are likely to observe a negative change between ~20-30°S. *These results imply that over subtropics ~20-30°S more calm atmospheric conditions are likely to prevail, whereas increased atmospheric activity over the midlatitudes ~32.5-47°S, resulting in vigorous storminess over midlatitudes during autumn.*

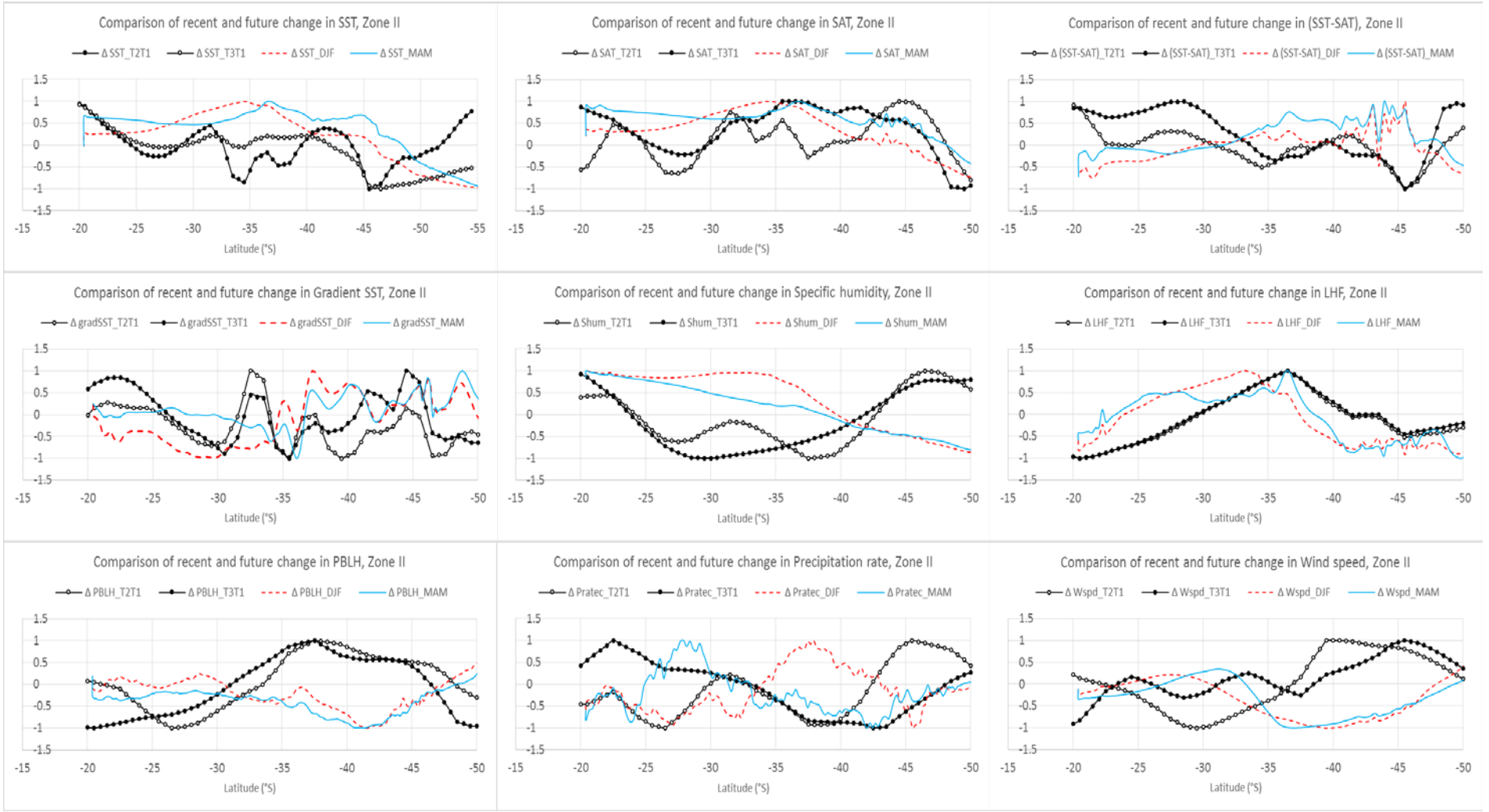

Figure 45 *Zone-II Comparison of recent and future change in large-scale climate indices: (a) gradient SST (b) SST (c) SAT (d) SST-SAT (e) Specific humidity (f) Latent heat flux (g) Precipitation rate (h) PBLH (i) Wind speed. Recent change: black dashed line, Red dotted and blue lines denote future (simulated) change in DJF and MAM, respectively.*

Δ Gradient SST: When compared to the respective recent curves: (i) Over subtropical to lower midlatitude (~20-34°S), the future summer curve is observed to show milder variation with reduced magnitude, (ii) the future autumn curve (~20-25°S) also shows lower values, (iii) whereas, the autumn curve over lower midlatitudes (~25-32°S) shows a rise in magnitude. Over midlatitudes, a greater variability for both summer and autumn curves is observed, ~34-40°S. Over subtropics not much variation is noted except in autumn (25-30). Most interesting part is the midlatitudes, polewards of 34°S, which show major variability in sharpness of future curve: (i) Peaks between 31-34°S observed in recent have shifted to ~34-36°S, (ii) a substantial rise in magnitude is observed for recent curve peaks between ~37-39°S, (iii) followed by a fall over ~42-43.5°S, (iv) Peaks between ~44-46°S observed in recent have shifted to ~46-50°S. *A greater variability in gradient SST is likely to reflect into greater variability in storm activity over midlatitudes for both the seasons. Further, the storm activity over Tasman Sea area is likely to shift poleward by 3° (from 31-34°S to 34-36°S) and by 2° (from ~44-46°S to 46-50°S). At the same time, a lower variability over subtropics, particularly during summer is expected.*

Δ Specific humidity: When future curves are seen in the light of recent changes, they show a considerable rise in atmospheric humidity from subtropics to mid-latitudes ~20-40°S, which though decreases poleward of 40°S. Further to this, major hike in magnitude especially for summer is observed over lower midlatitudes ~26-37°S. *This increase in specific humidity (~20-40°S) also overlaps with rise in SST over subtropics (~28-36°S) – such a rise in atmospheric humidity is likely to aid in the development of more intense summer storms due to availability of increased amount of trapped energy over subtropics. During autumn, similar change is likely at least over the midlatitudes ~36-40°S.*

Δ Latent Heat Flux: Both the future curves show significant rise over subtropics (~20-30°S), which further extends to ~35°S during summer and fall over midlatitudes. Apart from this, a reduction in the flux is likely for midlatitudes, poleward of ~36°S. *Therefore it is highly possible that during summer (~20-35°S) and autumn (~20-30°S), these areas are likely to support rapid growth of more intense and prolonged storms due to availability of extra latent heat energy in the atmosphere.*

Δ PBLH: A significant decrease in height over midlatitudes (~32-47°S) and an increase over subtropics (23-31°S) is observed. *As a result midlatitudes (~32-47°S) are likely to host lesser number of storms whereas subtropics (~23-31°S) are likely to host more number of storms, particularly during summer.*

Δ Rate of precipitation: The future curves show a mixed variation when compared to recent cases, yet neither of the future curves follow trends of the recent curves and show intra-seasonal differences. During autumn the rate is observed to increase substantially over subtropics (26-30°S), with no change observed for lower midlatitudes (30-34°S), and with minimum rise observed for midlatitudes (36-47°S) relative to T3T1 curve. During summer, major increase in rate is seen for midlatitudes (34-45°S) along with a reduction in rate for subtropics (20-34°S).

In addition to above changes, it is observed that compared to T2T1 curve, the meridional extent with peak precipitation rate in summer is likely to show an equatorial shift (~6°), moving from ~40-50°S (T2T1) to ~34-43°S. Similarly, the meridional extent with peak precipitation rate in autumn is likely to show a poleward shift by ~5°, from ~20-25°S to ~25-30°S. *This imply that future precipitation during summer is likely to occur more over middle latitudes (~34-43°S), whereas during autumn over lower midlatitudes (~25-30°S). This shift in precipitation belt is likely to cause more floods in the newer areas mentioned and drought in the areas erstwhile receiving normal precipitation.*

Δ Wind speed: Both the future curves show minor deviation with each other, however they show major deviations over recent curves: (a) during autumn growing wind intensity is likely to increase over midlatitudes (~26-33.5°S) and (b) during summer over subtropics (~25-31°S), (c) however both the seasons show a reduced intensity over midlatitudes, south of 35°S. *This implies that it is likely that the subtropics (25-33°S) might receive stronger winds whereas midlatitudes, south of ~34°S might witness weaker winds.*

C. Zone III (East of NZ)

Referring to **Figure 46**, change in different climate indices for zone-II for T2T1 and T3T1 cases for zone III is presented:

Δ SST: The peak change lies between ~40-43°S for both the recent and future curves, implying ongoing change in surface temperature is mainly around midlatitudes. Future curves are in phase with both the recent curves, however, they show relatively greater rise in surface temperature for both the seasons for larger meridional extent (~25-40°S). Beyond ~40°S (~43°S), the summer (autumn) future curves show a gradual decline unlike sharp fall that is seen for recent curves. Although this peak is matching for with recent curves, the meridional extent of the future peak has widened considerably both equatorward and poleward. *This implies, that during summer a warmer sea surface is likely over subtropics to midlatitudes (~25-40°S) and during autumn over midlatitudes (beyond ~39°S), implying a southward shift in warming pattern from summer to autumn.*

Δ SAT: Future curves in contrast to that of ΔSST do not show any rise in air temperature for subtropics until ~32°S. However, for midlatitudes ~32-38°S, it is likely to get warmer, particularly in summer compared to autumn, which is in contrast to the recent changes. In contrary to summer, the autumn near-surface air temperature continues to remain warm for higher midlatitudes, south of 38°S alike the recent curve T3T1. Note that poleward of 38°S, it is likely that the air temperature may gradually reduce compared to the recent past. For higher latitudes, south of ~44°S, alike ΔSST, T2T1 air temperature is markedly higher compared to T3T1 and both the simulated future curves.

Δ (SST-SAT): The future curves are showing negative change in index over subtropics (~20-30°S), implying SAT to be dominating over SST and positive change over midlatitudes (~33-44°S), implying

SST greater than SAT. *This implies, midlatitudes are likely to witness a higher instability in summer, especially south of ~37°S until ~45°S, which further extends poleward during autumn (until ~47°S).*

Δ Gradient SST: In future scenario, apart from a few minor deviations over subtropics, the major changes can be expected over midlatitudes, south of ~35°S (~37.5°S) during summer (autumn). The peak observed between 22-24°S in recent curves has widened to 20.5-27.5°S and reduced in magnitude for autumn. Similarly, the next peak in midlatitudes (~42-45°S) is also observed to expand its coverage to ~35-47°S. *Alike SST, SAT, and their differences, gradient SST in future autumn also registers a positive change at relatively higher midlatitude (~37.5°S) relative to summer (~35°S), which further expands poleward. This implies an early, heightened and wider coverage of change in midlatitude SST gradient that also is likely to strongly effect higher midlatitudinal storm activity.*

Δ Specific humidity: A significant rise is observed for both seasons over entire subtropics and midlatitudes at least until ~40-43°S. *This rise is particularly observed for summer and matches with rise in ΔSST – such a rise in atmospheric humidity is likely to aid in the development of more intense summer storms due to availability of increased amount of trapped energy over subtropics and midlatitudes, with greatest intensity likely over ~30-40°S. Similar changes are noted for autumn, with major intensity likely for subtropics (until ~35°S), which gradually declines toward midlatitudes.*

Δ Latent heat flux: The recent curves show similar profile, with minor deviations in magnitude. Future curves clearly show that both the seasons are likely to witness greater rise in flux for a larger meridional extent from ~20-43°S for summer and ~20-48°S for autumn, augmented over ~20-38°S for summer and ~34-43°S for autumn. *This extra amount of energy available in the atmosphere at subtropics and midlatitudes (~20-43°S for summer, ~20-48°S for autumn) is likely to play a major role to support rapid growth of more intense and prolonged storms with* ***heightened*** *storm activity likely to occur over subtropics to midlatitudes of ~20-38°S summer and over midlatitudes ~34-43°S during autumn.*

Δ Rate of precipitation: The future curves indicate a consistent pattern over the meridional extent from 20-44°S, with maximum rise in the rate observed during summer for midlatitudes (~34-42°S) and during autumn over midlatitudes (~31-34°S, ~42-44°S). Overall, the future rate is likely to reduce over a large meridional extent, from 27°S to 50°S. *This implies that in general rate of precipitation in future is likely to decline considerably polewards of ~25°S, however, heightened precipitation is likely to occur for small pockets of midlatitudes, ~34-42°S for summer and ~31-34°S for autumn.*

Δ PBLH: Unlike recent changes, the future curves are more consistent. They show overall reduction for midlatitudes, and only minor increase in small pocket of subtropics (~27-30°S) when compared to change in recent curve T2T1 and (~20-30°S) during summer when compared to change in recent curve T3T1. *This implies that PBLH are likely to decrease for future over midlatitudes and minor rise for subtropics (~27-30°S).*

Figure 46 *Zone-III Comparison of recent and future change in large-scale climate indices: (a) gradient SST (b) SST (c) SAT (d) SST-SAT (e) Specific humidity (f) Latent heat flux (g) Precipitation rate (h) PBLH (i) Wind speed. Recent change: black dashed line, Red dotted and blue lines denote future (simulated) change in DJF and MAM, respectively.*

Δ Wind speed: Future curves show only minor difference over midlatitudes (~32-36°S), however a substantial change is noted for future curves relative to recent changes. An increase is noted over subtropics to lower midlatitudes (~23.5-32°S), a sharp fall over lower midlatitude (~32-36°S) and significant decrease over midlatitudes, poleward of ~36°S for both the seasons. *This implies that it is likely that the subtropics to lower midlatitudes (~23.5-32°S) might receive stronger winds whereas midlatitudes, south of ~36°S might witness weaker winds.*

6.2.2 Relationship between change in observed storminess and large-scale climate variables

Large scale environmental variables are known to be the driving force behind several ongoing ocean-atmospheric processes and can be used as key indicators to distinguish dynamic changes like abrupt vertical instability in lower atmosphere, availability of greater amount of energy in the atmosphere, phase change of water, which together can influence the general circulation of the atmosphere along with the storm pattern of a locality. A comparative analysis of recent data of change in large scale variables and respective change in storm indices for three zones is described below, followed by the regression analysis equations. Accordingly, the predicted storm indices are formulated based on regression model equations (described in **section 6.1**) independently for each zone and for each storm index using 95% confidence interval (except for zone III storm counts that used 90% confidence interval). **Appendix IV** gives detail of each regression model constructed where p-values, errors, and variable-coefficients are highlighted for reference. In total 18 cases (3 zones * 3 storm indices * 2 timescales) are analysed producing two different scenarios based on two different changes noted for respective time-scales (T2-T1 and T3-T1). Based on these two change in recent past storm data each zone is constructed. *These regression analysis coefficients are not recommended for application to entire SWP region, as they are constructed specifically for smaller target zones and the resulting equations differ from each other.* The set of equations is given separately for each zone.

D. Zone I (EAC pathway)

(i) Storm and climate indices and their relation (zone-I)

Climate index	Remarks
1. Δ Storm counts	
Δ (SST-SAT)	- Inversely proportional - A sharp fall in the index value for both cases is synchronous with increase in storm counts for 24-28°S extent.
Δ Gradient SST	- Any positive or negative steep change leads to a positive change in storm counts
Δ Specific humidity	- Directly proportional - The gradually rising specific humidity curve leads to an abrupt rise in storm counts (24-31.5°S), distinctly seen for T3T1 case.
Δ Latent heat flux	- directly proportional

	- Rising profiles of LHF can be noted over 25-38°S without any change between two cases. LHF shows direct proportionality from 20-30°S, thereafter not much change in counts is noted.
Δ Rate of precipitation	- directly proportional - with rising storm numbers rate of precipitation rises (24-31.5°S)
Δ PBLH	- directly proportional - A considerable rise in index is witnessed for T3T1 compared to T2T1 for 24-28°S is synchronous to abrupt rise. A gradual fall in the index over 28-31.5°S matches to minimal deviation in counts
Δ Wind speed	- Substantial rise in t3t1 is noted compared to t2t1, which matches to the rise in storm counts as well (24-29.5°S). - A gradual increase in wind speed also matches to the gradual rise in storm counts

2. Δ Storm intensity

Δ SAT	- Is proportional to storm intensity - An overall rise in SAT is synchronous to a significant rise in storm intensity, clearly shown by T2T1 index curve over 20-34°S
Δ (SST-SAT)	- is directly proportional over subtropics ~20-26°S - index is inversely proportional over lower midlatitudes ~26.5-36°S
Δ Gradient SST	- Any positive or negative abrupt change in the index results in rise in storm intensity (20-31°S)
Δ Specific humidity	- The index is directly proportional to storm intensity over 20-28°S for T3T1 case, whereas, inversely proportional over 22.5-31°S for T2T1 case. This implies other factors are also influencing. - For both subtropics and midlatitudes. The comparison clearly show that an increased humidity can lead to an increased storm intensity (see T3T1 vs. T2T1) valid until 43°S
Δ LHF	- Is proportional to storm intensity, however, other factors must be influencing
Δ PBLH	- T3T1 index being substantially higher than T2T1, leads to an abrupt increase in storm intensity (23.5-25°S). This is followed by a gradual fall (25-30°S), which leads to more stable storm intensity. - T2T1 index show a mild rise (25-30°S), which is synchronous to the corresponding rise in T2T1 storm intensity
Δ Rate of Precipitation	- Is proportional to storm intensity for subtropics (20-31°S)
Δ Wind speed	- Is proportional to storm intensity

3. Δ Storm central pressure

Δ (SST-SAT)	- It is directly proportional to SP over 20-25°S - It is inversely proportional to SP over 25-30°S
Δ Gradient SST	- Is directly proportional to SP over ~20-28°S
Δ Specific humidity	- Direct proportionality to SP over 20-32.5°S is distinct for T3T1. Similar phenomena noted for T2T1, however slightly mild
Δ Latent heat flux	- Is directly proportional to SP for both cases
Δ PBLH	- Is directly proportional to SP over 20-25°S and inversely proportional over 25-32.5°S
Δ Wind speed	- Is directly proportional to SP for both cases over 20-32.5°S

(ii) Regression model equations (zone-I)

Zone-I	**Regression model equations for different cases ($Y_{\Delta T,\ storm\text{-}index}$)**
T2T1	$Y_{(T2T1,scount)} = 0.106+\Delta LHF.x1+\Delta Wspd.x2$
	$= 0.1063+0.1297x1+0.2261.x2$
	$Y_{(T2T1,sintensity)} = 0.251+ \Delta Shum.x1+\Delta LHF.x2+\Delta Wspd.x3$
	$= 0.251+0.1161x1+0.2691x2+0.2176x3$
	$Y_{(T2T1,scpressure)} = 0.5288+\Delta(SST-SAT).x1+\Delta LHFx2$
	$= 0.5288+0.2172x1+0.1979x2$
T3T1	$Y_{(T3T1,scount)} = 0.1517+\Delta Shum.x1$
	$= 0.1517+0.2096x1$
	$Y_{(T3T1,sintensity)} = 0.00453 +\Delta Shum.x1+\Delta SAT.x2+\Delta LHF.x3$
	$= 0.00453+0.33471x1-0.1583x2+0.1057x3$
	$Y_{(T3T1,scpressure)} = 0.3691+\Delta SST.x1+\Delta Shum.x2+ \Delta LHF.x3$
	$= 0.3691-0.31145x1+0.7339x2+0.298x3$

Figure 47 *Large scale climate variability and changing storm counts (recent past) for Zone-I*

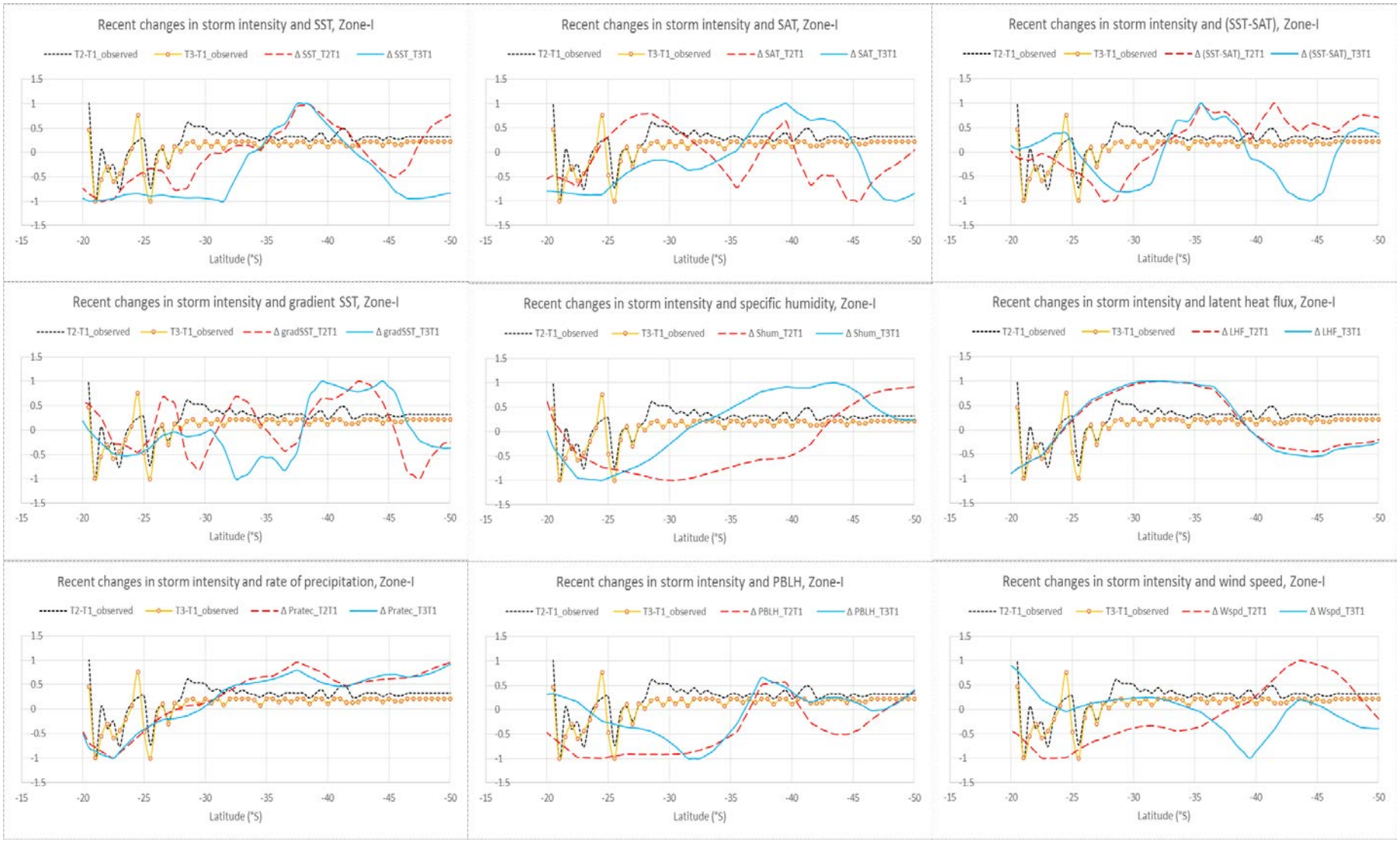

Figure 48 *Large scale climate variability and changing storm intensity (recent past) for Zone-I*

Figure 49 *Large scale climate variability and changing storm central pressure (recent past) for Zone-I*

E. Zone II (Tasman Sea)

(iii) Storm and climate indices and their relation (zone-II)

Sl. No.	Climate index	Remarks
1. Δ Storm counts		
	Δ(SST-SAT)	- Inversely proportional - Implying that a negative change leads to increase in SC and vice versa. This phenomena is consistent over subtropics to midlatitudes until ~45°S.
	Δ Gradient SST	- A steep change leads to positive change in storm counts
	Δ PBLH	- Is directly proportional to change in storm counts (noted until 43°S)
	Δ Wind speed	- Is directly proportional to change in storm counts (noted until 37°S)
2. Δ Storm intensity		
	Δ (SST-SAT)	- Is directly proportional to storm intensity until ~40°S - - For T2T1, the index difference shows a mild increase in storm intensity over subtropics and midlatitudes until 42°S. Similarly, for T3T1, the index shows a significant rise in storm intensity over subtropics and medium increase for midlatitudes until 40°S.
	Δ SST	- Is proportional to storm intensity
	Δ SAT	- Is proportional to storm intensity - The change in SAT shows significant collinearity with change in storm intensity throughout the meridional extent covering subtropics and midlatitudes at least until 42°S
	Δ Specific humidity	- Is proportional to storm intensity for both subtropics and midlatitudes. The comparison clearly show that an increased humidity can lead to an increased storm intensity (see T3T1 vs. T2T1) valid until 43°S
	Δ LHF	- Is proportional to storm intensity for midlatitudes only (30-41°S) for both cases, but inversely proportional for subtropics (20-30°S)
	Δ PBLH	- Is proportional to storm intensity for midlatitudes for both cases, with significant collinearity noted for T3T1 compared to T2T1. However, for subtropics, it is inversely proportional to storm intensity
	Δ Rate of precipitation	- Is proportional to storm intensity for subtropics (20-30°S) for both cases. However, is inversely proportional to storm intensity for midlatitudes south of 35°S onwards
	Δ Wind speed	- Is proportional to storm intensity for both subtropics and midlatitudes until 42°S
3. Δ Storm central pressure		
	Δ SST	- Is directly proportional to SP for both cases over 20-40°S
	Δ SAT	- Is directly proportional to SP for both cases over 20-42°S - Major rise of the index is marked over midlatitudes poleward of 30°S, where SP is found more stabilized - In subtropics, SAT is rising strongly, which though continues for midlatitudes, however shows a milder effect along with substantial lowering of SP. This implies that increased SAT can be related to decreased SP, hence stronger storms are witnessed, south of 30°S.
	Δ (SST-SAT)	- For T3T1, 20-23°S, more intense storms noted

	- This increased difference in index seems to be contributing towards multiple peaks over the subtropics compared to the T2T1.
Δ Specific humidity	- Is directly proportional to SP for both cases - Over 20-23°S, T3T1 is greater to T2T1 and is reflected by peak in SP T3T1 - Similarly several peaks noted over 36-43.5°S synchronizes to rise in SP - Although T2T1 is greater than T3T1 over 25-36°S, SP are nearly similar for the two cases
Δ Latent heat flux	- The change in T3T1 almost exactly same to that of T2T1 with minor rise witnessed poleward of 37°S for T3T1 index - Overall, it is found to be inversely proportional to SP over 20-42°S - 20-23.5°S: Multiple peaks are noted for SP observed in contrary to relatively lower LHF index - 25-28°S: Contrary to the overall graph, the rising index shows direct proportionality to SP for both cases - Note that substantial rise in the index is distinct only over midlatitudes between 30-42°S. Additionally, the considerably lower SPs are also noted over the same extent, reinforces the presence of intense storms over 30-42°S during both the cases.
Δ Rate of precipitation	- Is directly proportional to SP over 20-36°S - T3T1 index value is greater than T2T1, which indicates higher rain rate over subtropics (~20-32°S) relative to T2T1 irrespective of the fact that both the cases follow similar trend. - Over ~36-42°S, rain rate is inversely proportional to SP, which implies that the rain rate decreases relative to the increased SP. This particular inverse relationship is likely due to the land-sea thermal contrast, which otherwise is in contrary to the open ocean conditions
Δ PBLH	- Over 25-33°S: PBLH is directly proportional to SP - Over 20-25°S and 33-42°S: PBLH is inversely proportional to SP
Δ Wind speed	- Major rise in wind index is noted polewards of 36°S, which is in contrary to the relatively very low SP between 33.5-43.5°S, implying intense wind is accompanied with storms over midlatitudes

Figure 50 *Large scale climate variability and changing storm counts (recent past) for Zone-II*

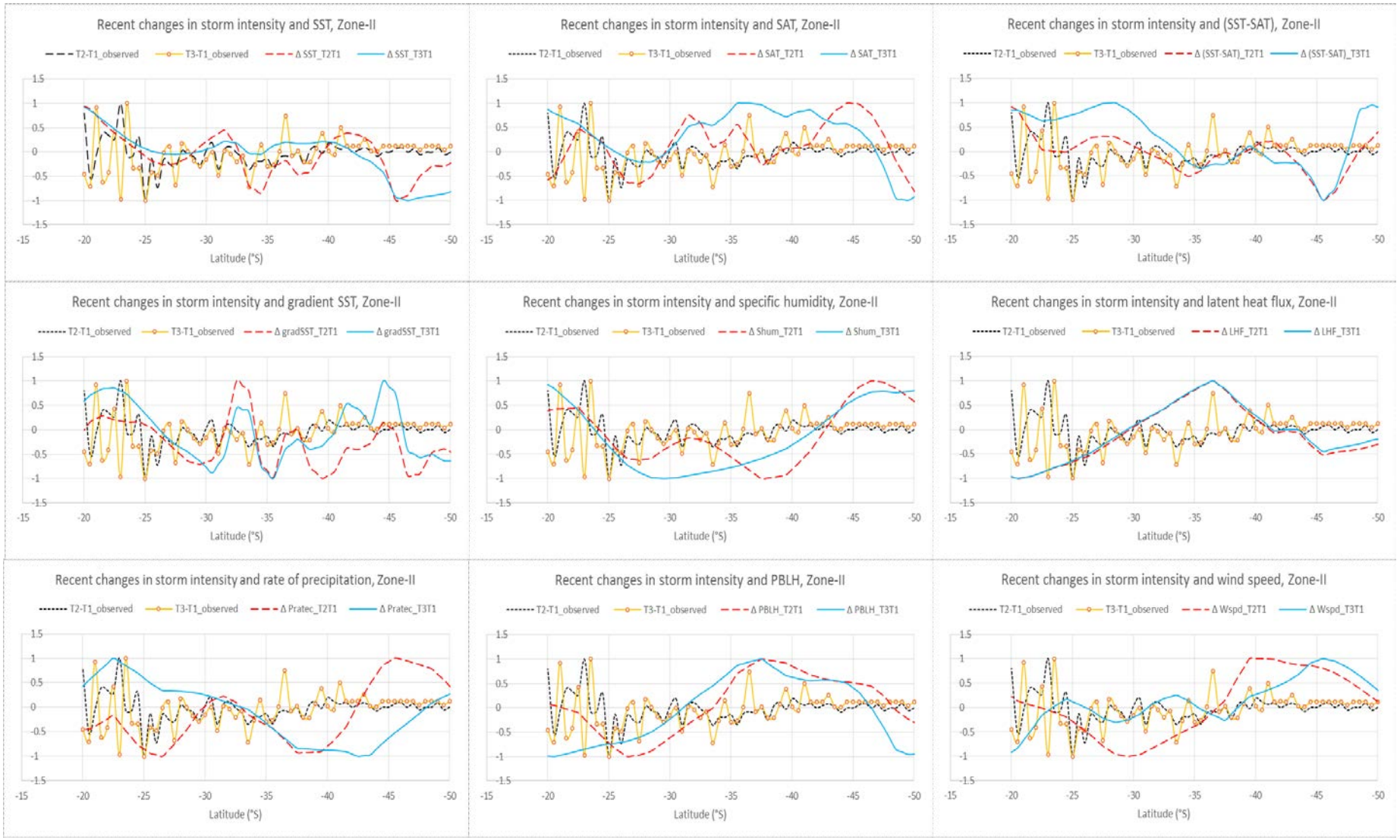

Figure 51 *Large scale climate variability and changing storm intensity (recent past) for Zone-II*

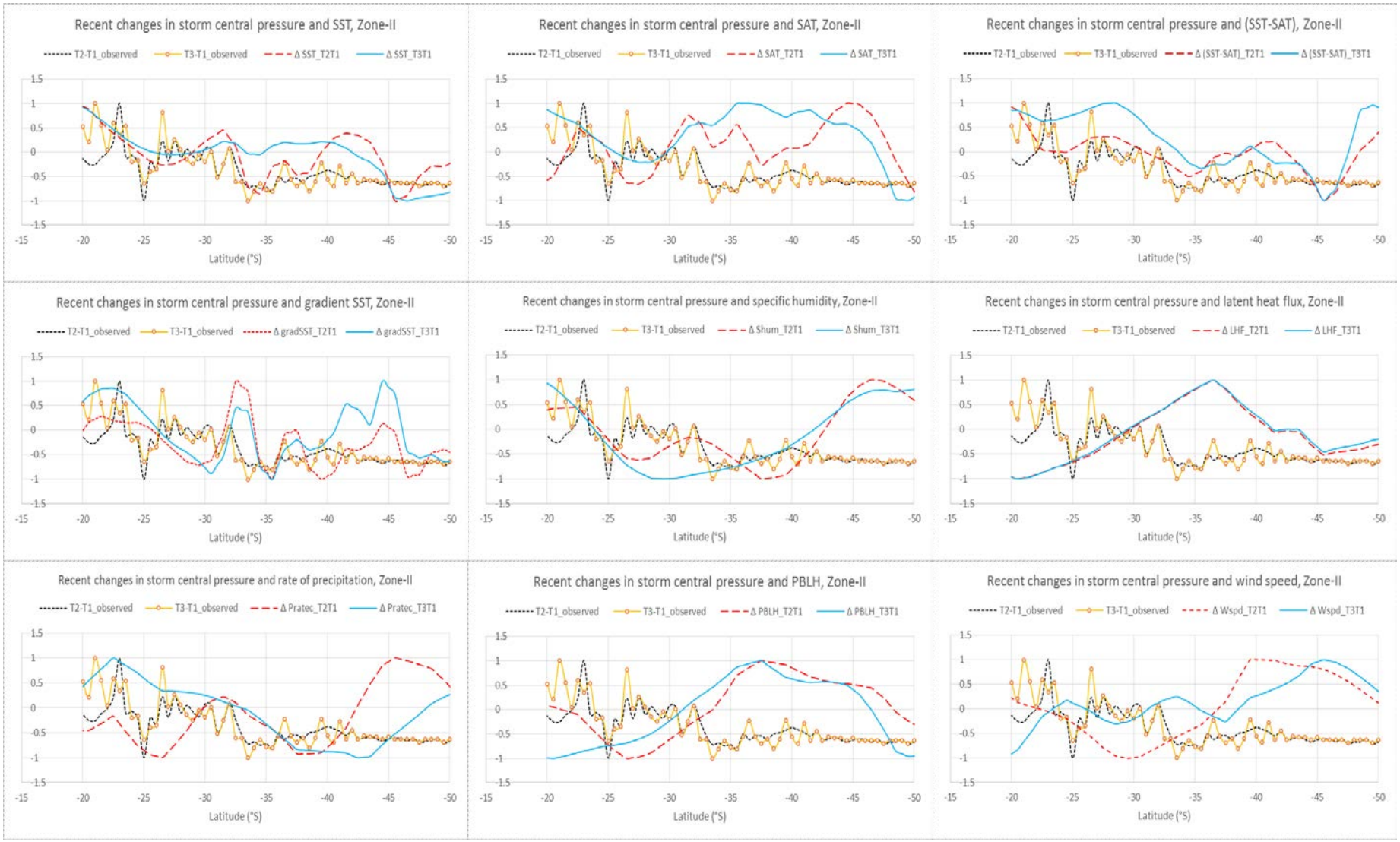

Figure 52 *Large scale climate variability and changing storm central pressure (recent past) for Zone-II*

(iv) Regression model equations (zone-II)

Case-study	Regression model equations for different cases ($Y_{\Delta T,\ storm\text{-}index}$)
T2T1	$Y_{(T2T1,scount)} = 0.06813+\Delta LHF.x1+\Delta Shum.x2+\Delta Wspd.x3+\Delta Pratec.x4$
	$= 0.06813+0.5419x1+0.8823.x2+0.303x3-0.5928.x4$
	$Y_{(T2T1,sintensity)} = -0.01766+ \Delta Shum.x1+\Delta SST.x2+\Delta PBLH.x3$
	$= -0.01766+0.1275x1+0.1859x2+0.1159x3$
	$Y_{(T2T1,scpressure)} = -0.482+\Delta LHF.x1+\Delta Shum.x2+\Delta Wspd.x3$
	$= -0.482-0.4413x1-0.3214x2-0.1591x3$
T3T1	$Y_{(T3T1,scount)} = 0.1743+\Delta LHF.x1+\Delta Shum.x3$
	$= 0.1743+0.4217x1+0.288x3$
	$Y_{(T3T1,sintensity)} = -0.0078 +\Delta Shum.x1+\Delta LHF.x2$
	$= -0.0078+0.2234x1+0.2386x2$
	$Y_{(T3T1,scpressure)} = -0.6798+\Delta LHF.x1+\Delta(SST-SAT).x2+ \Delta SAT.x3$
	$= -0.6798-0.3825x1+0.5417x2+0.4966x3$

F. Zone III (East of NZ)

(v) Storm and climate indices and their relation (zone-III)

Sl. No.	Climate index	Remarks
***1. Δ Storm counts**: an overall rise is witnessed with abruptly (gradual) over ~20-37°S (~37-41°S)*		
	Δ(SST-SAT)	- Throughout T3T1 shows greater change in the index compared to T2T1. - For T3T1, over ~23-27°S, an increased index matches to increased storm counts; south of 27°S a sharp decline matches to lower counts; both implies to a directly proportionality for subtropics. - For T2T1, over lower midlatitudes (27-32°S) the index for T2T1 are inversely proportional to counts - T2T1, over midlatitudes (32-42°S) index increases however, with comparatively lower rise in counts, - T3T1 over midlatitudes (32-42°S) index increases but counts reduces
	Δ Gradient SST	- Any steep rise or fall in the index leads to a rise in counts - T2T1 index is greater than T3T1 (except over 23-24°S), which is synchronous to considerable increase in T2T1 counts compared to that of T3T1 - Note that sharpest change in index is witnessed over midlatitudes (~38-45°S), however the counts show lesser change
	Δ Specific humidity	- It is witnessed that the index for T2T1 possibly is playing a vital role in increasing corresponding storm counts over subtropics (25-33°S)

	- However, over midlatitudes (33-36.5°S) it remains unchanged synchronous with minimal change in T2T1 counts - A heightened rise in T3T1 index is synchronous with rise in T3T1 counts over 20-32°S. Further, polewards of 32°S the index decreases along with a decline in counts - Implies that specific humidity is directly proportional to counts
Δ LHF	- In general, a rising trend of LHF is witnessed throughout the meridional extent (20-50°S) and case T2T1 shows greater than T3T1. Rising storm counts are also noted for T2T1 - index is directly proportional to counts
Δ Rate of precipitation	- 24°S polewards rate of precipitation increases for both cases - Note that T2T1 though with lower index still have more counts - Relatively higher rate of precipitation for T3T1 (24°S polewards) corresponds to lower number of counts for T3T1, whereas lower rate corresponds to higher T2T1 counts. This implies a inverse proportionality hence more intense rainfall with lower storms

2. Δ Storm intensity

Δ (SST-SAT)	- T3T1 index is greater than T2T1, however, T3T1 counts are lower than T2T1. Hence, index is inversely proportional to storm intensity throughout the extent.
Δ Gradient SST	- Although the index are in phase with each other for either cases, T2T1 shows greater changes than T3T1. Overall any steep change in the index leads to a corresponding increased intensity. Also note that maximum rise in index is noted for midlatitudes (~38-46°S), which do match with increased T3T1 intensity compared to T2T1 case - This implies that the storm intensity in midlatitudes shows a rising trend irrespective of any change in counts
Δ Specific humidity	- Rising index is supporting a rise in intensity - Even steeper rise near midlatitudes (~south of 40°S) shows increased intensity for T3T1 - Index is proportional to storm intensity for both subtropics and midlatitudes. The comparison clearly show that an increased humidity can lead to an increased storm intensity (see T3T1 vs. T2T1) valid throughout
Δ LHF	- There is an increase in the index for T2T1 compared to T3T1, synchronous with the increased T2T1 storm intensity - An increased index over midlatitudes (40-45°S) supports increasing storms relative to T2T1 over midlatitudes. - The index is proportional to the storm intensity throughout
Δ Rate of precipitation	- Intense precipitation is witnessed over subtropics-midlatitudes (~26-33°S) even with lower storm intensity

3. Δ Storm central pressure

Δ SST	- Major rise of the index is observed over midlatitudes south of ~30-35°S, wherein storm central pressure (SP) is found more stabilized. Peak is observed between ~38-43°S
Δ SAT	- Major rise of the index is observed over lower midlatitudes south of ~27°S wherein storm central pressure (SP) is found more stabilized. Peaks are observed at middle (~37-43°S for T3T1) and higher latitudes between (~44-49°S for T2T1)

Δ (SST-SAT)	- Is directly proportional to SP for subtropics and lower midlatitudes (~20-32°S). South of 32°S the sea minus air difference greatly increases until ~43°S.
Δ gradSST	- It is directly proportional to SP except for midlatitudes (~40-45°S)
Δ LHF	- There is a gradual increase in the index for midlatitudes (~30-45°S)
Δ Rate of precipitation	- This index is observed to show similar behaviour as Δ LHF but with greater magnitude
Δ PBLH	- Greater rise is observed for middle and higher latitudes, polewards of ~34°S
Δ Wind Speed	- Overall rise in the index is observed over middle and higher latitudes

(vi) Regression model equations (zone-III)

Case-study	**Regression model equations for different cases ($Y_{\Delta T,\ storm\text{-}index}$)**
T2T1	$Y_{(T2T1,scount)} = -0.0499+\Delta SAT.x1+\Delta(SST-SAT).x2+\Delta LHF.x3+\Delta Shum.x4$
	$= -0.0499-0.51166x1-0.4191.x2-0.2005x3+0.2751.x4$
	$Y_{(T2T1,sintensity)} = 0.01132+\Delta SAT.x1+\Delta PBLH.x2$
	$= 0.01132+0.263x1-0.2445x2$
	$Y_{(T2T1,scpressure)} = -0.5928+\Delta Shum.x1+\Delta LHF.x2+\Delta SST.x3$
	$= -0.5928-0.2423x1-0.2811x2-0.3808x3$
T3T1	$Y_{(T3T1,scpressure)} = -0.3845+\Delta Shum.x1+\Delta SST.x2+\Delta PBLH.x3+\Delta Pratec.x4$
	$= -0.3845-0.1826x1+0.3106x2-0.14491x3-0.3829x4$

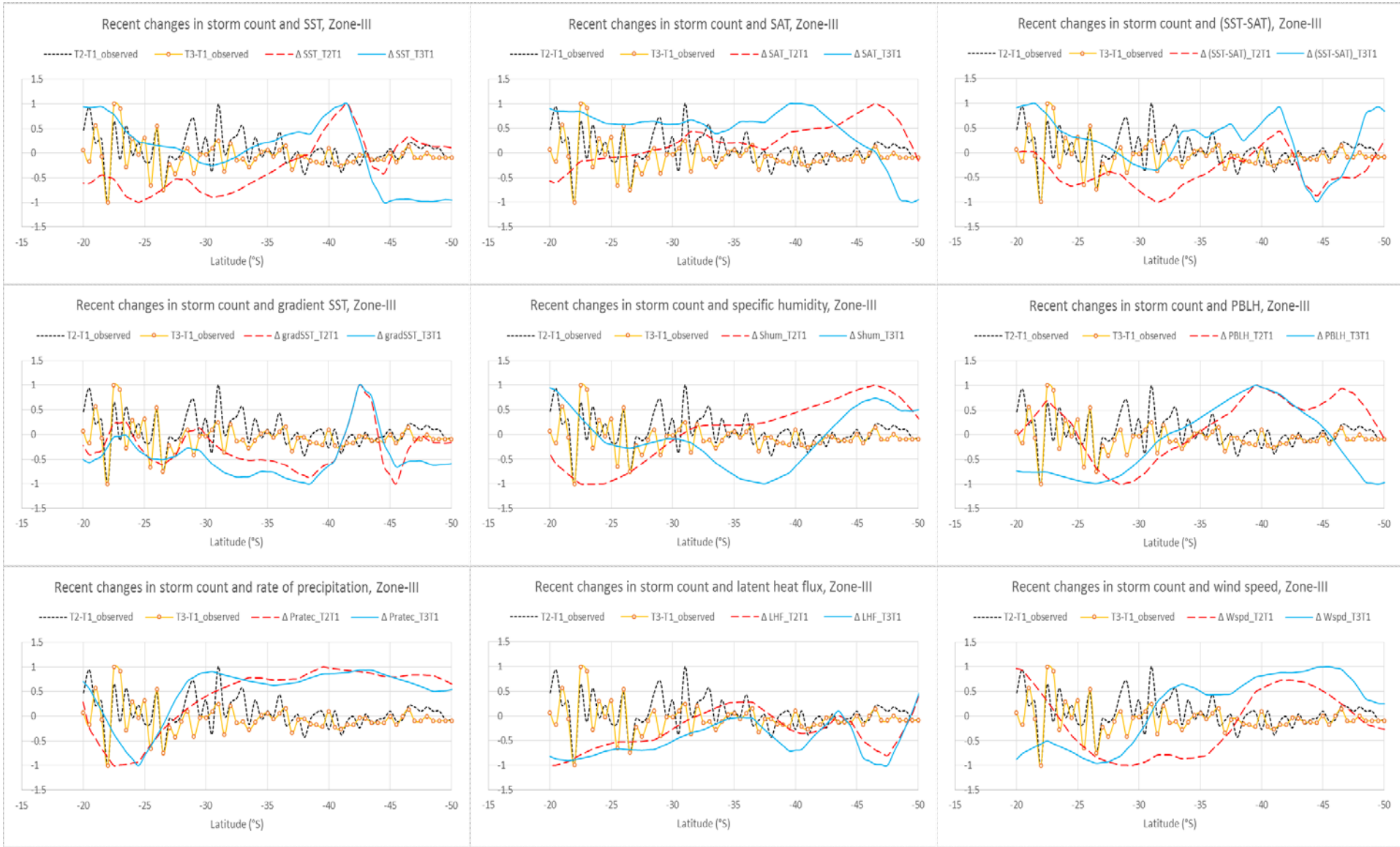

Figure 53 *Large scale climate variability and changing storm counts (recent past) for Zone-III*

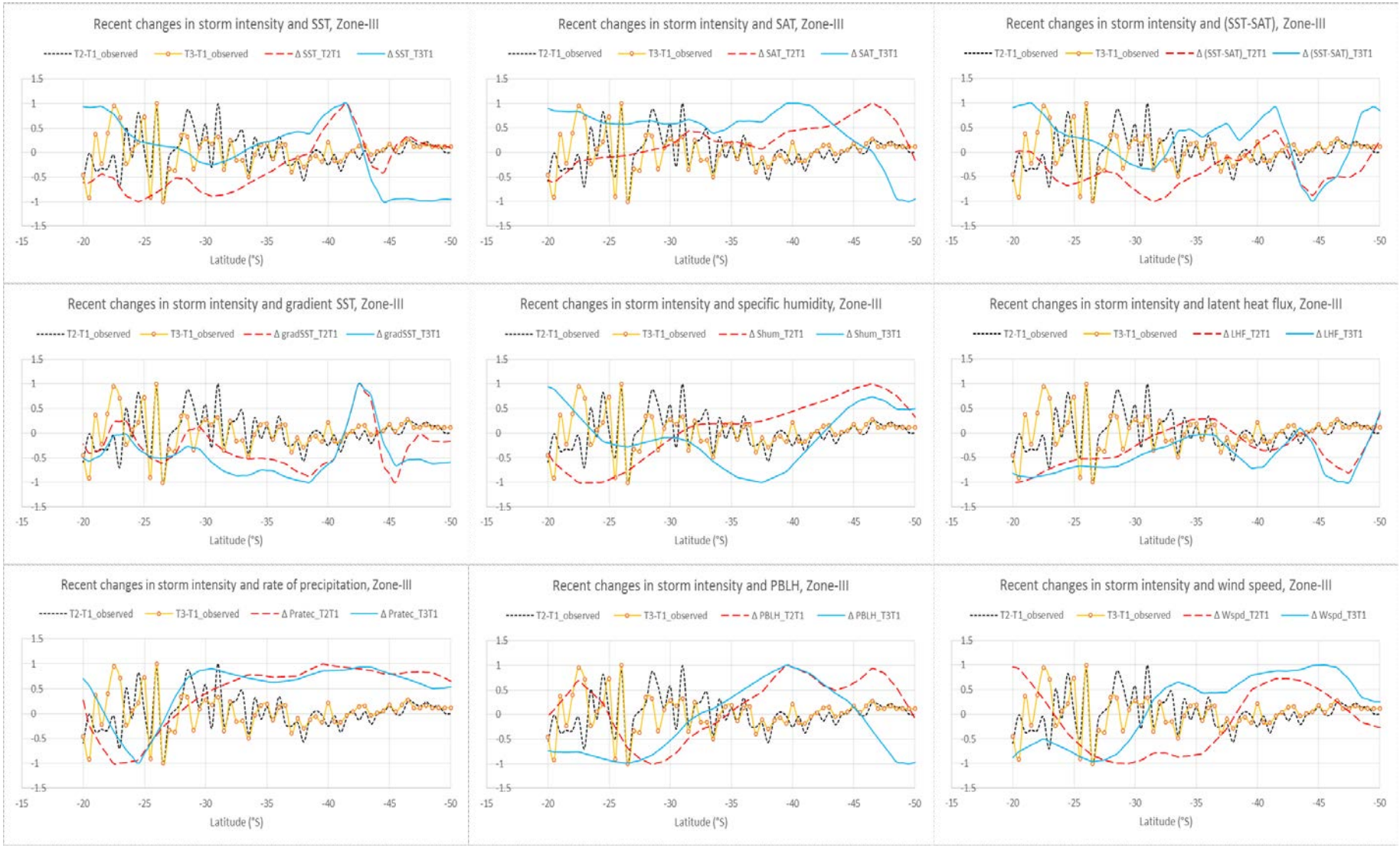

Figure 54 *Large scale climate variability and changing storm intensity (recent past) for Zone-III*

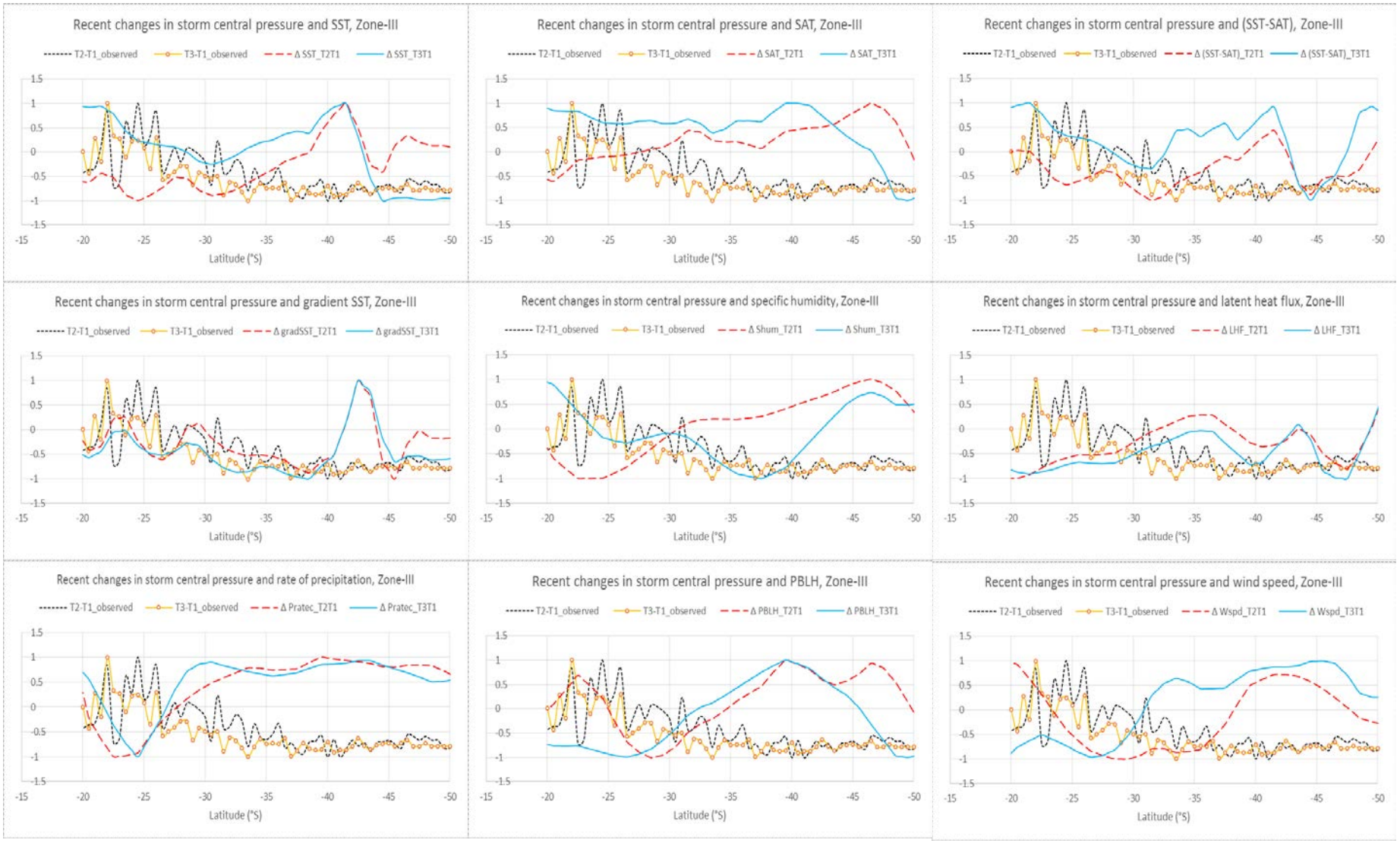

Figure 55 *Large scale climate variability and changing storm central pressure (recent past) for Zone-III*

6.2.3 Application of regression model equations to predict future change in storminess

The second objective of this chapter aims at prediction of change in the storm indices by the end of 21st century. This will employ 15 set of regression equations that are constructed in previous section and applied on the SWP14 downscaled (~25 km resolution) variables to obtain two different scenarios of future change in storminess for three different zones. Note that only one likely scenario could be presented for zone-III due to weak correlation established between recent past climate and storm dataset. A zone-wise explanation is sequentially given below whose corresponding correlation and regression analysis are detailed under **Appendix IV**. The regression equations are already listed in the previous **section 6.2.3**. Except zone-III, two possible scenarios based on cases T2T1 and T3T1 are presented:

A. Zone I (EAC pathway)

Change in future storm counts: In general, the scenario-A storm counts (**Figure 56a**) when compared to the recent past are likely to reduce by the end of 21st century, especially for the midlatitudes (poleward of ~28°S). Apart from this overall reduction, subtropical area (~25-30°S) is likely to witness a rise in counts, especially during summer. To be more specific, the predicted change in storm counts when compared to recent change are expected to: (a) increase for subtropics (~23-28.5°S); (b) gradually decrease over midlatitudes (~30-43.5°S); (c) sharply increase poleward of ~45°S. In addition to these, it is noteworthy that only minor reduction in counts is expected for midlatitudes (~37.5-40°S). Although both summer and autumn shows an overall reduction in storm counts by the end of 21st century, it is during autumn that the counts are likely to substantially fall except for ~25-30°S, where minor rise is expected. Apart from this overall reduction in counts for autumn, the midlatitudes (~37 and 42°S) show relatively lower fall in future storm counts. Another notable possibility is that over midlatitudes, south of ~37°S, an equal number of storms are likely to hit the area during both summer and autumn. Note that summer show minor reduction in storms when compared to the recent changes until 40°S, whereas autumn shows the same for a brief area between ~37-42°S and major reduction for ~30-37°S and south of ~42°S.

The scenario-B storm counts (**Figure 56b**) are likely to show a substantial increase in summer and autumn storm counts for larger meridional extent ~20-40°S. However, since this regression analysis is based on single variable, it is rejected and only T2T1 based conclusions are included. It is noteworthy that the prediction for T3T1 change in storm counts is based on single variable (change in specific humidity) regression model unlike T2T1 model. To conclude, for zone-I storm counts change, the predictability of T2T1 based formulation is likely to be more accurate and consistent.

Change in future storm intensity: For scenario-A (**Figure 56c**), summer shows a substantial increase in intensity, especially for subtropics (~23.5-32.5°S) and midlatitudes with substantial rise noted for an area between ~23-28°S and between ~37-42°S. Autumn shows nil or minor variation in subtropics

(~20-25°S; medium rise for ~25-28°S; fall for ~28-37°S) along with a substantial rise in the area ~37-42°S.

In case of scenario-B, the storm intensity (**Figure 56d**), both summer and autumn are likely to show a substantial increase in intensity, where both the seasons are following similar pattern of rise until ~31.5°S, thereafter summer shows a sharp fall in storm intensity, whereas autumn continues to maintain it and even shows greater increase (~38-41.5°S). Summer in comparison to autumn shows lesser increase in intensity (~31.5-40°S).

Change in future storm central pressure: For summer, the storm central pressure **(Figure 56e)** is likely to: (a) reduce for meridional extents of ~20-25°S and ~28.5-37°S; and (b) increase for ~25-28.5°S. This implies that the storms between ~20-37°S except ~25-28°S are likely to further lower their central pressure, which in tandem with predicted intensity confirms an increased storms activity with intense storminess. Similar phenomena of lowering of central pressure is noted for autumn, however it does not synchronize with any intensity change, which actually shows a fall. This is perhaps commensurate with lower number of counts during autumn, implying that the storms are likely to be more intense even during autumn, although their numbers will be reduced compared to that of summer.

In scenario-B (**Figure 56f**), for storm central pressure during summer and autumn, it is likely to increase and remain unchanged until ~31.5°S. After ~31.5°S, the summer curve shows a reduction in central pressure until ~37°S. For autumn, between ~37-40°S, a rise in central pressure is predicted along with a substantial fall south of ~40°S. Poleward of ~40°S both summer and autumn show similar falling trends, however with different values.

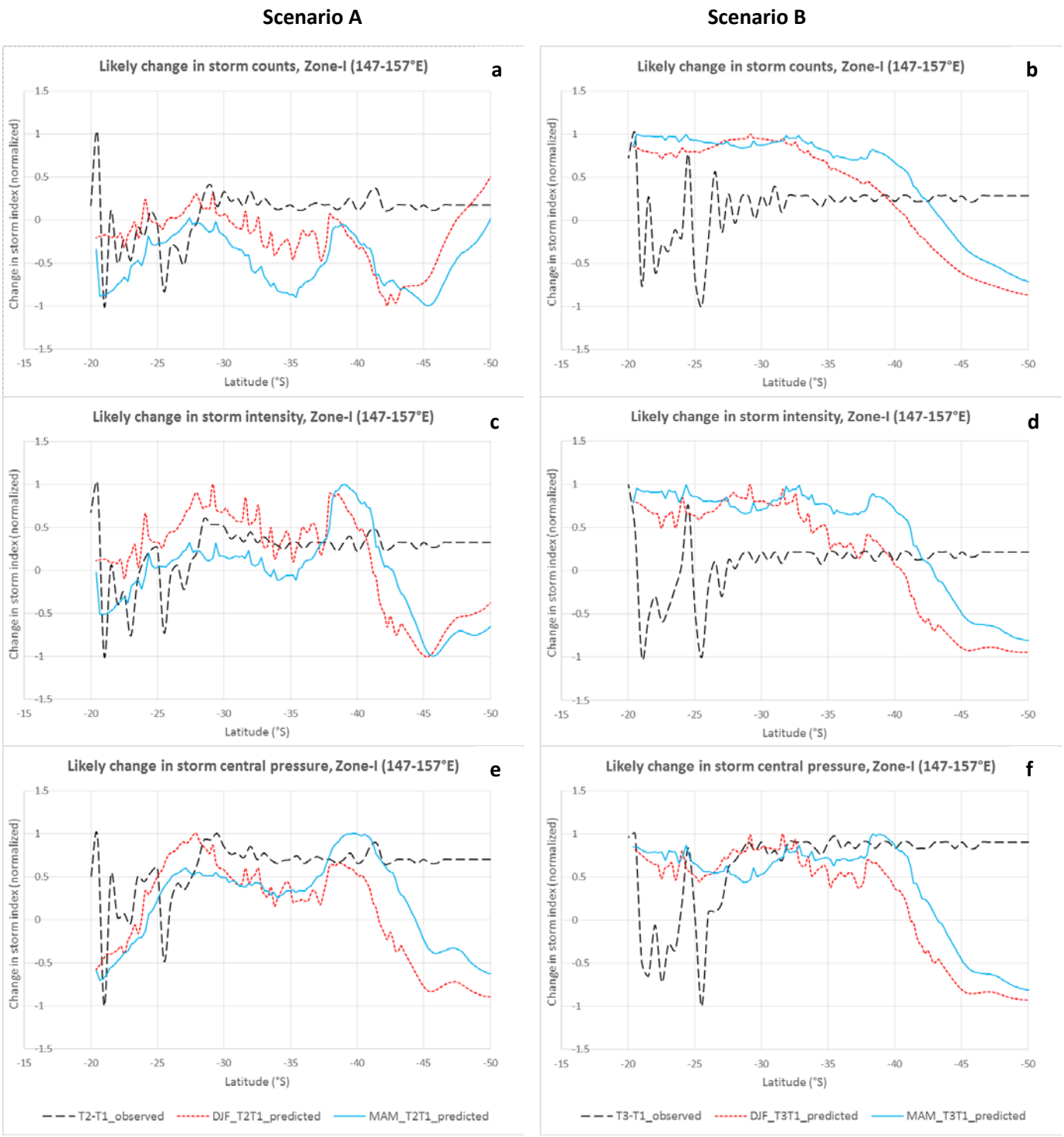

Figure 56 *Scenarios of likely change in future storminess for* ***Zone-I*** *(147-157°S)*

The respective regression model equations for T2T1 and T3T1 are constructed based on (a) LHF, wind speed; (b) specific humidity; (c) specific humidity, LHF, wind speed; (d) specific humidity, SAT, LHF; (e) (SST-SAT), LHF; (f) SST, specific humidity, LHF.

Note that based on two different regression model analysis, two possible scenarios of change in future storminess is presented for austral summer-autumn: scenario-A is based on T2-T1 regression analysis and scenario-B based on T3-T1 regression analysis (Section-XX). Each row illustrate change in three different storm indices: (a) storm counts, (b) storm intensity, (c) storm central pressure respectively.

B. Zone II (Tasman Sea)

The corresponding regression analysis for zone-II are detailed under **Appendix IV** and equations are listed in previous **section 6.1**. Under these two different possible scenarios, each based on cases T2T1 and T3T1 are discussed below.

Change in storm counts: Referring to scenario-A (**Figure 57a**), overall the predicted storm counts are likely to increase by the end of 21st century over the subtropics and lower midlatitudes (~20-37°S) when compared to the recent past. The predicted change during summer (autumn) shows that a substantial reduction in storm counts is possible, poleward of 36°S (38°S). Compared to autumn, conspicuously greater number of storms are likely to hit the subtropical extent (~25-35°S) during summer. In addition, autumn also shows relatively higher number of storms for two different extents: ~20-25°S over subtropics and ~35-38°S over midlatitudes.

In case of scenario-B (**Figure 57b**), similar changes for summer and autumn are likely, except few variation in meridional extent, which is explained here: Compared to recent change, the predicted storm counts are likely to conspicuously increase over the subtropical extent ~21-36°S and for poleward of 36°S (38°S) counts are likely to fall sharply for summer (autumn).

Both these predictions hence are confirming the overall change in storm counts prediction discussed under scenario-A. While comparing the predicted changes between summer and autumn, little changes are to be noted: summer is showing a gradual increase in storm counts, with greater number of storms limited between ~25-36.5°S, while in scenario-A, a relatively sharp increase poleward of 26.5°S with greater number of storms between 26.5-37.5°S is predicted.

It is noteworthy that scenario-B shows greater change for autumn when compared to scenario-A, covering larger extent from ~21-38°S including a sharp but brief peak ~36-36.5°S. This peak, which is also present for recent change curve, is also being replicated by autumn curve but has further widened polewards ~36-38°S. This implies that entire subtropics and lower midlatitudes are expected to receive significantly higher number of storms for zone-II. Within this increase in number of storm counts, the counts are dominated in summer over an extent of ~30-35°S and in autumn over the extent of ~24-30°S and ~35.5-39.5°S.

Change in storm intensity: The scenario-A predicted storm intensity (**Figure 57c**) for summer more or less matches to that of the change in predicted storm counts, specifically for the subtropical and lower mid-latitudinal extent between ~20-36°S, with substantial increase likely for ~25-35°S. Similarly, for autumn, the storms are likely to grow stronger for subtropics as well as for midlatitudes (~20-40°S). Additionally, during autumn, more intense storms are likely to arrive over subtropics (~20-27°S) and higher midlatitudes (close to 3-40°S) compared to summer. The scenario-B predicted storm intensity (**Figure 57d**) for summer and autumn follows similar trend of that of the predicted storm counts.

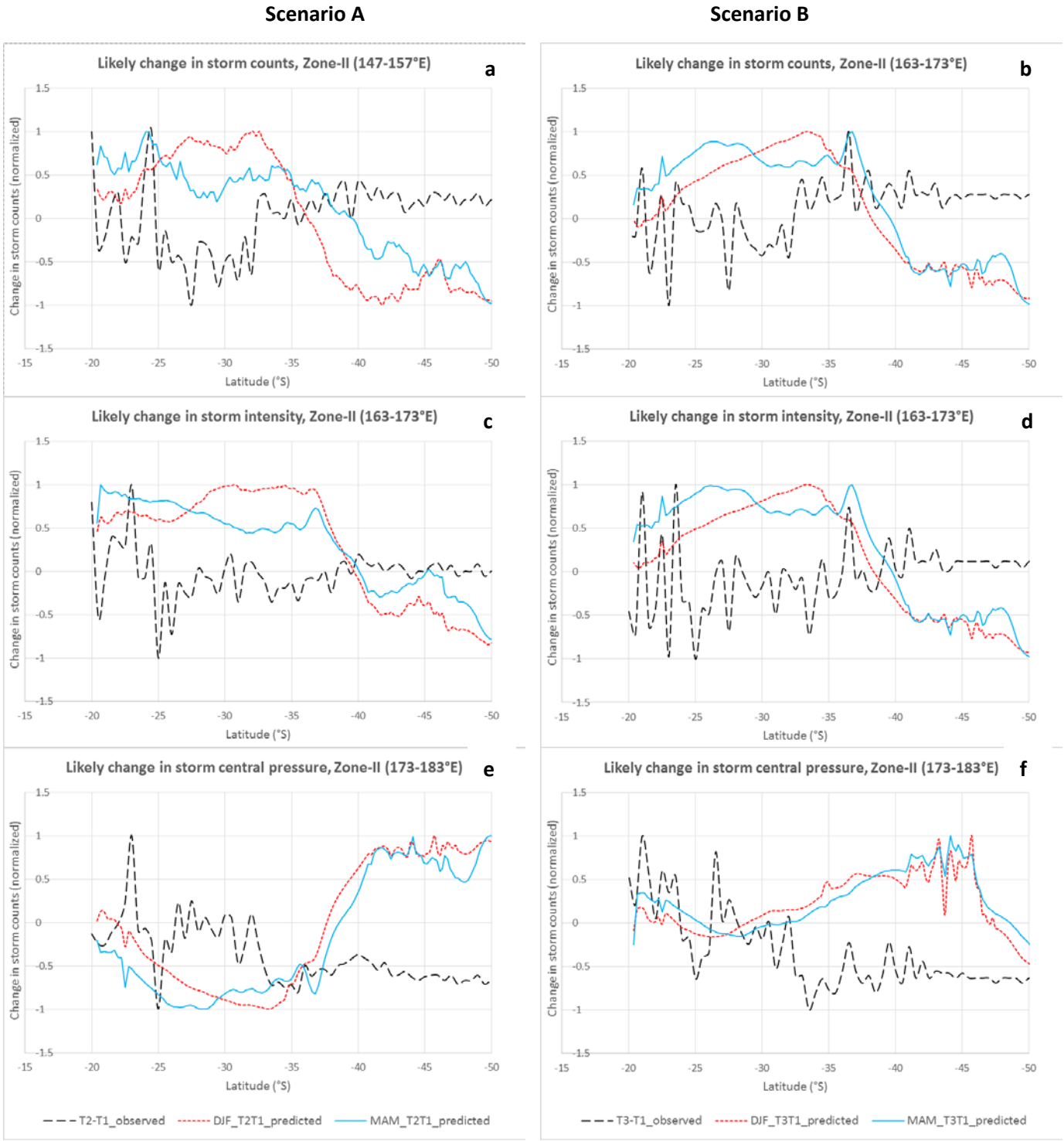

Figure 57 *Scenarios of likely change in future storminess for* ***Zone-II*** *(163-173°S)*

It is based on regression model analysis, two different scenarios of storminess that are likely to change by the end of 21st century is presented: (A) Scenario-A is based on T2-T1 regression analysis and Scenario-B based on T3-T1 regression analysis (Section-XX). Each row illustrate change in three different storm indices: (a) storm counts, (b) storm intensity, (c) storm central pressure respectively.

Change in storm central pressure: The predicted storm central pressure (**Figure 57e**) are likely to be lower for the subtropics between ~20-38°S, with major decrease noted between ~25-37°S. Poleward to 38°S, a rise in pressure is likely. This change lowering (~20-38°S)/rising (south of 38°S) of pressure is corresponding to the rise/fall in storm intensity over the respective meridional extent. The scenario-B (**Figure 57f**) predicted storm central pressure is likely to be lower for the subtropics ~20-32°S and likely to rise south of 32°S.

Conclusion zone-II Although the predicted storm counts during summer are likely to reduce for midlatitudes (south of 36°S) when compared to the recent change, there is interestingly a considerable increase in the intensity for an extent between ~36-40°S. It is also interesting to note that both the storm counts and corresponding storm intensity are likely to fall poleward of 40°S, when compared to the recent changes. The number of midlatitude (~36-40°S) intense storms are likely to reduce poleward of 36°S during summer. Although the storm counts during autumn are likely to increase for ~35-48°S, there is a considerable rise in its corresponding intensity. The storm intensity remains unchanged for higher midlatitudes (~43.5-46.5°S) during autumn, which implies that storms are likely to continue reach these latitudes even in future autumn season.

C. Zone III (East of NZ)

The corresponding regression analysis for zone-III are detailed under **Appendix IV** and equations are listed in previous **section 6.1**. Under this, only one possible scenario could be constructed based on T2T1 regression model equations, as T3T1 regression equations could not be established for storm counts and intensity.

Change in storm counts: Referring to the scenario-A (**Figure 58a**), the predicted storm counts during DJF are likely to remain unchanged for subtropics between ~20-30°S; reduce for midlatitudes (~30-45°S), substantially reduce between (~34-43°S); and sharply rise for higher midlatitudes (poleward of 45°S). Similarly for MAM, the numbers are likely to remain unchanged for subtropics (~20-34°S); reduce between ~34-47°S, with major reduction noted between ~35-45°S; and thereafter sharply rise poleward of 47°S.

Change in storm intensity: The scenario-A storm intensity curves (**Figure 58b**) do not follow the storm counts prediction and contrarily show an overall rise in intensity by the end of 21st century during DJF and MAM. It is predicted that during DJF, the intensity is likely to increase for ~20-40°S with substantial increase noted between ~30-41.5°S; and reduce poleward of 47.5°S. Similarly for MAM, the intensity is likely to substantially increase for entire meridional extent covering both subtropics and midlatitudes, and is likely to decrease south of 48.5°S.

Scenario A

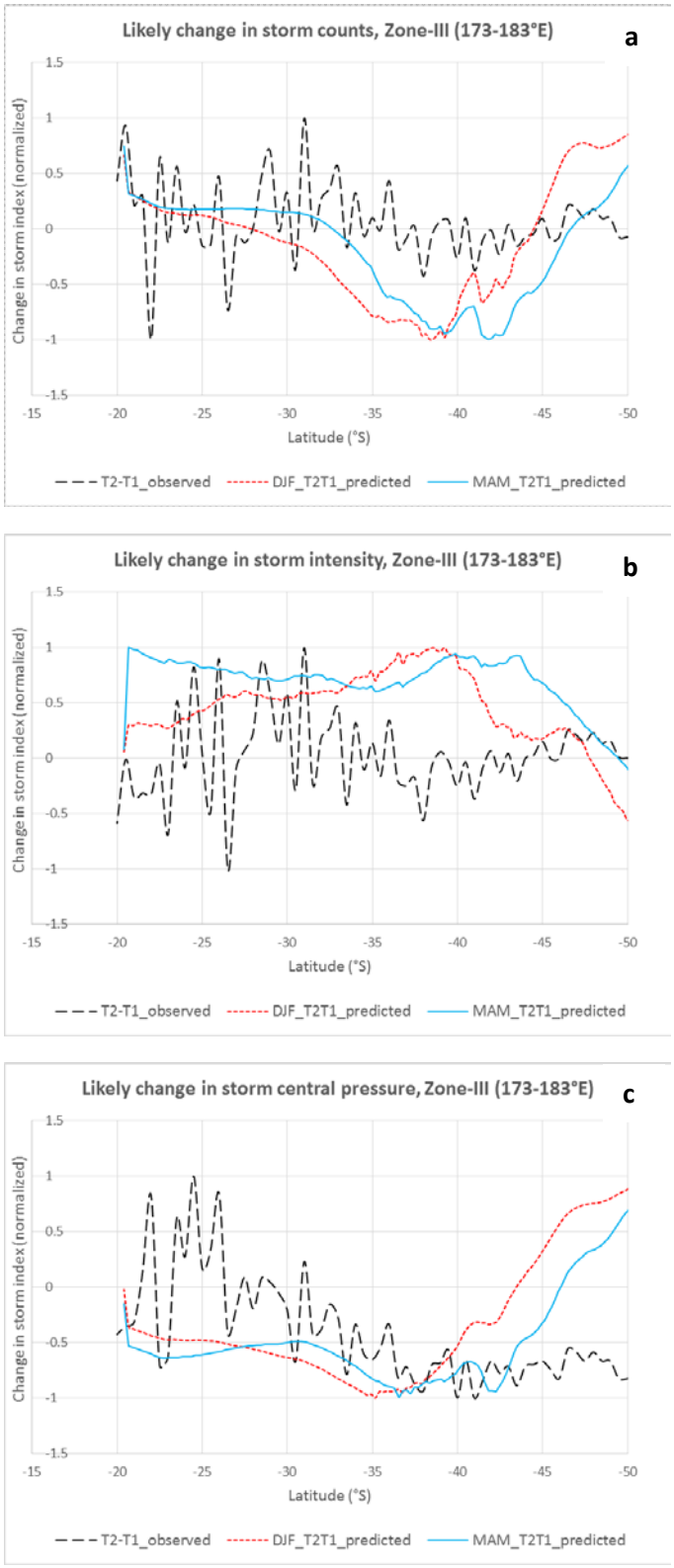

Figure 58 *Scenarios of likely change in future storminess for* ***Zone-III*** *(173-183°S)*

It is based on regression model analysis, only one scenario of likely change in storminess by the end of 21st century is presented: Scenario-A is based on T2-T1 regression analysis. Three rows illustrate change in three different storm indices: (a) storm counts, (b) storm intensity, (c) storm central pressure

Change in storm central pressure: The predicted storm central pressure curves (**Figure 58c**) for DJF (MAM) when compared to the recent change indicates a substantial lowering of storm central pressure by the end of 21st century for ~20-40°S (~20-41.5°S).

Conclusion zone III: Hence it can be concluded that although the MAM storm counts are reducing between ~34-47°S, as compared to other two zones, zone-III is likely to receive substantially increased number of intense storms over ~32-48.5°S, i.e. covering higher midlatitudes when compared to the recent past. The intense storms during DJF are likely to remain between ~30-45°S and during autumn between ~20-48.5°S. This implies that there is a greater likelihood of intense storms reaching higher midlatitudes by the end of 21st century during autumn months. Similarly, during DJF substantial rise in storm intensity is expected, especially between ~30-41.5°S accompanied by substantial reduction in number of storms.

6.3 Validation of historical storm indices

To assess how well the future storm indices are predicted for the study area, it is necessary to validate the efficacy of the historical modelled output in capturing the recent storm activities using the observational SPEArTC storm data for the same period, 1960-64. Comparative graphs for three zones are described for respective storm data, viz. storm counts, storm intensity and storm central pressure. In addition to the comparative graphs, the Root Mean Square Difference (RMSD) corresponding to each zone (following the depiction of latitudinal variation in storm counts shown by **Figure 4** of chapter 1) separately for austral summer (DJF) and autumn (MAM) is provided. Both the graphical representation and RMSD would help get a clear picture on efficacy of the modelled future storminess. Following steps have been carried out to perform validation of historical storms.

1. Historical simulation time ranges from 1960 to 1964. The large scale environmental variables are extracted for coupled historical output (hcw) for all the 7 latitudinal bands for each zones. This exercise was repeated twice, each for austral summer (DJF) and austral autumn (MAM) season.
2. Similarly, corresponding observational storm data (SPEArTC, Diamond et al., 2010) are also extracted for the same period (1960-64) to have consistent data for validation for austral summer (DJF) and autumn (MAM) seasons. The storm observational data are geographically limited based on the corresponding geographical extent of each zone where storms occurred and were recorded by the responsible agency for the evaluation period. Since this evaluation period is before the satellite era, where data are considered to be more reliable (Diamond et al. 2012), therefore gap between storms that occurred and actually recorded persists. This gap is further widened by missing corresponding maximum wind speed and central pressure data to even few recorded storms.
3. As major SWP storm season lies between December and April, the observational data included storms mainly for two storm seasons: December to February (DJF) and March to May (MAM), similar to the regression analysis.

4. Austral autumn storm data included corresponding storm data simply between March to May. However, extra care is taken while extracting storm data for austral summer months because it should include storm data from December of previous year. For example, DJF for 1961 includes storms starting from December 1960 to February 1961.
5. Previous **section 6.2.2** formulates two different (T2T1 and T3T1 based) regression model equations that can be utilized to compute storm indices given large scale environmental variables. By applying these two regression model equations, historical storm indices have been computed for the evaluation period 1960-64.
6. Storm indices are computed for all the 3 zones and 7 latitude bands for austral summer and autumn seasons and are compared with corresponding observational storm indices, whose geographical extent varies for each zone.
7. The comparative graphs are arranged such that at each latitude band, histograms for observation, predicted based on T2T1 case and predicted based on T3T1 case are compared. **Figures 59 to 61** are arranged starting for zone I giving storm indices (counts, intensity, and central pressure) for austral summer (DJF) followed by austral autumn (MAM). Similarly, **Figures 62 to 64** present comparative graphs on storm counts, intensity and central pressure corresponding to zone II.
8. Finally, these comparative graphs should help draw confidence level to assess future change in storminess. An additional index, root mean square difference (RMSD, see equation 1 in **section 3.1)** is computed for each comparative graphs to further state the overall efficacy of the modelled prediction of changing storminess.

A. Zone I (EAC Pathway)

The Zone I extends between 147-157°E longitudinally, basically representing the EAC pathway. While searching for the observational storm data for this zonal extent from 1960 to 1964, it was noticed that the meridional extent available for storm data reaches maximum until 35°S, which hence also formed the extent for the comparison graphs (see **Figures 59, 60 and 61**). So only four latitude bands are compared.

Storm Counts

a) The lower latitude band (15-20°S) shows most accurate prediction for both the T2T1 and T3T1 cases for both the seasons.
b) For all the four latitude bands (15-20°S, 20-25°S, 25-30°S, 30-35°S), overall T2T1 case provides comparatively the most accurate prediction for recent storm counts with as low RMSD as 0.0087 for DJF and 0.0241 for MAM.
c) Slight over-estimation is noted for T2T1 case for 20-25°S band in DJF and MAM. This overestimation is seen also seen for 30-35°S band. A slight underestimated prediction is also noted for 25-30°S, which is seen even for DJF, but with insignificant magnitude.

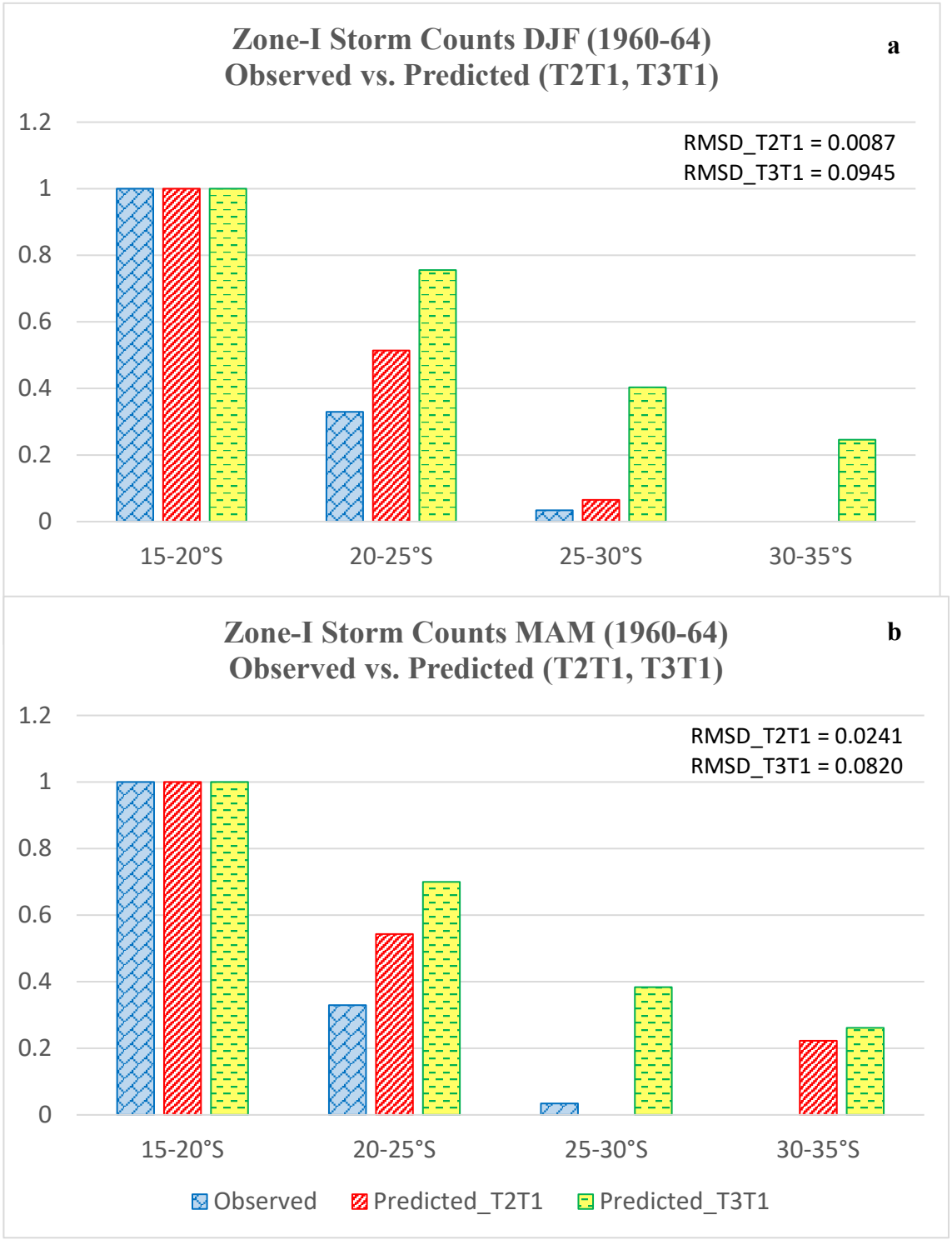

Figure 59 Storm Counts *Observation vs. Predicted cases (a) DJF (b) MAM* ***(Zone I)***

Storm Intensity

a) For austral summer (DJF), it is clearly seen that T2T1 predicted storm intensity matches well with observed intensity over all the latitude bands (with RMSD of ~0.0032), which otherwise shows greater deviation for T3T1 predicted intensity.

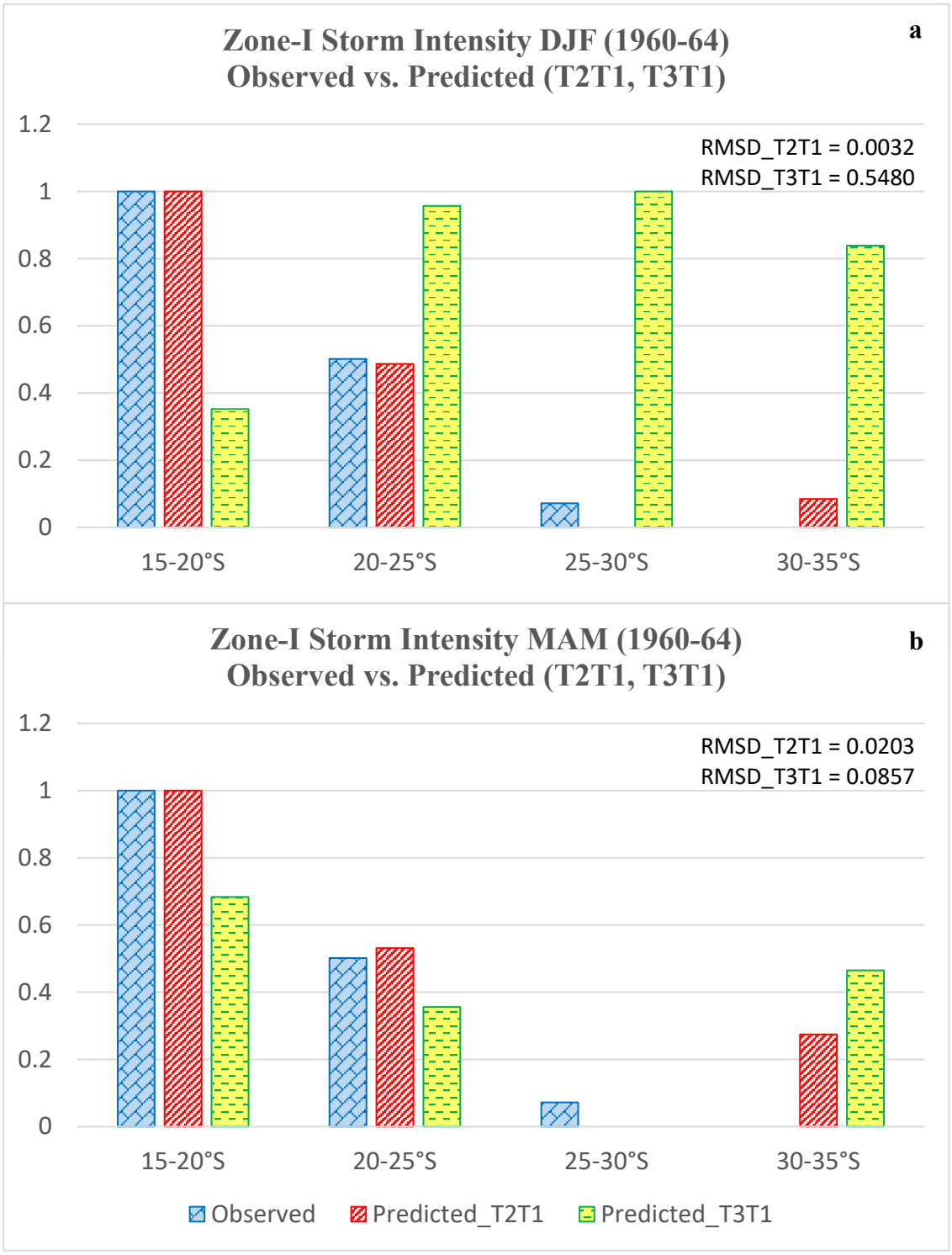

Figure 60 Storm Intensity *Observation vs. Predicted cases (a) DJF (b) MAM* ***(Zone I)***

b) The above does not hold true for MAM. T3T1 predicted intensity shows closer match for 20-25°S compared to T2T1 and equally good match as that by T2T1 for 25-30°S for MAM.

c) The RMSD for T2T1 (0.0203) is still lower than T3T1 (0.0857) for both the austral summer-autumn seasons, mainly as the former show more accurate prediction of storm intensity for band 15-20°S and closer match for 30-35°S than T3T1.

Storm Central Pressure

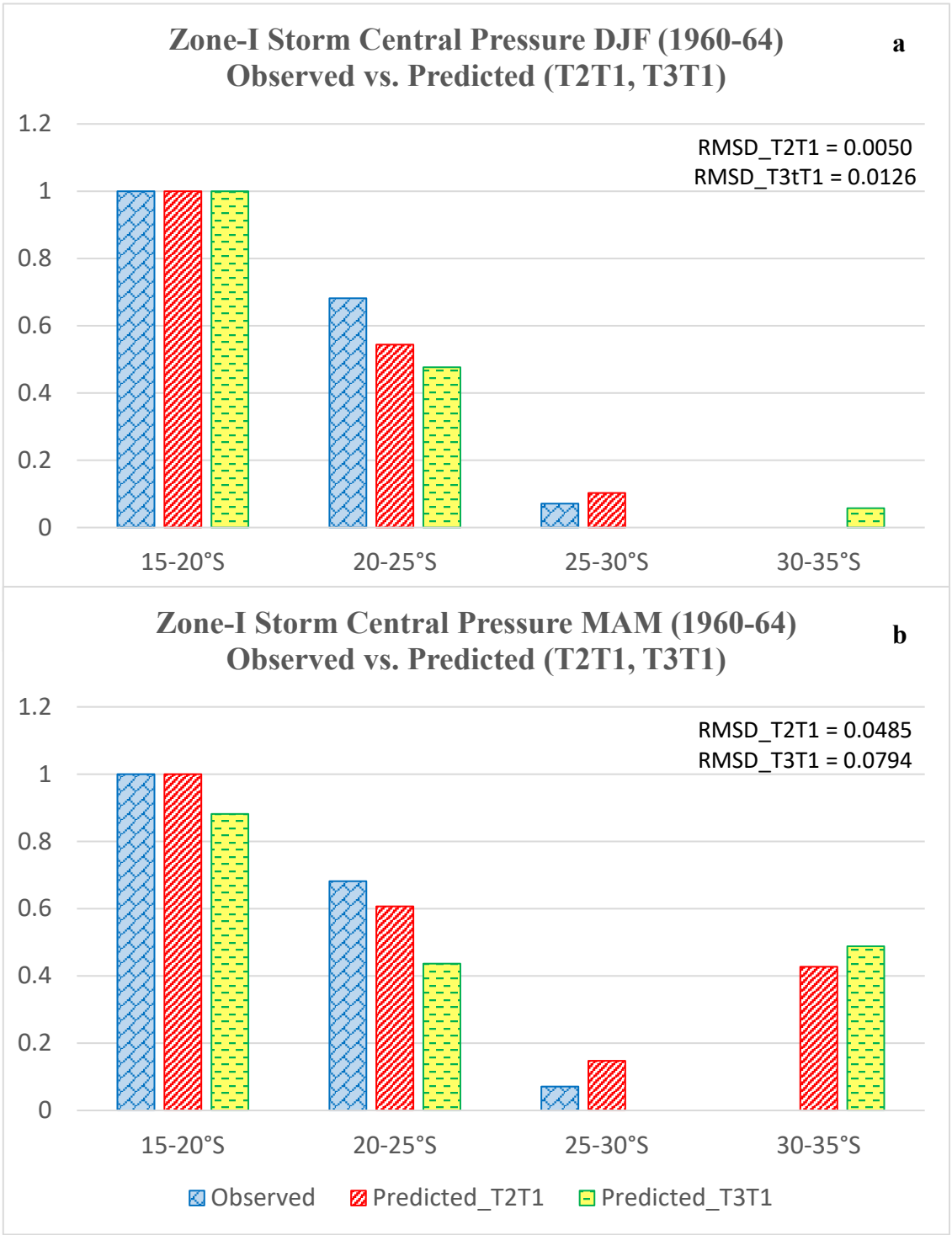

Figure 61 Storm central pressure *Observation vs. Predicted cases (a) DJF (b) MAM* ***(Zone I)***

a) Although both T2T1 (~0.005) and T3T1 (~0.0126) predicted central pressure closely matches with that of observation, it can be clearly seen that T2T1 case shows more accurate match for 15-20°S, 20-25°S and 30-35°S; with slight underestimation for 25-30°S for DJF.
b) These predictions remain similar for MAM, with slight mismatch of T2T1 predictions, like, slight overestimation for 20-25°S that increases to greater magnitude for midlatitudes, 30-35°S.
c) On comparison of the RMSDs of DJF and MAM on predicted storm central pressure, T2T1 gives highly accurate prediction with least deviation (~0.005 and 0.0485 respectively) among the two.

B. Zone II Tasman Sea Pathway

The Zone II extends between 163-173°E longitudinally, covering the area across Tasman Flow pathway. The observational storm data could be extracted for the meridional extent reaching nearly 45°S, which hence also formed the extent for the comparison graphs (see **Figures 62, 63 and 64**).

Storm Counts

a) For DJF: Both T2T1 (0.056) and T3T1 (0.017) gave exact match for first three bands: 15-20°S, 20-25°S, 35-40°S and 40-45°S; followed by minor overestimation in counts for middle to higher midlatitudes i.e. for bands: 30-35°S, 35-40°S and 40-45°S. Hence, for austral summer, T3T1 storm counts are accurately predicted, with least deviation of about 0.0031 for zone II.
b) For MAM: the scenario is slightly different than DJF: Both the T2T1 (~0.146) and T3T1 (~0.152) show comparatively greatly overestimates the counts for all the bands except for 20-25°S and 35-40°S; underestimated predicted counts for 15-20°S and only match for 40-45°S band.

Storm Intensity

a) For DJF: Compared to T3T1, T2T1 case show greater deviations, especially south of 25°S in predicting storm intensity for zone II. This is also shown by overall RMSD for the two cases: T2T1 (~0.117) and T3T1 (~0.042). Bands 15-20, 20-25°S 30-35°S, 35-40°S, 40-45°S gave closer match to past storm intensity
b) For MAM: Although RMSD for both cases show greater value, overall, T3T1 case show better match for most of the bands in this zone than that of T2T1 case. A mixed result is seen for this zone: an underestimation (by half) for 15-20°S by T3T1; a reasonable match for 20-25°S and 25-30°S, 35-40°S, by both T2T1 and T3T1; a slightly overestimated intensity for midlatitudes (30-35°S) by T3T1 (underestimated by T2T1) and an accurate prediction for higher midlatitudes 40-45°S by T3T1

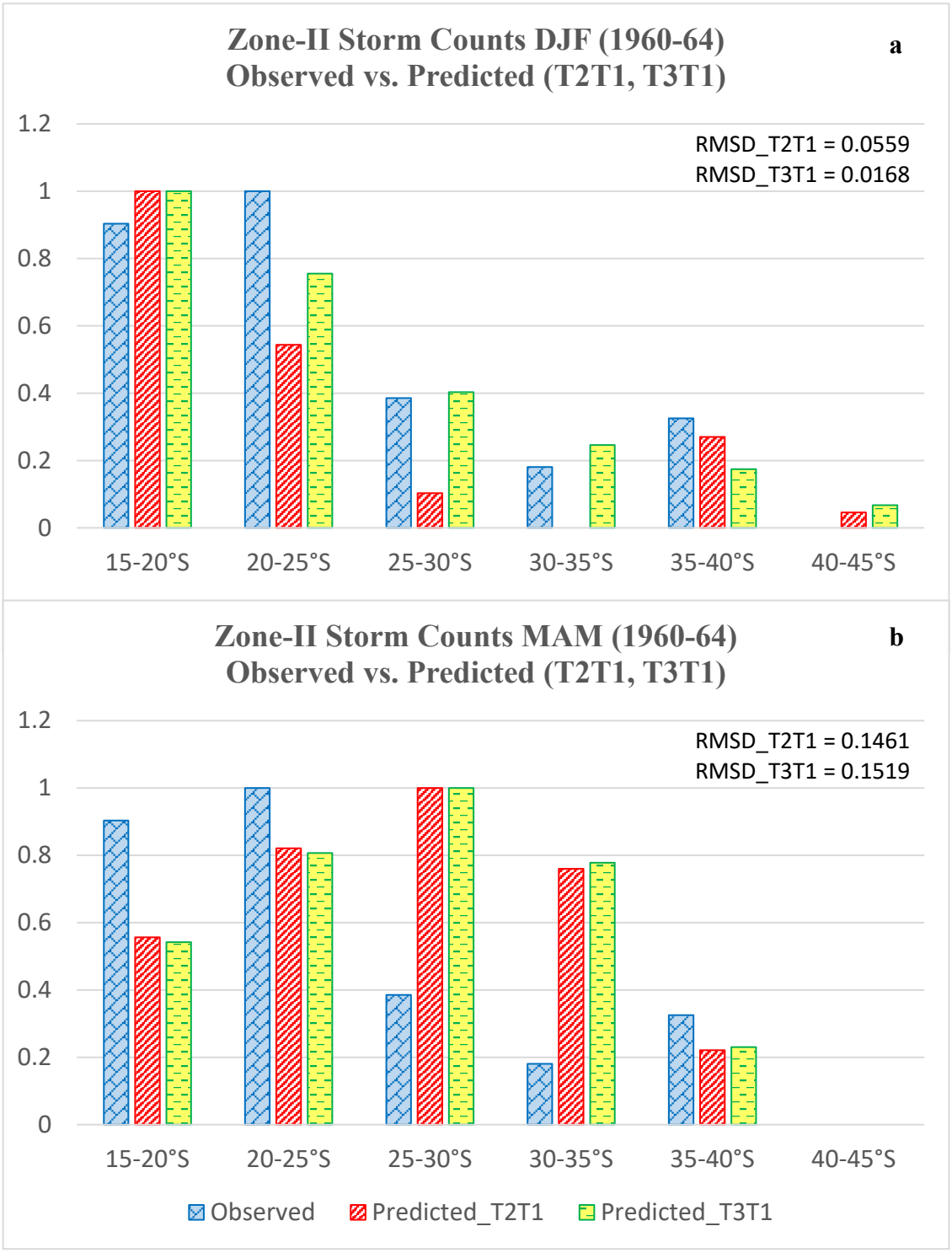

Figure 62 Storm Counts *Observation vs. Predicted cases (a) DJF (b) MAM* ***(Zone II)***

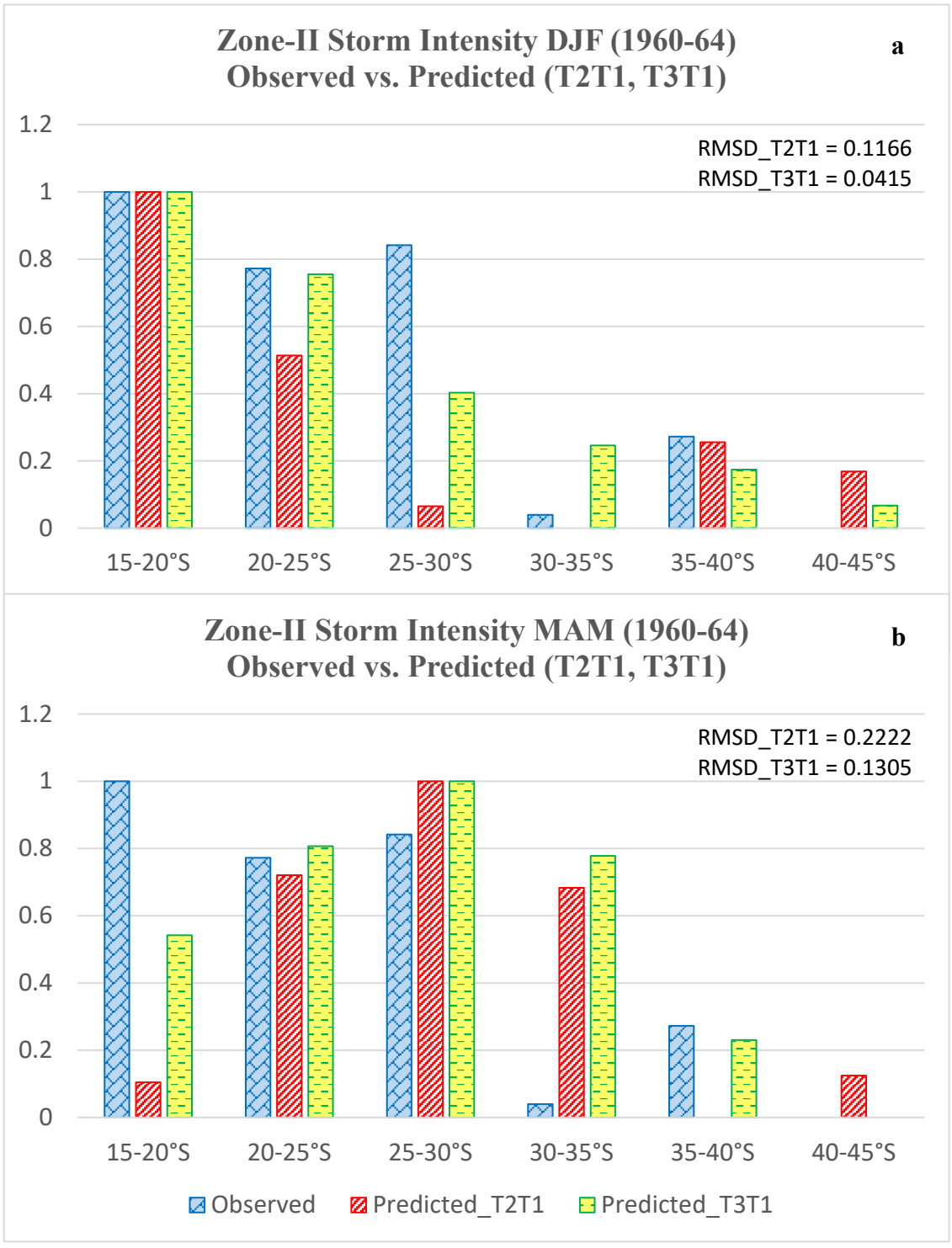

Figure 63 Storm Intensity *Observation vs. Predicted cases (a) DJF (b) MAM* ***(Zone II)***

Storm central pressure

a) For DJF: The predicted storm central pressure is equally good for both cases, especially for 15-20°S and 30-35°S for T2T1. Overall, the RMSD for T2T1 (0.337) and T3T1 (0.288) cases show more or less similar estimation, however its reliability varies with different bands.
b) T2T1 predicts accurate recent storm central pressure for bands 15-20°S and 30-35°S, whereas T3T1 show closer estimation for 15-20°S, followed by 25-30°S with slight overestimated values for the latter band. Both T2T1 and T3T1 over-estimate the past storm central pressure for band 20-25°S with T2T1 case showing better predictability. On one hand, T2T1 did worse in predicting 25-30°S, whereas T3T1 did so for 30-35°S.
c) For MAM: Overall, RMSD show greater value for both cases T2T1 (0.266) and T3T1 (0.271) and even though they show a mixed result, the overall RMSD for T3T1 is lower and can be relied upon mainly for 20-25°S. For this season, both the cases gave underestimated values for 15-20°S and 25-30°S, whereas overestimation for 30-35°S.
d) The two predictions are similar for all the bands, except for 20-25°S, with RMSD T2T1 (~0.266) and T3T1 (~0.271), with slightly more reasonable for T3T1 due to its closest prediction for 15-20°S.

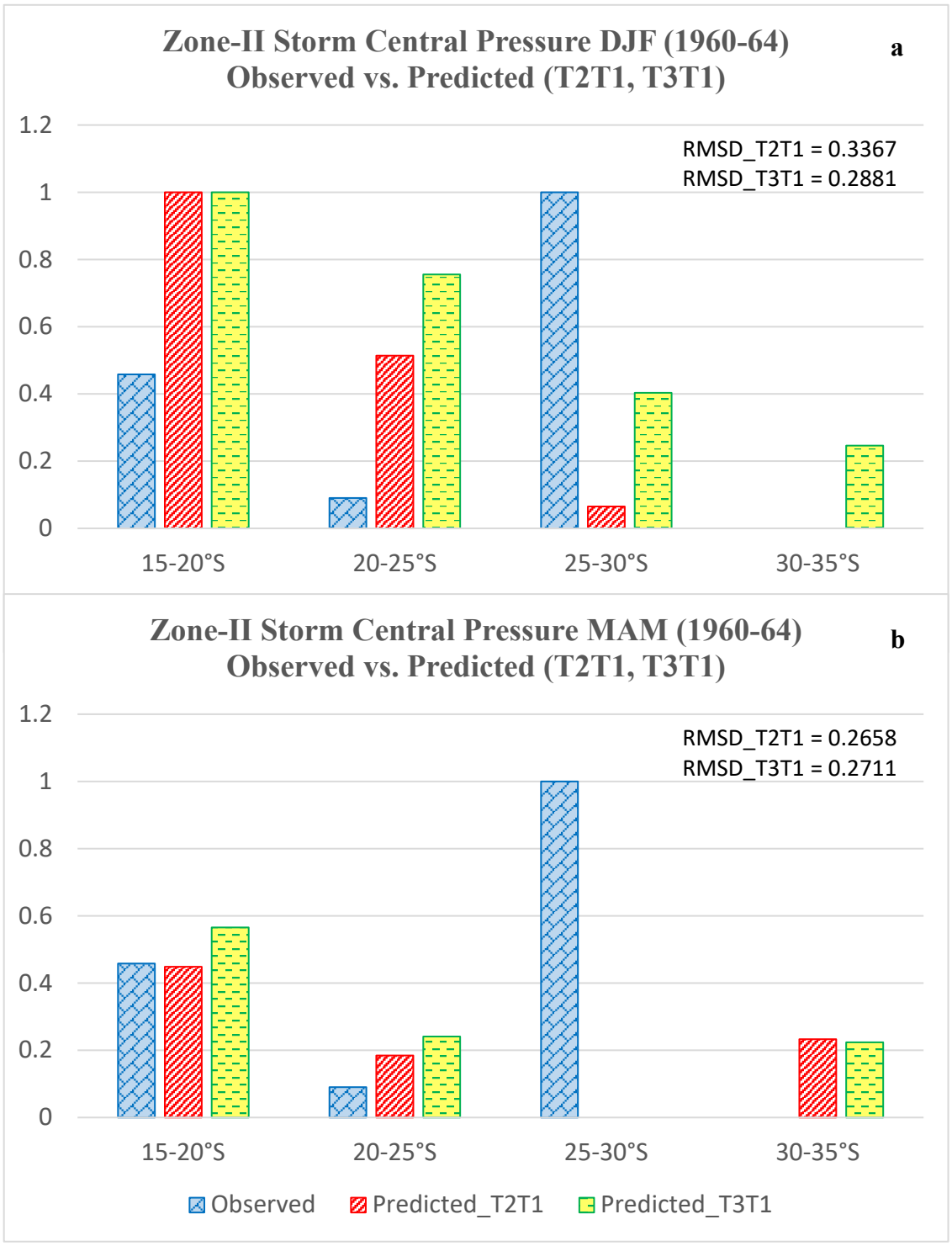

Figure 64 Storm central pressure *Observation vs. Predicted cases (a) DJF (b) MAM* ***(Zone II)***

6.4 Summary

This chapter aims at (a) establishing relationship between changing large scale climate variables and changing storminess for selected sampling locations from recent data available, and (b) application of this relationship on simulated (RCP8.5 minus historical) differences, to construct scenario of likely change in future storminess. The analysis is based on recent past storm changes compared to the corresponding large scale climate indices for two different case studies using Pearson's correlation coefficient and multiple linear regression analysis method. It aims to determine the relationship between the two and define the background mechanisms active behind change in the storm conditions.

6.4.1 *Changing storm conditions and large scale variability*

Large scale environmental variables or climate indices are known to be the driving force behind several ongoing ocean-atmospheric processes and can be used as key indicators to detect/distinguish dynamic changes like abrupt vertical instability, availability of greater amount of atmospheric energy, change in phase, which collectively are capable to drive the general circulation of the atmosphere as well as change the storm pattern of a region or locality. In present study, it can be summarized that storm counts are influenced by the following climate indices:

- SST-SAT is inversely proportional to storm counts for all the zones. However, note that for zone-III this remains valid only for midlatitudes as direct proportionality could also be witnessed over subtropics (T3T1 case only)
- Any change in meridional gradient SST is proportional towards a positive change in storm counts. However little change in counts could is marked for 38-45°S
- Specific humidity is proportional to the storm counts, whose influence is found to be most vital for zone III
- Latent heat flux, rate of precipitation, PBLH and wind speed are also found to be proportional the storm counts
- Although rate of precipitation is found to be proportional to the counts, it shows an inverse proportionality relation for zone-III. Hence with higher rate of precipitation is connected with lower storm counts, implying extreme precipitation accompanied during recent past comparatively lower events of storm
- From regression analysis, considering all the three zones, it is concluded that in general:- latent heat flux, wind speed, specific humidity, rate of precipitation, air temperature, and air-sea temperature difference - are found to be vital ingredient to determine changing storm counts. To be more zone specific: latent heat flux and wind speed (for zone-I); latent heat flux, specific humidity, wind speed and rate of precipitation (for zone-II); air temperature, along with air-sea temperature difference, latent heat flux and specific humidity (for zone-III) are found to be

vital. *This implies that latent heat flux, specific humidity, wind speed are three most critical indices when change in storm counts is concerned, along with air temperature and air-sea temperature differences.*

The storm intensity is influenced by another set of climate indices:

- Surface air temperature is directly proportional over (20-34°S for zone-I)
- SST-SAT is found proportional over subtropics (20-26°S), whereas inversely proportional over midlatitudes (26.5-36°S).
- Any change in gradient SST has a positive impact on storm intensity
- specific humidity is directly proportional (for T3T1 case) over 20-28°S; whereas inversely proportional over 22.5-31°S (T2T1 case) in addition to contribution from other factors, especially for zone-I
- Latent heat flux is found to be directly proportional in addition to contribution from other factors
- PBLH is directly proportional to the intensity (an increase (decrease) is noted over 25-30°S for T2T1 (T3T1) with intense storm intensity noteworthy over ~23.5-25°S for T3T1 case
- The rate of precipitation shows an increase with increase in counts especially over ~20-31°S for zone-I
- The local wind speed is found to be proportional to intensity

In addition to above graphical inferences, the regression analysis for storm intensity highlights: specific humidity, latent heat flux, air and sea surface temperature, PBLH to be most influential ingredients. More specifically, for zone-I: specific humidity, latent heat flux wind speed and air temperature; for zone-II: specific humidity, SST, PBLH; and for zone-III: air temperature and PBLH are found to be the most vital climate index in influencing change in storm intensity of respective zones. *This implies that when storm change in storm intensity is concerned, (a) specific humidity and latent heat flux are most influential, (b) followed by air temperature and PBLH as important, (c) in addition to sea surface temperature and 10 m wind speed climate indices are playing respective role.*

Finally, the storm central pressure is influenced by another set of climate indices:

- Change in SST is directly proportional to SP (~20-40°S) for zone-II
- Change in SAT is directly proportional to SP (~20-42°S) for zone II with major rise in SAT noted over ~30-42°S along with lower and more stable storm central Pressure. *This implies that increased SAT can be related to decreased storm central pressure and stronger storms formed over the recent past over ~30-42°S.*
- Change in gradient SST is directly proportional to storm central pressure (~20-28°S) for zone-I.

- Change in SST-SAT indicates direct proportionality (20-25°S) for both zones I and II and inverse proportionality noted over ~25-30°S for zone-I
- Change in specific humidity is directly proportional to storm central pressure over ~20-32.5°S, for zone-I and over ~20-23°S for zone-II distinctly seen for T3T1. Over ~36-43.5°S several storm central pressure peaks are noted. Over 25-3°S T2T1 is greater than T3T1, however the corresponding change in storm central pressures are the same.
- Change in latent heat flux is proportional to storm central pressure for zone I. However, the index is found to be inversely proportional to storm central pressure for zone-II over ~20-42.5°S, with major rise in index witnessed over 20-23.5°S, except for the subtropics (~25-28°S). In zone II, for both the cases, a major rise in the index over midlatitudes (~30-42°S) is noted which when related to corresponding lower and more stable storm central pressure, hints at the possibility of the presence of intense storms in the midlatitudes due to increased index there.
- Change in rate of precipitation is found to be directly proportional to the storm central pressure for zone II over ~20-36°S, which shows an inverse proportionality relation over midlatitudes (~36-42°S). This maybe explained on the basis of increased land-sea thermal contrast over the midlatitudes among other factors, which is missing over the open ocean for subtropical extent.
- Change in PBLH is proportional to storm central pressure over ~20-25°S and inversely proportional over ~25-32.5°S for zone-I. In case of zone-II, similar variations in behaviour is noticed but at different meridional extent: directly proportional over ~25-33°S and inversely proportional over subtropics (~20-25°S) and midlatitudes (~33-42°S).
- Change in the wind speed at 10 m shows a direct proportionality with storm central pressure over subtropics (~20-32.5°S) for zone-I. However, it presents an opposite phenomena for zone-II, showing an inverse relation to storm central pressure polewards of 36°S, mainly in midlatitudes, between ~33.5-43.5°, indicating midlatitude storms are accompanied with intense winds.

In addition to above graphical inferences, the regression analysis for storm central pressure highlights: latent heat flux, specific humidity, sea surface temperature, air-sea temperature difference, air temperature, rate of precipitation, 10 m wind speed, PBLH as most influential ingredients. More specifically, for zone-I: air-sea temperature, latent heat flux, SST, specific humidity; for zone-II: latent heat flux, specific humidity, wind speed, air-sea temperature and air temperature; and for zone-III: specific humidity, latent heat flux, sea surface temperature, rate of precipitation and PBLH are found to be the most vital climate index in influencing change in storm intensity of respective zones. *This implies that when change in storm central pressure is concerned, (a) latent heat flux and specific humidity are most influential, (b) followed by sea surface temperature and air-sea temperature difference as*

important, (c) in addition to air temperature, rate of precipitation, PBLH and 10 m wind speed climate indices are playing respective role.

When storm counts are concerned, latent heat flux, specific humidity and wind speed are primarily found to be the most influential indices, followed by air temperature and air-sea temperature differences. Similarly, for storm intensity, again latent heat flux, specific humidity are the vital elements, in addition to the secondary elements like air temperature, PBLH and finally SST and wind speed. The change in storm central pressure is also found to be mainly driven by the change in latent heat flux and specific humidity, followed by SST, air-sea difference, in addition to low impact indices like air temperature, rate of precipitation, PBLH and wind speed. In this study, the change in storminess or storm activity implies to three storm indices, namely, storm counts, intensity and central pressure.

6.4.2 Seasonal comparison of estimated changes in the storm indices

Referring to seasonal comparison of likely changes in summer-autumn storminess by the end of 21st century, illustrated by **Figure 65**. The major comparative changes have been summarized in this section.

(a) Zone-I (EAC pathway)

- **Figure 65a** Greater number of storms are likely to develop along the subtropical part of the EAC, particularly close to the EAC split location, somewhere close to ~26.5-29.5°S). Both summer and autumn change in counts for north of EAC remains until midlatitudes (~39°S) remain same. In case of scenario B (**Figure 65d)** Similar but more pronounced rise in counts for north of EAC split location is observed, particularly between 21-28°S. In contrary to scenario A, a minor rise in counts is noted over entire midlatitudes along EAC (30-42°S). A major fall in counts observed over south of ~40°S (~42°S) for summer (autumn)
- The southwest Tasman Sea hotspot also shows **minor** rise in counts, especially during MAM which is likely to influence the southeast coastal area of Australia until east of Tasmania
- Along higher midlatitudes, south of 46°S, a medium to major rise in counts is likely with slightly higher counts during autumn at high latitudes (south of 38°S).
- A medium fall in counts over ~31-37°S is observed for both summer-autumn, over ~40-46°S for summer and over ~41.5-46°S for autumn.
- **Figure 65b** A minor to medium rise in intensity is observed for entire subtropics and midlatitudes, covering east coast of Australia (21-43.5°S), with majority of intense storms likely over (a) north of split location, medium (major) rise in intensity over the hotspot in summer (autumn)
- a major decrease in intensity noted over ~42-50°S, and medium fall south of 50°S.
- In case of Scenario B, **Figure (65e)** similar results valid for scenario A except for a minor rise in hotspot intensity rather than medium to major shown by A.

This implies that scenario A estimated a medium to major rise in counts over subtropics, and that also matches to that of scenario B; medium to major rise in counts for high latitudes, which is however, exactly contrary to that of scenario B; a minor rise over the hotspot, which matches to that of scenario B; and a medium reduction over EAC remnant (after split of EAC), which is in contrary to scenario B; and a major (minor) fall over Tasmania in summer (autumn), which matches to B. The future change in storm intensity is likely to rise greatly for subtropics (~21-30°S); a medium over EAC remnant (~30-38°S); and minor to medium (scenario A) rise over the hotspot, especially during autumn. These areas also roughly define the areas of likely extreme events in future. The storm central pressure is likely to follow similar pattern of change as storm intensity, however, at further milder scale.

*Conclusion: All the above changes for zone I when seen in the light of the model performance (**section 6.3**) for austral summer show that the three predicted storm indices (computed based on T2T1 and T3T1 cases) gave low deviation when compared to the observational storm data with an error of 0.009 (storm counts), 0.003 (storm intensity) and 0.005 (storm central pressure). T2T1 predicted historical storm counts show higher confidence than that by T3T1 case with least deviation for all the three indices. For 20-30°S counts are slightly overestimated, implying that definite rise in future storm counts is likely over EAC pathway. Similarly, the predicted storm intensity shows slight overestimation over 20-25°S and 30-35°S bands, whereas, slight underestimation over 25-30°S, and exact match for 15-20°S. Referring to the mapped changes for zone I (**Figures 65, 66**), slightly lesser intense storms is definite to occur over 20-25°S and 30-35°S, minor rise over 25-30°S, and same as mapped for 15-20°S. The storm central pressure that is more accurate for all the four latitudinal bands, implies more or less same changes as mapped in **Figure 65 and 66**.*

Similarly, for zone I austral autumn, T2T1 predicted historical storm indices show higher confidence than that of T3T1. Hence, the changes in future storm indices are likely to follow the model performance as mentioned for DJF with only one exception, where the storm central pressure near 30-35°S show overestimation.

(b) Zone-II (Tasman Flow)

- Greater rise in counts is observed for DJF (MAM) from ~21 to 36°S (~40°S). The rise is similar for both seasons and more pronounced over ~28-36°S.
- Greater fall in counts noticed over south of 36°S (40°S) for DJF (MAM)
- Referring to **Figures 65b and 65e**, the storm intensity is likely to host medium to major rise for both seasons.
- Referring to **Figure 65c and 65f**, scenario A shows that storm central pressure is likely to reduce greatly over the subtropics and midlatitudes (~21-36°S), however, south of 36°S (covering mid and high latitudes), it is will greatly increase.

- In case of Scenario B, a minor reduction for subtropics (higher midlatitudes), especially in autumn until ~36°S (south of 40°S) is likely. In contrary to this, a major rise in central pressure is likely for mid and high latitudes between ~37-46°S.

To conclude, the South Island and its western ocean area is expected to host lesser number of storms in future, whereas the North Island and its western ocean area will see a medium rise in storms.

Greater number of extreme events are likely to occur during summer, especially over Tasman Sea area (between ~28-38°S). This consequently might also influence the Tasman Sea storm intensification, implying that the extratropical transitioning is likely to be more vigorous between ~28-38°S. This is followed by a medium rise in intensification of storms over higher midlatitudes (~38-40°S), also accompanied with major lowering of the future storm central pressure (scenario A only) forming or passing through the Tasman Sea.

*Conclusion: Above prediction on changes in storm indices for zone II (austral summer) when seen in the light of model performance (**section 6.3**), show T3T1 to closely represent the predicted historical storm counts. This implies that the future change in storm counts shown by **Figures 65 and 66** are underestimated for 20-25°S and 35-40°S; and as a result storm counts are expected to rise even more than mapped in the said figures. Apart from the confidence in increase in counts for the above said bands, validated data contrarily show minor overestimation for 15-20°S, 30-35, 40-45°, and medium overestimation for 25-30°S. This implies that the rise in counts is definite across all latitudinal bands (15-45°S) with slightly lower rise over 25-35°S as compared to mapped changes (**Figures 65 and 66**).*

*For midlatitudes (35-40°S), the estimated fall in counts would be rather milder than that shown by **Figures 65 and 66**. Similar significance of estimated intensity fits for all the latitude bands except considerable underestimation observed for 25-30°S, implying occurrence of more intense storms there.*

*The predicted storm central pressure is significantly overestimated for 15-25°S, minor for 30-35°S and significantly underestimated for 25-30°S, implying that the predicted future central pressure would be much lower than shown by **Figures 65 and 66** for 15-25°S and 30-35°S, whereas it would be moderately high for 25-30°S.*

*For zone II austral autumn season, both T2T1 and T3T1 predictions are almost similar and show an underestimated storm counts for 15-25°S and 35-40°S, implying that the increase in counts is definite but with higher magnitude for these bands. On the other hand, for 25-35°S both the predictions show considerably overestimated counts, implying definite increase in counts but with much lower magnitude. The higher midlatitudinal storm count is expected to be as mapped in **Figures 65 and 66**.*

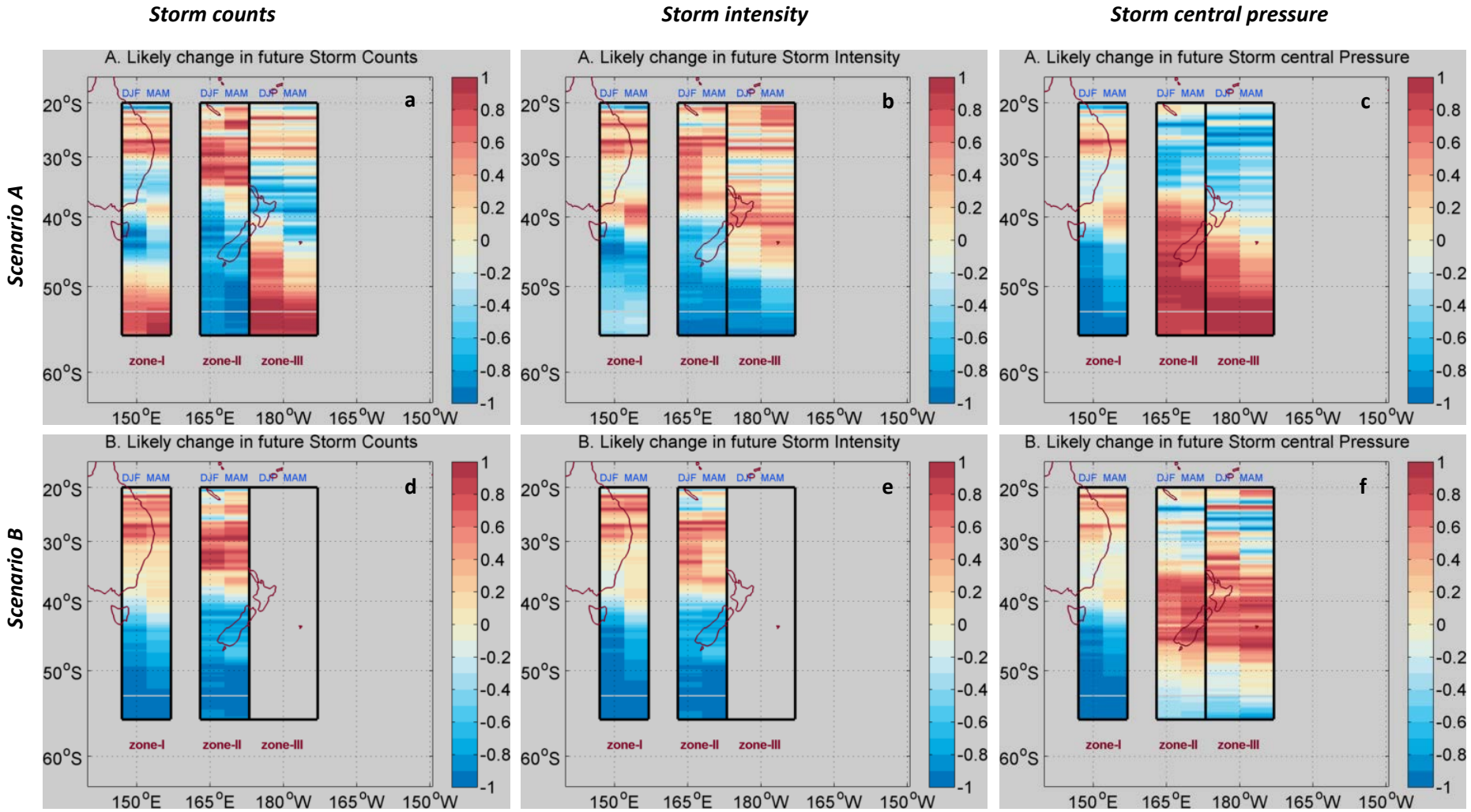

Figure 65 *Composite mapping of seasonal variability of future storm indices for two different scenarios*

Rows depicts different scenarios (A and B); Each Storm indices (i) counts, (ii) intensity, and (iii) central pressure are depicted under three columns

In case of historical storm intensity, T3T1 prediction gives closer estimation than T2T1. It shows minor overestimation for 20-30°S, and major for 30-35°S, implying that the future change in storm intensity would be slightly (significantly) lower for 20-30°S (30-35°S) than the mapped intensity shown in ***Figures 65 and 66****. For other bands, 15-20°S (35-40°S) considerable (minor) underestimation is seen, which will definitely cause comparatively higher future storm intensity than that mapped in the said Figures. The higher midlatitudes (40-45°S) show accurate estimation of change in intensity.*

The historical storm central pressure shows similar estimation for both T2T1 and T3T1, with major underestimation for 25-30°S. However, as per the future change in storm central pressure for 21-36°S, it is likely to fall greatly. These contradictory estimations imply definite but mild reduction in magnitude of storm pressure around this band.

(c) Zone-III (East of North Island, NZ)

- Over subtropics (~20-30°S), storm counts are likely to see minor to medium rise for both seasons and south of 40°S (45°S) for DJF (MAM), implying that southern NI and east of SI might receive medium to major rise in storms in future
- Over the midlatitudes areas including north of NI, Bay of Plenty, northeast of NI, east of NI - are likely to receive much lesser number of storms for both summer (and autumn) until ~39°S (~44°S).
- For higher midlatitudes, the number of storms are likely to greatly increase from south of 39°S (~44°S) for DJF (MAM)
- During summer, north and east of NI until 39°S (i.e. until Taranaki and northern Hawke Bay) are likely to receive minor to medium rise in storm counts. This during autumn however,
- Strom intensity over subtropics to midlatitudes until ~49°S is likely to go through minor to medium rise for both seasons
- Interesting part is the change in the midlatitudes, covering entire NI and its surrounding including BOP and east of NI and SI, which is expected to receive greater number of intense storms even when total counts are likely to reduce drastically. For subtropics to midlatitudes, this rise in intensity is accompanied with lowering of central pressure (scenario A)

There is an exception for Zone III, lying east of NZ, an open sea area. Due to missing and insufficient storm data on maximum wind speed and storm central pressure for the validation period (1960-64), the historical storm activities could not be validated. Lack of sufficient data for the evaluation period lead to lack of validation, hence the future storm changes mentioned above for Zone III cannot be confirmed with confidence.

CHAPTER 7

Discussion

The goal of this research study is to eventually delineate possible scenario(s) of changes in future storminess for Southwest Pacific region, keeping New Zealand as the focal area. With this goal in mind, we started studying the observational Southwest Pacific storm dataset for past four decades that illustrated geographical distribution of change in storm indices (see **Figure 3**). It further gave clue on (a) reducing storm counts over the years and (b) comparatively more number of storms attempting to intrude the higher latitudes. The intrusion of storms into newer areas also has a direct implication on vulnerability of life, economic loss due to rise in precipitation and windy conditions, as well as due to the surge accompanied with such events. Thus it is imperative to learn more on how storminess might be changing in future.

To illustrate clearly the meridional storm variability, a histogram **(Figure 4**) is drawn. Unlike other regions of the world, the midlatitudes of SWP is fascinating area to study when storm change in concerned, as these areas receive both midlatitude winter storms as well as summer-autumn tropical storms. In addition to these recent change in storminess, previous studies (as mentioned in **section 1.1.4**) highlight the possibility of reduction in number of convectively driven tropical storms in general, but an increase in intense ones, perhaps caused due to ongoing climate change. It is important to note that this region is less studied compared to other parts of the world ocean, along with non-availability of reliable observational dataset on atmospheric and oceanic parameters due to lack of buoys or gauges. Additionally, at times, two different set of data on same parameter do not match with each other. While studying change in storminess, coarser resolution global model data has limitations (described in

section 1.2.1). We therefore, used a tool that can resolve the global signature into regional scale to make best estimation of future changes. As part of the study, three different objectives are set to meet the goal mentioned in the beginning. Please refer section 1.3 for an overview of these research objectives. It is to be noted that some terminologies used in this study are exchangeable, for example (i) environmental or climate or climatic; and (ii) variables or indices.

This chapter begins with a discussion on linkages between recent changes in storm climate and large scale environmental variability that can help determine underlining mechanisms instrumental in change in storminess (refer **section 7.1**). The following **section 7.2** describes the scenarios of likely changes in the future austral summer-autumn storminess. At the end of **section 7.2**, change in future winter storminess is discussed based only on large scale variables as data on austral winter storm is not available.

7.1 *Influence of large scale environmental variability on change in storminess*

The analysis of relationship between large scale environmental variables and storm indices in the current study show that latent heat flux and specific humidity are the most crucial environmental indices in influencing the Southwest Pacific change in storminess. They are followed by air-sea temperature difference, and several low impact indices, like, air and sea surface temperature, PBLH, local wind and precipitation rate. Here it may be noted that some of these indices like wind speed and rate of precipitation, could be the result of changing storminess in the area, and may not be the cause or source of change in storminess. In the following paragraph, the respective changes in large scale environmental variables that are presented in chapter 5 are discussed first. Based on the precedence of change in various large scale environmental indices, their influence on the process of changing storminess, the basic mechanism that works behind such changes is discussed.

Further, the simulated regional SWP14 model results clearly depict that by the end of 21st century, both SAT and SST are likely to increase considerably over midlatitudes followed by subtropics and over an unique location, lying south of the Tasman Sea or northeast of Tasmania (~40°S, 150°E), which is also sometimes called the *southwest Tasman Sea hotspot* (see Ganachaud et al. 2014). Over the subtropics the air is likely to become warmer by 3.5-4.8°C, whereas crucial rise in temperature (4.5-6.8°C) is likely over the midlatitudes (~28-45°S). Thus, warming of air and sea in future days are likely to become more pronounced over the middle latitudes (~30°S to 45°S), especially near the south of Tasman Sea (by 6.8 °C), the southwest Tasman Sea hotspot and around northeast of North Island (by 6°C). This implies that the hotspot, which is otherwise much colder region at the southwest of Tasman Sea is likely to acquire by the end of 21st century, a peculiar but significant warming of 6.8°C. Similar pattern of change is seen for SST (refer **Figure 37)**, where among all the four seasons, summer and autumn sea surface temperature rise is predominant for middle latitudes (~ 30-40°S), with maximum value reaching ~ 8 °C

(9 °C) in summer (autumn) near southwest of Tasman Sea hotspot (~ 40°S, ~ 150°E), ~ 5 °C along Tasman Front, and ~ 6 °C east of North Island.

From future storminess analysis, it is noted that although SAT and SST are the key indicators of upper ocean and lower atmosphere conditions, their difference rather is found to be more crucial than the two variables, especially when atmospheric instability is concerned. The air-sea temperature difference defines the vertical stability in the near-surface region (Cayan, 1980). The author further suggests that during stable conditions, the overall pattern of this index (SST-SAT) is found to be negative over larger ocean, which implies usual sensible heat transport from ocean to atmosphere.

Within the dynamics of marine atmosphere boundary layer, the magnitude and sign of buoyancy flux between ocean and atmosphere assists in defining the change in strength of coupling between the two, which further can assist categorize the near-surface atmospheric conditions of an area as stable or unstable. The unstable conditions are particularly potent to lead to enhanced vertical transport via atmosphere (Kettle 2015) and may be related to convection, enhanced near-surface fluxes and reduced near-surface wind shear (Thomas et al., 2013). In current storminess analysis, sea minus air index (SST-SAT) is found to be positive, i.e. unstable conditions are particularly likely over areas where western boundary current is flowing, like EAC, Tasman Sea, Bay of Plenty, eastern and southeastern parts of North Island for austral summer-autumn. This index is considered important in driving atmospheric instability, cloud formation, and precipitation pattern, especially along the coastal areas (Nouri et al. 2013). In other words, the positive values of (SST-SAT) index prominently identifies the mid-latitudinal areas with a potential for atmospheric instability (see the shades of red in **Figure 12d-15d** in chapter 5). Among these three seasons, autumn is likely to host major atmospheric instability, followed by summer, especially in the mid-latitudinal areas ~32-45°S. Significant instability is likely for the southwest Tasman Sea hotspot and only minor for north to northeast of North Island during winter. This however, further expands to open ocean at higher latitudes, down southern ocean, south of 50°S during spring.

Over tropics, one of the many necessary conditions that decide the tropical storm formation is the minimum SST of 27-28°C. From current analysis of change in storm activity, it is concluded that any change in gradient SST has a vital impact on all the three storm indices, whereas SST does not evolve as the most influential parameter. This fact is also supported by other literatures (Bengtsson et al. 2009; Inatsu et al. 2003), who claimed that mid and high latitude storm formation and intensification are proportional to the change in gradient SST rather than SST itself. However, it is emphasised that SST in midlatitudes has a major role in the background, as a 'causal agent' that aids in developing favourable conditions for storm formation and intensification, which are defined by various derived indices, like, latent heat, specific humidity, including air-sea temperature differences. The regional SWP14 modelled specific humidity (**Figure 31)** follows the changing pattern of SST, and it is expected to increase for

subtropical to midlatitude regions up to 50°S, illustrating a maxima near subtropics, along EAC, in Tasman Sea along EAC path, and north of North Island extending northeast. Further an increase in LHF (**Figure 34)** for summer-autumn seasons is likely, especially over the midlatitudes (~20-40°S) to rise by at least 20 Wm^{-2} in summer, with maxima noted over the Southwest Tasman Sea hotspot (of ~74 Wm^{-2}). However, poleward of 40°S, especially close to the coasts (such as, Tasmania and South Island), the latent heat has reduced by ~12 Wm^{-2}.

Based on above information, to further understand the importance of SST as a causal agent, it is essential to discuss about the Clausius-Clapeyron relation: accordingly, when surface temperature is increased, the amount of water vapor in the atmosphere (or humidity) is increased too, which is capable to power up the severe weather systems. This in turn is capable to stimulate the role of water vapor by increasing evaporation and amount of warmer air that further increases the atmosphere's heat trapping or holding capacity. As a result, this increased amount of heat trapped not only helps a storm to strengthen faster but also keeps it active for a longer duration due to availability of extra energy. In addition to all these, a number of studies emphasize the role of warmer sea surface and its response on storms in a region. In similar context, importance of the role of SST in hurricane-ocean energy exchange and as a source to boost the static energy of PBL in attaining as well as maintaining a specific level of hurricane category is discussed by Ooyama (1969). In the current analysis, PBLH is also found to play an active role in change in storminess. The processes that control the planetary boundary layer (PBL) depth are important to further understand the processes related to various fields of weather, climate, and air pollution (Mcgrath-Spangler & Denning 2013). This turbulent wind layer is the lowest layer of troposphere, lying closer to the earth's surface and responds to the surface frictional disturbances (from surface vegetation or topography) within an hour or less (Wisse & Arellano 2004). This layer actively participates in the exchange of energy, moisture, momentum, carbon and pollutants between surface and atmosphere. With reference to **Figure 33**, the downscaled PBLH during summer-autumn shows minor increase around north of North Island, east-southeast of North Island, and at subtropical east of Australia. The only location that shows a maximum rise in middle latitude is around southwest of Tasman Sea hotspot. The corresponding values of heat (**Figure 35**) and moisture fluxes (**Figure 36)** are also likely to rise for the Southwest Tasman Sea hotspot by ~17-19 Wm^{-2}. At the same time, these fluxes are likely to reduce for south, southeast and east of the South Island. As both wind speed and volume of air are function of temperature, the PBL depth tends to be enhanced during warmer seasons and daytime allowing greater convective mixing. Similarly, it contracts during colder seasons and night time, identical to compact and denser layer of cold air mass. Further, an increasing amount of moisture and heat within the PBL may drive it to instability. Consequently, the intensity of any convectively driven system, (like thunderstorm or tropical storm) is deeply related to the source of heat and moisture available at its base/surface and is defined by the physical characteristics of PBL, which supports in driving and even sustaining such systems via vertical transport of energy and moisture (Wisse & Arellano 2004). An increased PBL height encourages increased vertical mixing, increased surface

temperature and reduced relative humidity (Zhang et al. 2011). As the PBL height controls both radial and vertical distribution of momentum and enthalpy, it plays an important role in transporting energy and hence has a major impact on storm formation and intensification (Mcgrath-Spangler & Denning 2013).

In addition to the above environmental indices, a dominant increase in LHF (see **Figure 34, 12-15g**) is visible over midlatitudes, which remains within the range of ~25-40°S, varying with season, covering the path of EAC (with lowest rise of 22 Wm^{-2} at subtropics) reaching a conspicuous peak rise by 74 Wm^{-2} covering areas of Southeast of Australia extending poleward until the northeast of Tasmania. The latent heat flux is involved in phase change of water and plays an important role in transfer of heat from equator to poles and hence participate in driving the general circulation of atmosphere. As we know, latent heat of condensation is the energy released into the atmosphere when phase change happens from water vapor to liquid. This extra amount of heat energy in the atmosphere is used to heat up the surrounding air, making it lighter enough to rise high in a faster pace, hence allowing more amount of air to flow into the system that may promote storm conditions. All together it implies that in future the area followed by the path of EAC alone would be able to support comparatively much higher quantum of the latent heat flux than its surrounding area of subtropics to midlatitudes latitude bands mentioned, when compared to the historical time slice. In general, a 5 Wm^{-2} rise is normal for the band, while looking around North Island, couple of conclusions could be drawn: considering the eastward flowing regional circulation, a poleward moving meridional pattern of increased LHF stretch can be seen at northwest and north of NI that even extends to the northeast of North Island. Note that this increase of 22 Wm^{-2} in LHF also covers the Bay of Plenty area, which remains an interesting research area from point of view of marine diversity coastal management and beach protection during extreme events.

All this implies that wherever the LHF increases, it leads to rise in the heat holding capacity of the air parcels there. Such a rise in LHF in all the above areas is likely to hold extra energy in the system, following Clausius-Clapeyron equation and hence would support at time of storm genesis and or intensification as well as its sustenance for relatively longer duration in these areas: along EAC, northwest to north to northeast of North Island including the Bay of Plenty area, areas far northeast of North Island might see an increase in its storminess.

The autumn (MAM) season continues to follow similar conclusions as mentioned above for summer, however, with more strong values, wider coverage than that seen during summer, where the likely increase in latent heat is likely to further rise. The wider coverage in autumn also covers a larger part of the area away from the EAC, the Tasman Sea area, which might rise by 35 Wm^{-2} at Northwest of North Island, by 24 Wm^{-2} for entire Bay of Plenty, by 46 Wm^{-2} at the southeast of North Island, apart from the wider coverage around northeast of the North Island.

Finally, on a different note, it is also observed that the difference maps related to temperature, also illustrate the extension in EAC path before it meanders eastward to Tasman Sea as Tasman Front. In control result, the EAC branched off at ~31°S, whereas in scenario it travels further south by 2-2.5°S before turning east.

7.2 *Scenarios of likely changes in storminess by the end of 21st century*

As mentioned earlier, the estimation of likely change in future storminess is purely based on the changes observed in the storm observation in past four decades and corresponding data on large scale environmental variables. From the analysis, two different case studies are investigated for respective changes: Scenario A is based on the changes in climate and storm indices between (1985-1999) and (1970-1984), whereas, Scenario B is based on the changes between (2000-2014) and (1970-1984). This way of choosing a constant reference period (1970-1984) also aids in gauging relative change in the magnitude. A ***composite*** figure depicting change in three different storm indices has been illustrated by **Figure 66**. Note that, for east of North Island (zone-III), perhaps due to non-linearity between the storm indices and corresponding environmental indices, the future change in storm counts and intensity could not be estimated and hence is not presented under scenario-B. Following paragraphs discusses on how the pattern of genesis and or intensification of storms might look like by the end of 21st century. The discussion is mainly focusing on significant areas of storm genesis and intensification, like, EAC, over Tasman Sea, over east of North Island and other areas of significance. Since the storm dataset covers only the austral summer-autumn time storm season records, therefore, in this study we are limiting our discussion to austral summer-autumn storms that undergo extratropical transitioning process while migrating from tropical to extratropical areas of the Southwest Pacific region.

The future storm scenarios have been illustrated for austral summer and autumn season in **Figure 65**. The likely change in all the storm indices are encapsulated within each zone to produce one compact figure for each season, where the abbreviations SC, SI, SP corresponds to storm counts, storm intensity and storm pressure, for respective zones. The discussion on future storminess will follow region's western boundary current flow, starting from subtropics to middle and then high latitudes. While moving poleward from 20°S, an overall rise in the number of storms and corresponding storm intensity are likely for the subtropical areas between 22-30.5°S, with substantial rise noteworthy somewhere between 26.5-29.5°S, i.e. just before the location where EAC is known to split. Note that this rising pattern is also accompanied by an increase in the storm central pressure. For subtropics (20.5-30.5°S), more or less similar pattern of changes in storm indices can be noted for the second scenario B.

Before moving on the main core of EAC, let us look into the remnant flow of EAC that still travels along with the east coast of Australia towards Tasmania. Here, the midlatitude storm activity (between 30.5 and 38°S) shows discrepancies between two scenarios. Scenario B continues to follow subtropical changes in a milder tone of increase in storm counts and central pressure (along 30.5-40°S), whereas,

scenario A contradicts, showing mild to medium reduction in storm counts that either originate or pass through. Except the mismatch in estimation of counts and central pressure, both the scenarios estimates likely increase in storm intensity, where scenario A (B) intensity is accompanied by slight reduction (rise) in storm central pressure. These changing patterns and discrepancies connote two possibilities: (a) either more number of storms are able to intrude the higher midlatitudes (30-40°S) due to availability of conducive environmental conditions and travel down south from subtropics (20-30°S) to midlatitudes 30-40°S along remnant EAC; (b) or, more number of storms are expected to develop along the EAC remnant pathway due to conducive large scale environmental conditions aiding in the growth of storms into more intense form than observed in the recent past.

To decide which option is more likely, let us also revisit the corresponding changes in couple of large scale environmental variables detected at south of Tasman Sea hotspot along the extreme south of Australian east coast: (a) maximum surface warming is likely at this hotspot (~39°S, ~152°E) for all the four seasons. It clearly illustrates the intensification of warming along the southern residual of EAC by the end of 21st century, which may also add to the warmth of the Southern Indian Ocean. (b) a positive feedback is potentially active towards the unusual warming at about 37°-42°S, 150°-152°E that works as a closed loop – 'at first, the area is in close proximity to two land masses (Tasmania at south and Australia at north-west); second, the warmer EAC in future scenario flows down to southern residual of EAC to the area of temperate colder water at 40°S' – both these factors are expected to result into considerable reduction of land-sea thermal contrast of the area. (c) Finally, the poleward shift in high pressure belt further weakens the wind system there, hence adds to the surface temperature of the region (also confirmed by point-a). This reduced thermal contrast along with weaker winds in this zone would make its weather more calm, raise its local surface temperature and may even reduce any possibility of midlatitude storm genesis. However, this condition is capable of sustaining the supply of extra amount of energy that is trapped within its near surface atmosphere due to warmer surface enabling longer duration of storms. In other words, such conditions suggest that the first option is more likely, where more number of storms that have already formed at subtropics (20-30°S) would be able to live longer and intrude into the higher midlatitudes (30-40°S) along remnant EAC. This further confirms the fact of gradual reduction in total storms over midlatitudes (30.5-42°S) that are seen to form/pass by during 1970s (See **Figure 3**) over the remnant flow of EAC (after branching off, south of 30°S towards Tasmania) continues to follow.

In addition to this, the area between ~38-41°S is likely to go through relatively medium rise in storm intensity along with slight reduction in counts and slight increase in central pressure. This feeble rise in storm counts close to ~38-41°S, along with a mild to medium rise in intensity along 36-42°S together indicate towards an increasing possibility of (i) although relatively lesser number of storms that travels down south from subtropics over southern residual of EAC (scenario B), (ii) however, are expected to quickly develop into more intense storms. In other words, even though smaller in numbers, the storms

travelling into the southern EAC residual might go through vigorous extratropical transitioning process over EAC remnant flow (~36-42°S), making the coastlines and open sea area of south-eastern Australia more vulnerable to storminess and accompanied surges. Such projection of storminess on one hand indicates development of unfavourable environmental conditions towards formation of storms in general, resulting into lower total counts over EAC remnant. Whereas on other hand it also indicates that once the environmental conditions become favourable towards storm formation, these storms are likely to grow into more intense storms. The corresponding environmental conditions includes changes noted in the large scale climate indices, like change in SST gradient, LHF, specific humidity, SST-SAT; and rise in SAT and SST, apart from other factors, also depends upon the zone.

Let us continue travelling eastward towards North Island along with the main core of EAC that is roughly known to branch off somewhere between 30-34°S (Imawaki et al. 2013), and more specifically observed in current study to split at ~33°S in future. This second area mainly focusses on the Tasman Sea storms, lying west of North Island, New Zealand, where storms are known to undergo extratropical transition more vigorously than those east of NZ (Sinclair, 2002). The estimation of Tasman Sea storm indices show similar changes for both the scenarios except for some discrepancies noted for storm central pressure index. In general, the estimated change shows a possibility of increase in both subtropical and midlatitude storminess mainly between ~26 and 40°S compared to the recent past. More precisely, a conspicuous rise in intense storm activity accompanied by lowering of storm central pressure is likely over Tasman Sea area and at its north. Such likely rise in Tasman Sea storm activity is also reported by Mullan et al. (2011) and Bengtsson et al. (2009).

While continuing our travel further east over North Island, it can be observed that the counts might drastically reduce in contrary to likely rise in intensity, along with a likely reduction in corresponding storm central pressure. It can be concluded from these two observations that (a) extratropical transition process is going to be more vigorous over Tasman Sea, (b) more number of intense storms are likely to intrude into the north of North Island. In addition to this, east of North Island however, shows slightly different pattern of change in future storminess: (c) although reduced number of storms are likely to form over east of North Island region, (d) however, once formed, they are likely to grow into extremely intense storms. This implies that reduced number of extratropical transitioning storms are likely to reach the North Island, however, they are likely to evolve into more intense storms than the ones recorded in the recent past due to accumulated energy available in the warmer atmosphere explained in previous section 7.1.

As we move down south, the South Island as well as entire area south of NZ are expected to receive considerably reduced storm activity, i.e. reduced counts and intensity. This fact of likely reduction of storm activity over the south of NZ also matches with the outcomes of Mullan et al. (2011) and Bengtsson et al. (2009). In addition to this, over east of North Island, an increase in storm counts along with minor rise in intensity over higher midlatitudes (south of 41.5°S) is also observed. This indicate

that although the number of storms (that form/intensify) over east of North Island are likely to reduce, significantly higher number of storms with slightly greater intensity are likely to continue to travel greater distances towards pole at least until ~48°S. Further, poleward of 48°S, although considerably higher number of storms will continue to travel polewards at least until 55°S, their intensity is expected to become weaker as compared to the recent past storms. Over higher midlatitudes: (a) 42-46°S, a substantial fall in all the three indices is noted; (b) south of 46°S, an increased number of weaker storms are expected along with substantially lower storm central pressure.

Overall, similar pattern of changes that are noted above for austral summer season can also be observed during austral autumn season, however, the latter shows more intense features for both simulated large scale environmental and estimated storm indices. Some of the major changes in MAM compared to DJF are: (a) it is observed that the storm counts and intensity along EAC remnant increases especially for southeast corner of the Australia, implying two possibilities: either that availability of favourable conditions that might support the process of transition of tropical storms to travel down south along the remnant EAC so that the tropical storms forming at subtropics near 30°S, somehow infringe into higher midlatitudes until 40°S. Or that there is a greater possibility that a conducive environment is developed over southeast corner of Australia (northeast of Tasmania, 38-42°S, 147-157°E) that might start to support both genesis and intensification of storms. In general, the changing pattern of storminess observed for Tasman Sea and east of NI during MAM is similar to that in DJF, however, with poleward expansion of the rising counts, slightly less in intensity. Note that the magnitude of rise in storm counts/intensity is more prominent during DJF in future days. It is concluded from this that (a) the extreme storminess that is known to be more likely during MAM, is expected to further rise in future, and that (b) the future DJF storminess might see a substantial rise similar to that occurring in MAM in recent past. Reduced counts and a hike in intense storms for MAM shows similar pattern of change as observed for DJF for east of North Island area. However, the storm counts are going to further reduce over southern part and south of North Island. So, almost similar number of storms might travel to higher midlatitudes during DJF and MAM. These findings of decrease in total storm counts along with increase in intense storminess have been supported by many studies (**section 1.1.4**).

The change in future winter storminess is based only on the changes noted in respective large scale variables. Storm data for this season is not available, and therefore it needs further work to confirm. The midlatitude storminess during winter is likely to slightly rise in two small pockets between 150°-154°S: lying south of about 36°S and northeast of Tasmania. This is supported by large scale variables: intensification of winds by 4-5 ms-1, along with substantial rise in PBL height by 60-300 m and accompanied by an increase in latent heat flux by 6-34 Wm^{-2}, in the middle latitudes between 37°-53°S. Further, a sharp change in meridional SST gradients especially around the southwest of Tasman Sea hotspot ranging from 37°-42°S, 150°-154°E are pronounced that may stimulate more frontal storm formation.

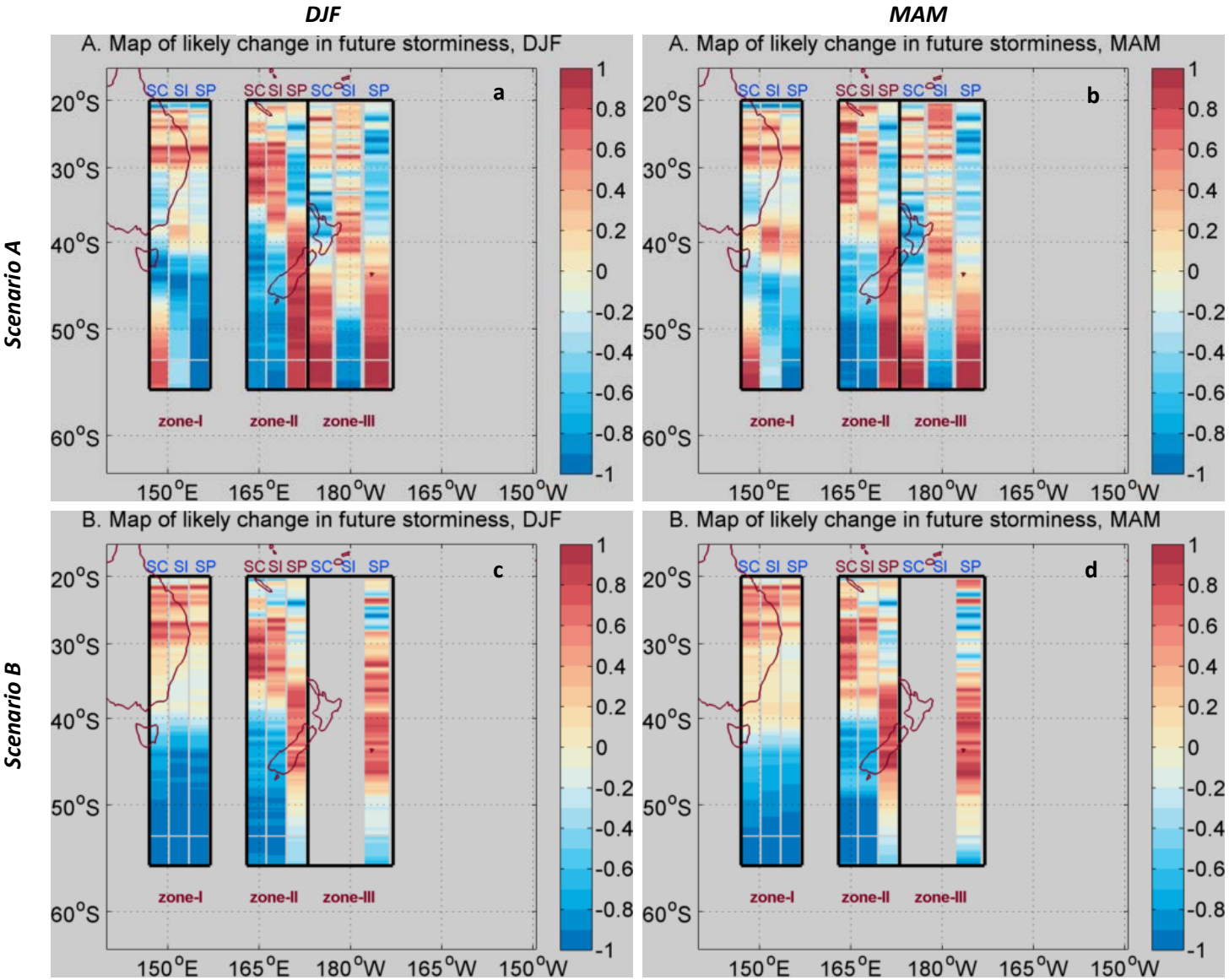

Figure 66 *Scenarios of future changes in the occurrence of storminess for SWP region. Rows depicts scenario A and B; and Columns depict austral summer (DJF) and autumn (MAM) seasons.*

SC → storm counts; SI → storm intensity; SP → storm central pressure

To conclude, these are the areas that are going to be influenced due to considerable rise in LHF a) ~20-40°S by at least 20 Wm^{-2}, b) maximum rise of 74 Wm^{-2} seen for areas closer to south of TS (~40°S, 150°E); c) open sea general rise of ~5 Wm^{-2}. The area of influence for decreasing LHF are (a) poleward of 40°S close to the coasts like Tasmania and South Island; (b) coastal areas closer to islands close to the northern boundary of study area reduced by 12 Wm^{-2}. This implies that wherever the LHF has increased that implies a direct implication of rise in the heat holding capacity of the air. An increase in the LHF also directly implies a rise in the heat carrying capacity of the air there. Such a rise in LHF of an area when seen singly, this held up energy following Clausius-Clapeyron equation would support at times: storm genesis, its intensification as well as its sustenance for longer duration (or increased storminess) in these areas. Accordingly, the areas along EAC, northwest to north to northeast of NI including the Bay of Plenty, areas far northeast of North Island might see an increase in its storminess.

As we have learnt in **section 1.1.4** on changing storminess that a number of literature speaks about: a) a reduction in total number of tropical storms or any convectively driven systems in future b) increase in number of intense tropical storms if favourable conditions occur, causing more destruction. This claim is backed by two simple mechanisms in tropical region: First, the warmer air parcels can hold higher amount of water vapor and so lesser precipitation. Such a condition has a negative implication on the vertical mass flux of the atmosphere-ocean system (Held and Soden, 2006), making less favourable conditions for the ***genesis/onset*** of the storms. Second, once a storm is formed at the tropics, the relatively warmer atmosphere then supports it to continue to intensify by supplying the additional amount of water vapour it has been holding. This extra amount of heat energy in the atmosphere is used to heat up the surrounding air, making it lighter enough to rise high in a faster pace, hence allowing more amount of air to flow into the system that may promote storm conditions. As per Clausius-Clapeyron relation, when surface temperature is increased, the amount of water vapor in the atmosphere is increased too, which is capable to power up the severe weather systems. The warming up of the earth surface, in turn, stimulates the role of water vapor by increasing evaporation and amount of warmer air that further increases the atmosphere's heat trapping or holding capacity. As a result, this increased amount of heat trapped not only helps a storm to strengthen faster but also keeps it active for a longer duration due to availability of extra energy.

To conclude on summer-autumn change in storm activity by end of 21st century, some points are noteworthy. During summer (DJF), the North Island and its surroundings until 39°S (i.e. until north of Taranaki and northern Hawke Bay) is likely to host major reduction in storm counts, whereas south of 39°S a minor rise is expected only over the land area of North Island and medium to major rise in counts is expected over the ocean area south of 45°S. In addition to counts, entire North Island and its surroundings until Cook Strait is likely to experience medium to major rise in intensity. Further south of Wellington, only minor to medium rise in intensity is likely. *This implies that even if the northern to central parts of North Island are likely to host reduced number of storms, they will be more intense.*

Further to this, during summer (i) a minor rise in counts with medium rise in intensity implying a slightly greater number of stronger storms are likely to travel until ~41-44°S. (ii) Although, comparatively a greater number of storms are likely to make their presence felt at higher midlatitudes (~44-55°S or further south) yet stronger ones are likely to influence only until ~49.5°S beyond which increased numbers but weaker intensity storms are more likely. Further south of Taranaki until Cook Strait a minor rise in number of storms with medium rise in intensity is likely to occur. In continuation to this change over land area, a major rise in counts along with minor rise in intensity is likely to occur over ocean. *This implies that the southern part of North Island is likely to receive slightly higher number of storms with medium rise in intensity. It can be concluded that greater number of intense storms will be driven to reach higher midlatitudes until ~49.5°S, beyond which the increased storms are no longer severe.*

During autumn (MAM), the scenario is likely to change slightly: as in summer (DJF), the storm counts continue to reduce, however with increased intensity – from minor to medium over North Island and its surroundings until 39°S (Taranaki and Hawke Bay) and – from medium to major over south of 39°S. *This implies that particularly from south of central North Island i.e. south of 39°S (that includes New Plymouth, Hawke Bay, Napier, Wanganui, Hastings, Palmerstone North, Wellington, and Cook Strait) over land and until ~44°S over ocean are expected to receive medium to major rise in intense storminess, which further continues over ocean until ~49°S to host minor to medium rise in intensity.*

The medium to extreme rise in storminess around North Island is in contrary to South Island, which is likely to experience reduced number of storms that too with weaker intensity for entire summer-autumn season. These results also indicate possibility of more intense storms likely to intrude into the higher latitudes. The density of stronger storm tracks will increase over the ocean area, lying south of North Island at least until ~49°S. Further south of ~49°S, density of only weaker storms are expected to rise considerably.

In addition to the above excerpt, the predicted change in future storm counts and intensity is further conditioned by the historical storm indices validation (section 6.3) for zone I and II. Due to lack of sufficient storm data for zone III for the analysis period (1960-1964), validation could not be performed, hence only zone I and II mapped changes (see **Figures 65 and 66)** are confirmed. The predicted future change in storm counts and intensity for EAC pathway, i.e. zone I, estimated by both T2T1 and T3T1 cases are significant, nevertheless, T2T1 predicted changes are confirmed for accurate mapping (see **Figures 65 and 66)**, with minute deviations in intensity. It confirms a definite rise in storm counts over 25-30°S and slightly lesser intense storms over 20-25°S; minor rise in intensity over 25-30°S; and exactly same intensity as mapped over 15-20°S.

In case of zone II, i.e. the Tasman Flow area, the historical storm indices validation confirms that the subtropical and midlatitude rise in storm counts and intensity would be relatively greater than the

mapped rise (see **Figures 65 and 66**), especially over 20-25°S and 35-40°S; followed by relatively milder rise than mapped over 15-20°S, 25-35°S, 40-45°S. At the same time, 25-30°S shows an exception in the light of validated storm indices: this particular band indicates medium overestimation of storm counts, i.e. comparatively lower number of storms are likely to occur against the mapped storm counts. On the contrary, a conspicuous rise in corresponding storm intensity is expected. These two possibilities together suggest that over 25-30°S latitudinal extent, an increased intense storm activity is confirmed, which further indicates that the storms in this band are likely to undergo an increase in more vigorous extratropical transitioning process.

CHAPTER 8

Summary and Outlook

The midlatitude countries of Southwest Pacific (SWP) region, like New Zealand (NZ), receive at least one-third of the total tropical storms that develop during summer and autumn (Sinclair 2002), apart from the winter midlatitude storms – this rare combination makes it a unique as well as an interesting area of study. NZ receives maximum number of storms during autumn and minimum during spring (Rao et al. 2002).The tropical storms are known to bring along substantial damage to the lives and properties it passes through. With the start of the year, the SWP middle latitudes start receiving extratropical transition summer-autumn storms. Though the season starts from November and lasts until May, the greater possibility of transforming of a tropical storm into extratropical is during February and March (Sinclair 2002) due to favourable conditions. These tropical origin transformed storms though infrequent yet bring with them large-scale destruction in the middle latitudes.

In conjunction with this, in recent decades, perhaps under the influence of changing climate, such storms over SWP region are observed to travel longer distances towards pole as illustrated in **Figures 3 and 4**. Such behavioural changes in storms in a warming climate is a vast scope of research, and an increasing number of studies are utilizing either global or regional general circulation model as tools to estimate likely changes. Since the genesis and sustenance of storms are largely dependent upon the processes related to interaction between the atmosphere and upper layers of the ocean, therefore it is a prerequisite to adopt a tool that is capable to allow frequent interaction between the atmosphere model and the ocean model. The next section summarizes all the chapters including research questions, data used, methodology followed, and results interpretation.

8.1 Summary

The summary comprises of four sections corresponding to four research objectives. The first section outlines the first research objective summarising the strategies adopted for model setup along with its performance.

8.1.1 SWP14: performance and caveats

Research Objective 1: Setting-up and evaluation of coupled atmosphere-ocean Southwest Pacific regional model

(i) setting up of stand-alone SWP regional atmosphere model,
(ii) setting up of stand-alone SWP regional ocean model,
(iii) setting up of coupled atmosphere-ocean SWP regional model (SWP14)
(iv) evaluation of SWP14 set-up

There is a general consensus that numerical models are excellent tools and are applied increasingly to study various environmental aspects, but many a times the relevant details regarding setting up of each model is missing in most of the studies that uses models as their tool. The ROMS and WRF technical/user manuals along with respective public forums provide an excellent resource for users to apply these open source codes for their research objectives. However, the learning curve may be steep and exhaustive if these models need to be developed afresh without previous experience. Therefore, besides presenting SWP14 model and its evaluation, this study also attempts to define different strategies followed with reasons besides defining different model specific terminologies that are used at different stages of model description (chapter 2). This may serve as a primer for a new user to develop his/her own application within comparatively shorter time.

The general circulation models are preferred tool to generate climate scenario, however, there are a couple of caveats to be kept in mind that are related to the use of numerical models for studying storms. These tools are limited by computational costs and as a result can resolve features equivalent to their horizontal grid scale. In addition to that, another caveat is related to the depiction of the moist process. Li et al., (2014) attributed the poor representation of the moist processes in present climate models to be responsible for not able to depict any large changes in the intensity of the extratropical storms with warming climate. Further, the CMIP5 suite of models were found to show an overall underestimation of storm representation (Zappa et al., 2013). Especially, the IPSL-CM5A-LR model (used to enforce regional coupled model boundaries) shows the largest intensity bias on the order of about 20% (austral summer, DJF) and more (for austral winter, JJA) when compared to ERA-Interim data. Apart from this underestimation in intensity, the storm numbers are also found to be lowest by this model during austral winter (JJA) storm season.

In terms of model performance, it is concluded that developed SWP14 model output credibly resembles its forcing data. However, this is not the case for all the samples in terms of validation to the respective regional climatology data. This implies that this coupled SWP14 model projection can further be improved by applying a higher quality forcing data.

It is noteworthy here that the SWP14 could not reproduce both climatology and IPSL forcing SST values for sampling boxes around EAC separation point and Tasman Front that represents strong coupling areas. The outlook **section 8.2.3** discusses on the possible reason behind this mismatch. Note that this part of ocean circulation is particularly complex (Ganachaud et al. 2014) due to EAC branching off as well as due to complex bathymetry (see **Figure 8b**) dominated circulation across Tasman Sea (Imawaki et al. 2013). Therefore, absence of insufficient higher quality observational data across EAC separation point and Tasman Front area perhaps could also be adding to this SST mismatch between SWP14 and climatology. Noteworthy is that while analyzing the SST data, it is surprising to find that CARS and HadISST data differs for the study domain. In this light of potentially missing good quality observational or climatological SST data for the study area, validation of SST is not performed (in chapter 3).

On a different note, in spite of incorrect values of IPSL salinity values, the SWP14 could simulate sea surface salinity (SSS) closer to the regional climatology values. It also does not reproduce the unusually fresher water across the western coast of NZ that is shown by IPSL data. A distinct change in the properties of surface temperature and salinity indicates the changed water properties after branching off of the EAC. Here, the regional scale circulation features, like, the eastward travelling Tasman Front whose path is modulated by the complicated bathymetry of that region seems to be very well resolved by the ocean model, hence, the meandering Tasman Front is also visible. *Although, the resulting regional circulation pattern are well resolved at chosen ~25 km regional scale, however, smaller eddies including few quasi-permanent eddies usually present across the northwest to southeast of the North Island are missing and perhaps demand finer grid resolution.*

The following section outlines the second research objective, summarising the lessons learnt from recent change in the storm activity and corresponding large scale environmental conditions.

8.1.2 Recent past storminess – an observational study

Research objective 2: To draw an overview of geographical distribution of recent (1970-2014) storminess from observational data and to understand large scale environmental conditions and mechanisms supporting such changes

(i) to develop an understanding on region's storm climate and to determine the changes in storminess in last four decades (1970 to 2014),

---

(ii) to understand the changes in large-scale environmental conditions that might have shaped up the recent change in the frequency and duration of storms

Southwest Pacific region hosts both tropical and extratropical storms, which allows it to receive good amount of precipitation almost throughout the year. However, in recent decades an overall reduction in storm and increase in total extreme storminess has been observed. Present study aims to determine change in the storminess of the region, where two fifteen year time-slices are chosen to detect changes during 1985-1999 (T2) with 1970-1984 (T1) as reference period and during 2000-2014 (T3) with 1985-1999 (T2) as reference period. The initial findings on change in overall storminess trend shows a decreasing trend in total storm counts by 5.69% for T2 relative to T1, and 28.64% for T3 relative to T2; a decreasing trend in mean annual storm central pressure reduced by 1.37% for T2 relative to T1, and 1.02% for T3 relative to T2; an increasing trend in mean annual storm wind speed by 13.05% from T2 relative to T1, and 6.99% for T3 relative to T2. The changed geographical distribution of storm track density shows an overall expansion during T2 period with respect to T1. The analysis shows densest storm tracks present during T1 and T2 period predominantly illustrating the vulnerability of the subtropical island nations throughout the period of analysis.

Apart from an overall reduction in the Southwest Pacific summer/autumn storminess from T1 to T3 period, it is interesting to note that the number of extreme storms (category 3 and above) has increased 2.8 (1.93) times during T2 (T3) to T1 (T2). The corresponding rise in mean maximum sustained storm wind speed is 3.47% (1.12%) with a decrease (slight increase) in corresponding mean minimum central pressure by 0.86% (0.10%). The transition time from category 1 (weakest) to 3 has reduced from an average of 42 hours to 30 hours. Further to this, earlier (during T1 and T2) where just one or two category 1 storms took less than 12 hours to intensify to category 3, now (during T3) at least six to seven storms take less than 12 hours to intensify to category 3. This indicates towards higher availability of favourable condition supporting quick intensification of storms to become a major storm. Further, it is concluded that the minimum time taken by category 1 to become 3 (4) is found to have reduced over the last four decades to less than 12 (18) hours.

The above findings on changing storm climatology (reduced counts, quick intensification) are further supported by the second part of the analysis on changing pattern of large scale environmental variables analysed for the same period, which indicated two important facts: firstly, any change in the strength of coupling between air and sea can be related to the SST minus SAT index, where a negative value implies possibility of vigorous atmospheric instability that is found to coincide with an increase in latent heat flux, precipitable water, convective cloud cover, PBLH as well as wind intensity. According to Clausius-Clapeyron relationship, a rise in surface atmospheric temperature results in the rise in amount of water vapour in the atmosphere, which consequently supports the air molecules to retain surplus amount of latent heat energy within them. Following this, the surplus latent heat energy available might

play an active role in intensifying storm conditions as well as support its sustenance. Secondly, any change in the pressure difference map indicates likely change in the storm tracks, where (a) a positive change indicates a likely reduction in the number of tracks passing through, (b) a negative change indicates more number of storm tracks are likely to pass by.

These recent changes in storm climatology (reduced counts, change in tracks, increased wind intensity) has become a cause of worry: insufficient precipitation in several areas than earlier; many new areas that are ill-prepared are now hosting major storms; increased coastal development is affected by erosion due to heightened waves and storm surges. This study appreciates the present changes in storminess as well as large-scale environmental conditions of the Southwest Pacific domain, and is used as a baseline data to further investigate the future changes in the region's storminess.

The next section presents the third research objective, summarising the seasonal comparison of simulated large scale environmental variables at regional scale for historical and future experiments, along with their differences.

8.1.3 Regionalization of large scale circulation

Research objective 3: To determine any likely changes in the simulated regional scale key climatic parameters that may follow by the end of 21st century

---

The following inferences are based on mean seasonal differences (RCP8.5 minus historical) of six large scale environmental variables that are simulated by SWP14 model. The likely change distinctly shows that although the near-surface (~2 m or lowest troposphere) warming is evident up to ~ 50°S for all seasons, an extraordinary warming at middle latitudes (between ~30°-40°S) during summer is conspicuous. This unusual coverage can easily be detected by following the path of EAC, at first instance starting from ~27°S up to south of Tasman Sea, ~40°S; at second instance, when EAC detaches itself (at ~31°S for control and at ~33°S for scenario) to continue along Tasman Front touching the northern coast of North Island; and at third instance it continues east of North Island extending beyond the dateline (from 170°E to 170°W) into open ocean without any land obstruction. Apart from these observations, the maximum warming is detected at south of Tasman Sea along the extreme south of Australian east coast at ~ 39°S, ~ 152°E, for all four seasons. It clearly illustrates the intensification of warming along the southern residual of EAC by end of 21st century, which may also add to the warmth of the Southern Indian Ocean.

We suggest that a positive feedback is active towards the unusual warming at about 37°-42°S, 150°-152°E that works as: (a) the area is in close proximity to two land masses (Tasmania at south and Australia at north-west), (b) the warmer EAC in future scenario flows down to southern residual of EAC to the area of temperate colder water at 40°S - Both the factors results into reduction of land-sea

thermal contrast of the area. Finally, the poleward shift in high pressure belt further weakens the wind system there, hence adds to the surface temperature of the region. This reduced thermal contrast along with weaker winds in this zone would make its weather calmer, raise its local surface temperature. Finally, based on the change in SST observed for area of EAC split, it is likely that the location where EAC usually bifurcates (at about 31°S) may move poleward by ~2°.

The following section presents the fourth research objective, which is also the concluding chapter of this study. It utilizes results from chapter 4 to establish relationship between changing large scale climate variables and apply it on to the simulated results from chapter 5 to estimate scenarios of likely changes in future storminess. The results are aligned to meridional variability taking into account zonal mean for selected sampling zones, following the histogram (**Figure 4**) detailing meridional variation in SWP recent storm activity.

8.1.4 Application of SWP14: changing scenarios of future storminess

---

Research objective 4: To eventually construct scenarios of likely changes in the future storminess as a result of the stimulus caused by change in large scale conditions

---

In this study, *storminess of an area* is analogous to the area's *storm activity*, and is defined by the observational records of total storm counts and intensity. Similarly, *change in storminess* is defined by the change in storm counts, intensity and central pressure. However, in the absence of storm observational records, the storm activity as well as its changes are estimated based on the changes in various large scale environmental conditions.

Specific sampling areas (**Figure 42**) where storm genesis or intensification is known to occur are considered for analysis (refer **section 1.1.3**): (a) along the east Australian coast, (b) mid-Tasman Sea, and (c) east of New Zealand. These three areas have been considered for constructing possible change in future scenarios. The multiple regression analysis method based on the least square criterion, where the best fitting line is achieved by computing a minimum sum of squared residuals (Brown, 2009; Alexopoulos, 2010) at 95% confidence interval along with Pearson's correlation coefficient method is used. In general, the analysis uses normalized dataset to compute the coefficients for different zones. The coefficients are computed between change in storm data and change in LSEVs for two cases (T2 minus T1 and T3 minus T1), where T1 is mean of 1970-1984, T2 is mean of 1985-1999 and T3 is mean of 2000-2014. The change in large scale climatic conditions for three different zones are summarised by **Tables 20 to 22**. This is followed by a summary on a set of large scale environmental variables identified to influence the storm indices. Finally, based on regression model equation estimation, scenarios of likely change in future storminess has been summarised from subtropical to higher midlatitude areas, illustrated by **Figure 66**. A seasonal comparison is also illustrated by **Figure 65** to distinctly illustrate how future summer to autumn storm activity might change.

Table 20 *Summary of meridional changes in large scale environmental conditions for Zone-I*

ZONE-I	**SST**	**SST-SAT**	**Gradient SST**	**Δ Specific humidity**
	Over subtropics (~20-35°S), both summer and autumn shows similar pattern of greater rise, however, over midlatitudes their pattern differs: in summer it is noted to be cooler (~37-40°S) followed by slight warming. During autumn, greater warming noted from ~20°S until higher midlatitudes ~47°S with peak at ~37-39° S is likely.	A sharp rise in sea minus air difference over subtropics (~24-33°S) and midlatitudes (~42-45.5°S) during summer and from subtropics to midlatitudes (~24-43.5°S) during autumn. In these areas, a vigorous transfer of heat and moisture is highly possible from subtropics to mid and higher latitudes, perhaps through heightened storm activity.	The sharp variability in future curves implies a major storm activity is likely: (a) over subtropics, north of split of EAC (~26.5-28°S) for both the seasons, with heightened activity possible during summer but unchanged during autumn, (b) over midlatitudes in summer (~38-45°S) and autumn (~37-43°S).	Rise in specific humidity over subtropics and lower midlatitudes (~20-35°S) during summer-autumn matches with SST rise, implying increase in severe storm activity due to increase in atmosphere's heat trapping capacity.
	Δ Latent heat flux	**Δ Precipitation rate**	**Δ PBLH**	**Δ Wind speed**
	A peak in LHF is seen between ~37-42°S. This sharp rise across midlatitudes also show noticeable poleward shift at least by ~5°. This increased amount of heat trapped has the potential to quickly strengthen storms passing by as well as maintaining their longevity.	Polewards of 35°S (40°S), a substantial decrease in summer (autumn) precipitation is likely implying increase in the number of summer storms for ~20.5-24°S and ~28-34°S. However number of autumn storms are likely to increase over entire subtropics (~20-28°S). Future summer precipitation is likely to dwindle substantially, particularly over the midlatitudes (~35-45°S) compared to autumn.	Due to development of possible environmental conditions supporting higher storm genesis and intensification over the subtropics (~21.5-33°S) and midlatitudes (~37.5-44°S), the future summer-autumn storms are likely to observe widened meridional extent towards pole by 4° (reaching until ~44°S). (~21.5-33°S) and midlatitudes (~37.5-44°S), particularly during summer.	The weakest winds that were centred at around 38°S earlier (for T3T1) are likely to shift poleward at around 42°S also resulting in increase in coverage area of weakened wind from ~38-41°S to ~35-45°S. This implies development of a weakened wind system as well as warmer sea surface particularly around the southwest Tasman Sea hotspot and its surroundings, affecting the southeast coastline of Australia, northeast to east of Tasmania.

Table 21 *Summary of meridional changes in large scale environmental conditions for Zone-II*

ZONE-II	**SST**	**SST-SAT**	**Gradient SST**	**Δ Specific humidity**
	An increase in SST is observed over subtropics (~24-40°S) with major rise observed over ~28-36°S during summer and *over midlatitude ~36-47°S during autumn*. This implies that greatest warming of the sea surface is likely to occur over the subtropics in summer, whereas over midlatitudes in autumn	Over subtropics (~20-30°S) more calm atmospheric conditions are likely to prevail, whereas increased atmospheric activity over the midlatitudes (~32.5-47°S), resulting in vigorous storminess over midlatitudes during autumn are likely to prevail	A greater variability is likely in storm activity over midlatitudes for both the seasons. The storm activity over Tasman Sea area is likely to shift poleward by 3° (from 31-34°S to 34-36°S) and by 2° (from ~44-46°S to 46-50°S).	A rise in atmospheric humidity (~20-40°S) together with rise in SST (~28-36°S) is likely to aid in the development of more intense summer storms due to availability of increased amount of trapped energy over subtropics. During autumn, similar change is likely over the midlatitudes ~36-40°S.
	Δ Latent heat flux	**Δ Precipitation rate**	**Δ PBLH**	**Δ Wind speed**
	The areas during summer (~20-35°S) and autumn (~20-30°S), are likely to support rapid growth of more intense and prolonged storms due to availability of extra latent heat energy in the atmosphere.	Midlatitudes (~32-47°S) are likely to host lesser number of storms whereas subtropics (~23-31°S) are likely to host more number of storms, particularly during summer.	Midlatitude (~32-47°S) are likely to host lesser number of storms whereas subtropics (~23-31°S) are likely to host more number of storms particularly during summer	It is likely that the subtropics (25-33°S) might receive stronger winds whereas midlatitudes, south of ~34°S might witness weaker winds.

Table 22 *Summary of meridional changes in large scale environmental conditions for Zone-III*

ZONE-III	**SST**	**SST-SAT**	**Gradient SST**	**Δ Specific humidity**
	During summer a warmer sea surface is likely over subtropics to midlatitudes (~25-40°S) and during autumn over midlatitudes (beyond ~39°S), implying a southward shift in warming pattern from summer to autumn.	Midlatitudes are likely to witness a higher instability in summer, especially south of ~37°S until ~45°S, which further extends poleward during autumn (until ~47°S).	Similar to SST, SAT, and their differences, gradient SST in future autumn registers a positive change at relatively higher midlatitude (~37.5°S) relative to summer (~35°S). This implies an early, heightened and wider coverage of change in midlatitude SST gradient that also is likely to strongly effect higher midlatitudinal storm activity.	Rise is particularly observed for summer and is likely to aid in the development of more intense summer storms due to availability of increased amount of trapped energy over subtropics and midlatitudes, with greatest intensity likely over ~30-40°S. Similar changes are noted for autumn, with major rise in intensity likely for subtropics (until ~35°S), which gradually declines toward midlatitudes.
	Δ Latent heat flux	**Δ Precipitation rate**	**Δ PBLH**	**Δ Wind speed**
	The extra amount of energy available in the atmosphere at subtropics and midlatitudes (~20-43°S for summer, ~20-48°S for autumn) is likely to support rapid growth of more intense and prolonged storms. Heightened storm activity is likely to occur over subtropics to midlatitudes (~20-38°S) in summer and over midlatitudes (~34-43°S) during autumn.	Rate of precipitation in future is likely to decline considerably polewards of ~25°S, however, heightened precipitation is likely to occur for small pockets of midlatitudes, ~34-42°S for summer and ~31-34°S for autumn.	PBLH is likely to decrease in future over midlatitudes and minor rise is likely in small pockets of subtropics (~27-30°S).	The subtropics to lower midlatitudes (~23.5-32°S) are likely to receive stronger winds whereas midlatitudes, south of ~36°S might witness weaker winds.

Most influential large scale factors driving change in storminess: Based on statistical regression analysis, a set of large scale environmental variables are identified to influence the storm indices: (a) When storm counts are concerned, latent heat flux, specific humidity and wind speed are primarily found to be the most influential indices, followed by air temperature and air-sea temperature differences. (b) Similarly, for storm intensity, again latent heat flux, specific humidity are the vital elements, in addition to the secondary elements like air temperature, PBLH and finally SST and wind speed. (c) The change in storm central pressure is also found to be mainly driven by the change in latent heat flux and specific humidity, followed by SST, air-sea difference, in addition to other indices like air temperature, rate of precipitation, PBLH and wind speed. To conclude, current analysis asserts that the latent heat flux and specific humidity are found to be the most crucial environmental indices influencing the Southwest Pacific change in storminess. They are followed by air-sea temperature difference, and other indices, like, air and sea surface temperature, gradient SST, PBLH, local wind and precipitation rate. Current study also noted that any change in gradient SST has a vital impact on all the three storm indices, whereas SST does not evolve as the most influential parameter. This fact is also supported by other literatures (Bengtsson et al. 2009; Inatsu et al. 2003), who claimed that mid and high latitude storm formation and intensification are proportional to the change in gradient SST rather than SST itself. However, it is emphasised that SST in midlatitudes has a major role in the background, as a 'causal agent' that aids in developing favourable conditions for storm formation and intensification, which are defined by various derived indices, like, latent heat, specific humidity, including air-sea temperature differences. Similarly, other indices in regression analysis, are also working within the system to ultimately influence the background mechanism resulting into change in crucial mechanisms. In another observation, it may be noted that some of these indices like wind speed and rate of precipitation, could be the result of changing storminess in the area, and may not be the cause or source of change in storminess. In the following paragraph, the respective changes in large scale environmental variables that are presented in chapter 5 are discussed first.

The location, lying south of the Tasman Sea or northeast of Tasmania (~40°S, 150°E), which is also sometimes called the *southwest Tasman Sea hotspot* (see Ganachaud et al. 2014) is likely to attain greater warmer (by ≥ 6 °C). This hotspot, which is otherwise much colder region at the southwest of Tasman Sea is likely to acquire by the end of 21st century, a peculiar but significant warming of 6.8°C. Similar pattern of change is seen for SST (refer **Figure 37)**, where among all the four seasons, summer and autumn sea surface temperature rise is predominant for middle latitudes (~ 30-40°S), with maximum value reaching ~ 8 °C (9 °C) in summer (autumn) near southwest of Tasman Sea hotspot (~ 40°S, ~ 150°E), ~ 5 °C along Tasman Front, and ~ 6 °C east of North Island.

Estimated scenarios of likely change in the future storminess: The estimation of likely change in future storminess is purely based on the changes observed in the storm observation in past four decades and corresponding data on large scale environmental variables. From the analysis, two different case studies are investigated for respective changes: Scenario A is based on the changes in climate and storm indices between (1985-1999) and (1970-1984), whereas, Scenario B is based on the changes between (2000-2014)

and (1970-1984). This way of choosing a constant reference period (1970-1984) also aids in gauging relative change in the magnitude. A ***composite*** figure depicting change in three different storm indices has been illustrated by **Figure 66**. Note that, for east of North Island (zone-III), perhaps due to non-linearity between the storm indices and corresponding environmental indices, the future change in storm counts and intensity could not be estimated and hence is not presented under scenario-B. The focus is on areas where storm genesis and intensification are known to occur: like, EAC, over Tasman Sea, over east of North Island. The storm dataset coverage is limited to austral summer-autumn time storm season records, which also sets the limits for the analysis.

In the absence of winter storm observational records, the change in future winter storminess is based only on the changes noted in respective large scale variables and hence needs further work to confirm. The higher latitude winter storms present between ~50°-55°S are active throughout the year, in contrary to the midlatitude winter storms that are active only from June to August (refer **section 1.1.3**). It is interesting to study the likely changes in the formation and intensification of the wintertime storms that form and live their lives in middle latitudes. Moving from west to east of the study domain, the first set of such storms, are known as Tasman storms. They are fuelled by warmer and moister EAC, somewhere over ~ 35°-40°S and once they move eastward over Tasman Sea they strengthen and continue to travel eastward till they reach New Zealand. The second set of such storms, form near east-southeast of North Island, at about 30°S, 150°W. These two extratropical winter storm genesis areas and their tracks are likely to be influenced due to changes in the atmospheric circulation. The midlatitude storminess during winter is likely to slightly rise in two small pockets between 150°-154°S: lying south of about 36°S and northeast of Tasmania. This is supported by large scale variables: intensification of winds by 4-5 ms-1, along with substantial rise in PBL height by 60-300 m and accompanied by an increase in latent heat flux by 6-34 Wm^{-2}, in the middle latitudes between 37°-53°S. Further, a sharp change in meridional SST gradients especially around the southwest of Tasman Sea hotspot ranging from 37°-42°S, 150°-154°E are pronounced that may stimulate more frontal storm formation.

To summarise on the response of changing climate on summer-autumn storm activity by the end of 21st century it is concluded that: The areas along EAC, northwest to north to northeast of NI including the Bay of Plenty, areas far northeast of North Island might see an increase in its storminess. During summer (DJF), the North Island and its surroundings until 39°S (i.e. until north of Taranaki and northern Hawke Bay) is likely to host major reduction in storm counts, whereas south of 39°S a minor rise is expected only over the land area of North Island and medium to major rise in counts is expected over the ocean area south of 45°S. In addition to counts, entire North Island and its surroundings until Cook Strait is likely to experience medium to major rise in intensity. Further south of Wellington, only minor to medium rise in intensity is likely. *This implies that even if the northern to central parts of North Island are likely to host reduced number of storms, they will be more intense. Further to this, during summer (i) a minor rise in counts with medium rise in intensity implying a slightly greater number of stronger storms are likely to travel until ~41-44°S. (ii) Although, comparatively a greater number of storms are likely to make their presence felt at*

higher midlatitudes (~44-55°S or further south) yet stronger ones are likely to influence only until ~49.5°S beyond which increased numbers but weaker intensity storms are more likely. Further south of Taranaki until Cook Strait a minor rise in number of storms with medium rise in intensity is likely to occur. In continuation to this change over land area, a major rise in counts along with minor rise in intensity is likely to occur over ocean. *This implies that the southern part of North Island is likely to receive slightly higher number of storms with medium rise in intensity. It can be concluded that greater number of intense storms will be driven to reach higher midlatitudes until ~49.5°S, beyond which the increased storms are no longer severe.*

During autumn, the scenario is likely to change slightly: as in summer, the storm counts continue to reduce, however with increased intensity – from minor to medium over North Island and its surroundings until 39°S (Taranaki and Hawke Bay) and – from medium to major over south of 39°S. *This implies that particularly from south of central North Island i.e. south of 39°S (that includes New Plymouth, Hawke Bay, Napier, Wanganui, Hastings, Palmerstone North, Wellington, and Cook Strait) over land and until ~44°S over ocean are expected to receive medium to major rise in intense storminess, which further continues over ocean until ~49°S to host minor to medium rise in intensity.*

The medium to extreme rise in storminess around North Island is in contrary to South Island, which is likely to experience reduced number of storms that too with weaker intensity for entire summer-autumn season. These results also indicate possibility of more intense storms likely to intrude into the higher latitudes. The density of stronger storm tracks will increase over the ocean area, lying south of North Island at least until ~49°S. Further south of ~49°S, density of only weaker storms are expected to rise considerably.

Change in extreme storminess: With respect to the recent change in storminess, some comments on extreme storm events are given here. The extreme storminess is likely to increase – for subtropical areas north of EAC split location during summer-autumn season; for southwest of Tasman Sea hotspot and its surroundings particularly in autumn; and over Tasman Sea and its north, for entire North Island, its surrounding islands, for coastal waters including Bay of Plenty, Cook Strait, and Hawke Bay particularly during summer season. Over ocean, this feature is likely to further continue to cover the larger ocean lying east and southeast of South Island particularly during autumn season. In addition to the above, the southern parts of Tasman Sea, especially west of New Zealand will receive lesser and weaker storms.

8.2 Outlook

8.2.1 Scope for estimation of change in winter storminess

The change in future winter storminess is based only on the changes noted in the simulated large scale environmental variables. Storm data for this season is not available, and therefore it needs further work to confirm.

8.2.2 Scope for improvement to resolve local scale eddies

There are at least four warm core anticyclonic quasi-permanent eddies documented (see Figure 7 in Ridgway & Dunn, 2003) starting from Norfolk eddy off northwest coast, North Cape eddy off north coast, East Cape eddy off northeast coast and Wairarapa eddy off southeast coast of North Island of New Zealand. These eddies are believed to be controlled by the surrounding bottom topography (Ridgway & Dunn 2003) in the vicinity of North Island and perhaps is the reason why the ~25 km mean grid resolution regional model could not resolve these eddies. This defines a tentative list of future work below:

(i) As detailed in chapter 3, the SWP14 model output illustrates limitations while validating with the long term climatological data of SWP region. At the same time, the SWP14 model performs well when compared to its own forcing input data. Therefore, there is a potential to improve the simulated results by replacing the IPSL_CM5A_LR global input forcing with long term climatological dataset or with another global model output that is known to show better performance in the SWP region (see **Zappa et al. (2010)**. This exercise is expected to show an improvement in model validation and hence an improvement in predictive skills for the region.

(ii) Further enhancement of SWP14 model: This ~25 km mean grid resolving SWP14 regional model may include a series of two-way nested domains that can resolve the bathymetry and air-sea interaction at finer scales. To make a smoother jump between parent and child, it is recommended to use a parent-child ratio of 1:3 spatial (grid structure) as well as temporal (time-step) scale. In another perspective, it is clear from the detailed evaluation of regional model that the SWP14 output closely reproduces the IPSL global forcing with enhanced regional circulation features that are missing in the global forcing data. However, the model results for higher latitudes beyond 55°S does not match to the regional climatology. For more accurate results it is recommended to drive the same regional model using either a long term climatology for general studies or select a more accurate global model data (see models listed in Zappa et al. (2013)) for real-time future projections.

In chapter-5 the results are concluded based on (the near-surface and surface variables) simulated differences between scenario and control experiments. Present analysis is based on the coupled WRF results. WRF stand-alone model results need to be compared with coupled WRF output. Apart from surface and near-surface levels, this analysis is suggested to be extended to utilize various levels of the atmosphere to find change in warming patterns in different levels to explore the causes of climate extremes. Other derived climate indices, like mean available potential energy may also be checked.

The current version of SWP14 model results may be utilized for various purposes as regional scale data source for coastal or impact assessment models that are configured mostly at a very fine scale. However, the above mentioned limitations must be kept in mind.

8.2.3 Scope for improvement of SWP14 settings

While investigating two different sets of simulated SSTs each from coupled ocean and atmosphere components, ocean SST showed larger deviation than atmosphere SST, with respect to the regional climatology. This mismatch of simulated SST between ocean and atmosphere components of SWP14 also indicates a mismatch in equilibrium surface heat flux between the interacting sub-models. Here a probability of climate drift in coupled ocean component cannot be denied. The ocean component could not resolve properly the mixed layer dynamics when compared to that of the regional climatology. These inherent deficiencies of the ocean component are clearly manifested mainly in the strongly coupled areas covering the EAC pathway and Tasman Front, which are represented by underestimated SST and 2 m air temperature values relative to regional climatology as well as to IPSL forcing (see mean trends for boxes 1, 2, 5, and 6 in **Figures 11** and **15**). Since ocean SST also represents optimality between various oceanic processes (like air-sea energy exchange, oceanic transport and vertical mixing) at oceanic PBL, therefore, there are chances that ocean component is potentially introducing errors in the coupled climate simulations.

Despite these errors from coupled ocean component, the coupled atmosphere component of SWP14 could accurately reproduce the input IPSL surface winds (see mean trends in **Figure 17**) for all the sixteen sampling stations. Therefore, coupled atmosphere results are used instead of coupled ocean results for both model evaluation as well as to investigate the applicability of SWP14 data in future storminess.

Coupled climate models are strong research tools to simulate the coupling processes at respective PBLs. So, an improvement of these processes at oceanic boundary layer are suggested to obtain improved vertical mixing of the ocean such that heat fluxes that are fed into the coupled atmosphere model are computed more accurately at every coupling interval. This demands an improvement in formulation of oceanic boundary layer physics by revisiting the vertical mixing parameterization, to represent more accurately the surface and ocean interior mixing in the next version of ocean component of SWP14. This shall help one to reap more accurate simulation of coupling processes, especially in the strongly coupled areas.

8.3 Conclusion

Based on the above analysis, following major conclusions are drawn:

- In the light of historical storm validation, it is confirmed that the predicted future change in storm counts and intensity for EAC pathway (zone I) is accurately mapped by **Figures 65 and 66**, with minute deviations in intensity. For Tasman Flow (zone II), it confirms that over 25-30°S latitudinal extent, an increased intense storm activity is possible, which further indicates that the storms in this band are likely to undergo rapid extratropical transitioning process.
- A new area of storm genesis or intensification has been detected, known as Tasman Sea hotspot (~38-41°S, ~150°E). As the extratropical transitioning process over Tasman Sea area is expected to become more vigorous over ~26-40°S, the North Island is going to receive an increased number of intense

Tasman Sea storms from its west. As we move eastward, lesser number of storms are likely to form or traverse through, however, once formed, they are likely to grow into extremely intense system. Further, these systems are expected to transit more vigorously, invading greater distances into the higher latitudes.

- Though austral autumn storms are known to be stronger and more devastating than the summer storms however, in our estimation in future the austral summer storms are likely to undergo greater transformations compared to the estimated autumn storms, such that the former storms might achieve the intensity/strength of the latter types.
- This premature attainment of intense storminess particularly in summer indicates towards a greater possibility that extratropical transitioning is expected to go through more vigorous process.
- The summer storms are likely to make an impact mainly over the northern part of NI, whereas the autumn storms will influence/cover almost entire NI. The extreme future storminess is likely to occur both during summer and autumn seasons.

References

Aldrian, E. et al., 2005. Modelling Indonesian rainfall with a coupled regional model. *Climate Dynamics*, 25, pp.1–17.

Alexopoulos, Evangelos. (2010). Introduction to Multivariate Regression Analysis. Hippokratia. 14. 23-8.

Bengtsson, L. & Hodges, K.I., 2006. Storm Tracks and Climate Change. *Journal of Climate*, 19, pp.3518–3543.

Bengtsson, L., Hodges, K.I. & Keenlyside, N., 2009. Will Extratropical Storms Intensify in a Warmer Climate ? *Journal of Climate*, 22, pp.2276–2301.

Black, P. et al., 2007. Layer Air – Sea Transfer Experiment. *American Meteorological Society*, (March), pp.357–374.

Boé, J. et al., 2011. What shapes mesoscale wind anomalies in coastal upwelling zones? *Climate Dynamics*, 36, pp.2037–2049.

Brown, S.H.. (2009). Multiple linear regression analysis: A matrix approach with MATLAB. Alabama Journal of Mathematics. 1-3.

Csanady, G., 2004. *Air-Sea Interaction: Laws and Mechanisms*, Cambridge University Press.

Diamond, H.J. et al., 2012. Development of an enhanced tropical cyclone tracks database for the southwest Pacific from 1840 to 2010. *International Journal of Climatology*, 32, pp.2240–2250.

Diamond, H.J., Lorrey, A.M. & Renwick, J.A., 2013. A Southwest Pacific Tropical Cyclone Climatology and Linkages to the El Nino-Southern Oscillation. *Journal of Climate*, 26, pp.1–25.

Diamond, H.J. & Renwick, J.A., 2014. The climatological relationship between tropical cyclones in the southwest pacific and the Madden-Julian Oscillation. *International Journal of Climatology*, 35, pp.676–686.

Döscher, R. et al., 2002. The development of the coupled regional ocean-atmosphere model RCAO. *Boreal Env. Res.*, 7(October), pp.183–192. Available at: http://www.borenv.net/BER/pdfs/ber7/ber7-183.pdf.

Edson, J. et al., 2007. The Coupled Boundary Layers and Air Sea Transfer Experiment in Low Winds. *Bulle*, (March).

Fairall, C.W., Bradley, E.F., Rogers, D.P., et al., 1996. Bulk parameterization of air-sea fluxes for Tropical Ocean-Global Atmosphere Coupled-Ocean Atmosphere Response Experiment. *Journal of Geophysical Research*, 101(C2), p.3747.

Fairall, C.W., Bradley, E.F., Godfrey, J.S., et al., 1996. Cool-skin and warm-layer effects on sea surface temperature. *J. Geophys. Res.*, 101(C1), pp.1295–1308. Available at: http://dx.doi.org/10.1029/95JC03190.

Ganachaud, A. et al., 2007. *Southwest Pacific Ocean Circulation and Climate Experiment (SPICE)-Part I. Scientific Background*, International CLIVAR Project Office, CLIVAR Publication Series No. 111, NOAA OAR Special Report, NOAA/OAR/PMEL, Seattle, WA.

Ganachaud, A. et al., 2014. The Southwest Pacific Ocean circulation and climate experiment (SPICE). *Journal of Geophysical Research: Oceans*, 119, pp.7660–7686.

Grotjahn, R., 2002. BAROCLINIC INSTABILITY. , pp.1–10. Available at: http://grotjahn.ucdavis.edu/Pubs/0076.pdf.

Haidvogel, D.B. et al., 2008. Ocean forecasting in terrain-following coordinates: Formulation and skill

assessment of the Regional Ocean Modeling System. *Journal of Computational Physics*, 227(7), pp.3595–3624.

Haidvogel, D.B. & Beckmann, a, 1999. *Numerical Ocean Circulation Modeling*, Available at: http://books.google.com/books?hl=en&lr=&id=EEvv41rWTTEC&oi=fnd&pg=PA3&ots=qH1OxmBodb&sig=u6pqj4jPYuF0tPkSODui3BGkQuA.

Haney, R.L., 1991. On the Pressure Gradient Force over Steep Topography in Sigma Coordinate Ocean Models. *Journal of Physical Oceanography*, 21(4), pp.610–619. Available at: http://journals.ametsoc.org/doi/abs/10.1175/1520-0485(1991)021%253C0610%253AOTPGFO%253E2.0.CO%253B2.

Hedström, K.S., 2009. *Technical Manual for a Coupled Sea-Ice / Ocean Circulation Model (V3)*,

Held, I.M. & Soden, B.J., 2006. Robust Responses of the Hydrological Cycle to Global Warming. *Journal of Climate*, 19.

Held, I.M. & Soden, B.J., 2000. *Water Vapor Feedback And Global Warming*,

Hoyos, C.D. et al., 2006. Deconvolution of the Factors. *Science*, 312, pp.94–97.

Hu, D. et al., 2015. Pacific western boundary currents and their roles in climate. *Nature*, 522(June), pp.299–308.

Hyötyniemi, H. (2001). Multivariate Regression Techniques and tools, Helsinki University of Technology Control Engineering Laboratory, Report 125.

Imawaki, S. et al., 2013. Western Boundary Currents. In J. G. and J. A. C. Gerold Siedler, Stephen M. Griffies, ed. *Ocean Circulation and Climate*. International Geophysics, Academic Press, pp. 305–338.

Inatsu, M., Mukougawa, H. & Xie, S.-P., 2003. Atmospheric Response to Zonal Variations in Midlatitude SST: Transient and Stationary Eddies and Their Feedback. *Journal of Climateclimate*, 16, pp.3314–3329.

Jimenez, P.A. et al., 2010. Surface wind regionalization over complex terrain: Evaluation and analysis of a high-resolution WRF simulation. *Journal of Applied Meteorology and Climatology*, 49(2), pp.268–287.

Jones, D.A. & Simmonds, I., 1993. Dynnmia A climatology of Southern Hemisphere extratropical cyclones. , (December 1958), pp.131–145.

Keable, M., Simmonds, I. & Keay, K., 2002. Distribution and temporal variability of 500 hPa cyclone. *International Journal of Climatology*, 150, pp.131–150.

Kettle, Anthony James, A Diagram of Wind Speed Versus Air-sea Temperature Difference to Understand the Marine atmospheric Boundary Layer, Energy Procedia, Volume 76, 2015, Pages 138-147, ISSN 1876-6102, https://doi.org/10.1016/j.egypro.2015.07.879.

Kiehl, J.T. & Trenberth, K.E., 1997. Earth's Annual Global Mean Energy Budget. *Bulletin of the American Meteorological Society*, 78(2), pp.197–208.

Klotzbach, P.J. & Landsea, C.W., 2015. Extremely Intense Hurricanes : Revisiting Webster et al . (2005) after 10 Years. *Journal of Climate*, 28, pp.7621–7629.

Lachlan-Cope, T. et al., 2009. Antarctic winter tropospheric warming – the potential role of polar stratospheric clouds , a sensitivity study. *Atmospheric Science Letters*, 266, pp.262–266.

Lambert, S.J. & Fyfe, J.C., 2006. Changes in winter cyclone frequencies and strengths simulated in enhanced greenhouse warming experiments : results from the models participating in the IPCC diagnostic exercise. *Climate Dynamics*.

Large, W., McWilliams, J. & SC, D., 1994. Oceanic vertical mixing: A review and a model with nonlocal boundary layer parameterization. *Reviews of GeophysicsGeophys*, 32(4), pp.363–403. Available at: http://onlinelibrary.wiley.com/doi/10.1029/94RG01872/epdf.

Leckebusch, G.C., Renggli, D. & Ulbrich, U., 2008. Development and application of an objective storm severity measure for the Northeast Atlantic region. *Meteorolohische Zeitschrift*, 17(5), pp.575–587.

Li, H. et al., 2013. Projected climate change scenario over California by a regional ocean–atmosphere coupled model system. *Climatic Change*, 122, pp.609–619. Available at: http://link.springer.com/10.1007/s10584-013-1025-8.

Li, M. et al., 2014. Extratropical cyclones in a warmer , moister climate : a recent Atlantic analogue. *Geophysical Research Letters*, 41, pp.8594–8601.

Li, W. et al., 2012. Intensification of Northern Hemisphere subtropical highs in a warming climate. *Nature Geoscience*, 5(11), pp.830–834. Available at: http://dx.doi.org/10.1038/ngeo1590.

Lim, E.-P. & Simmonds, I., 2009. Effect of tropospheric temperature change on the zonal mean circulation and SH winter extratropical cyclones. *Climate Dynamics*, 33, pp.19–32.

Liu, W.T., Katsaros, K.B. & Businger, J.A., 1979. Bulk parameterization of air-sea exchanges of heat and water vapor including the molecular constraints at the interface. *Journal of the Atmospheric …*, 36, pp.1722–1735. Available at: http://journals.ametsoc.org/doi/abs/10.1175/1520-0469(1979)036%3C1722:BPOASE%3E2.0.CO;2.

Lozano, I. et al., 2001. Storminess and associated cyclone tracks along the Atlantic coastlines of Europe : recent evolution and analysis of an CO_2 - induced climate scenario. , (September).

Magee et al., 2016, An intercomparison of tropical cyclone best-track products for the southwest Pacific. Natural Hazards and Earth Systems Sciences, 16, 1431–1447, 2016

Mcgrath-spangler, E.L. & Denning, A.S., 2013. Global seasonal variations of midday planetary boundary layer depth from CALIPSO space-borne LIDAR. , 118(October 2012), pp.1226–1233.

Mcgrath-Spangler, E.L. & Denning, A.S., 2013. Global seasonal variations of midday planetary boundary layer depth from CALIPSO space-borne LIDAR. *Journal of Geophysical Research: Atmospheres*, 118(January), pp.1–8.

Moum, J.N. & Smyth, W.D., 2001. Upper ocean Mixing processes. *Encyclopedia of Ocean Sciences*, pp.3093–3100. Available at: http://eprints.soton.ac.uk/58872/.

Mullan, B. et al., 2011. *Scenarios of storminess and regional wind extremes under climate change*, Wellington, New Zealand. Available at: https://www.niwa.co.nz/sites/niwa.co.nz/files/slmacc_extremewinds_slew093_may2011.pdf.

Nazarenko, L., et al. (2015), Future climate change under RCP emission scenarios with GISS ModelE2, J. Adv. Model. Earth Syst., 7, 244–267, doi:10.1002/2014MS000403.

Nouri, H. et al., 2013. The Effect of Sea Surface Temperature and 2m Air Temperature on Precipitation Events in the Southern Coasts of Caspian Sea. *Ecopersia*, 1(4), pp.369–383.

Ooyama, K., 1969. Numerical Simulation of the Life Cycle of Tropical Cyclones. *Journal of the Atmospheric Sciences*, 26(1), pp.3–40.

Penven, P. et al., 2001. A regional hydrodynamic model of the Southern Benguela. *South African Journal of Science*, 97, pp.472–476. Available at: http://www.myroms.org/Papers/s_afr_j_sci_2001_97_11-12.pdf.

Petchey, F. et al., 2010. The marine reservoir effect in the Southern Ocean : An evaluation of extant and new deltaR values and their application to archaeological chronologies. *Journal of Royal Society of New Zealand*, 38(4), pp.243–262.

Rao, B. V., Do Carmo, A. & Franchito, S.H., 2002. Seasonal Variations in the Southern Hemisphere Storm Tracks and Associated Wave Propagation. *Journal of the Atmospheric Sciences*, 59(6), pp.1029–1040. Available at: http://journals.ametsoc.org/doi/pdf/10.1175/1520-0469%282002%29059%3C1029%3ASVITSH%3E2.0.CO%3B2.

Rayner, N.A. et al., 2003. Global analyses of sea surface temperature , sea ice , and night marine air temperature since the late nineteenth century. *Journal of Geophysical Research*, 108(D14).

Renault, L. et al., 2010. Ocean-atmosphere-wave coupling : extreme event analysis, forecast and effects in the Mediterranean Sea in May 2010 Motivations • Testing the system : it is still under development -and it is meant to. , (May).

Riahi et al., 2011. RCP 8.5-A scenario of comparatively high greenhouse gas emissions. *Climate Change,* 109, pp. 33–57, DOI 10.1007/s10584-011-0149-y

Ridgway, K.R. & Dunn, J.R., 2003. Mesoscale structure of the mean East Australian Current System and its relationship with topography. *Progress In Oceanography*, 56, pp.189–222.

Rummukainen, M., 2010. State-of-the-art with regional climate models. *Wiley Interdisciplinary Reviews-Climate Change*, 1(1), pp.82–96.

Shchepetkin, A.F. & McWilliams, J.C., 2005. The regional oceanic modeling system (ROMS): A split-explicit, free-surface, topography-following-coordinate oceanic model. *Ocean Modelling*, 9, pp.347–404.

Sikirić, M.D., Janeković, I. & Kuzmić, M., 2009. A new approach to bathymetry smoothing in sigma-coordinate ocean models. *Ocean Modelling*, 29(2), pp.128–136. Available at: http://linkinghub.elsevier.com/retrieve/pii/S1463500309000742 [Accessed August 2, 2011].

Simmonds, I. & Keay, K., 2000. Variability of Southern Hemisphere Extratropical Cyclone Behavior , 1958 – 97. *Journal of Climate*, 13, pp.550–561.

Sinclair, M.R., 1995. An extended climatology of extratropical cyclones over the southern hemisphere. *Weather and Climate*, 15, pp.21–32.

Sinclair, M.R., 1994. An objective cyclone climatology for the southern hemisphere. *American Meteorological Society*, 122, pp.2239–2256.

Sinclair, M.R., 2002. Extratropical Transition of Southwest Pacific Tropical Cyclones . Part I : Climatology and Mean Structure Changes. *American Meteorological Society*, 130, pp.590–609.

Sinclair, M.R., 2004. Extratropical Transition of Southwest Pacific Tropical Cyclones . Part II : Midlatitude Circulation Characteristics. *Monthly Weather Review*, 132, pp.2145–2168.

Skamarock, W. & Klemp, J., 2008. A time-split nonhydrostatic atmospheric model for weather research and forecasting applications. *Journal of Computational Physics*, 227(7), pp.3465–3485.

Skamarock, W.C. et al., 2008. A Description of the Advanced Research WRF Version 3. *Technical Report*, (June), p.113.

Small, E.E., Giorgi, F. & Sloan, L.C., 1999. Regional climate model simulation of precipitation in central Asia : Mean and interannual variability. *Journal of Geophysical Research*, 104, pp.6563–6582.

Soden, B. & Held, I., 2006. An Assessment of Climate Feedbacks in Coupled Ocean – Atmosphere Models. *Journal of Climate*, 19(2003), pp.3354–3360. Available at: http://www.gfdl.noaa.gov/bibliography/related_files/bjs0601.pdf.

Song, Y. & Haidvogel, D., 1994. A Semi-implicit Ocean Circulation Model Using a Generalized Topography-Following Coordinate System. *Journal of Computational Physics*, 115(1), pp.228–244. Available at: http://www.sciencedirect.com/science/article/pii/S0021999184711892.

Stephens Scott A. Stephens, D.L. Ramsay, Extreme cyclone wave climate in the Southwest Pacific Ocean: Influence of the El Niño Southern Oscillation and projected climate change, Global and Planetary Change, Volume 123, Part A, 2014, Pages 13-26, ISSN 0921-8181, https://doi.org/10.1016/j.gloplacha.2014.10.002.

Stocker, T.F., 2013. The Ocean as a Component of the Climate System. In http://dx.doi.org/10.1016/B978-0-12-391851-2.00001-5. Gerold Siedler, Stephen M. Griffies, John Gould and John A. Church, Editor(s), International Geophysics 2013, Volume 103, Pages 3-30, ISSN 0074-6142, ISBN 9780123918512, ed. *Ocean Circulation and Climate*. Academic Press, pp. 3–30. Available at: http://www.sciencedirect.com/science/article/pii/B9780123918512000015.

Taljaard, J.J., 1967. Development, distribution and movement of cyclones and anticyclones in the southern hemisphere during the IGY. *Journal of Applied Meteorology*, 6(6), pp.973–987.

Taylor, K.E., Stouffer, R.J. & Meehl, G. a., 2012. An overview of CMIP5 and the experiment design. *Bulletin of the American Meteorological Society*, 93, pp.485–498. Available at: http://journals.ametsoc.org/doi/abs/10.1175/BAMS-D-11-00094.1.

Thomas, N & Seim, Harvey & Haines, Sara. (2015). An observational, spatially explicit, stability-based estimate of the wind resource offshore of North Carolina. Journal of Applied Meteorology and Climatology. 54. 150828110930006. 10.1175/JAMC-D-15-0090.1.

Tilburg, C.E. et al., 2001. The Dynamics of the East Australian Current System : The Tasman Front , the East Auckland Current , and the East Cape Current. *Journal of Physical Oceanography*, 31, pp.2917–2943.

Wang, S. et al., 2008. The impact of climate change on storm surges over Irish waters. *Ocean Modelling*, 25, pp.83–94.

Warner, J.C. et al., 2010. Development of a Coupled Ocean-Atmosphere-Wave-Sediment Transport (COAWST) Modeling System. *Ocean Modelling*, 35(3), pp.230–244. Available at: http://woodshole.er.usgs.gov/publications/warner/2010/90015_Warner2010.pdf.

Webster, P.. et al., 2005. Changes in Tropical Cyclone Number , Duration , and Intensity in a Warming Environment. *Science*, 309, pp.1844–1846.

Wisse, J.S.P. & Arellano, J.V.-G. de A., 2004. Analysis of the role of the planetary boundary layer schemes during a severe convective storm. *Annales Geophysicae*, 22, pp.1861–1874.

WRF_User's_Guide, v3, 2012. Version 3 Modeling System User's Guide April 2012. , (April).

Wu, Y. et al., 2010. Changes in storm tracks and energy transports in a warmer climate simulated by the GFDL CM2.1 model. *Climate Dynamics*, 37(1), pp.53–72.

Yin, J.H., 2005. A consistent poleward shift of the storm tracks in simulations of 21st century climate. *Geophysical Research Lettersr*, 32, pp.2–5.

Yu, J., 2004. Identification and Applications of Coupled Climate Models. In *Environmental Systems*. [Ed. Achim Sydow], in Encyclopedia of Life Support Systems (EOLSS). Developed under the Auspices of the UNESCO, Eolss Publishers, Oxford , UK, [http://www.eolss.net] [Retrieved October 18, 2006]. Available at: http://www.eolss.net.

Zappa, G., Shaffrey, L.C. & Hodges, K.I., 2013. The ability of CMIP5 models to simulate North Atlantic extratropical cyclones. *Journal of Climate*, 26, pp.5379–5396.

Zeng, X. & Beljaars, A., 2005. A prognostic scheme of sea surface skin temperature for modeling and data assimilation. *Geophysical Research Letters*, 32(14), pp.1–4.

Zhang, J.A. et al., 2011. On the Characteristic Height Scales of the Hurricane Boundary Layer. *American Meteorological Society*, 139, pp.2523–2535.

Zhang, Y., Seidel, D.J. & Zhang, S., 2013. Trends in Planetary Boundary Layer Height over Europe height using a method based on the bulk Richardson and two climate models . The present study extends that. *American Meteorological Society*, 26, pp.10071–10076.

Zou, L.W. & Zhou, T.J., 2012. Development and evaluation of a regional ocean-atmosphere coupled model with focus on the western North Pacific summer monsoon simulation: Impacts of different atmospheric components. *Science China Earth Sciences*, 55(5), pp.802–815.

20th Century Reanalysis V2c data provided by the NOAA/OAR/ESRL PSD, Boulder, Colorado, USA, from their Web site at http://www.esrl.noaa.gov/psd/

Appendices

Appendix I WRF Pre-processing System input script (namelist.wps)

For historical experiments

```
&share
 wrf_core = 'ARW',
 max_dom = 1,
 start_date = '1960-01-01_03:00:00',
 end_date   = '1964-12-31_21:00:00',
 interval_seconds = 10800,
 io_form_geogrid = 2,
 debug_level = 1000,
/
&geogrid
 parent_id         =   1,
 parent_grid_ratio =   1,
 i_parent_start    =   1,
 j_parent_start    =   1,
 e_we              =  252,
 e_sn              =  236,
 geog_data_res     = '10m',
 dx = 27226.75,
 dy = 27226.75,
 map_proj = 'mercator',
 ref_lat   =  -43.5,
 ref_lon   =  175.0,
 truelat1  =  -30.5,
 truelat2  =  -60.0,
 stand_lon =  175.0,
 geog_data_path = '/m/raid3/nma/WPS_geog/'
/
&ungrib
 out_format = 'WPS',
 prefix = 'IPSL_hisfilename',
/
&metgrid
 constants_name = ‘IPSL_LAND',
 fg_name = 'IPSL_filename',
 io_form_metgrid = 2,
```

For scenario experiments: Respective RCP8.5 data path and their corresponding simulation dates are to be changed (as listed below)

```
start_date = '2095-01-01_03:00:00',
end_date   = '2099-12-31_21:00:00',
&metgrid
 fg_name = 'IPSL_rcpfilename',
```

Appendix II WRF input script (namelist.input)

```
&time_control
 run_days                            = 0,
 run_hours                           = 0,
 run_minutes                         = 0,
 run_seconds                         = 0,
 start_year                          = 1960,
 start_month                         = 11,
 start_day                           = 01,
 start_hour                          = 00,
 start_minute                        = 00,
 start_second                        = 00,
 end_year                            = 1960,
 end_month                           = 12,
 end_day                             = 01,
 end_hour                            = 00,
 end_minute                          = 00,
 end_second                          = 00,
 interval_seconds                    = 10800
 input_from_file                     = .true.,
 history_interval                    = 360,
 frames_per_outfile                  = 250,
 restart                             = .true.,
 restart_interval                    = 1440,
 io_form_restart                     = 2
 io_form_boundary                    = 2
 debug_level                         = 0
 auxinput4_inname                    = "wrflowinp_d<domain>",
 auxinput4_interval                  = 180
 io_form_auxinput4                   = 2
 io_form_auxinput2                   = 2
 iofields_filename                   = "d01",
 ignore_iofields_warning             = .false.,
 output_diagnostics                  = 1,
 auxhist3_outname                    = "wrfxtrm_d<domain>"
 io_form_auxhist3                    = 2
 auxhist3_interval                   = 60,
 frames_per_auxhist3                 = 1000,
 /
 &domains
 time_step                           = 90,
 time_step_fract_num                 = 0,
 time_step_fract_den                 = 1,
 max_dom                             = 1,
 s_we                                = 1,
 e_we                                = 252,
 s_sn                                = 1,
 e_sn                                = 236,
 s_vert                              = 1,
 e_vert                              = 34,
 num_metgrid_levels                  = 34,
 dx                                  = 27226.75,
 dy                                  = 27226.75,
 grid_id                             = 1,
 parent_id                           = 0,
 i_parent_start                      = 1,
 j_parent_start                      = 1,
 parent_grid_ratio                   = 1,
 parent_time_step_ratio              = 1,
 feedback                            = 1,
 smooth_option                       = 0,
```

```
nproc_x                             = 7,
nproc_y                             = 6,
num_metgrid_soil_levels             = 4,
max_ts_locs                         = 27,
ts_buf_size                         = 100,
/
&physics
mp_physics                          = 6,
ra_lw_physics                       = 4,
ra_sw_physics                       = 4,
radt                                = 30,
sf_sfclay_physics                   = 2,
sf_surface_physics                  = 2,
bl_pbl_physics                      = 2,
bldt                                = 0,
cu_physics                          = 2,
cudt                                = 5,
isfflx                              = 1,
ifsnow                              = 1,
icloud                              = 1,
surface_input_source                = 1,
num_soil_layers                     = 4,
sf_urban_physics                    = 0,
maxiens                             = 1,
maxens                              = 3,
maxens2                             = 3,
maxens3                             = 16,
ensdim                              = 144,
sst_update                          = 1,
tmn_update                          = 1,
sst_skin                            = 1,
bucket_mm                           = 100.0,
bucket_J                            = 1.e9,
/
&fdda
/
&dynamics
w_damping                           = 0,
diff_opt                            = 1,
km_opt                              = 4,
diff_6th_opt                        = 0,
diff_6th_factor                     = 0.12,
base_temp                           = 290.
damp_opt                            = 0,
zdamp                               = 5000.,
dampcoef                            = 0.2,
khdif                               = 0,
kvdif                               = 0,
non_hydrostatic                     = .true.,
moist_adv_opt                        = 1,
scalar_adv_opt                       = 1,
/
&bdy_control
spec_bdy_width                       = 5,
spec_zone                           = 1,
relax_zone                          = 4,
specified                           = .true., .false.,.false.,
nested                              = .false.,
/
&grib2
/
&namelist_quilt
nio_tasks_per_group                 = 0,
```

```
 nio_groups                      = 1,
 /
&tc
insert_bogus_storm               =.true.
remove_storm                     =.false.
latc_loc                         =-13.2
lonc_loc                         =178.6
vmax_meters_per_second           =60.0
rmax                             =100000.0
vmax_ratio                       =0.85
/
```

Appendix III ROMS standalone CPP options

SP14RRR2	South Pacific SP14, 0.25 Resolution, rcpr2
ATM_PRESS	Impose atmospheric pressure onto sea surface.
ANA_BSFLUX	Analytical kinematic bottom salinity flux.
ANA_BTFLUX	Analytical kinematic bottom temperature flux.
ASSUMED_SHAPE	Using assumed-shape arrays.
AVERAGES	Writing out time-averaged fields.
AVERAGES_FLUXES	Writing out time-averaged surface fluxes.
BULK_FLUXES	Surface bulk fluxes parameterization.
COOL_SKIN	Surface cool skin correction.
CURVGRID	Orthogonal curvilinear grid.
DIAGNOSTICS_TS	Computing and writing tracer diagnostic terms.
DJ_GRADPS	Parabolic Splines density Jacobian (Shchepetkin, 2002).
DOUBLE_PRECISION	Double precision arithmetic.
EAST_FSCHAPMAN	Eastern edge, free-surface, Chapman condition.
EAST_M2FLATHER	Eastern edge, 2D momentum, Flather condition.
EAST_M3NUDGING	Eastern edge, 3D momentum, passive/active outflow/inflow.
EAST_M3RADIATION	Eastern edge, 3D momentum, radiation condition.
EAST_TRADIATION	Eastern edge, tracers, radiation condition.
EMINUSP	Compute Salt Flux using E-P.
LMD_BKPP	KPP bottom boundary layer mixing.
LMD_CONVEC	LMD convective mixing due to shear instability.
LMD_DDMIX	LMD double-diffusive mixing.
LMD_MIXING	Large/McWilliams/Doney interior mixing.
LMD_NONLOCAL	LMD convective nonlocal transport.
LMD_RIMIX	LMD diffusivity due to shear instability.
LMD_SKPP	KPP surface boundary layer mixing.
LONGWAVE_OUT	Compute outgoing longwave radiation internally.
M3CLIMATOLOGY	Processing 3D momentum climatology data.
M3CLM_NUDGING	Nudging toward 3D momentum climatology.
MASKING	Land/Sea masking.
MIX_S_TS	Mixing of tracers along constant S-surfaces.
MIX_S_UV	Mixing of momentum along constant S-surfaces.
MPI	MPI distributed-memory configuration.
NONLINEAR	Nonlinear Model.
NONLIN_EOS	Nonlinear Equation of State for seawater.
NORTH_FSCHAPMAN	Northern edge, free-surface, Chapman condition.
NORTH_M2FLATHER	Northern edge, 2D momentum, Flather condition.
NORTH_M3NUDGING	Northern edge, 3D momentum, passive/active outflow/inflow.
NORTH_M3RADIATION	Northern edge, 3D momentum, radiation condition.
NORTH_TRADIATION	Northern edge, tracers, radiation condition.
POWER_LAW	Power-law shape time-averaging barotropic filter.
PROFILE	Time profiling activated .
RADIATION_2D	Use tangential phase speed in radiation conditions.
RAMP_TIDES	Ramping tidal forcing for one day.
!RST_SINGLE	Double precision fields in restart NetCDF file.
SALINITY	Using salinity.
SOLAR_SOURCE	Solar Radiation Source Term.
SOLVE3D	Solving 3D Primitive Equations.
SOUTH_FSCHAPMAN	Southern edge, free-surface, Chapman condition.
SOUTH_M2FLATHER	Southern edge, 2D momentum, Flather condition.
SOUTH_M3NUDGING	Southern edge, 3D momentum, passive/active outflow/inflow.
SOUTH_M3RADIATION	Southern edge, 3D momentum, radiation condition.
SOUTH_TRADIATION	Southern edge, tracers, radiation condition.
SPLINES	Conservative parabolic spline reconstruction.
SPONGE	Enhanced horizontal mixing in the sponge areas.
SSH_TIDES	Add tidal elevation to SSH climatology.
STATIONS	Writing out station data.
STATIONS_CGRID	Extracting station data at native C-grid locations.
TCLIMATOLOGY	Processing tracer climatology data.
TCLM_NUDGING	Nudging toward tracer climatology.
THREE_GHOST	Using three Ghost Points in halo regions.
TS_A4HADVECTION	Fourth-order Akima horizontal advection of tracers.

TS_A4VADVECTION	Fourth-order Akima vertical advection of tracers.
TS_DIF2	Harmonic mixing of tracers.
TS_DIF4	Biharmonic mixing of tracers.
UV_ADV	Advection of momentum.
UV_COR	Coriolis term.
UV_U3HADVECTION	Third-order upstream horizontal advection of 3D momentum.
UV_C4VADVECTION	Fourth-order centered vertical advection of momentum.
UV_QDRAG	Quadratic bottom stress.
UV_TIDES	Add tidal currents to 2D momentum climatologies.
UV_VIS2	Harmonic mixing of momentum.
UV_VIS4	Biharmonic mixing of momentum.
VAR_RHO_2D	Variable density barotropic mode.
WEST_FSCHAPMAN	Western edge, free-surface, Chapman condition.
WEST_M2FLATHER	Western edge, 2D momentum, Flather condition.
WEST_M3NUDGING	Western edge, 3D momentum, passive/active outflow/inflow.
WEST_M3RADIATION	Western edge, 3D momentum, radiation condition.
WEST_TRADIATION	Western edge, tracers, radiation condition.

Appendix IV Correlation and Regression analysis

The correlation and regression analysis that are performed are presented here sequentially from zone I to II to III, each accompanied for two different cases, T2T1 and T3T1 except for the zone-III.

A. Zone I (EAC pathway)

(a) Case study - T2 minus T1

Correlation												
	ΔStorm counts	*ΔStorm intensity*	*ΔStorm central pressure*	*Δgradient SST*	*Δ (SST-SAT)*	*Δ SST*	*Δ SAT*	*Δ Shum*	*Δ LHF*	*Δ PBLH*	*Δ Pratec*	*Δ Wspd*
Δ Storm counts	1.000											
Δ Storm intensity	0.940	1.000										
Δ Storm central pressure	0.909	0.925	1.000									
Δ gradient SST	0.010	0.012	-0.035	1.000								
Δ (SST-SAT)	0.355	0.248	0.282	0.066	1.000							
Δ SST	0.374	0.351	0.416	0.056	0.691	1.000						
Δ SAT	-0.038	0.079	0.109	-0.024	-0.531	0.244	1.000					
Δ Shum	0.181	0.140	0.075	-0.095	0.514	0.349	-0.280	1.000				
Δ LHF	0.093	0.178	0.273	-0.087	-0.262	0.179	0.562	-0.628	1.000			
Δ PBLH	0.310	0.267	0.274	0.023	0.652	0.864	0.139	0.651	-0.173	1.000		
Δ Pratec	0.479	0.489	0.560	0.037	0.698	0.852	0.061	0.428	0.203	0.750	1.000	
Δ Wspd	0.369	0.345	0.368	0.219	0.572	0.254	-0.470	0.431	-0.372	0.309	0.568	1.000

a) Storm counts								
Regression Statistics								
Multiple R	0.44531427							
R Square	0.19830480							
Adjusted R Square	0.17437360							
Standard Error	0.25060676							
Observations	70							
ANOVA								
	df	*SS*	*MS*	*F*	*Significance F*			
Regression	2	1.04084084	0.52042042	8.28645453	0.00060857			
Residual	67	4.20785126	0.06280375					
Total	69	5.24869210						
	Coefficients	*Standard Error*	*t Stat*	*P-value*	*Lower 95%*	*Upper 95%*	*Lower 95.0%*	*Upper 95.0%*
Intercept	0.10633290	0.03149891	3.37576400	0.00122850	0.04346080	0.16920500	0.04346080	0.16920500
Δ LHF	0.12969428	0.05702986	2.27414690	0.02616558	0.01586220	0.24352636	0.01586220	0.24352636
Δ Wspd	0.22611808	0.05680396	3.98067470	0.00017156	0.11273690	0.33949925	0.11273690	0.33949925

b) Storm intensity								
Regression Statistics								
Multiple R	0.521465842							
R Square	0.271926624							
Adjusted R Square	0.23883238							
Standard Error	0.263274699							
Observations	70							
ANOVA								
	df	*SS*	*MS*	*F*	*Significance F*			
Regression	3	1.708593563	0.569531188	8.216734636	0.000100417			
Residual	66	4.574695429	0.069313567					
Total	69	6.283288992						
	Coefficients	*Standard Error*	*t Stat*	*P-value*	*Lower 95%*	*Upper 95%*	*Lower 95.0%*	*Upper 95.0%*
Intercept	0.250710079	0.033113018	7.571344806	1.54894E-10	0.184597805	0.316822353	0.184597805	0.316822353
Δ Shum	0.116124639	0.057999653	2.002160912	0.049379588	0.000324595	0.231924683	0.000324595	0.231924683
Δ LHF	0.269106552	0.072230741	3.725651262	0.000406015	0.124893224	0.41331988	0.124893224	0.41331988
Δ Wspd	0.217601142	0.062036453	3.507633506	0.000818879	0.093741367	0.341460917	0.093741367	0.341460917

c) Storm central pressure

Regression Statistics	
Multiple R	0.456308321
R Square	0.208217284
Adjusted R Square	0.184581979
Standard Error	0.27391028
Observations	70

ANOVA

	df	*SS*	*MS*	*F*	*Significance F*
Regression	2	1.321911026	0.660955513	8.80958737	0.000401145
Residual	67	5.026798363	0.075026841		
Total	69	6.348709388			

	Coefficients	*Standard Error*	*t Stat*	*P-value*	*Lower 95%*	*Upper 95%*	*Lower 95.0%*	*Upper 95.0%*
Intercept	0.52875518	0.038873306	13.60201209	5.99623E-21	0.451163736	0.606346623	0.451163736	0.606346623
Δ (SST-SAT)	0.217182631	0.064522605	3.36599289	0.001266267	0.088394971	0.34597029	0.088394971	0.34597029
Δ LHF	0.197854965	0.059934901	3.301164466	0.001545957	0.078224402	0.317485528	0.078224402	0.317485528

(b) Case study – T3 minus T1

Correlation

	ΔStorm counts	*ΔStorm intensity*	*ΔStorm central pressure*	*Δgradient SST*	*Δ (SST-SAT)*	*Δ SST*	*Δ SAT*	*Δ Shum*	*Δ LHF*	*Δ PBLH*	*Δ Pratec*	*Δ Wspd*
Δ Storm counts	1.000											
Δ Storm intensity	0.878	1.000										
Δ Storm central pressure	0.748	0.872	1.000									
Δ gradient SST	0.177	0.162	0.243	1.000								
Δ (SST-SAT)	-0.009	0.011	-0.035	-0.604	1.000							
Δ SST	0.159	0.180	0.313	0.212	0.306	1.000						
Δ SAT	0.166	0.175	0.336	0.566	-0.273	0.832	1.000					
Δ Shum	0.431	0.458	0.690	0.531	-0.023	0.647	0.667	1.000				
Δ LHF	0.007	0.062	0.158	-0.496	0.106	0.193	0.133	-0.149	1.000			
Δ PBLH	0.118	0.084	0.108	0.453	0.196	0.175	0.062	0.351	-0.563	1.000		
Δ rain	0.419	0.495	0.752	0.230	0.122	0.361	0.293	0.795	0.115	0.333	1.000	
Δ wspd	-0.115	-0.178	-0.349	-0.303	-0.302	-0.576	-0.406	-0.531	0.010	-0.480	-0.619	1.000

a) Storm counts

Regression Statistics	
Multiple R	0.431376365
R Square	0.186085569
Adjusted R Square	0.174116239
Standard Error	0.281827987
Observations	70

ANOVA

	df	*SS*	*MS*	*F*	*Significance F*
Regression	1	1.234841152	1.234841152	15.54686607	0.000192758
Residual	68	5.401036964	0.079427014		
Total	69	6.635878116			

	Coefficients	*Standard Error*	*t Stat*	*P-value*	*Lower 95%*	*Upper 95%*	*Lower 95.0%*	*Upper 95.0%*
Intercept	0.151712287	0.034742999	4.366700938	4.40628E-05	0.082383712	0.221040863	0.082383712	0.221040863
Δ Shum	0.209617405	0.053162563	3.942951442	0.000192758	0.103533162	0.315701648	0.103533162	0.315701648

b) Storm intensity

Regression Statistics	
Multiple R	0.52893294
R Square	0.279770055
Adjusted R Square	0.24703233
Standard Error	0.262660708
Observations	70

ANOVA

	df	*SS*	*MS*	*F*	*Significance F*
Regression	3	1.768740861	0.589580287	8.545800186	7.11469E-05
Residual	66	4.553382725	0.068990647		
Total	69	6.322123586			

	Coefficients	*Standard Error*	*t Stat*	*P-value*	*Lower 95%*	*Upper 95%*	*Lower 95.0%*	*Upper 95.0%*
Intercept	0.004528592	0.043367355	0.104423986	0.917149578	-0.082057126	0.091114311	-0.082057126	0.091114311
Δ Shum	0.33470781	0.070281416	4.762394196	1.08714E-05	0.194386434	0.475029185	0.194386434	0.475029185
Δ SAT	-0.158279297	0.072290265	-2.189496697	0.032101465	-0.302611469	-0.013947126	-0.302611469	-0.013947126
Δ LHF	0.105700972	0.055986557	1.887970569	0.063426966	-0.006079796	0.21748174	-0.006079796	0.21748174

c) Storm central pressure

Regression Statistics	
Multiple R	0.797120933
R Square	0.635401783
Adjusted R Square	0.618829136
Standard Error	0.282366426
Observations	70

ANOVA

	df	*SS*	*MS*	*F*	*Significance F*
Regression	3	9.170730617	3.056910206	38.34039375	1.82651E-14
Residual	66	5.262232697	0.079730798		
Total	69	14.43296331			

	Coefficients	*Standard Error*	*t Stat*	*P-value*	*Lower 95%*	*Upper 95%*	*Lower 95.0%*	*Upper 95.0%*
Intercept	0.369115884	0.060555707	6.095476471	6.32922E-08	0.248212515	0.490019253	0.248212515	0.490019253
Δ SST	-0.311446414	0.077207432	-4.033891619	0.000144904	-0.465596026	-0.157296802	-0.465596026	-0.157296802
Δ Shum	0.733943034	0.075086058	9.774691268	1.86878E-14	0.584028882	0.883857185	0.584028882	0.883857185
Δ LHF	0.297996833	0.061849913	4.818063933	8.85037E-06	0.174509498	0.421484168	0.174509498	0.421484168

B. Zone II (Tasman Sea)

(a) Case study - T2 minus T1

Correlation

	ΔStorm counts	*ΔStorm intensity*	*ΔStorm central pressure*	*Δgradient SST*	*Δ (SST-SAT)*	*Δ SST*	*Δ SAT*	*Δ Shum*	*Δ LHF*	*Δ PBLH*	*Δ Pratec*	*Δ Wspd*
Δ Storm counts	1.000											
Δ Storm intensity	0.453	1.000										
Δ Storm central pressure	-0.420	0.431	1.000									
Δ gradient SST	-0.068	0.005	0.293	1.000								
Δ (SST-SAT)	-0.102	0.085	0.271	-0.083	1.000							
Δ SST	-0.059	0.280	0.356	0.096	0.695	1.000						
Δ SAT	0.090	0.123	-0.069	0.198	-0.786	-0.102	1.000					
Δ Shum	0.233	0.257	-0.176	0.039	-0.092	0.015	0.140	1.000				
Δ LHF	0.021	-0.222	-0.306	-0.107	-0.368	-0.375	0.187	-0.664	1.000			
Δ PBLH	0.536	0.176	-0.462	-0.190	-0.412	-0.142	0.448	-0.117	0.483	1.000		
Δ Pratec	0.174	0.173	-0.350	-0.102	-0.376	-0.194	0.354	0.834	-0.228	0.061	1.000	
Δ Wspd	0.587	0.258	-0.383	-0.212	-0.254	-0.073	0.290	0.274	-0.091	0.739	0.246	1.000

a) Storm counts

Regression Statistics	
Multiple R	0.689794874
R Square	0.475816968
Adjusted R Square	0.44355955
Standard Error	0.27989709
Observations	70

ANOVA

	df	*SS*	*MS*	*F*	*Significance F*
Regression	4	4.622395374	1.155598843	14.75062191	1.25815E-08
Residual	65	5.092254772	0.078342381		
Total	69	9.714650146			

	Coefficients	*Standard Error*	*t Stat*	*P-value*	*Lower 95%*	*Upper 95%*	*Lower 95.0%*	*Upper 95.0%*
Intercept	0.068125932	0.036120544	1.88607157	0.063754494	-0.004011777	0.140263641	-0.004011777	0.140263641
Δ LHF	0.541868983	0.139104274	3.895415765	0.000234115	0.264058563	0.819679402	0.264058563	0.819679402
Δ Shum	0.882292362	0.225609724	3.910701828	0.000222448	0.431718629	1.332866095	0.431718629	1.332866095
Δ Wspd	0.309256599	0.057653627	5.36404414	1.15855E-06	0.194114355	0.424398843	0.194114355	0.424398843
Δ Pratec	-0.592781984	0.170769017	-3.471250204	0.000925727	-0.933831261	-0.251732707	-0.933831261	-0.251732707

b) Storm intensity

Regression Statistics	
Multiple R	0.451526416
R Square	0.203876104
Adjusted R Square	0.167688654
Standard Error	0.243028217
Observations	70

ANOVA

	df	*SS*	*MS*	*F*	*Significance F*
Regression	3	0.998258471	0.332752824	5.633889786	0.001685572
Residual	66	3.898139155	0.059062714		
Total	69	4.896397626			

	Coefficients	*Standard Error*	*t Stat*	*P-value*	*Lower 95%*	*Upper 95%*	*Lower 95.0%*	*Upper 95.0%*
Intercept	-0.017657929	0.029244881	-0.60379554	0.548049331	-0.076047217	0.04073136	-0.076047217	0.04073136
Δ Shum	0.127479657	0.050063588	2.546354775	0.013226557	0.027524478	0.227434835	0.027524478	0.227434835
Δ SST	0.185857067	0.066220382	2.806644423	0.006573773	0.053643808	0.318070327	0.053643808	0.318070327
Δ PBLH	0.115876721	0.051193379	2.263509931	0.026898176	0.013665843	0.218087599	0.013665843	0.218087599

c) Storm central pressure

Regression Statistics	
Multiple R	0.654417222
R Square	0.4282619
Adjusted R Square	0.402273804
Standard Error	0.258531254
Observations	70

ANOVA

	df	*SS*	*MS*	*F*	*Significance F*
Regression	3	3.30432188	1.101440627	16.47915679	4.24864E-08
Residual	66	4.411335014	0.066838409		
Total	69	7.715656894			

	Coefficients	*Standard Error*	*t Stat*	*P-value*	*Lower 95%*	*Upper 95%*	*Lower 95.0%*	*Upper 95.0%*
Intercept	-0.481826892	0.033330474	-14.45604684	3.94713E-22	-0.54837333	-0.415280454	-0.54837333	-0.415280454
Δ LHF	-0.441316252	0.078219095	-5.642052616	3.8099E-07	-0.597485715	-0.285146789	-0.597485715	-0.285146789
Δ Shum	-0.321428173	0.073814157	-4.354559948	4.75024E-05	-0.468802893	-0.174053453	-0.468802893	-0.174053453
Δ Wspd	-0.159106453	0.052940289	-3.005394515	0.003747461	-0.26480515	-0.053407757	-0.26480515	-0.053407757

(b) Case study – T3 minus T1

Correlation

	ΔStorm counts	*ΔStorm intensity*	*ΔStorm central pressure*	*Δgradient SST*	*Δ (SST-SAT)*	*Δ SST*	*Δ SAT*	*Δ Shum*	*Δ LHF*	*Δ PBLH*	*Δ Pratec*	*Δ Wspd*
Δ Storm counts	1.000											
Δ Storm intensity	0.722	1.000										
Δ Storm central pressure	-0.378	0.043	1.000									
Δ gradient SST	-0.095	-0.104	0.400	1.000								
Δ (SST-SAT)	-0.470	-0.243	0.544	-0.080	1.000							
Δ SST	-0.299	-0.258	0.580	0.413	0.246	1.000						
Δ SAT	0.095	-0.041	0.093	0.418	-0.541	0.682	1.000					
Δ Shum	0.234	0.241	-0.075	0.148	-0.102	-0.499	-0.356	1.000				
Δ LHF	0.306	0.082	-0.527	-0.464	-0.438	0.057	0.380	-0.597	1.000			
Δ PBLH	0.331	0.116	-0.436	-0.019	-0.731	0.165	0.695	-0.486	0.821	1.000		
Δ rain	-0.423	-0.233	0.503	0.022	0.719	0.071	-0.480	0.198	-0.645	-0.890	1.000	
Δ wspd	0.331	0.228	-0.550	0.078	-0.548	-0.675	-0.172	0.245	0.086	0.313	-0.512	1.000

a) Storm counts

Regression Statistics	
Multiple R	0.602802521
R Square	0.363370879
Adjusted R Square	0.344367025
Standard Error	0.261184102
Observations	70

ANOVA

	df	*SS*	*MS*	*F*	*Significance F*
Regression	2	2.608746605	1.304373302	19.12090422	2.69276E-07
Residual	67	4.570548038	0.068217135		
Total	69	7.179294643			

	Coefficients	*Standard Error*	*t Stat*	*P-value*	*Lower 95%*	*Upper 95%*	*Lower 95.0%*	*Upper 95.0%*
Intercept	0.17430073	0.032072006	5.434668801	8.27249E-07	0.110284738	0.238316722	0.110284738	0.238316722
Δ LHF	0.421655999	0.074008271	5.697417201	2.95439E-07	0.273934871	0.569377127	0.273934871	0.569377127
Δ Shum	0.287951081	0.054019514	5.330501174	1.23882E-06	0.18012768	0.395774481	0.18012768	0.395774481

b) Storm intensity

Regression Statistics	
Multiple R	0.370822719
R Square	0.137509489
Adjusted R Square	0.111763504
Standard Error	0.338963142
Observations	70

ANOVA

	df	*SS*	*MS*	*F*	*Significance F*
Regression	2	1.227320818	0.613660409	5.341007041	0.007043198
Residual	67	7.6980328	0.114896012		
Total	69	8.925353618			

	Coefficients	*Standard Error*	*t Stat*	*P-value*	*Lower 95%*	*Upper 95%*	*Lower 95.0%*	*Upper 95.0%*
Intercept	-0.007803293	0.041622855	-0.187476158	0.851853914	-0.090882859	0.075276273	-0.090882859	0.075276273
Δ Shum	0.223420872	0.070106197	3.186891901	0.00218538	0.083488317	0.363353427	0.083488317	0.363353427
Δ LHF	0.238620988	0.096047486	2.4844064	0.015482341	0.046909404	0.430332572	0.046909404	0.430332572

c) Storm central pressure

Regression Statistics	
Multiple R	0.824990335
R Square	0.680609053
Adjusted R Square	0.666091282
Standard Error	0.248331333
Observations	70

ANOVA

	df	*SS*	*MS*	*F*	*Significance F*
Regression	3	8.673254602	2.891084867	46.88110068	2.39144E-16
Residual	66	4.070117776	0.061668451		
Total	69	12.74337238			

	Coefficients	*Standard Error*	*t Stat*	*P-value*	*Lower 95%*	*Upper 95%*	*Lower 95.0%*	*Upper 95.0%*
Intercept	-0.679825685	0.042504339	-15.99426564	2.15082E-24	-0.764688336	-0.594963035	-0.764688336	-0.594963035
Δ LHF	-0.382541927	0.063940788	-5.982752748	9.92215E-08	-0.51020383	-0.254880024	-0.51020383	-0.254880024
Δ (SST-SAT)	0.541653038	0.068527182	7.904207121	3.92948E-11	0.404834105	0.67847197	0.404834105	0.67847197
Δ SAT	0.496605441	0.065100174	7.628327407	1.2249E-10	0.36662875	0.626582131	0.36662875	0.626582131

C. Zone III (East of NZ)

(a) Case study - T2 minus T1

Correlation												
	Δ Storm counts	Δ Storm intensity	Δ Storm central pressure	Δ gradient SST	Δ (SST-SAT)	Δ SST	Δ SAT	Δ Shum	Δ LHF	Δ PBLH	Δ Pratec	Δ Wspd
Δ Storm counts	1.000											
Δ Storm intensity	0.662	1.000										
Δ Storm central pressure	0.298	0.436	1.000									
Δ gradient SST	0.057	0.104	0.067	1.000								
Δ (SST-SAT)	-0.266	-0.252	-0.449	0.026	1.000							
Δ SST	-0.294	-0.161	-0.670	0.060	0.648	1.000						
Δ SAT	0.033	0.154	-0.128	0.030	-0.602	0.218	1.000					
Δ Shum	-0.098	0.046	-0.664	-0.036	0.008	0.661	0.683	1.000				
Δ LHF	-0.187	0.026	-0.453	-0.135	0.324	0.194	-0.212	0.289	1.000			
Δ PBLH	-0.128	-0.230	-0.298	0.005	0.076	0.565	0.496	0.469	-0.280	1.000		
Δ Pratec	-0.118	0.020	-0.733	-0.155	0.213	0.648	0.407	0.892	0.512	0.203	1.000	
Δ Wspd	-0.113	-0.324	-0.333	0.225	0.412	0.584	0.084	0.292	-0.280	0.730	0.115	1.000

a) Storm counts

Regression Statistics	
Multiple R	0.383330998
R Square	0.146942654
Adjusted R Square	0.094446818
Standard Error	0.310791334
Observations	70

ANOVA

	df	*SS*	*MS*	*F*	*Significance F*
Regression	4	1.081485772	0.270371443	2.799129678	0.032990752
Residual	65	6.278431449	0.096591253		
Total	69	7.359917221			

	Coefficients	*Standard Error*	*t Stat*	*P-value*	*Lower 95%*	*Upper 95%*	*Lower 90.0%*	*Upper 90.0%*
Intercept	-0.049864427	0.048979675	-1.018063654	0.312422177	-0.147683593	0.047954739	-0.131593675	0.031864821
Δ SAT	-0.51165883	0.239039677	-2.140476576	0.036073135	-0.989054031	-0.034263629	-0.910529035	-0.112788625
Δ (SST-SAT)	-0.419124759	0.146568638	-2.859580085	0.005696635	-0.711842543	-0.126406976	-0.663694462	-0.174555056
Δ LHF	-0.200540917	0.109472058	-1.831891352	0.071549834	-0.419171714	0.018089881	-0.383209931	-0.017871902
Δ Shum	0.275061756	0.160765941	1.710945453	0.091860032	-0.046009999	0.596133511	0.006801923	0.543321589

b) Storm intensity

Regression Statistics	
Multiple R	0.384831966
R Square	0.148095642
Adjusted R Square	0.122665661
Standard Error	0.330382351
Observations	70

ANOVA

	df	*SS*	*MS*	*F*	*Significance F*
Regression	2	1.271334755	0.635667378	5.823663147	0.004656859
Residual	67	7.313217338	0.109152498		
Total	69	8.584552093			

	Coefficients	*Standard Error*	*t Stat*	*P-value*	*Lower 95%*	*Upper 95%*	*Lower 95.0%*	*Upper 95.0%*
Intercept	0.011331553	0.04077349	0.277914729	0.781933637	-0.070052673	0.092715779	-0.070052673	0.092715779
Δ SAT	0.262966976	0.096090294	2.736665316	0.007938789	0.071169945	0.454764006	0.071169945	0.454764006
Δ PBLH	-0.244533969	0.078191814	-3.127360244	0.002609636	-0.400605482	-0.088462456	-0.400605482	-0.088462456

c) Storm central pressure								
Regression Statistics								
Multiple R	0.780600948							
R Square	0.609337841							
Adjusted R Square	0.59158047							
Standard Error	0.296391037							
Observations	70							
ANOVA								
	df	*SS*	*MS*	*F*	*Significance F*			
Regression	3	9.043381898	3.014460633	34.31464288	1.74788E-13			
Residual	66	5.797944698	0.087847647					
Total	69	14.8413266						
	Coefficients	*Standard Error*	*t Stat*	*P-value*	*Lower 95%*	*Upper 95%*	*Lower 95.0%*	*Upper 95.0%*
Intercept	-0.592826696	0.046744797	-12.68219648	2.33843E-19	-0.686155694	-0.499497698	-0.686155694	-0.499497698
Δ Shum	-0.242334976	0.082122294	-2.950903632	0.004382054	-0.406297426	-0.078372526	-0.406297426	-0.078372526
Δ LHF	-0.281070964	0.079656569	-3.528534678	0.000766404	-0.440110435	-0.122031494	-0.440110435	-0.122031494
Δ SST	-0.380797409	0.095162773	-4.001537557	0.000161777	-0.570796015	-0.190798803	-0.570796015	-0.190798803

(b) Case study – T3 minus T1

Correlation												
	ΔStorm counts	*ΔStorm intensity*	*ΔStorm central pressure*	*Δgradient SST*	*Δ (SST-SAT)*	*Δ SST*	*Δ SAT*	*Δ Shum*	*Δ LHF*	*Δ PBLH*	*Δ Pratec*	*Δ Wspd*
Δ Storm counts	1.000											
Δ Storm intensity	0.697	1.000										
Δ Storm central pressure	0.305	0.381	1.000									
Δ gradient SST	0.064	0.152	0.218	1.000								
Δ (SST-SAT)	0.046	-0.079	0.245	-0.133	1.000							
Δ SST	0.067	-0.167	0.408	0.116	0.534	1.000						
Δ SAT	0.051	-0.148	0.331	0.220	0.014	0.853	1.000					
Δ Shum	0.072	0.166	0.140	0.192	-0.127	-0.553	-0.575	1.000				
Δ LHF	-0.090	0.023	-0.456	-0.088	-0.006	-0.431	-0.506	0.080	1.000			
Δ PBLH	-0.081	-0.140	-0.479	0.053	-0.085	0.369	0.489	-0.620	0.026	1.000		
Δ rain	-0.183	-0.135	-0.749	-0.108	-0.291	-0.273	-0.143	0.021	0.348	0.500	1.000	
Δ wspd	-0.088	0.044	-0.743	-0.036	-0.280	-0.385	-0.283	0.030	0.402	0.622	0.688	1.000

c) Storm central pressure								
Regression Statistics								
Multiple R	0.859640104							
R Square	0.738981109							
Adjusted R Square	0.722918408							
Standard Error	0.206367216							
Observations	70							
ANOVA								
	df	*SS*	*MS*	*F*	*Significance F*			
Regression	4	7.837113991	1.959278498	46.00603026	2.75468E-18			
Residual	65	2.768182815	0.042587428					
Total	69	10.60529681						
	Coefficients	*Standard Error*	*t Stat*	*P-value*	*Lower 95%*	*Upper 95%*	*Lower 95.0%*	*Upper 95.0%*
Intercept	-0.384541394	0.055568623	-6.920117392	2.4002E-09	-0.495519598	-0.273563191	-0.495519598	-0.273563191
Δ Shum	0.182630228	0.061659665	2.961907571	0.004266223	0.059487374	0.305773081	0.059487374	0.305773081
Δ SST	0.310635782	0.050216507	6.185929735	4.62475E-08	0.210346493	0.410925071	0.210346493	0.410925071
Δ PBLH	-0.149130535	0.065709346	-2.269548295	0.026559787	-0.280361161	-0.017899908	-0.280361161	-0.017899908
Δ rain	-0.382881179	0.074501417	-5.139246957	2.72761E-06	-0.531670783	-0.234091576	-0.531670783	-0.234091576